Chemical control of the photoluminescent properties of up-converting phosphors

Thesis

Chemical Control of the Photoluminescent Properties of Up-Converting Phosphors

By

Maria del Puy Rebollo Pedruelo

A thesis submitted to the Open University in partial fulfilment for the Degree of Doctor of Philosophy

Department of Chemistry, Open University
Walton Hall
Milton Keynes
MK7 6AA

November 2006

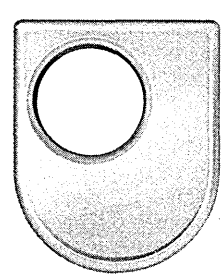

To Oscar, for lighting my life up.

Abstract

Up-conversion luminescence of Er^{3+} based phosphors was studied in the following host lattices: Y_2O_3, Gd_2O_3, $Gd_{2-x}Y_xO_3$, and YVO_4, with a view to developing an understanding of how emission can be tailored by manipulating the local chemical environment of the activator ion.

Laser induced luminescence measurements of Y_2O_3:Er phosphors showed evidence of Stokes and Anti-Stokes emission bands arising from excited levels under 632.8 nm radiation. Emission from $^4F_{7/2} \rightarrow {}^4I_{15/2}$ transitions were found to be weaker in Gd_2O_3 phosphors and were not detected in YVO_4 hosts. Relative intensity of Stokes / Anti-Stokes radiation were studied as a function of the host lattice, and variations found as a consequence of crystal field changes in the activator environment.

This work was extended to an investigation of the effect of co-dopants. Low levels of Yb^{3+} used as sensitizer, enhanced luminescence from $^4F_{7/2} \rightarrow {}^4I_{15/2}$ and $^4F_{9/2} \rightarrow {}^4I_{15/2}$ transitions, and a novel relaxation mechanism involving energy transfer from excited states is proposed to account for the variation observed in the intensity of the emission bands. Eu^{3+} used as co-dopant produced energy loss due to resonant energy transfer. This phenomenon was demonstrated by undertaking thermal studies on YVO_4:Er,Eu co-doped phosphors. Enhancement of $^4H_{11/2}$ transitions from Er^{3+} ions in S_6 symmetry sites was observed together with $^4F_{7/2} \rightarrow {}^4I_{15/2}$ transition activation with increasing Eu^{3+} concentration.

With a view to producing phosphor powders suitable for device application, wet chemical routes were investigated in order to prepare the materials studied in this work. The synthetic approaches studied were urea co-precipitation and combustion synthesis, the reaction conditions were carefully manipulated in order to optimise the composition and morphology of the product. Spherical uniform particles in the 300 – 600 nm range were routinely prepared.

Maria del Puy Rebollo Pedruelo

Table of Contents

Chapter 3 Experimental

Chapter 4 Wet Chemical Preparation and Characterisation of Rare-Earth Doped Yttria

List of Figures

List of Tables

Chapter 1 Introduction

Introduction

The phenomenon of luminescence where light is emitted after initial excitation is an inherent property of a class of compounds called phosphors. The aforementioned process is different to an incandescent source of light where heat is involved.

Luminescence has been known since ancient times, but an understanding of the phenomenon has only been achieved in the last few centuries. The first historical references to luminescence can be found in ancient books from China and India where naturally occurring luminescence is mentioned. The Chinese referred to luminescence observed in fireflies and glow-worms in the book "Shih Ching" (Book of Odes) written sometime in the period 1500-1000 BC. Similarly references to luminescence can be found in the "Vedas", the sacred books of India (of similar antiquity) by the word "khadoyta" (glow-worms in Sanskrit), which is used frequently. Aristotle (384-322 BC), in his treatise "De Coloribus" (About Colours), introduced the idea of light of non incandescent origin and stated that "Some bodies, though they are not fire, nor participate in any way of nature of fire, yet seem to produce light" which is a very reasonable definition of the process of luminescence.

In 188-140 B.C the luminescence phenomena was mentioned by Zhang Xian, who found some seashells near a volcano (which is thought to have been a source of sulphur) that emitted light[1]. This one may have been the first made phosphor.

Meanwhile, the production of phosphor materials was accidentally discovered in 1602 by the alchemist Vincentinus Casciarolo when sulphur-rich barium sulphate ($BaSO_4$) was synthesised by heating a stone he found close to a volcano ("Bologna stone") with coal, and observed a glow in the dark after the product had cooled. It gave a red emission after irradiation by sunlight which would have been an example of photoluminescence[2].

Ovidio Montalbani, professor of astronomy and mathematics, published (in 1634) a brief report on the various colours of the light from the "Bologna stone" and he realized that the light was produced by the process of burning[3]. But it was Fortunius Licetus who made the most important contribution to the subject in 1640, with a lengthy and detailed treatise[4]. It was the first monograph on the Bolognian 'stone', with the title 'stony phosphorus'. This essay led to a controversy with Galileo Galilei, because Licetus maintained that moonlight was caused by the same reason as light emitted from the "Bologna stone", Galileo believed that the reason was the reflection of the sun.

However, it was not until the 19th century that fluorescent effects were controlled and put to use. In 1852 the true science of luminescence was brought to life by George Stokes who developed what is called 'Stokes Law'. But it was not until 1888 that the term 'luminescenz' was first used by Eilhard Wiedemann, a German physicist, to refer to all light phenomena, which are not solely caused by a rise in temperature. Nowadays, the word luminescence is defined as a phenomenon in which the electronic state of a substance is excited by some kind of external energy and the excitation energy is emitted as light[5]. The word phosphor was first used in Greece, meaning "light bearer", which was the ancient name for the planet Venus, and it is used to refer to microcrystalline solid luminescent materials. The word phosphor itself is not clearly defined but it normally refers to inorganic phosphors, usually those in powder form and synthesised for the purpose of practical applications.

Scientific research on phosphors has a long history going back more than 100 years. A ZnS based phosphor that was to have a later application in television tubes was first prepared accidentally by Theodore Sidot in 1866[5]. This may be considered the beginning of scientific research and synthesis of phosphors. Lenard was the first to describe the importance of activator ions in phosphors in 1890. He established the principle that phosphors are compounds synthesised by introducing an impurity (activator) into the

materials (host). He not only tested heavy metals but also several rare-earth ions as potential activators. Pohl and co-workers in cooperation with F. Seitz in the U.S introduced the configurational coordinate model of luminescence and established the basics of present day luminescent physics. Leverenz and co-workers also investigated many practical phosphors with the purpose of obtaining materials with desirable characteristics to be used in television tubes. These studies mainly involved ZnS type phosphors[6].

All of the early 1950's electronic displays made use of phosphor systems, but the colour gamut that was available was limited, thus only monochrome or black and white was used. Although good green and efficient blue emitters were available, the development of a saturated red proved to be more difficult. It was not until the 60's when intensive phosphor research started to try to find a saturated red phosphor that would lead to a three-colour television. This intensive research involved a more detailed knowledge of rare-earth based phosphors and by 1964, Levine and Palilla[7] produced a red phosphor based on europium (YVO_4:Eu). It became the first red primary colour used in colour TV picture tube screens. They claimed improved brightness, thus opening the door for the industrial use of yttrium oxide and europium oxide and subsequently other rare earths. For the last forty years, intensive research has been carried out to develop better quality and higher resolution displays. The green and the blue phosphors used as primary colours have not undergone much change, but the red phosphor has shifted from YVO_4:Eu to other systems such as Y_2O_3:Eu, Gd_2O_3:Eu, and finally Y_2O_2S:Eu[8].

The conventional synthesis of yttrium oxide based phosphors involved solid state reactions[9] between powder oxides or reactants (such as oxalates) that decomposed thermally into oxides. These powders were blended and calcined at high temperatures up to ~1500 °C. With the use of solid state techniques the final particle sizes were in the range between 5-20 μm, and were very irregular without a defined shaped. However, some characteristics such as grain size and shape appeared to be relevant to the final

performance of the phosphor. Therefore, a necessity for a new method of synthesis that would lead to a defined shape and smaller particle size was recognised. For an improvement on the morphology of a phosphor researchers looked back to the methods of synthesis of uniform monodispersed colloidal particles. In general, a powder preparation method should meet several important criteria such as being simple, reproducible, and economically flexible. Although several novel methods are available for preparing oxide powders, only a few appear to have any potential for industrial application. The most common approach employs precipitation from homogeneous solutions. Well-defined particles of submicrometre size can be obtained by decomposition of urea at elevated temperatures in the presence of solutions of the rare-earth salts. In 1988, Sordelet and Akinc[10] prepared spherical monosized Y_2O_3 precursor particles by homogeneous precipitation from aqueous solution by reaction with the thermal decomposition products of urea. Since then, Sordelet and Matijevic[11,12,13] have published several articles preparing uniform yttrium, lanthanum, cerium and neodymium based carbonate particles using homogeneous precipitation. In 1991, Matijevic[14] produced a patent for the synthesis of uniform colloidal particles of rare earth oxides using the above homogeneous precipitation method.

Not long after that, in 1995, Nishisu and Kobayashi[15] applied the urea homogeneous precipitation method used for the synthesis of materials such as ceramics to phosphors. They published a patent to produce a fluorescent material of spherical particles consisting of Y_2O_3 and Eu_2O_3. The particles had a very narrow size distribution and much smaller particle sizes than the commercial red phosphors. Over the last decade, variations of this method and other new methods have been used to synthesise uniform Y_2O_3:Eu particles. These include: combustion synthesis[16], sol-gel methods using spin coating[17], and forced hydrolysis[18].

Initial research on up-conversion phosphors did not start until the late 1950's. The generation of visible luminescence in rare earth ion doped materials as a result of successive photon absorption in excited state was proposed in 1959[19].

Later, up-conversion luminescence properties were improved by Auzel[20] in $NaWO_4$ crystals using Yb^{3+} as a sensitizer. The Yb^{3+} is excited and the energy is transferred to ions such as Er^{3+} and Tm^{3+} to emit visible luminescence. Shortly after, it was found that fluoride materials such as LaF_3 and YF_3 proved to be more suitable host lattices for rare-earth doped up-converting phosphors[21]. Much of the work was aimed at producing up-converting phosphor lamps by coupling the halide Er^{3+} and Yb^{3+} doped phosphors with light emitting diodes (LEDs). However, these devices could not compete with more efficient systems as GaP LEDs, and therefore the interest in anti-Stokes materials waned[22,23].

In 1974, Sommerdijk et al[24] studied phosphors for the up-conversion of infrared light into visible. A year after, Bril and co-workers[25] published a study on the efficiency of Yb^{3+}-Er^{3+} activated up-conversion phosphors. The efficiency is dependent on the excitation power density of the infrared excitation, as multiple infrared quanta are involved in the excitation.

In recent years, renewed interest has been directed towards up-conversion materials. At the present time, the most important applications of infrared up-conversion materials are: the detection of infrared light from laser diodes[26], the production of infrared up-conversion lasers pumped with laser diodes[27], and in the area of optical fiber based communications. The critical component in this application is the Er^{3+} ion doped fiber amplifier[28].

Not only infrared radiation, but also red light have been used to study the green up-conversion emission from Er^{3+} phosphor powders. From 1995[29,30] , Silver et al carried out numerous studies on anti-Stokes Y_2O_3:RE^{3+} phosphors, assessing the effect of particle size

and temperature in luminescence using red light. A natural extension of these studies was to investigate the effect of the crystal lattice and the co-dopants on the anti-Stokes properties of the activator. It is also important to ascertain if energy transfer between different ions occurs, when the energy supplied for the excitation does not match the energy difference between ground level and first excited state of any of the co-dopants. Hence the aim of this thesis was an in-depth investigation of the anti-Stokes properties of Er^{3+} ions in lattices with different symmetries (cubic, monoclinic and tetragonal) and the effect produced by the addition of co-dopants to red light excitation.

The background for this thesis is explained, and naturally splits into two parts. The first introduces luminescence and describes the properties of phosphors, and will be covered in this chapter. The second introduces the basic theoretical background needed to understand the materials and processes reported in this thesis and will be the subject of Chapter 2.

1.2 What is a phosphor?

Luminescent materials are often called phosphors, which are solids able to convert certain types of energy into electromagnetic radiation[31, 32, 33]. Usually, the word phosphor is only used to mean inorganic phosphors, generally in powder form and synthesised for practical applications. Other materials such as thin films, single crystals and organic molecules although emitting light, are rarely called phosphors[32].

Phosphors are composed of a transparent microcrystalline matrix (host lattice) containing a small amount of intentionally added impurity atoms (activator) randomly distributed over the host lattice (Figure 1.1). These foreign ions are the luminescent centre,

which can be excited to luminesce. Usually, activators are added in concentrations about 1 mol%, although sometimes a few ppm are enough to produce emission.

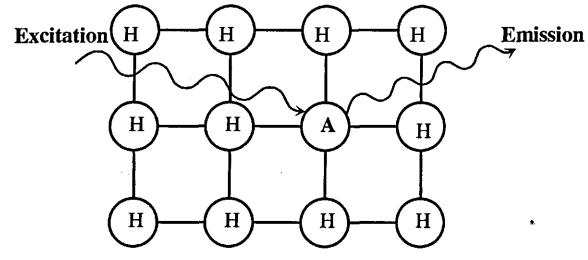

Figure 1.1 Activator (A) doped in a host lattice (H)[34].

It may be that an activator with the desired emission does not have a significant absorption for the available excitation energy. In such cases it is necessary to incorporate another foreign ion called a sensitizer, which absorbs the excitation energy and transfers it to the activator, thus inducing luminescence (Figure 1.2).

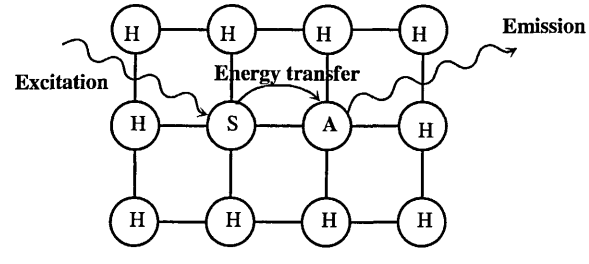

Figure 1.2 Sensitizer (S) and its relationship to an Activator (A) and the host lattice (H)[34].

This excitation-relaxation process suggests that any activator in any host lattice shows luminescence, but it is not the case. During excitation, the incident radiation is absorbed. It can be absorbed directly by the activator or the sensitizer, but it could also be absorbed by the host lattice and transferred to the activator. The energy of the activator is then raised to an excited state by electron promotion from the ground state to higher levels.

When this absorbed energy is released, competition between two different processes takes place[33]. The first process is a radiative one, where photons are emitted. The photon energy equals the energy difference between the excited and the ground state. The second process is a non radiative relaxation to the ground state. In this process the energy is dissipated, exciting the quantized modes of vibration occurring in the rigid crystal lattice. These vibrations are called phonons, and transport the energy as heat. To extend excited state lifetimes and avoid this undesired effect, lattices with low phonon energy must be selected[35].

1.3 Light and luminescence

Electromagnetic radiation is of the same fundamental nature throughout its frequency spectrum, from frequencies of less than 1 Hz to energetic gamma rays (Figure 1.3.b), but the evident properties and means of working with the radiation differ greatly, so the radiation is usually classified on this basis.

Eyesight is one of the most powerful senses we have. The eyes can detect certain interactions between matter, and visible electro-magnetic waves. It is possible to distinguish differently coloured materials that absorb in different parts of the visible spectrum. Even materials having no appreciable absorption in the visible spectrum can be detected, such as polished metals, that reflect the visible light and appear shiny and non-transparent, or well-cut diamonds, that reflect visible light at certain angles while being transparent at other angles. But only wavelengths in a narrow range of the electromagnetic spectrum can be detected by the eye (Figure 1.3.a), and it is the radiation in this narrow band of frequencies that it is referred to as visible light. This band comprises radiation from ~400 nm to ~700 nm (violet to red). It has the familiar property of rectilinear

propagation, undergoes reflection and refraction, and is imperceptible to us except through vision. The frequency of this radiation is about 5.4 x 10^{14} Hz, a very rapid oscillation.

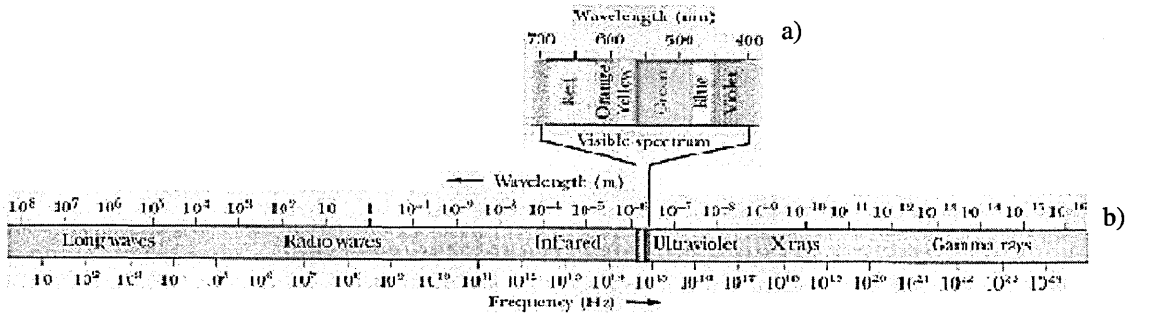

Figure 1.3 a) Visual range of the electromagnetic spectrum and b) full range of the electromagnetic spectrum.(http://maeweb.ucsd.edu/~mckittrick/projects/luminorganica/luminescent.html).

The human eye has evolved to detect radiation in the range emitted by our primary natural light source, the sun, and its relative sensitivity to the visible spectrum is illustrated in Figure 4. However, only 38 % of the sun's energy emission is provided as light. 53 % is supplied at longer wavelengths, which makes sunlight a very effective source of warmth, whereas 9 % of the energy emitted is provided as shorter wavelengths. These radiations can also be called "light" since they have similar properties to radiation in the visible range. In this case, the term "visible light" is not redundant. Shorter wavelength radiation is termed ultraviolet and longer wavelength radiation is called infrared. Both of these, when having the same properties as visible light, may be qualified as "near." The "near ultraviolet" is then 300-400 nm, and the "near infrared" 700 to 2500 nm. There are no sharp breaks in properties at any wavelength, and they change smoothly

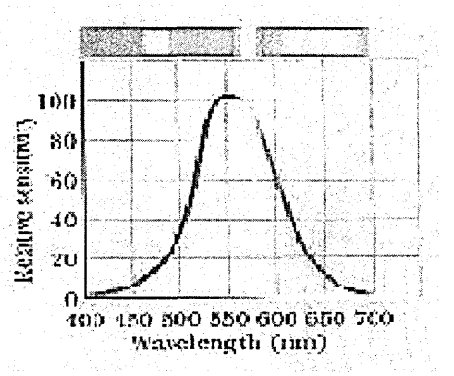

Figure 1.4 Relative sensitivity of the human eye to the visible range of the electromagnetic spectrum.

(http://maeweb.ucsd.edu/~mckittrick/projects/luminorganica/luminescent.html).

Luminescence is known as the incoherent emission of light as a result of any sort of electronic excitation by external energy[33]. This light emission depends on the nature of the emitting matter, as the processes involved are electronic transitions between the characteristic energy levels of the activator[31]. The radiation is usually in the range of visible wavelengths, but since some excitation processes can generate ultraviolet or infrared radiation, those emissions are also considered luminescence. The distinguishing principle of luminescence is that the radiation is non-thermal and its spectrum is determined by transitions between the energy levels of the luminescent material excited in some determinate way, not by random thermal motion, which produces incandescence.

Luminescent radiation may therefore be called "cold light," in contrast to the "hot light" of incandescence. The sun is an incandescent source, the Aurora Borealis a luminescent one.

Luminescent phenomena can be classified using different criteria. Classification can be focused on the excitation source or the nature of the emission.

Depending on the excitation source, luminescence can be classified as[31]:

- photoluminescence, when the energy source is light often UV.
- electroluminescence, when the energy source is an electric field.

- cathodoluminescence, when the energy source is an electron beam.
- triboluminescence, when the energy source is mechanical energy.
- thermoluminescence, when the energy source is heat.
- chemiluminescence, when the energy source is a chemical reaction.

The second criterion to classify the general phenomena of luminescence is in terms of the nature of the emission. If the electronic transition taking place is spin-allowed ($\Delta S=0$), the process is called fluorescence. Meanwhile, if the emission occurring is spin-forbidden ($\Delta S=1$) the emission is known as phosphorescence[36].

Moreover, considering the duration of the process, afterglow detected when excitation stops is also known as phosphorescence[36].

Phosphors that emit light in the visible range of the electromagnetic spectrum are the most important for practical applications, such as television and computer monitors. To produce a colour display, the majority of the light emission from phosphors must be within the visible range.

Once light emission has been defined, its properties, such as colour must be described. There are many colour classification systems enabling to specify characteristics of the radiation. One of these international standards is the CIE chromaticity diagram, established in 1931 (Figure 1.5). It allows all other colours to be defined as the weighted sum of the three "primary" colours. There are no real three colours that can be combined to give all possible colours. Therefore the standard "primary" colours established by CIE do not correspond to real colours. So the 3 "primary" colours are the virtual colours A, B, and C. Then for a given real colour, its components with respect to the primaries are as follows:

$$x = A/(A+B+C)$$

$$y = B/(A+B+C)$$

$$z = C/(A+B+C)$$

Since x + y + z = 1, if x and y are known then z can be determined. With only two variables, such as x and y, it is possible to construct a two-dimensional diagram, or chromaticity diagram.

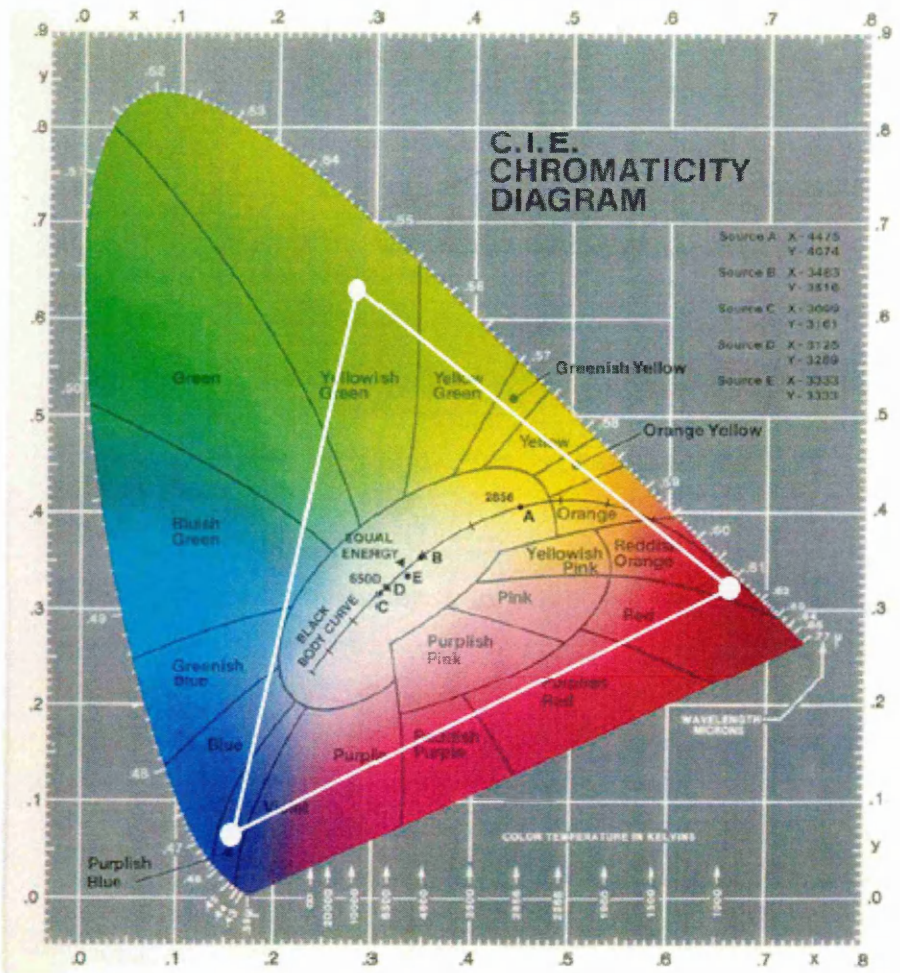

Figure 1.5 1931 CIE chromaticity diagram with chromaticity coordinates shown for the CRT phosphors. red x = 0.662, y = 0.332; green x = 0.290, y = 0.614; blue x = 0.147, y = 0.054.

(http://maeweb.ucsd.edu/~mckittrick/projects/luminorganica/luminescent.html).

If only one colour (C_1) is taken into account (Figure 1.6) and C corresponds to white light. For the colour in consideration, the dominant wavelength is C2. The purity

equals line length (C1-C) / line length (C-C2). The colour gamut is the range of colours from C1 to C2.

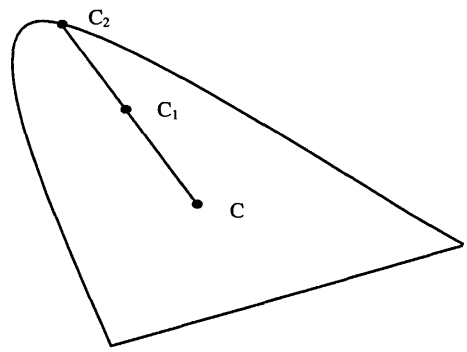

Figure 1.6 Chromaticity diagram for colour C_1.

The chromaticity diagram is also used to define colour gamuts (Figure 1.7), or colour ranges, that show the effect of adding colours together. Colour gamuts are simple polygons positioned on the diagram. All colours that are additive mixtures of the vertices of a gamut are necessarily located inside the gamut. So any 3 real colours cannot be mixed additively to generate all colours. The diagram is thus useful for comparing the gamuts of various colour monitors, printers, slide films, and other hardcopy devices.

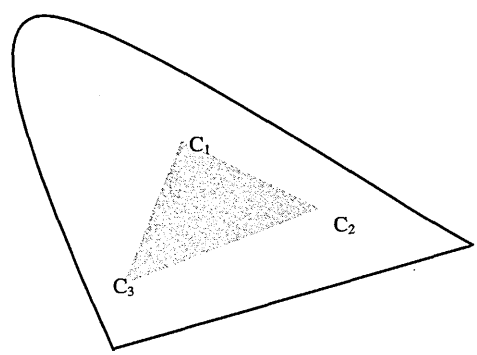

Figure 1.7 Chromaticity diagram showing gamut for colours C_1, C_2 and C_3.

Stokes and anti-Stokes luminescence

Phosphors are generally used to convert radiation of relatively short wavelength (such as ultraviolet radiation) into visible light. In these phosphors the Stokes radiation law is satisfied[34]. This states that the energy of an emitted photon is usually less than that of the exciting photon ($h\upsilon_{excitation} > h\upsilon_{emission}$).

However it is known that certain kinds of trivalent rare-earth phosphors emit intense visible luminescence under near-infrared light excitation[37]. This is known as anti-Stokes luminescence (up-conversion). The lanthanide ions absorb and emit the radiation. As can be seen in figure 3, the up-conversion process takes place in two steps.

1. an activator ion from the ground state A is excited to a higher energy state B by the absorption of a photon of radiation.
2. before this ion has time to lose energy another photon is absorbed, and it is taken to the excited state C.

This process will excite the activator ion to twice the energy of the input photon, i.e. optical pumping.

When this energy is released by a downward transition to the ground level (or to an intermediate excited level) the emission that takes place is a photon of shorter wavelength than the incident photon[24].

The ion used as an activator must possess an energy level at distances above the ground state that corresponds to the energy of the photon (B) and to twice this energy (C). It is not desirable that there should be a large number of levels between A, B and C, since the excited state should decay non-radiatively.

An essential condition for multi-step excitation is that the lifetime of this excited state should be sufficiently long for a second quantum to be taken up before the ion reverts to the ground state. However, the long lifetime of the level B corresponds to a low

probability for the transition A → B, and hence to a low infrared absorption. This absorption can be enhanced by adding an ion capable of absorbing the exciting radiation, and transferring it to the activator, both when it is in the ground state (A) or in the excited state (B).

The up-conversion efficiency is strongly dependent upon a choice of host materials, and activator and sensitizer concentrations.

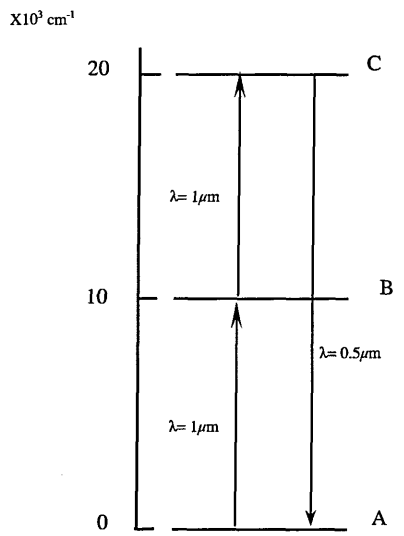

Figure 1.8 Up-conversion process from infrared to visible light [24].

1.4 Absorption and emission spectra

Phosphors are characterised by their absorption and emission spectra.

Two immediate characteristics of phosphors can be noted by both looking at the excitation spectrum and the Stokes law. Firstly the luminescent emission usually occurs at longer wavelength than the excitation radiation and, secondly, the peaks in the excitation are of different intensity because the efficiency of conversion of the excitation energy into emission energy is not the same as for the absorption process.

Not all compounds show the same absorption band. It can be broad or narrow and have different intensities. This can be explained using a configurational coordinate diagram[38] as shown in Figure 1.9. The potential energy curves of the activator (g for the ground state level and e for an excited state level) are shown in the diagram as a function of a configurational coordinate, which describes one of the vibrational modes of the centre involved. If the metal ion is considered at rest with the ligands moving in phase, away from the metal ion and back, the plot is reduced to a diagram of the energy (E) versus the metal-ligand distance (R) being R_0 the equilibrium distance in the ground state.

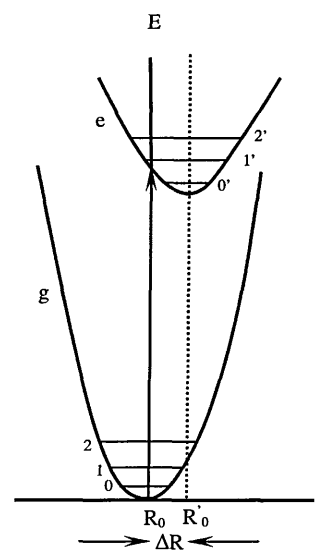

Figure 1.9 Configurational coordinate diagram[38].

Transitions between the two parabolas are electronic transitions. The centre is promoted from its ground state to an excited state by means of an optical photon. They are represented as vertical transitions in the diagram. The optical absorption transition starts from the lowest vibrational level (v=0). The most probable transitions occur at R_0 where the vibrational wavefunction has its maximum value.

This transition ends on the edge of the excited state parabola. The transition corresponds to the maximum of the absorption band (Figure 1.10). It is also possible

although less probable to start at R values different from R_0. This leads to the width of the absorption band.

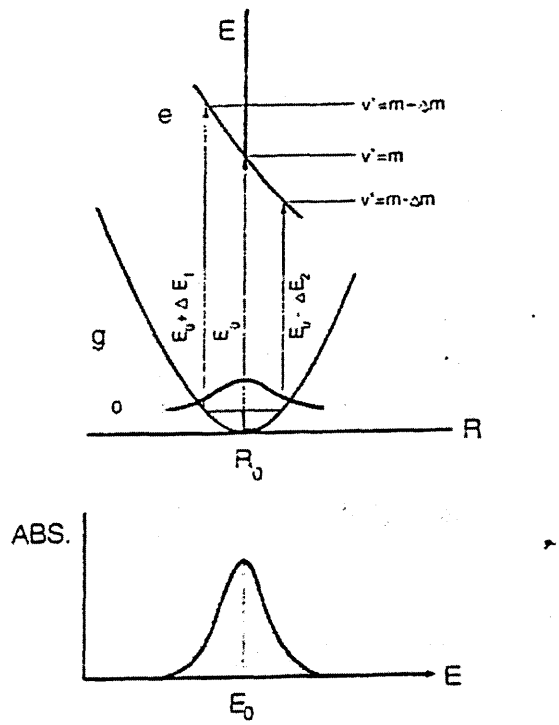

Figure 1.10 Optical absorption transitions between two parabolas [38].

It can be concluded that the larger value of ΔR, the broader the absorption band.

However, it has to be taken into account that not every possible transition between ground and excited states takes place as an optical transition, since these are governed by selection rules. Selection rules will be explained later in Chapter 2, but briefly two important selection rules are

- the spin selection rule, which forbids the transitions between levels with different spin states.
- the parity selection rule which forbids electronic transitions between levels of the same parity.

Once the excited state has been achieved, a process called relaxation takes place[39]. It consists of an energy release to return the activator to the lowest level of the excited states. During this process no light is usually emitted. It can be explained through the configurational coordinate diagram (Figure 1.11).

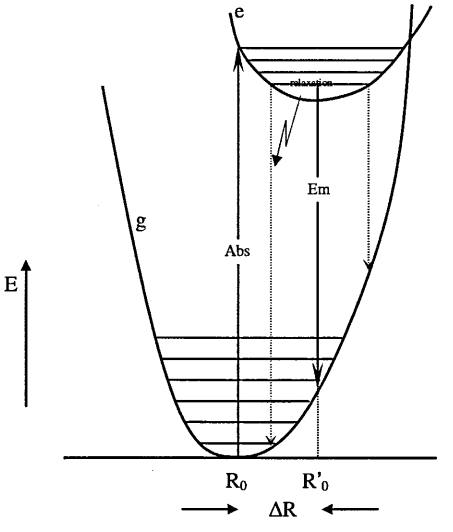

Figure 1.11 Optical absorption and emission transitions between two parabolas [39].

When the lowest of the excited energy levels is reached, emission occurs spontaneously. The vibrational level reached in the ground state parabola through this process normally is not the one with lowest associated energy, and further relaxation takes place. Figure 1.11 shows how the energy of the emitted radiation is lower than that of the excitation source, following the Stokes law.

Non radiative transitions[40], the process competing with radiative decay can also be explained through Figure 1.11. When the temperature is high, it may occur that the relaxed-excited state reaches the cross-over of the two electronic wavefunctions g and e. An alternative way to return to the ground state is offered, and the energy will be released as heat. This is accounted by for resonant vibrational levels. It is evident that it will occur more often if the offset of the parabolas is big. Non radiative processes can occur as well

when the wavefunctions are parallel and no resonant modes exist[40]. In this case it is necessary that the difference in energy between ground and excited state is 4 or 5 times higher than the vibrational frequency of the surroundings. Then this released energy contributes to the excitation of other centres and is released radiatively. The process is then called multi-phonon emission.

1.5 Energy transfer. Up-conversion mechanism

Relaxation mechanisms have been discussed earlier in this chapter, they involved internal processes. External interactions can also be considered such as energy transfers between an excited centre (S*) to another centre (A).

$$S^* + A \longrightarrow S + A^*$$

When this energy transfer is followed by emission, S* is called sensitizer. On the contrary, if A* decays non radiatively A is considered a poison for the centre S, causing quenching[41].

These energy transfers were first studied and described by Förster[42] and Dexter[43] in the late 40's and early 50's and are nonradiative processes. A few conditions are necessary for the transfer to take place. It is necessary to have resonance between donor and acceptor. That is, the energy difference between ground and excited state of donor and acceptor are equal. But also interaction in the form of wavefunction overlap or electric or magnetic interaction is required.

Förster excitation transfer (dipole–dipole excitation transfer) is a mechanism of excitation transfer which can occur between molecular entities separated by distances considerably exceeding the sum of their van der Waals radii (normally 30-100 Å). It is described in terms of an interaction between the transition dipole moments (resonant dipole-dipole coupling), and donor-acceptor transitions must be allowed.

Dexter excitation transfer (electron exchange excitation transfer), occurs as a result of an electron exchange mechanism. It requires an overlap of the wavefunctions of the energy donor and the energy acceptor. It is the dominant mechanism in triplet-triplet energy transfer. For this mechanism the spin conservation rules are obeyed.

At the time, it was assumed that energy transfer processes occurred between an ion in excited state releasing energy to another ion in the ground state[44]. However, F. Auzel suggested in 1966 that these energy transfers could also take place between ions being both in excited states[45]. From 1970 T. Miyakawa and D.L. Dexter[46] and E. Okamoto et al[47] studied the probability of these processes, recognising the importance of phonon assistance.

Energy transfer processes occur by a number of mechanisms[48] summarised in Figure 1.12. The first to be studied was the excited state absorption (ESA), although sequential energy transfer (also known as APTE), cooperative up-conversion and photon avalanche effect are also known.

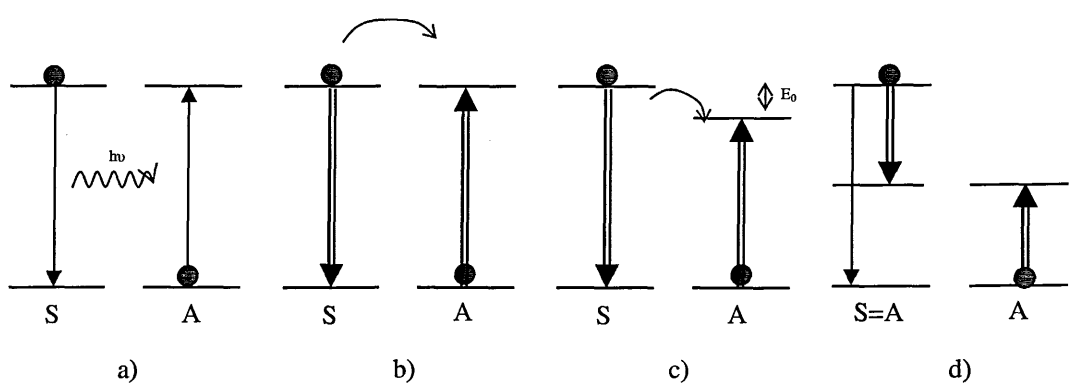

Figure 1.12 Energy transfer mechanisms between activator (A) and sensitizer (S) a) resonant radiative transfer b) resonant energy transfer c) energy transfer assisted by phonons and d) cross relaxation mechanism (concentration quenching).

1.6 Factors affecting luminescence.

Factors affecting luminescence characteristics of a phosphor are the composition of the material, concentration of impurities, level of purity, temperature, and the particle size. Adding the wrong concentration, wrong kind of co-dopant or setting the wrong working temperature can lead to effects such as concentration quenching, poisoning or thermal quenching[34], respectively.

If the concentration of the activator in the host lattice of a phosphor material is steadily increased, it would be expected that the luminescence would increase. Generally this expected behaviour is true at low concentration of activator, but at high concentration of activator the phosphor brightness actually decreases. This effect is called concentration quenching, and it is caused by a cross relaxation mechanism[41].

Phosphors can be very sensitive to the presence of impurities as they can trigger unexpected relaxation processes. When luminescence efficiency decreases due to the presence of impurities the observed effect is called poisoning.

Under high temperature conditions the potential energy of the ground state rises. As a consequence a resonant state between g and e parabolas may occur[40] (Figure 1.11). The absorbed energy is hence dissipated to the lattice as heat. This effect is called thermal quenching of luminescence.

If a given luminescent centre is considered in different host lattices, the optical properties of the centre are usually also different. This phenomenon occurs because the direct surroundings of the luminescent centre change.

Factors such as covalency and the electric field at the site of the ion under consideration (crystal field) must be taken into account. For increasing covalence, the interaction between the electrons is reduced, since they spread out over wider orbitals. Moreover, electronic interactions between energy levels with an energy difference that is

determined by electron interaction shift to lower energy. The spectral position of certain optical transitions is determined by the strength of the crystal field. In addition the crystal field is responsible for the splitting of certain optical transitions.

The particle size and morphology of the powder phosphor are critical for determining the resolution for some phosphor applications[49,50]. For example, in CRT phosphors, the particle size determines the minimum pixel size and uniformity of the screen. When considering different display systems, the phosphors will have to be designed for each specific application.

Easy production methods can yield good reproducibility from batch to batch. But systems that are sensitive to the smallest traces of impurities and stoichiometric variations require strict control methods. Therefore it is essential to be aware of the problems of the synthesis of a phosphor when it is being manufactured.

1.7 Common applications of phosphors

Phosphors have been developed to be used in many devices everyone has around. Fluorescent lamps, cathode ray tubes in televisions, low voltage field emission displays (FED), plasma display panel (PDPs), and X-ray detectors used in diagnostic equipment[33] are examples of phosphors applications.

Some phosphors used for colour TV screens are, ZnS:Ag for blue emission, ZnS:Cu,Al and ZnS:Au,Cu,Al for green emission and Y_2O_2S:Eu and Y_2O_3:Eu for red emitting phosphors.

Materials used in up-converting phosphors have become very useful for optical applications such as optical fibre telecommunications. In the phosphors applications field,

uses include manufacturing of volumetric 3D displays, visualisation of infrared beams, up-conversion lasers and remote sensing thermometers for high-temperature applications[51].

Classification of phosphors applications can be done according to its excitation source. Table 1 shows several kinds of phosphor devices according to the method used to excite the phosphor.

Table 1.1 Phosphor devices classified according to the excitation source[6].

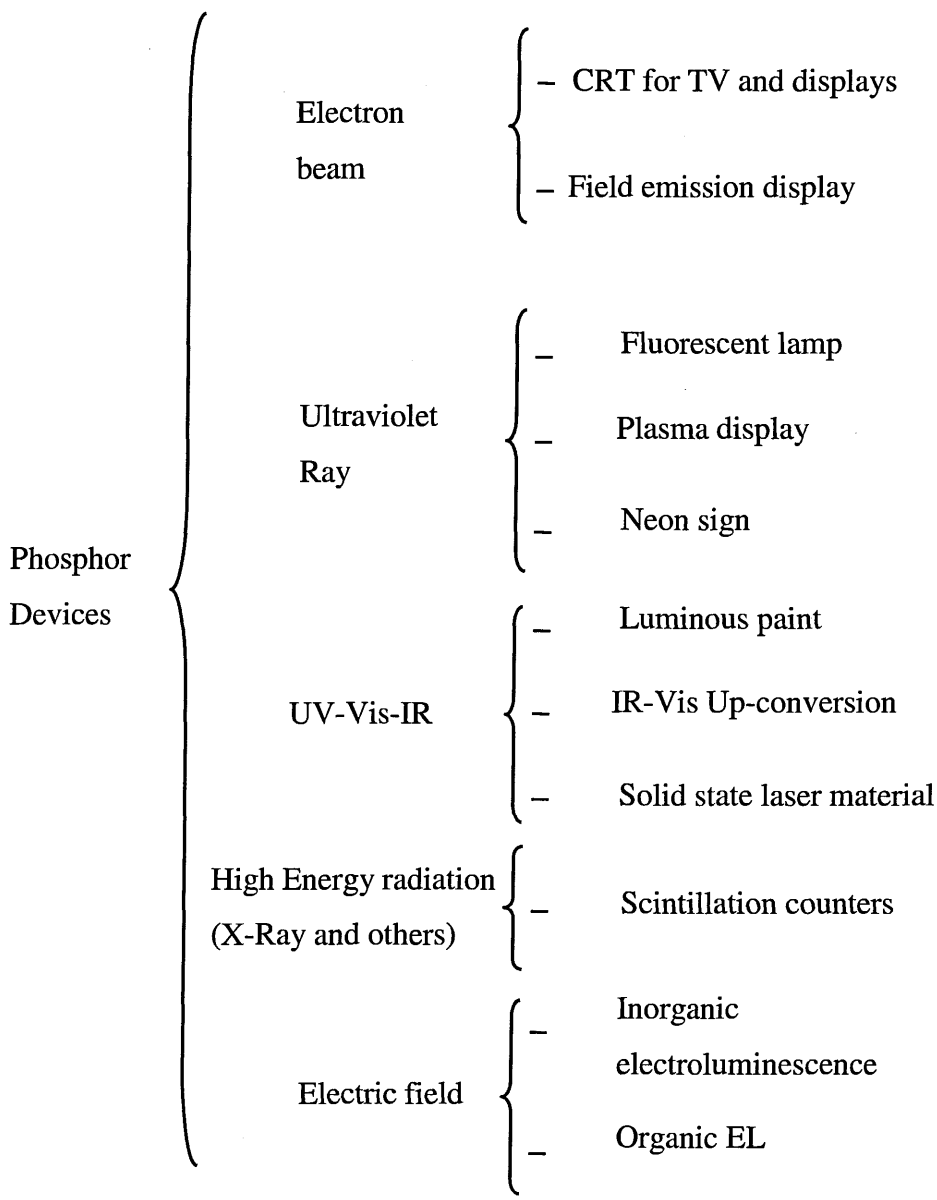

References

[1] Xiang-Shan Ye-Lu, **2**,23 (collected in Wen-Yuan-Ge Si-Ku-Quan-Shu, **1037**, 225, Tiwan Shang-Wu Yin-Shu-Guan (Taiwan Commercial Press) (1983-1986)).

[2] S. Shionoya and W. M. Yen, *Phosphor Handbook*, pp 3, CRC press LLC, (1999).

[3] O. Moltabani. *De Illuminablili Lapide Bononiensi Epistola*, (1634).

[4] F. Licetus. *Litheosphorus Sive De Lapide Bononiensi*, (1640).

[5] Humboldt W. Leverenz, *An introduction to luminescence of solids*, preface, Dover publications, New York, (1968).

[6] S. Shionoya and W. M. Yen, *Phosphor Handbook*, chapter 1, CRC press LLC, (1999).

[7] A. K. Levine and F. C. Palilla, *Trans N. Y. Acad Sci. Ser.* **27**, 517, (1965).

[8] G. E. Peterson and P. M. Bridenbaugh, *J. Opt. Soc. Am.* **53**, 494, (1963).

[9] D. L. Segal and A. Atkinson, *British Ceramic Transactions*, **95**, 103, (1996).

[10] D. Sordelet and M. Akinc, *J. Colloid and Interface Science*, **122**, 47, (1988).

[11] M. Akinc and D. Sordelet, *Adv. Ceramic Mater.*, **2**, 232, (1987).

[12] E. Matijevic and W Peter Hsu, *J. Colloid and Interface Sci.*, **118**, 506, (1987).

[13] E. Matijeviv, *Langmuir*, **10**, 8, (1994).

[14] E. Matijevic, *patent number 5015452*, (1991).

[15] Y. Nishisu and M. Kobayashi, *patent 5413736,* (1995).

[16] M. Kottaisamy,, D. Jeyakumar, R. Jagannathan and M. M. Rao, *Mat. Res. Bull.*, **31**, 1013, (1996).

[17] R. P. Rao, *Solid State Communications*, **99**, 439, (1996).

[18] Y. D. Jiang and Z. Wang, F. Zhang, H. G. Paris and C. J. Summers, *Mat.l Res. Soc.*, **13**, 2950, (1998).

[19] N. Bloembergen, *Phys. Rev. Lett.*, **2**, 84, (1959).

[20] F. Auzel, *Compt. Rend*, **262**, 1016, (1966).

[21] R. A. Hawes and J. F. Sarver, *Phys. Rev.*, **182**, 427, (1969).

[22] L. F. Johnson, J. E. Gensic, H. J. Guggenheim, T. Kushuda, S. Sigh, and L. G. Van Uitert, *Appl. Phys. Lett.*, **15**, 48, (1969).

[23] F. W. Ostermayer, J. P. Van der Ziel, H. H. Marcos, L. G. Van Uitert, J. P. Gensic, *Phys. Rev B*, **3**, 2698, (1971).

[24] J. L. Sommerdijk and A. Bril, *Philips Tech. Rev.*, **34**, 24, (1974).

[25] A. Brij, J. L. Sommerdijk, and A. W. de Jager, *J. Electrochem. Soc*, **122**, 660, (1975).

[26] F. Auzel, *Rev. Phys. Appl*, **20**, 273, (1985).

[27] Y. Wang, J. Ohwaki, *Appl. Phys. Lett.*, **63**, 3268, (1993).

[28] M. J. Denjeka, B. Samjon, *Mater. Res. Soc. Bull*, **8**, 39, (1999).

[29] A. Newport, G. R. Fern, T. Ireland, R. Withnall, J. Silver, A. Vecht, *J. Mater. Chem.*, **11**, 1447, (2001).

[30] J. Silver , M. I. Martinez-Rubio, T.G. Ireland, G.R. Fern, R. Withnall, *J Phys Chem B*, **105**, 948 (2001).

[31] P. Goldberg, *Luminescence of Inorganic Solids*, pp 2, Academic Press (1966).

[32] S. Shionoya, W. M. Yen, *Phosphors Handbook*, pp 4, CRC Press LLC, (1999).

[33] G. Blasse and B. C. Grabmaier, *Luminescent materials*, Springer-Velag, chapter 1, (1994).

[34] J. A. Deluca, *J. Chem. Education*, **57**, 541 (1980).

[35] J. Silver , M. I. Martinez-Rubio, T. G. Ireland, G. R. Fern, R. Withnall, *J Phys Chem B*, **105**, 948 (2001).

[36] G. Blasse and B. C. Grabmaier, *Luminescent materials*, Springer-Velag, appendix 4, (1994).

[37] S. Shionoya, W. M. Yen, *Phosphors Handbook*, pp 643, CRC press LLC, (1999).

[38] G. Blasse, B. C. Grabmaier, *Luminescent materials*, chapter 2, Springer-Verlag Berlin (1994).

[39] G. Blasse, B. C. Grabmaier, *Luminescent materials*, chapter 3, Springer-Verlag Berlin (1994).

[40] G. Blasse, B. C. Grabmaier, *Luminescent materials*, chapter 4, Springer-Verlag Berlin (1994).

[41] G. Blasse, B. C. Grabmaier, *Luminescent materials*, chapter 5, Springer-Verlag Berlin (1994).

[42]T. Förster, *Annalen der Physik* **2**,55, (1948).

[43] D. L. Dexter, *J. Chem. Phys.*, **21**, 836, (1953).

[44] F. Auzel, *Chem. Rev.*, **104**, 139, (2004).

[45] F. Auzel, *C. R. Acad. Sci. (Paris)*, **262**, 1016, (1966).

[46] T. Miyakawa; D.L. Dexter, *Phys. Rev. B*, **1**, 2961, (1970).

[47] E. Okamoto et al, *J. Appl. Phys.*, **43**, 2122, (1972).

[48] F. Auzel, *J. Luminescence*, **45**, 341, (1990).

[49] X. Jing, T. Ireland, C. Gibbons, D. J. Barber, J. Silver, A. Vetch, G. Fern, P. Trowga, D.C. Morton, *J. Electrochem. Soc.*,**146**, 4654 (1999).

[50] J.A. Capobianco, F. Vetrone, J. C. Boyer, *J.Phys. Chem. B*, **106**, 1181 (2002).

[51] S. Shionoya and W. M. Yen, *Phosphor Handbook*, chapter 12, p643, CRC press LLC, (1999).

Chapter 2 Theoretical Background

2. 1 Basic quantum mechanics

2. 1. 1 Introduction and Principles

Classical mechanics is based on laws of motion introduced by Newton. For a long time, these laws were thought to be applicable to the study of very small objects such as atoms and molecules. However, classical mechanics allow systems to possess arbitrary amounts of energy, and results observed in experiments differed with the predictions of classical mechanics. It was at the beginning of the 20^{th} century that a new approach to quantifing these systems was developed, using probability functions. It was named quantum mechanics, and describes the behaviour of matter and electromagnetic waves on the scale of atoms and subatomic particles, although it may be extended to certain macroscopic phenomena.

Max Planck's observations on black-body radiation lead to the limitation of energy for a given frequency (v) to a discrete set of values[1]. A frequency (v) could only possess energy of an integral multiple of hv, where h was a constant and the same for all frequencies. This phenomenon was called the quantization of energy. It is expressed by the equation:

$$E = n\,h\,v$$
$$\text{with } n = 0, 1, 2,\ldots$$

where h is a fundamental constant known as Planck's constant ($h = 6.62608 \times 10^{-34}$ J s).

A new approach to the study of electromagnetic waves was also made when Planck described them as packets of energy (quanta), whereas Einstein described them in terms of particles called photons. This led to a theory of unity between subatomic particles and electromagnetic waves called wave-particle duality in which a particle and a wave

were neither one nor the other, but had the properties of both simultaneously. It was from this that the uncertainty principle arose, setting the basis for quantum mechanics.

The clearest evidence for the quantization of energy of particular relevance to the work described in this thesis, comes from the observation of radiation absorbed and emitted by atoms and molecules. A typical atomic emission spectrum is shown in Figure 2.1.

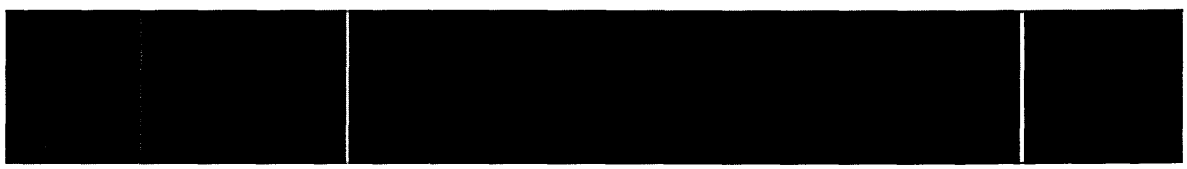

Figure 2.1 Emission spectrum of an excited hydrogen atom.

The obvious feature shown in this spectrum is the appearance of radiation only at a series of discrete wavelengths (410.2, 434.5, 486.1 and 656.7nm): they are called the spectral lines. This spectrum can be understood if the energy of the atoms or molecules is confined to discrete values (Figure 2.2), and energy can only be absorbed or emitted in discrete steps. Light is emitted as it drops from one energy state to a lower one. The frequency of the radiation, if the energy of an atom decreases ΔE, will be $\nu = \Delta E/h$, resulting in a line in the spectrum. The unit of frequency of the electromagnetic radiation is called the wavenumber, which is defined as the number of complete waves per unit length (typically, per cm).

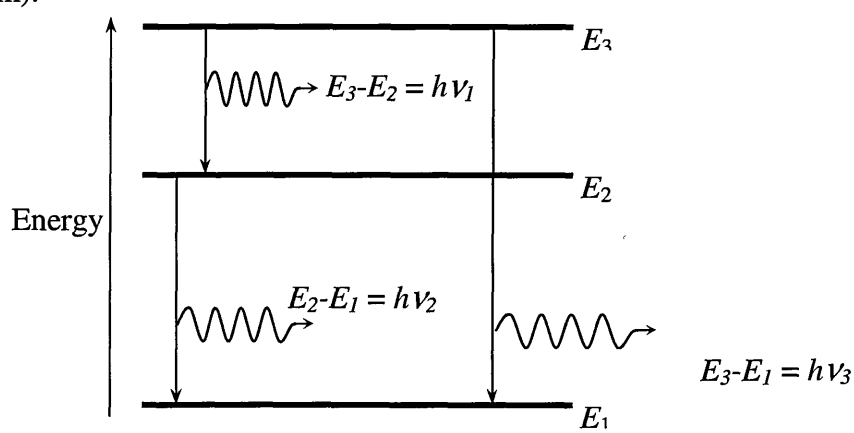

Figure 2.2 Spectral lines can be explained if it is assumed that a molecule emits a photon as it undergoes a transition between discrete energy levels. The bigger the energy change, the higher the frequency of radiation.

In quantum mechanics the idea of probability arises from the likelihood of finding a particle such as an electron in a particular region around the nucleus at a certain time. As the classical approach of localised particles was abandoned, it had to be replaced with the idea that the position of a particle is distributed through space like the amplitude of a wave. Therefore, wavefunctions (Ψ) replace the classical concepts of trajectory. Wavefunctions are mathematical functions containing all of the information possible to describe the location and motion of the particle (potential and kinetic energy elements). Its value can be large at a particular point showing high probability for the particle to be at that point, or zero at a point (the particle will not be found there). The quicker a wavefunction changes from place to place, the higher the kinetic energy of the particle it describes. These wavefunctions are known as Schrödinger equations, and for a particle free to move in one dimension is given by:

$$H\psi(x) = \left(-\hbar^2/2m\right)\left(d^2/dx^2\right)\psi(x) + V(x)\psi(x)$$

where Ψ is the wavefunction, V(x) is the potential energy of the particle , H is the Hamiltonian and $\hbar$ is a modification of Planck's constant ($\hbar = h/2\pi$)

In summary, new concepts introduced by quantum mechanics include quantization of energy, the uncertainty principle and wave-particle duality; all phenomena that cannot be adequately explained by classical physics. The restrictions on the wavefunction lead automatically to the quantization of energy, as the energy of the system is confined to only certain values in order for the equation to have an aceptable solution. Position and momentum are complementary properties of a particle, and the same way its momentum is related to a particular wavelength, the wavefunction of the localised particle is given by the superposition of several wavelengths. From this concept, a consequence of the uncertainty principle is that it is impossible to specify simultaneously, with arbitrary precision, both the momentum and the position of a particle[1].

2. 1. 2 Applications of quantum theory

The theory of quantum mechanics can be used to describe the motion of particles, but it has also applications related to the atom. From atomic emission spectra, information about electronic structure and the arrangement of electrons around the nucleus can be extracted.

The simplest atom to be studied is a one electron atom, hydrogen and hydrogen like atoms. The permitted energy levels for this atom can be obtained from the Schrödinger equation solved for a three dimensional system. Solving the equation, three numbers are obtained, two arising from the spherical symmetry of the atom (the angular momentum l and magnetic momentum m_l) and another called n appearing from the freedom of the electron to change its distance from the nucleus. These numbers represent the allowed energy values for an electron in the atom, and are called quantum numbers. As the allowed energies depend only on n for the hydrogen atom, it was called *principal* quantum number. Wavefunctions are labelled Ψ_{nlm_l} , showing the set of quantum numbers compiling its solution. But not every combination of quantum numbers constitute a solution to the Schrödinger equation. Certain restrictions must be imposed so that these quantum numbers allow the square of the wavefunction to indicate the probability of finding a particle at each point of the space.

$$n = 1, 2, 3,..$$

$$l = 0, 1, 2,... n\text{-}1$$

$$m_l = l, l\text{-}1, l\text{-}2, ..., -l$$

	$l = 0$	1	2	3	4
$n = 1$	$m_l =$ 0				
2	0	-1, 0, 1			
3	0	-1, 0, 1	-2, -1, 0, 1, 2		
4	0	-1, 0, 1	-2, -1, 0, 1, 2	-3, -2, -1, 0, 1, 2, 3	
5	0	-1, 0, 1	-2, -1, 0, 1, 2	-3, -2, -1, 0, 1, 2, 3	-4, -3, -2 -1, 0, 1, 2, 3, 4

In summary, for the first 5 allowed values of n, the following values of l and m_l are allowed:

A fourth quantum number is necessary to define the motion of the electron about its own axis. This motion is called spin, and the spin angular momentum is an intrinsic property of the electron, like its rest mass and its charge, and every electron has exactly the same value. Only one value of s is allowed for electrons ($s = ½$) and its projection on the z-axis gives rise to m_s, the spin magnetic quantum number. The spin may lie in any of 2s+1=2 different orientations. One orientation correspond to ½ and is often denoted as ↑, the other orientation corresponds to –½ and is denoted as ↓.

The wavefunctions describing the movement of electrons in atoms and molecules are called orbitals, by analogy with Newton's laws for macroscopic solids. All of the orbitals of a given value of n form a single shell of the atom, and all the orbitals in a particular shell have associated the same energy.

The orbitals with the same value of n but different values of l form the sub-shells of a given level. These sub-shells are generally referred to by letters, as follows:

l	0	1	2	3	4	.	.
Name of the orbital	s	p	d	f	g	.	.

As a consequence of the uncertainty principle, an electron may be found at any instant at any distance from the nucleus, regardless of the orbital it occupies, but it is most likely to be found in certain regions of the atom. These areas can be drawn attending to the spatial variation of the Schrödinger function for each $|\Psi_{nlm}|^2$, and the shapes of the different orbitals are obtained. Normally, the surface represents the area capturing 90% of the function probability. A higher energy orbital (greater n) will spread further from the nucleus.

2. 1. 3 Polyelectronic atoms

When an atom with more than one electron orbiting around the nucleus is studied, the wavefunction describing its motion is complicated by electronic interactions[2]. The solution of these equations is out of the scope of this thesis, but not the qualitative results indicated by those solutions, which are of importance when considering the emission processes in phosphor systems described later. It can be concluded that in general polyelectronic atoms do not differ greatly from hydrogen, and its electronic structures can be described using the same kind of energy levels and orbitals.

With more than one electron to place in an orbital, a new question arises: how many electrons can share a given orbital? The Pauli exclusion principle, explaining the helium spectrum, states that in the same atom two electrons cannot share the same four quantum numbers. Therefore, no more than two electrons may occupy any given orbital, and if two do occupy one orbital, their spins must be paired.

When orbitals are occupied, electron-electron interactions prevent the orbitals becoming degenerate. In general, as a consequence of penetration and shielding, for a

given n, $E_s < E_p < E_d$.[2] Consequently, an s electron is more tightly bound than a p electron of the same shell. Similarly, a d electron penetrates less than a p electron of the same shell, and therefore experiences more shielding. The Aufbau principle is the generalization of these observations, and constitutes a series of rules to determine the electronic configuration, the expression of the electronic structure, of an atom.

The order of occupation of orbital shells for the ground state configuration of neutral atoms is:

- 1s 2s 2p 3s 3p 4s 3d 4p 5s 4d 5p 6s 4f and each orbital may accommodate up to two electrons.
- electrons occupy different orbitals of a given subshell before doubly occupying any one of them.
- Hund's rule: an atom in its ground state adopts the configuration with the greatest number of unpaired electrons.

An electron has magnetic moment due to its spin and, as it is in effect a circulating current (with an associated orbital angular momentum), produces a magnetic field proportional to its angular momentum. Therefore, an electron possesses an associated magnetic moment arising from its spin. The interaction of the spin and orbital magnetic moments is called spin-orbit coupling. The relative orientations of the spin and orbital magnetic moments determine the strength of the coupling.

Taking into account two angular momenta with quantum numbers l and s. The spin of the electron can be aligned (parallel) to the orbital momentum l or opposite (antiparallel) causing a different total angular momentum. A new quantum number (j), the *total angular momentum quantum number*, is therefore necessary to represent possible combinations of electron angular momenta. This depends on the total angular momentum

of the electron, the vector sum of its spin and orbital momenta. The total angular momentum of a spinning orbiting electron is described by the quantum numbers j and m_j. The vector has a maximum with $j = l + ½$ when l and s lie parallel and a minimum with $j = l - ½$ when their relative orientation is antiparallel. Other intermediate values can also be found. In general the values allowed can be calculated by the Clebsch-Gordan series

$$j = l+s,\ l+s-1,\ l+s-2\ \ldots\ldots \mid\ l-s\ \mid$$

with j always being a positive number.

To summarize all the information given by the quantum numbers described up to now a term symbol is used to label overall states. A term symbol gives three pieces of information: $^{2S+1}L_J$

- L indicates the total orbital angular momentum
- the left superscript indicates all the possible orientations of the total spin and
- the right subscript indicates the total angular momentum quantum number (J).

In an atom with more than one electron, the total orbital angular momentum is calculated combining the orbital angular momenta (l) of the individual electrons using the Clebs-Gordan series, L being one of the following values $L=l_1+l_2, l_1+l_2-1, l_1+l_2-2\ \ldots\ldots \mid l_1-l_2\mid$. They are referred to with the symbolism S, P, D, F, G, H, I ... corresponding to L= 0, 1,2,3,4,5,6... respectively.

Spin-orbit coupling depends very strongly upon the nuclear charge. In atoms with large nuclear charge (typically Z>30) spin0spin and orbit-orbit interactions may be outweighed by large spin-orbit interactions. In this situation, each orbital angular momentum l tends to combine with each individual spin angular momentum s_i, originating individual j_i total angular momenta. The combination of them adds up to the total angular momentum J

To calculate J, orbital momenta are added up to form a total L and spins are combined to form a total S. Then L and S are combined as interacting by the magnetic spin-orbit coupling. Values allowed for J are J = L+S, L+S-1, L+S-2 ..... | L-S |, with J a positive number.

2. 1. 4 Parity

A monochromatic polarised beam of light can be defined by the association of an electric and a magnetic vector. They are perpendicular to each other and both perpendicular to the direction of propagation of the light. Normally, attention is confined to the electric vector because calculations indicate that the interaction between the magnetic vector and a molecule is much weaker than that involving the electric vector.

Magnetic vectors, and magnetic fields cause circular displacements of charge. Such rotations of charge are symmetric with respect to inversion in a centre of symmetry (Figure 2.3). This type of symmetry is called g (g= gerade = even or symmetric).

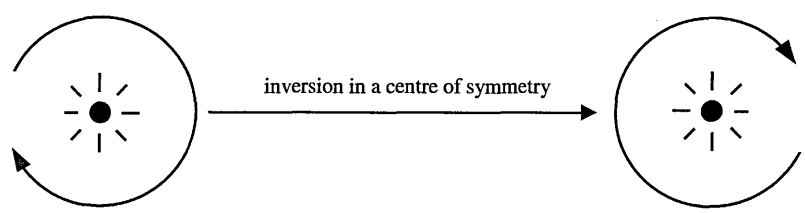

Figure 2.3 Rotation has g symmetry.

This is in contrast to an electric vector and the linear charge displacements to which it gives rise. They are antisymmetric with respect to inversion in a centre of symmetry (Figure 2.4). This type of symmetry is called u (u= ungerade = odd or asymmetric).

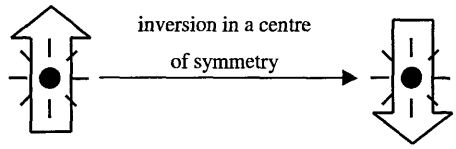

Figure 2.4 Translation has u symmetry.

So, magnetic-dipole allowed transitions are g in nature, whereas electric-dipole-allowed transitions are u.

2. 1. 5 Selection rules

When an electron undergoes a change of state from an orbital to another of lower energy, it undergoes a change of energy ΔE and discards the excess energy as a photon of electromagnetic radiation of frequency ν. But not all transitions are allowed. If a photon is generated by an electron undergoing a transition, then the angular momentum of the electron must change to compensate for the angular momentum carried away by the photon, its spin being unity. Therefore, it is clear that some transitions are allowed, (they have a high probability), whereas others are forbidden (they have a low probability). A selection rule is a statement about which transitions are allowed. For hydrogenic atoms the selection rules are:

- $\Delta l = \pm 1$
- Δn = any integrer

as the principal quantum number (n) it is related to the total energy, and not the angular momentum.

Spectra of atoms rapidly become very complicated as the number of electrons increases, but they still consist of lines appearing when the atom undergoes an orbital

transition associated with a change of energy ΔE (when emitting or absorbing a photon of frequency $\nu = \Delta E/h$), although the lines of all the possible energy combinations cannot be found.

Selection rules arise from the conservation of angular momentum during a transition, and from the fact that a photon has a spin of 1. For polyelectronic atoms term symbols can be used to express them, because they carry information about angular momentum. A detailed analysis leads to the following rules:

- $\Delta S = 0$ allowed transitions must involve the promotion of electrons without a change in their spin. There must be no change in spin multiplicity during electronic transitions
- $\Delta L = 0, \pm 1$ with $\Delta l = \pm 1$ (Laporte selection rule). If the molecule has a centre of symmetry, transitions within a given set of orbitals (i.e. those which only involve a redistribution of electrons within a given subshell) are forbidden.
- $\Delta J = 0, \pm 1$ but not $J = 0 \longleftrightarrow J = 0$

$\Delta S = 0$ because light does not affect the spin. The rules about ΔL and Δl express the fact that the orbital angular momentum of an individual electron must change, but whether or not this results in an overall change of orbital momentum depends on the coupling.

The selection rules given above only apply in light atoms. When the atomic number increases, then the selection rules progressively fail. For this reason, transitions between singlet and triplet states (for which $\Delta S = \pm 1$), while forbidden in light atoms, are allowed in heavy atoms[1].

2. 2 Lanthanides

Introduction

Lanthanide is the name usually used to indicate the elements which have in common an open 4f shell. Strictly, this series is formed by the elements from Ce to Yb, the block filling the 4f shell, although it is very common to include in the group the fifteen elements: from lanthanum to lutetium[3]. Sometimes other elements, such as yttrium and scandium[4], are also referred to as lanthanides. All of these elements are also known as rare earths, although they are neither rare, as modern industrial processes now allow purification from their oxides, nor they are "earths", an obsolete term to designate oxides. New recommendations from International Union of Pure and Applied Chemistry (IUPAC) suggest the name lanthanoid rather than lanthanide. Table 2.1 shows the fifteen elements from lanthanum to lutetium.

Table 2.1 Lanthanide elements

ELEMENT	SYMBOL	Z
Lanthanum	La	57
Cerium	Ce	58
Praseodymium	Pr	59
Neodymium	Nd	60
Promethium	Pm	61
Samarium	Sm	62
Europium	Eu	63
Gadolinium	Gd	64
Terbium	Tb	65
Dysprosium	Dy	66

Table 2.1 (cont.) Lanthanide elements		
Holmium	Ho	67
Erbium	Er	68
Thulium	Tm	69
Ytterbium	Yb	70
Lutetium	Lu	71

Some properties of the lanthanides include:

- they occur together in nature, in minerals
- they have similar chemical and physical properties, with gradual changes occurring across the lanthanide series, making them difficult to separate from each other
- the 3+ oxidation state is adopted primarily for all lanthanide elements[5] in solution and solid state chemistry. All the lanthanides have stable trivalent species, although other oxidation states exist[6] (Eu^{2+}, Sm^{2+}, Yb^{2+}, and Ce^{4+}).
- their coordination numbers are usually high, greater than 6 (usually 8 and 9) in compound form.
- the $4f^n$ electrons in the core are shielded from their environment[5], being unable to participate in bonding. For this reason their bonding is primarily ionic.
- they have a preference for hard-donor atoms binding in order of electronegativity.
- they are strongly paramagnetic
- pale colours arise from weak, narrow forbidden f-f optical transitions.
- their magnetic and optical properties are largely environment independent.
- present similar spectra in gas, solid or liquid state.

- there is renewed technological interest in the lanthanides elements mainly as optical magnetic materials.

The main characteristics of the rare-earth elements ions used in this thesis are described below.

Erbium

Pure Er_2O_3 was successfully isolated in 1905 by Urbain and James[7]. The chemical behaviour of trivalent Er^{3+} is similar to that of yttrium. The ion has a narrow absorption band, in the green region, at ~530 nm colouring Er^{3+} salts pink. Other prominent Er-absorption bands are at ~650, 800 and 980 nm[8].

atomic number	68
atomic weight	167.26
electron configuration	$[Xe]4f^{12}6s^2$

The current major high technology interest in Er pertains to its use in amplifiers for fiber-optic data transmission. Optical telecommunication relies on signals, transmitted along silica fibers, which need regular amplification because of a loss of signal strength as transmission distance increases. The signals use a wavelength 'window' in the fibre. Erbium lases efficiently at this wavelength (visible or near infrared) thereby providing a very efficient optical method of amplification. Phosphors for the conversion of infrared radiation into visible light, up-conversion, can be based on erbium[9].

Europium

The discovery of europium is generally credited to Demarcay, who separated the rare earth in reasonably pure form in 1901[7].

This element is characterised by having two stable oxidation states: Eu^{2+} and Eu^{3+}. The trivalent europium ion forms aqueous insoluble carbonates and oxalates, but soluble nitrates and chlorides[8].

atomic number	63
atomic weight	151.96
electron configuration	$[Xe]4f^{7}6s^{2}$

Elements in the lanthanide series derive most of their characteristic properties from the 4f electrons, and this is typified by europium's luminescent behaviour. Almost all practical uses of europium utilise this luminescence.

Ytterbium

Marignac[7] in 1878 discovered a new material, which he called ytterbia. Urbain separated ytterbia into two components, which he called neoytterbia and lutecia. The elements in these earths are now known as ytterbium and lutetium, respectively[8].

atomic number	70
atomic weight	173.04
electron configuration	$[Xe]4f^{14}6s^{2}$

Its chemical behaviour is similar to that of yttrium. This penultimate member of the lanthanide series, however, has a moderately stable divalent state, Yb^{2+}, with a full shell electron configuration. Ytterbium has a single dominant spectral absorption band independent of the environment, in the infrared, at ~985 nm.

Yttrium Oxide

The very stable oxide, Y_2O_3, known as yttria, adopts the cubic structure. It is resistant to aggressive chemical attack at high temperatures and its thermal stability underlies many of its uses. It is essential for cathode ray tube phosphors, for microwave garnet crystals, for certain lasers and for several high performance ceramics.

The crystal structure of Y_2O_3 readily accepts similarly sized Ln ions such as europium or erbium; the dopants can be chosen to provide visible emission upon excitation by energy sources such as energetic electrons or ultra-violet radiation[8].

All of the lanthanide elements have stable 3+ oxidation states. Our discussion of the lanthanide elements from here will be confined only to their trivalent cations, as this is the valence state used for the systems studied in this thesis.

2. 2. 2 The lanthanide contraction

The 4*f* electrons are ''inner'' electrons in the sense that the maximum of their charge density functions is well inside the outermost ($5s^2$ $5p^6$) electrons; thus they are shielded from the surroundings of the lanthanide ion. The 5*s* and 5*p* orbitals, however, penetrate the 4*f* subshell and thus are not shielded from the increasing nuclear change, contracting as the lanthanide series is traversed[6].

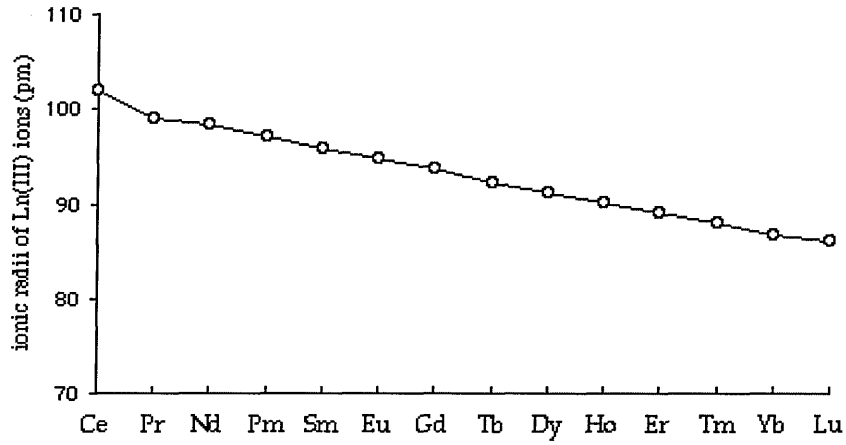

Figure 2.5 Ionic radii of the Ln(III) ions.

(www.hull.ac.uk/php/chsajb/heavy-ho/lanthanides.html, 15/09/04).

Along the lanthanide series a decrease in ionic radii is detected from cerium to ytterbium. This effect is known as *lanthanide contraction* (Figure 2.5) and it is caused by the poor shielding ability of 4f orbitals. Due to their spatial characteristics, they protect outer electrons only partially from the nuclear charge, causing an increase in effective nuclear charge for increasing z.

This effect is seen in every period as a shell is filled, but it is particularly important for the lanthanides because of the length of an f-series (14 elements in an f-block) and the directional characteristics of *f*-orbitals allowing the electrons to occupy different volumes of space in order to avoid each other.

2. 2. 3 Oxidation state of the lanthanides

As stated previously, the dominant oxidation state for the lanthanide elements is 3+. This is a consequence of the increasing positive nuclear charge on the valence electrons. When electrons are removed from a lanthanide atom, the orbitals are stabilised

in the order $4f > 5d > 6s$. In the 3+ oxidation state, the $4f$ has become core-like (as shown by spectroscopy and magnetic properties). Any remaining electrons occupy the $4f$ and the $6s$ and $5d$ are empty. Many of the lanthanides have the configuration $4f^n\ 6s^2$ but form trivalent ions Ln^{3+} ($4f^{n-1}$) because it is at this point that the most stable energies are obtained[10].

At the beginning of the series (Figure 2.6), the $5d$ subshell is lower in energy than the 4f, so that the ground state configuration of Ce is $4f^1\ 5d^1\ 6s^2$. As additional protons are added to the nucleus, the $4f$ orbital rapidly contracts and is stabilised relative to the $5d$ so that the lanthanide ions from Pr to Eu have the ground state $4f^n\ 6s^2$. At gadolinium, however, the stability due to a set of half-filled $4f$ orbitals is such that the next electron is added to a $5d$ orbital, giving Gd the configuration $4f^7 5d^1 6s^2$. This effect is short lived, because from Tb to Yb the configuration is $4f^n\ 6s^2$, until the $4f$ subshell is filled. So lutetium has a configuration of $4f^{14}\ 5d^1\ 6s^2$.

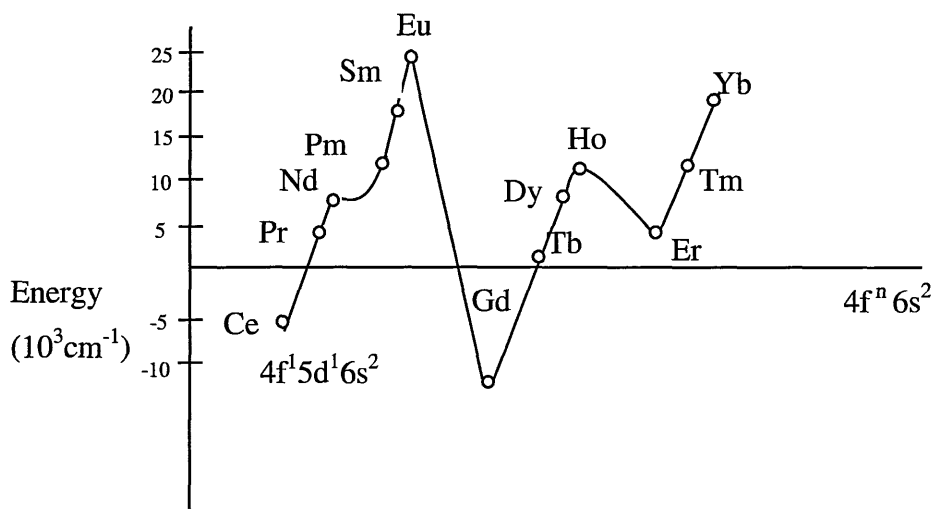

Figure 2.6 Approximate relative energies of the two possible ground state configurations of lanthanide atoms[3].

2. 2. 4 Magnetic and spectroscopic properties of f electron systems

When spin-orbit coupling is weak, the Russell-Saunders coupling scheme[5] may be used to establish the spectroscopic term of ground state lanthanides. Electrons will fill

orbitals with the highest available angular momentum, to minimize repulsion. The energy of the lanthanide elements is summarised by using the expression previously discussed:

where the term defined by a pair of S and L values is associated with a number of component states, the number of different orientations allowed for the resultant J. Where J is the resultant angular momentum associated with an overall quantum number where the angular momentum vectors S and L are associated together.

Nowadays, not only the ground states of all the rare earth trivalent ions can be detailed but also some of the low-lying excited states when the results from the spin-orbit splitting are considered. These states are shown in Table 2.2. Excitation to these low-lying levels corresponds to energies in the infrared or near infrared regions of the spectrum for the lanthanides, the splittings resulting from spin-orbit coupling being of the order of 1000 cm^{-1}.

4f electrons in the inner core of an atom are shielded from the environment. Therefore, spin-orbit coupling for those electrons will be greater than the effect of the crystal field. The strength of this spin-orbit coupling is represented by the separation between adjacent states of a term. This separation is sufficient in all but two cases (Sm and Eu) to render the first excited state of the trivalent lanthanides ions inaccessible, and so only the ground J state is populated. The magnetic moment of a J state can be calculated using the Landé formula:

$$\mu_e = g\sqrt{J+(J+1)}$$

$$\text{where } g = \frac{3}{2} + S(S+1) - L(L+1)/\,2J(J+1)$$

A correspondence of the observed and calculated magnetic properties of the lanthanides is shown in Table 2.3.

Table 2.2 Ground and low-lying electronic levels of the lanthanides.

Ln^{3+}	$4f^n$	Ground level	Low-lying excited levels
Ce	1	$^2F_{5/2}$	$^2F_{7/2}$
Pr	2	$^3H_4$	$^3H_5$, $^3H_6$
Nd	3	$^4I_{9/2}$	$^4I_{11/2}$, $^4I_{13/2}$, $^4I_{15/2}$
Pm	4	$^5I_4$	$^5I_5$, $^5I_6$, $^5I_7$, $^5I_8$
Sm	5	$^6H_{5/2}$	$^6H_{7/2}$, $^6H_{9/2}$, $^6H_{11/2}$, $^6H_{13/2}$, $^6H_{15/2}$
Eu	6	$^7F_0$	$^7F_1$, $^7F_2$, $^7F_3$, $^7F_4$, $^7F_5$, $^7F_6$
Gd	7	$^8S_{7/2}$	-
Tb	8	$^7F_6$	$^7F_5$, $^7F_4$, $^7F_3$, $^7F_2$, $^7F_1$, $^7F_0$
Dy	9	$^6H_{15/2}$	$^6H_{13/2}$, $^6H_{11/2}$, $^6H_{9/2}$, $^6H_{7/2}$, $^6H_{5/2}$
Ho	10	$^5I_8$	$^5I_7$, $^5I_6$, $^5I_5$, $^5I_4$
Er	11	$^4I_{15/2}$	$^4I_{13/2}$, $^4I_{11/2}$, $^4I_{9/2}$
Tm	12	$^3H_6$	$^3H_5$, $^3H_4$
Yb	13	$^2F_{7/2}$	$^2F_{5/2}$
Lu	14	$^1S_0$	-

For lanthanide elements, the most common electronic transitions involve excited states which are either components of the ground term or which arise from the same $4f^n$ configuration as the ground term. These are in principle forbidden *f-f* transitions, an electronic rearrangement within the *f* orbital[11], although the distortion of symmetry caused by the crystal field may allow them. These absorption bands are sharp, because the energies of the electronic states are only slightly affected by ligand nature of thermal vibrations. The crystal field also causes (2J+1) degeneracy of the energy states, producing fine structure in some bands.

Table 2.3 Summary of the magnetic properties of Ln(III) ions.

Ln^{3+}	Colour	Number of unpaired e^-	$g[J(J+1)]^{1/2}$	μ_{obs}
Ce	colourless	0	2.54	2.3-2.5
Pr	green	1	3.58	3.4-3.6
Nd	lilac	2	3.62	3.5-3.6
Pm	pink	3	2.68	-
Sm	yellow	4	0.85	1.4-1.7
Eu	pale pink	5	0	3.3-3.5
Gd	colourless	6	7.94	7.9-8.0
Tb	pale pink	7	9.72	9.5-9.8
Dy	yellow	6	10.65	10.4-10.6
Ho	yellow	5	10.6	10.4-10.7
Er	rose-pink	4	9.58	9.4-9.6
Tm	pale green	3	7.56	7.1-7.5
Yb	colourless	2	4.54	4.3-4.9
Lu	colourless	1	0	0

2. 2. 5 Excited states of *f* electrons systems

To obtain the terms and spin orbit states for the $4f$ configurations, a study of the $4f^2$ configuration is carried out as an exemplar. In a first instance, the spin-orbit coupling is

ignored. If any restriction on spin multiplicity is ignored, then the different spin multiplicities can be mixed using the mechanism of spin-orbit coupling.[2]

For the f^2 configuration, the corresponding ground term is ^3H characterised by angular momentum of 3 and 2. But these electrons could both be placed in the orbital with angular momentum 3, to give a ^1I term:

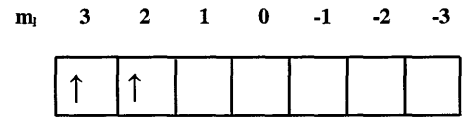

$s = 1$

$2s+1 = 3$ ⟶ ^3H

$M_L = 3+2 = 5 \quad L = H$

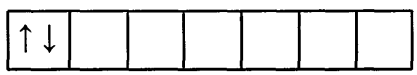

$s = 0$

$2s+1 = 1$ ⟶ ^1I

$M_L = 3+3 = 6 \quad L = I$

The greatest orbital angular momentum these electrons can have as a pair is 6 and the smallest 0, seven values in all. Here written in order are all the term symbols corresponding to all values of the orbital angular momenta from 0 to 6. For the case where only two possible spin labels, 1 and 3 are added, alternatively, in such a way as to include ^3H and ^1I. These are:

$$^1S,\ ^3P,\ ^1D,\ ^3F,\ ^1G,\ ^3H,\ ^1I$$

In Table 2.4 the complete list of the terms arising from the f^2 configuration is shown. Spin-orbit coupling has been introduced[12], showing in the same column the levels that can interact together as they have the same value of J. Figure 2.7 shows the Pr^{III} ($4f^2$) energy level diagram, which shows how the primary separation between levels is due to electron repulsion, and the changes produced when spin-orbit coupling is taken into account[12].

Table 2.4 Terms arising from the f^2 configuration and states consequently resulting from spin –orbit coupling.

Russell-Saunders term	Spin-orbit states
^1S	$^1S_0$
^3P	$^3P_0$, $^3P_1$, $^3P_2$
^1D	$^1D_2$
^3F	$^3F_2$, $^3F_3$, $^3F_4$
^1G	$^1G_4$
^3H	$^3H_4$, $^3H_5$, $^3H_6$
^1I	$^1I_6$

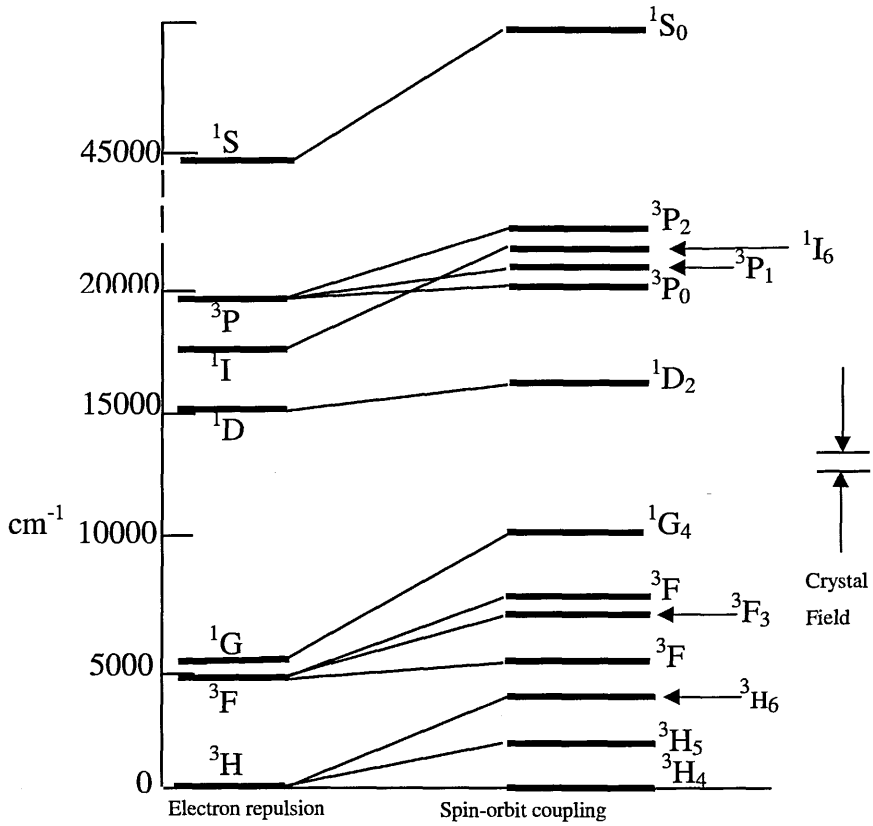

Figure 2.7 The electronic energy level diagram for Pr^{III} ($4f^2$).

Table 2.5 gives a more complete list of the Russell-Saunders terms arising from all f^n configurations. It does not include the effects of spin-orbit coupling, which have to be worked out for each case individually.

Table 2.5 Terms arising from f^n configurations.

f electron configuration	Terms arising
f^1, f^{13}	^2F
f^2, f^{12}	$^3H+^3F+^1G+^1D+^3P+^1I+^1S$
f^3, f^{11}	$^4I+^4F+^4S+^2H+^2G+^2K+^4G+^2D+^2P+^2I+^2J+^4D$
f^4, f^{10}	$^5I+^5F+^5S+^3K+^5G+^3H+^3G+^3J+^3D+^3P+^3I+^5D$
f^5, f^9	$^6H+ ^6F+^4D+^6P+^4I+^4S$
f^6, f^8	^7F
f^7	$^8S+^6P+^6I+^4S+^4D+^4H+^4I+^4K+^6D+^6G+^6F+^6H$

2. 2. 6 Selection rules for the lanthanides

Luminescence originates from electronic transitions between 4*f* electrons and is predominantly due to two different transitions between two energy levels. These are:

- electric dipole transitions (ED).
- magnetic dipole transitions (MD).

Electric dipole *f-f* transitions in free 4*f* ions are parity forbidden, but become partially allowed by mixing with orbitals having different parity via a crystal field component. For example, for lanthanide ions, the rule can be relaxed by mixing the $4f^{n-1}$ and 5*d* states. The selection rule in this case is $|\Delta J| \leq 6$, (but not $J = 0 \longleftrightarrow J = 0$, $0 \rightarrow 1$, $0 \rightarrow 3$, $0 \rightarrow 5$). Typical examples of this mechanism are demonstrated by the luminescence from the ^5D_J states of Eu^{3+}; the intensity of these transitions depends strongly on the site of the symmetry in a host crystal.

Magnetic dipole *f-f* transitions are not greatly affected by the site symmetry because they are parity-allowed. The *J* selection rule in this case is $\Delta J = 0, \pm 1$ (not $J = 0 \longleftrightarrow J = 0$).

Now, *f-f* transitions are u→u and u x u=g. So, although *f-f* transitions are electric-dipole forbidden they are magnetic dipole allowed. This is why a magnetic-dipole mechanism is responsible for the appearance of the emission bands originating in the spectra of lanthanide ions doped in host lattices.

2. 2. 7 Electronic transitions in lanthanide ions

The absorption bands that can be detected in lanthanide spectra are associated with electronic transitions of one of these types[7]:

- $4f \rightarrow 4f$ transitions. Electrons in the $4f$ shell are shielded from the external environment by filled 5s and 5p shells, therefore the influence of the host lattice on transitions within the 4f shell is small compared to Coulomb interaction and spin-orbit coupling. These transitions are forbidden, the same way as $d \rightarrow d$ transitions. However, bands arising from these transitions can be detected, giving rise to a large number of weak, sharp bands from the infrared through to the visible region. In the case of d→d transitions (also forbidden in transition metal compounds) they gain intensity when molecular vibrations distort the crystal field. It has been found that this effect also broadens the bands. In the case of $4f \rightarrow 4f$ orbitals, the effects of ligands are very weak, and therefore the transitions are not very intense.

- $4f \rightarrow 5d$ transitions. In addition, lanthanide ions show parity allowed transitions where an electron is promoted to a 5d orbital. They give rise to intense and broad bands in the optical spectra
- $4f^{n} \rightarrow 4f^{n+1}L^{-1}$ where L is a ligand. These are electron-transfer bands. They usually are intense, broad bands which lie in the ultraviolet region. The charge transfer means that in the excited state there is one more f electron than in the ground state.

Of all of these transitions, the first has been studied in more depth even though they are relatively weak.

2. 2. 8 Luminescence of rare earth element ions

Ions without $4f$ electrons such as Y^{3+} do not have electronic energy levels that can induce excitation and luminescence processes in or near the visible region, that is why their oxides are suitable hosts for luminescent lanthanide ions. In contrast, the ions from Ce to Yb have characteristic $4f$ electronic energy levels for each ion showing a variety of luminescence properties in the visible, near infrared and near ultraviolet spectral regions. These levels are not greatly affected by the surrounding environment due to the shielding provided by $5s^2$ and $5p^6$ electrons. The characteristic energy levels of $4f$ electrons of trivalent lanthanide ions were investigated by Dieke[11] who plotted them in what became known as a Dieke digram. This diagram is applicable to ions in almost any environment because the maximum variation of the energy level is, at most, of the order of several hundred cm^{-1}. A modified version of the Dieke diagram published by Carnall et al[13] is shown in Figure 2.8. Each level designated by the J number is split into sublevels, this is the Stark effect due to the crystal field. The number of split sublevels is, at most, $2J+1$, and is determined by the symmetry of the crystal field surrounding the rare-earth ion. The width of each level indicates the range of splitting within each component. Most of the

emitting levels are separated from the new lower level by at least 2 x 10^3 cm^{-1} or more. This is because the excited states relax via two competitive paths: one is by light emission and the other by phonon emission. The phonon emission decreases with an increase in ΔE, therefore the radiative process becomes dominant. For example, the high luminescence efficiency for ^5D_o of Eu^{3+} is based on the large energy gap of more than 10^4 cm^{-1}. In the luminescence spectra of trivalent lanthanide phosphors there are groups of several sharp lines. Each group corresponds to a transition between an excited and ground state designated by the total angular momentum *J*. The assignment of the transition corresponding to each group of lines can be made by comparison with Dieke's diagram. The excitation spectra generally consist of sharp lines due to the 4*f*-4*f* transition and broad bands due to the 4*f*-5*d* transitions and/or charge transfer processes (CTS).

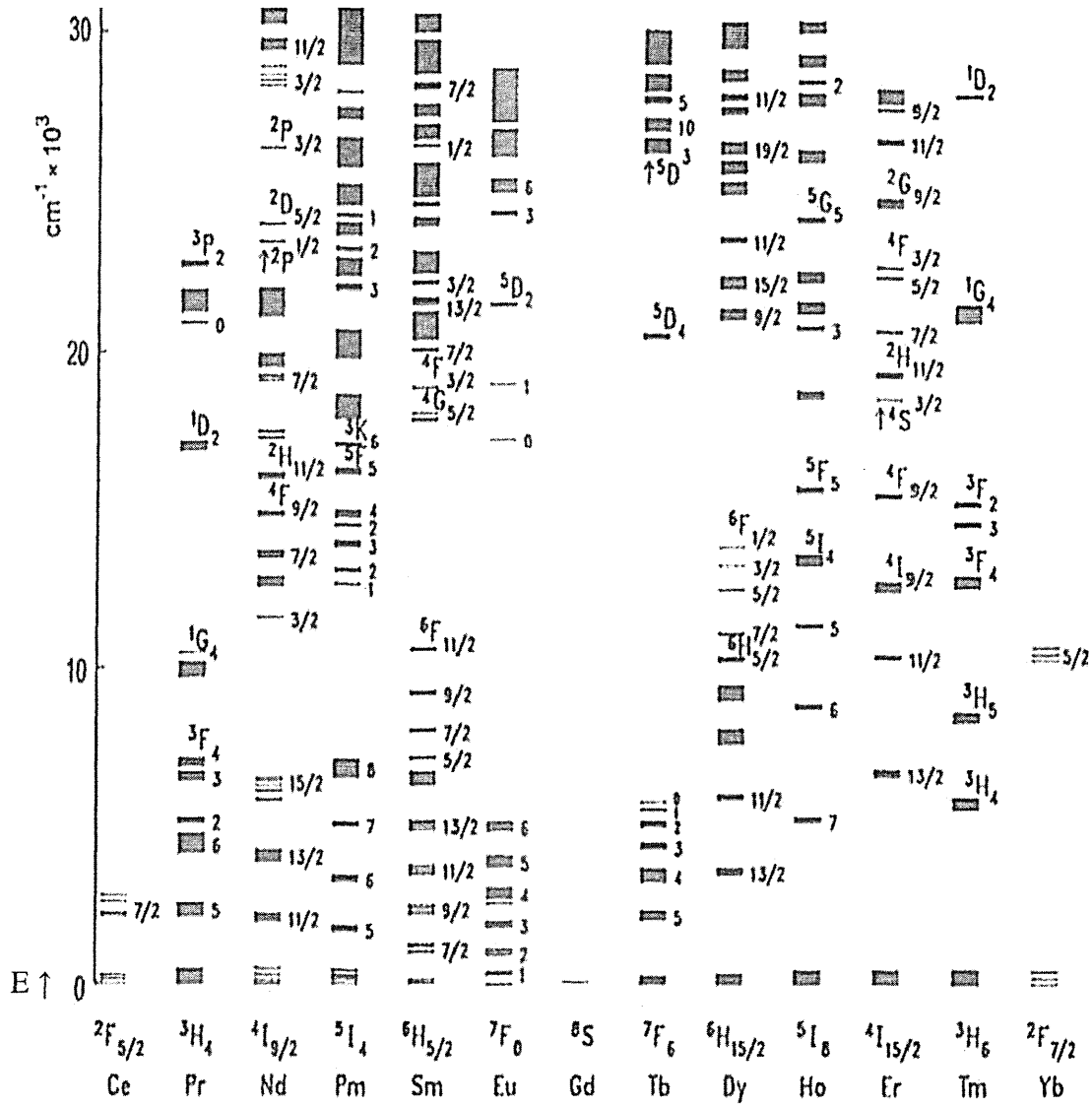

Figure 2.8 Energy levels of trivalent lanthanide cations[13].

2. 3 Lasers

When electrons in an atom are populated to a high energy state, they release the absorbed energy as a photon in the de-excitation process. The way this energy is released can be controlled in a device called a laser. Laser is an acronym for **light amplification by stimulated emission of radiation.**

There are many different types of lasers, and the laser medium can be either a gas, a liquid or a solid. But they all have certain essential features. When the lasing medium is excited to higher levels, a condition called **population inversion**[14] must be achieved. This state is characterised by having more atoms excited into some upper atomic level than in some lower atomic level. When a beam of light tuned to the transition frequency of those two levels is directed to the pumped laser material it can be amplified by a process called **stimulated emission**, when the electromagnetic fields of this beam cause the transition from the populated high energy level to the lower energy level. If a pair of mirrors (one half-silvered to let light through) is placed at each end of the lasing medium, the lightwave can bounce back and forth many times, stimulating other electrons to make the downward energy jump that cause the emission of more photons of the same wavelength and phase.

The light output from a laser device has special features. The light released is monochromatic, its wavelength determined by the amount of energy released when the electron drops to the lower energy level, and it is coherent, i.e. in phase with the exciting field. Moreover the mirror alignment facilitates directional control, and laser light beams are spatially coherent.

2.3.1 Laser parameters

Several characteristics are used to define a laser beam, such as laser power, energy and intensity, but also mode, spot size and depth of focus are important characteristics.

The power of a laser is its output optical power, but lasers operate in either continuous wave state or pulsed state. Therefore normal working power and maximum allowable power must be known. For a pulsed laser, an important parameter is the peak power. In general, CO_2 lasers have relatively high continuous wave power, while Nd:YAG lasers can provide relatively high peak power for pulsed operation. The absolute energy is the total energy in a laser pulse or system, and a typical value for a single laser pulse is 100 mJ. The energy intensity is the area average of laser power and is closely related to the laser focus spot size and pulse lasting time.

ers are also defined by the shape of the beam. For transverse electromagnetic mode (TEM), the labels TEM_{plq} or TEM_{pl} are often used to specify a mode, where p is the number of radial zero fields, q is the number of angular zero fields and l is the number of longitudinal fields. Figure 2.9 shows different TEM laser modes.

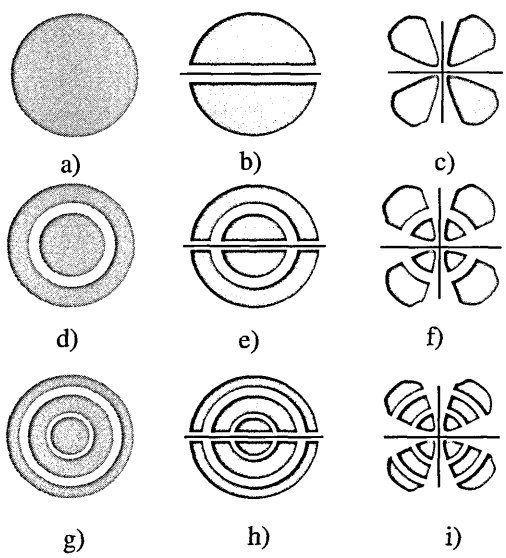

Figure 2.9 Laser cylindrical transverse mode patterns TEM_{pl} a) TEM_{00} b) TEM_{01} c) TEM_{02} d) TEM_{10} e) TEM_{11} f) TEM_{12} g) TEM_{20} h) TEM_{21} and i) TEM_{22}

The ideal mode for laser applications is the TEM_{00} mode, and helium neon lasers and argon-ion lasers are a very close approximation. The amplitude function representing the ideal Gaussian beam is well characterised[15], and its transverse profile is shown in Figure 2.10. This representation allows the definition of another very useful parameter, the beam width which is commonly defined as the diameter for which the beam intensity has fallen to $1/e^2$ (13.5%) of its peak or axial value.

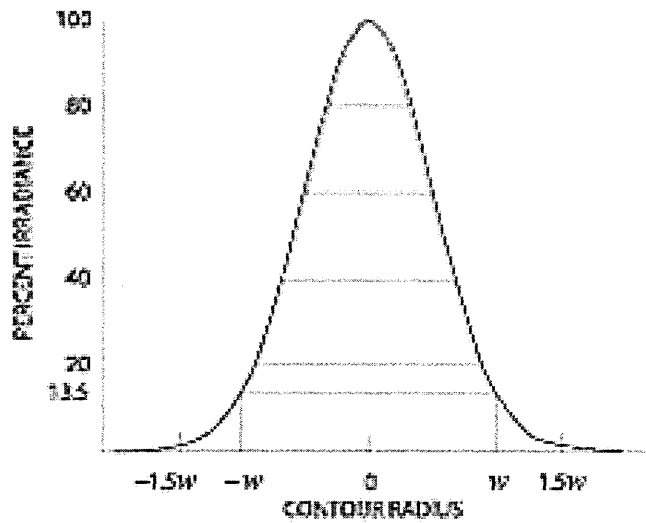

Figure 2.10 Transverse profile of an ideal Gaussian beam.

In general, as the energy density of a laser-beam is not constant when moving outward from the centre of the beam, this parameter is needed to be taken into account when designing applications for laser devices.

References

[1] P. W. Atkins, *Physical Chemistry*, 2nd edition, Oxford University Press, chapter 13, (1982).

[2] I. Butler, J. Harrod, *Inorganic Chemistry*, Benjamin/Cummings Publishing Company, chapter 2, (1989).

[3] S. Cotton, *Lanthanide and Actinides*, Oxford University Press, chapter 2, p10, (1991).

[4] H. B. Kagan, M. Sasaki, J. Collin, *Pure & Appl. Chem.*, **60**, 1725, (1988).

[5] N. N. Greenwood, A. Ernshaw, *Chemistry of the elements*, 2nd edition, chapter 20,30, Butterworth Heinemann, (1997).

[6] S. F. A Kettle, *Physical Inorganic Chemistry*, Spektrum, University Science Books, chapter 11-13, (1996).

[7] N. E. Topp, *The Chemistry of the Rare Earth Elements*, Eleservier, (1965).

[8] B. T. Kilbourn, *A Lanthanide Lanthology*, Molycorp. Inc., Mountain Pass, Ca, USA, (1994).

[9] J. L. Sommerdijk, A. Bril, *Philips Tech. Rev.*, **34**, 24, (1974).

[10] N. N. Greenwood, *Ionic Crystal Lattice Defects and Nonstoichiometry*, Butterworths, chapter 2, p24, (1970).

[11] G. H. Dieke, H. M. Crosswhite, H. Crosswhite, *Spectra and Energy Levels of Rare Earth Ions in Crystals*, New York, Interscience Publishers (1968).

[12] R. Eisberg, R. Resnick, *Quantum Physics of Atoms, Molecules, Solids, Nuclei and Particles*, 2nd edition, Wiley, chapter 10 (1985).

[13] W. T. Carnall, G. L. Goodman, K. Rajnak, R. S. Sane, *J. Chem. Phys.*, **90**, 3443, (1989).

[14] J. R. Whinnery, J. H. Ausubel, H. D. Langford, *Lasers Invention to Application*, National Academy Press (1987).

[15]J. Alda, *Encyclopedia of Optical Engineering*, Marcel Dekker Inc., 999-1013, (2003).

Introduction

Since the 1960's active research in luminescent materials applications led to a range of synthetic routes for phosphors being examined. Examples include wet chemical synthesis, combustion, and pulsed laser deposition[1-3]. During the past decade the development of new devices such as field emission displays (FED) and plasma panel displays (PDP) has led to a demand for materials with improved characteristics[4, 5]. This has provided further impetus to the development of improved synthetic methodologies. The requirement for the close packing of the phosphor grains required control of particle size distribution to tight tolerances, hence research has been focused on the preparation of sub-micrometer particles with uniform morphology[6-8] which show different optical properties depending on particle size[9-10].

In this chapter, the preparative routes to the materials examined in this thesis are described. This is extended to a consideration of the physical characterization techniques routinely employed throughout this work.

Phosphors based in Y_2O_3, Gd_2O_3, and YVO_4 were prepared and doped with different rare earth elements (Eu, Er, Yb). Table 3.1 summarises the systems synthesised for this study.

Table 3.1 Phosphor systems synthesised

Host lattice	Activator	Sensitizer	Phosphor
Y_2O_3	Er		Y_2O_3:Er
		Yb	Y_2O_3:Er,Yb
		Eu	Y_2O_3:Er,Eu
Gd_2O_3	Er		Gd_2O_3:Er
		Yb	Gd_2O_3:Er,Yb
		Eu	Gd_2O_3:Er,Eu

Table 3.1 (cont.) Phosphor systems synthesised

Host lattice	Activator	Sensitizer	Phosphor
$Gd_{2-x}Y_xO3$	Er		$Gd_{2-x}Y_x O_3$:Er
		Yb	$Gd_{2-x}Y_x O_3$:Er,Yb
		Eu	$Gd_{2-x}Y_x O_3$:Er,Eu
YVO_4	Er		YVO_4:Er
		Yb	YVO_4: Er,Yb
		Eu	YVO_4: Er,Eu

Two synthetic routes were used:

- a homogeneous urea precipitation method[11-12], and
- a solid state route, a novel powder processing technique that can produce a multicomponent oxide material using an exothermic reaction between dissolved metal nitrates and an organic fuel. The metals and the fuel are mixed in water to maximize the atomic mixing of the elements, and the solution boiled in an oven to dryness. Once the solvent has evaporated, nitrates and fuel react and ignite. The reaction is self-propagating and able to sustain a high temperature long enough for the reaction to be completed. For the synthesis of YVO_4, 3-methylpyrazole-5-one ($C_4H_6N_2O$) was used as fuel[13].

3.2 Urea homogeneous precipitation

The precipitation reaction to obtain the precursor particles can generally be expressed as follows

$$RE_2O_{3\,(aq)} + 2\,CO_{2\,(g)} + 3\,H_2O_{\,(l)} \longrightarrow 2\,REOHCO_3{\cdot}H_2O_{(s)}$$

If the reagents used to produce the insoluble salt are mixed in solution, huge concentration gradients are created, making it nearly impossible to obtain uniform particles reproducibly. Better results are achieved when the solid phase is generated simultaneously throughout the solution[6]. A homogeneous precipitation can be produced by introducing the ligand slowly in the solution until the solubility limit of the hydroxycarbonate is exceeded.

The method described in this section is based on a process patented in 1995 by Nishisu et al[11] for preparing spherical phosphor precursor particles using the decomposition of urea at high temperature. In general, a basic preparation containing the host lattice oxide dissolved in dilute nitric acid, the activator, and urea, is heated to obtain a mixture of precipitated hydroxycarbonates. Thermal decomposition of urea is necessary in order to supply the reactants in sufficient quantities.

When a solution of urea is heated above 85 °C the following reaction takes place:

$$H_2NCONH_{2\,(aq)} \longrightarrow NH_4^{+}{}_{(aq)} + OCN^{-}{}_{(aq)}$$

Since the reaction is carried on under acid conditions, a rapid quantitative conversion of the cyanate ion into ammonium ion takes place:

$$OCN^{-}{}_{(aq)} + 2H^{+}{}_{(aq)} + 3\,H_2O_{\,(aq)} \longrightarrow H_2CO_{3\,(aq)} + NH_4OH_{(aq)}$$

The carbonic acid is produced in solution, and decomposes rapidly producing CO_2, one of the precipitation reagents:

$$H_2CO_{3\,(aq)} + 2\,H_2O_{\,(l)} \longrightarrow CO_{2\,(g)} + 3\,H_2O_{\,(l)}$$

If the decomposition of urea is carried out in a solution containing Y^{3+} and RE^{3+}, the slow release of carbonate causes the precipitation of the precursor particles when the

solubility limit of their hydroxycarbonate is reached. The supersaturation achieved is never very high, and all nuclei are formed at the same time and grow uniformly. Only one burst of nucleation occurs during the process which is followed by particle growth, creating spherical particles. This phenomenon allows narrow particle size distribution and makes the results repeatable. The overall reaction taking place is as follows:

$$(1\text{-}x)\ Y(NO_3)_{3\ (aq)} + x\ RE(NO_3)_{3\ (aq)} + CO(NH_2)_{2\ (aq)} + H_2O_{(l)} \rightarrow [Y_{1-x}\ RE_x](OH)CO_3 \cdot H_2O_{(s)}$$

The initial pH of the solution is about 2, and it carries on increasing during the reaction process. Precipitation starts at pH 4-5 and the reaction terminates at pH between 7.5 and 8.

The precipitate obtained was then filtered and washed with deionised water and left in the oven for 12 hours to dry. Once the powder was dried, the precursor particles were fired for 6 hours at different temperatures (800°C, 900°C and 1200°C) to transform them into rare earth doped oxide phosphors.

During this process the precursor decomposes in two steps, releasing CO_2 as shown below:

$$2\ YOHCO_{3\ (s)} \xrightarrow{180^oC} Y_2O_2CO_{3\ (s)} + H_2O_{\ (g)} + CO_{2\ (g)}$$

$$Y_2O_2CO_{3\ (s)} \xrightarrow{610^oC} Y_2O_{3\ (s)} + CO_{2\ (g)}$$

The releasing of C from the sample was assumed to be complete and presence of carbon in the fired samples has not been investigated.

The urea homogeneous precipitation method has also been used for the synthesis of YVO_4 based phosphors[14]. Although a number of aqueous precipitation methods to prepare this material have been developed since 1965, when Arbit and Serebrennikov

reported the first synthetic route[15]. One problem that has frequently prevented successful synthesis of YVO_4 arises from the amphoteric nature of V_2O_5[16]. Complete precipitation of YVO_4 only occurs at pH values above 8[15], and yellow powders characteristic of the co-precipitation of polyvanadate species are often obtained.

The initial solution used for the synthesis of YVO_4 contained ammonium metavandate and yttrium oxide together with the activator nitrate and urea. A problem encountered when developing the urea precipitation method for YVO_4:RE synthesis was the premature precipitation of a brown precipitate of hydrated V_2O_5 when adding Y_2O_3 to a NH_4VO_3 aqueous solution. To remedy this, the hexadentate ligand Na_2EDTA was added prior to the addition of yttria to keep it in solution as a complex. EDTA forms very stable complexes in solution with most metals, with some trivalent metal complexes being stable even in strong mineral acid media[17]. When the solution was heated at temperatures above 85°C, precipitation started. The precipitate obtained changes colour during the ageing process, as pH changes and different polyvanadates predominate, but the final precipitate is yellow-light brown. This precipitate was filtered, washed and dried for 12 hours at 105°C, followed by calcination at 980 °C for 6h to obtain YVO_4. Any V_2O_5 formed on the surface of the phosphor was removed by washing with NaOH.

Yttrium oxide (99.9%, Rhone Poulenc, France), gadolinium oxide (99.9%,Aldrich) ammonium metavandate (99%, Aldrich), europium nitrate pentahydrate (99%, Aldrich), erbium nitrate pentahydrate (99%, Aldrich), ytterbium nitrate penthahydrate (99%, Aldrich), urea (AnalaR), nitric Acid (AnalaR), and Na_2-EDTA (Analar) were used to carry out the reactions described in this section.

3.3 Combustion synthesis of YVO_4

In order to avoid the problems encountered during the homogeneous precipitation of yttrium orthovanadate doped phosphors, a combustion method was followed as described by Ekambaram and Patil[13]. The RE doped YVO_4 powders were prepared by rapidly heating an aqueous solution containing yttrium nitrate (oxidiser), the activator, ammonium nitrate (oxidiser) using ammonium metavanadate and 3-methylpyrazole-5-one (3M5O) as fuel.

The fuel was prepared by adding ethyl acetoacetate to hydrazine hydrate cooled in an ice bath according to the following reaction

$$CH_3COCH_2COOC_2H_{5\,(l)} + N_2H_4{\cdot}H_2O_{\,(l)} \longrightarrow C_4H_6N_2O_{(aq)} + H_2O_{(l)} + C_2H_5OH_{(aq)}$$

When the redox mixture was heated at 370 °C, it ignited forming a white voluminous white powder. The product obtained was calcined at 600 and 980 °C to bring about the transformation to YVO_4.

The vanadate formation can be represented by the following reaction sequence:

$$2\ NH_4VO_3 + 3\ NH_4NO_3 \longrightarrow V_2O_{5(s)} + 5\ N_{2(g)} + 10\ H_2O_{(g)}$$

$$4\ Y(NO_3)_3 + 3\ C_4H_6N_2O \longrightarrow 2\ Y_2O_{3(s)} + 12\ CO_{2(g)} + 9\ H_2O_{(g)} + 9\ N_{2\,(g)}$$

$$4\ Y(NO_3)_3 + 4\ NH_4VO_3 + 6\ NH_4NO_3 + 3\ C_4H_6N_2O \rightarrow 4\ YVO_{4(s)} + 12\ CO_{2(g)} + 29\ H_2O_{(g)} + 19\ N_{2(g)}$$

3. 4 Characterisation of physical properties

3. 4. 1 X-Ray Diffraction (XRD)

The crystalline phases present in the powder samples were determined using an X-ray powder diffractometer (XRPD), X-ray generator PW1729, diffractometer control PW1710 and on line recorder PM8203A. Figure 3.1 shows a photograph of the X-ray diffraction apparatus. The basic components are illustrated in Figure 3.2. A small portion

of the X-ray signal, generated from the specimen passes out of the electron optical chamber and impinges on an analysing crystal. If Bragg's law is satisfied,

$$n\lambda = 2d \sin \theta$$

where n is an interger (1, 2, 3, ...), λ is wavelength of the X-rays, d is the interplanar spacing of the crystal, and θ is the angle of incidence of the x-ray in the crystal. The X-rays will be diffracted and detected by a proportional counter. The signal from the detector is amplified, converted to a standard signal and recorded. A typical qualitative analysis therefore involves obtaining a recording of the X-ray intensity as a function of the crystal angle, converting peak positions to interplanar spaces through Bragg's law, and then following indexing, can be related to the presence of specific phases and crystal identification. Standard tables (JCPDS database) can then be used for compound identification by comparison[18].

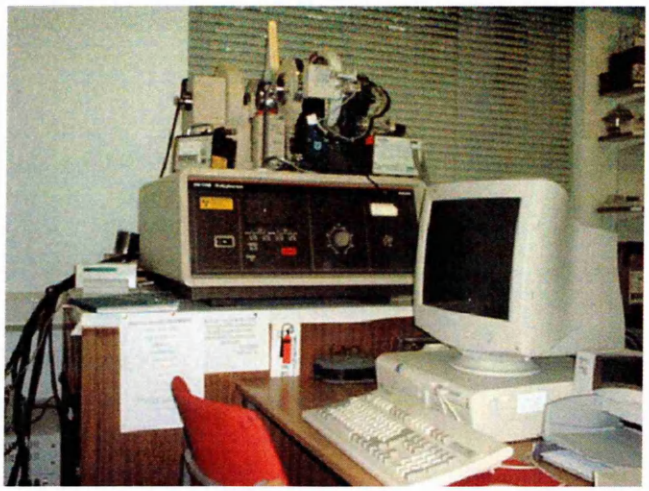

Figure 3.1 X-ray diffraction system.

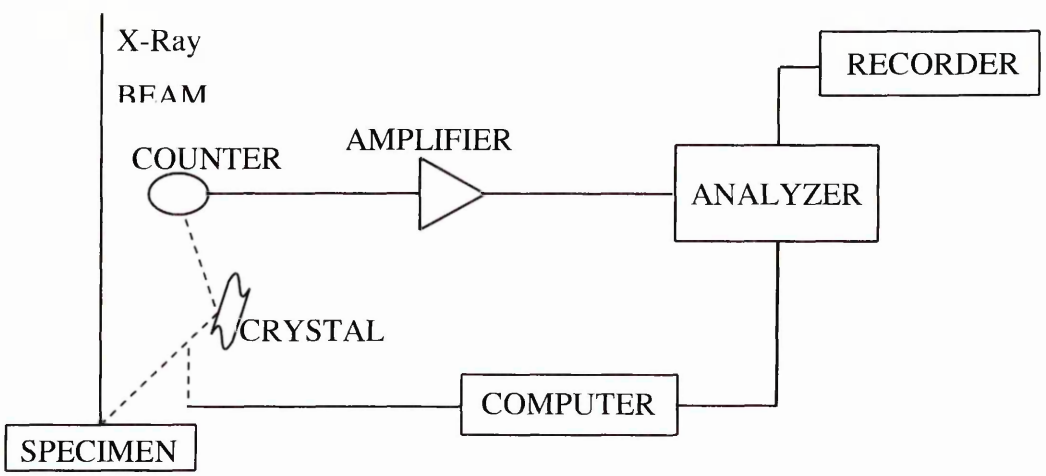

Figure 3.2 Schematic representation of an XRD apparatus.

3. 4. 2 Scanning electron microscope (SEM)

The basic function of an SEM is to produce an image of three dimensional appearance derived from the action of an electron beam scanning across the surface of a specimen. Figure 3.3 shows a schematic of a SEM. In general, the electron gun produces a large, high intensity electron beam which is shaped into a size useable for scanning microscopy. The beam is scanned over the sample releasing electrons from the surface. The electron

collector and display collects these electrons and converts them to an image which can be viewed by the operator. All these functions are directed by electronic controls. The SEM can have a magnification range from a few times to several hundred thousand times. The upper magnification is limited only by the resolution available.

A Stereoscan 90 Cambridge Instruments SEM was used to analyse the morphology and the particle size of rare-earth doped phosphor powders. It has a resolution of around 50 nm. The measurement of particle size may be made directly using the visual image produced by an optical microscope; in most cases, however, sizes are measured using micrographs of the particles. The size of the particles in the photographs is determined using an appropriate scale once the magnification factors have been established. The average diameter of the particles (and standard deviation) were estimated from measuring 25 particles per micrograph. Figure 3.4 shows a picture of the SEM equipment used to carry out these measurements

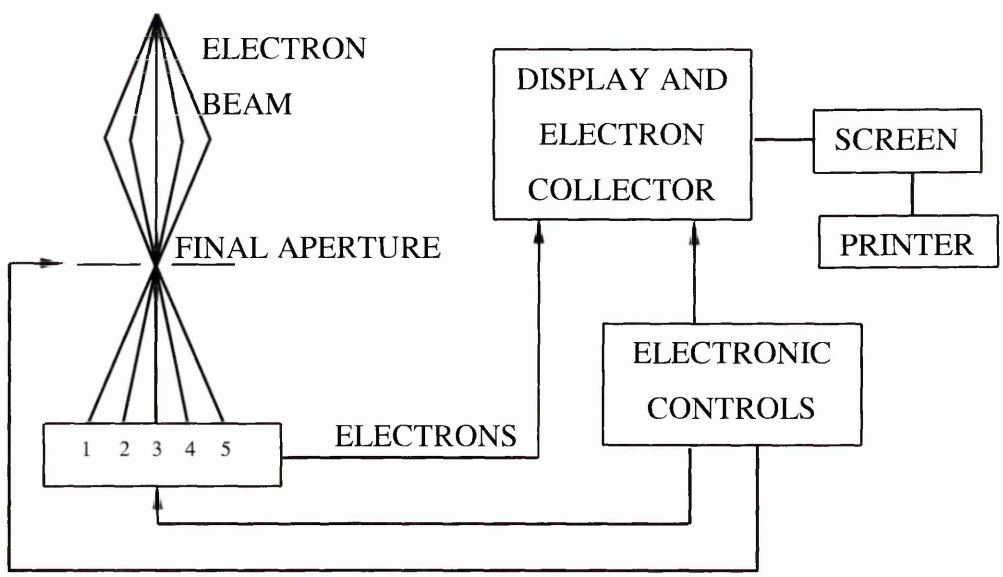

Figure 3.3 Schematic of a SEM. Numbers 1-5 indicate successive beam positions during a scanning sequence.

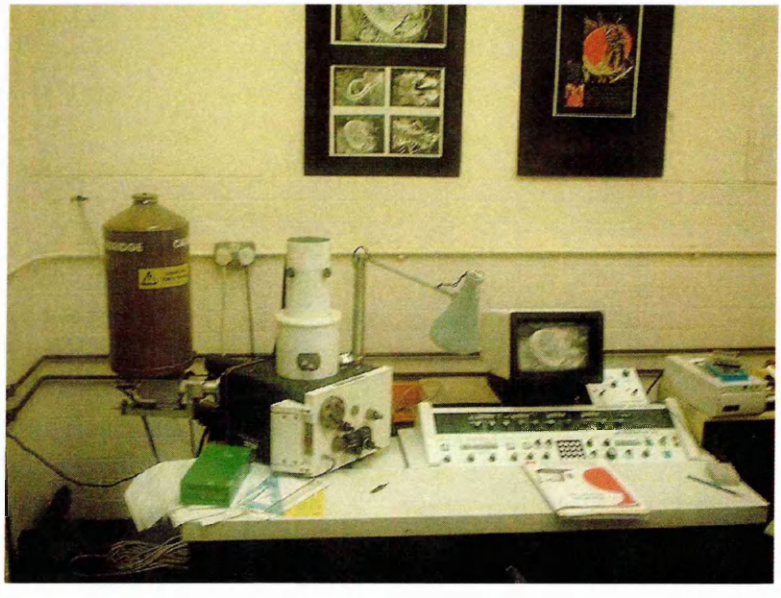

Figure 3.4 Stereoscan 90 Cambridge Instruments SEM.

3. 4. 3 Luminescence and Raman spectroscopy

Raman spectroscopy is based on the inelastic scattering of light by a gas, liquid or solid with a shift in wavelength from that of the usually monochromatic incident radiation (the Raman effect). When the scattered radiation from a medium irradiated with an intense source of monochromatic light is spectroscopically analysed, light of the exciting frequency is observed (Rayleigh scattering) together with some weaker bands of shifted frequency. Moreover, there will be shifted bands coexisting at lower frequency called Stokes bands, and shifted bands at higher frequency called anti-Stokes bands (Figure 3.5). Both are equally displaced about the Rayleigh band[19].

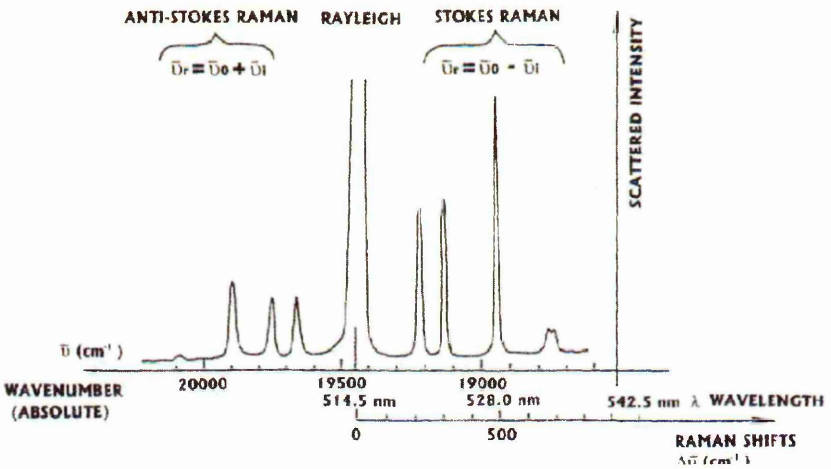

Figure 3.5 Schematic representation of a Raman spectrum obtained using green line of an argon-ion laser. λ= 514.5 nm.

Raman spectroscopy is a valuable tool for the characterisation of phosphors, due to its sensitivity to composition and structure of the lattices. It provides information about the host lattice and also about the site symmetries occupied by the activators. The majority of Raman spectroscopy studies of the solid state are concerned with the vibrational properties of the solids. The vibrational Raman spectrum of a phosphor can be collected in a matter of minutes and, it enables the identification of the phosphor lattice.

A small number of solid state studies have concentrated on the electronic Raman effect. The effectiveness of electronic Raman spectroscopy arises from the fact that internal electronic transitions take place between levels of the same parity, thus they are Raman active but electric dipole forbidden. Therefore, laser induced emission spectroscopy enables the localization of low-lying levels of the ground states of lanthanide ions, something that may be very difficult to characterise by other means[20].

Luminescence and Raman spectra were obtained using a Labram Raman spectrometer equipped with an 1800 g/mm holographic grating, a holographic supernotch filter, and a peltier-cooled CCD detector (Figure 3.6). Samples were excited using a helium-neon laser with an output of 8 mW of power at the sample on the 632.8 nm line, unless an attenuation filter was used. Precise control of sample temperature was achieved by means of a Linkam THM600 temperature programmable heating/cooling microscope stage. For cooling, the THMS stage was used in conjunction with a Linkam LNP cooling system. Spectral intensities were normalised using the Stokes Raman band at 375 cm^{-1} of undoped host lattices. The Labram is an integrated Raman system. The microscope is coupled confocally to a 300 mm focal length spectrograph equipped with two switchable gratings. The main parts of the instrument seen when the cover was removed are shown in Figure 3.7.

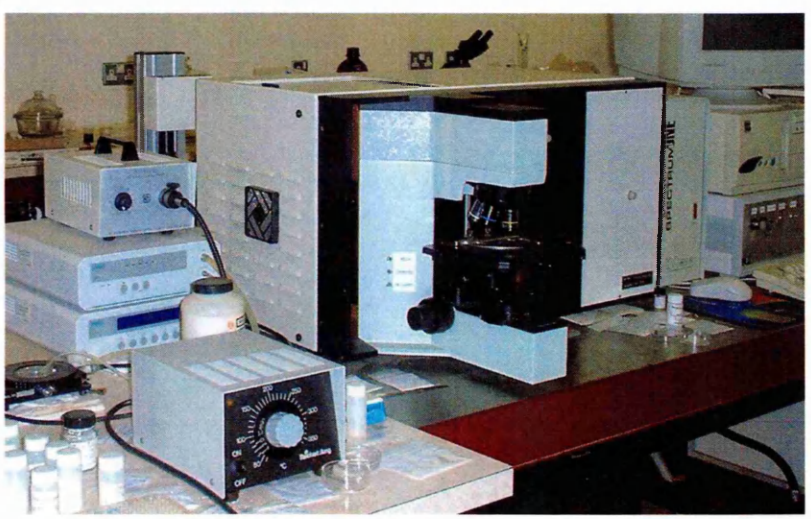

Figure 3.6 Labram Raman spectrometer.

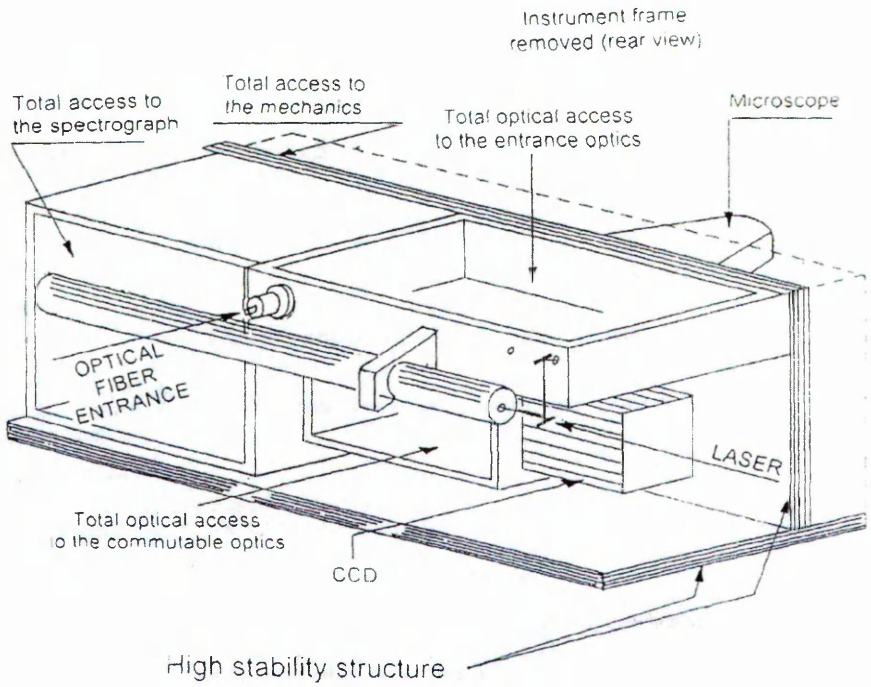

Figure 3.7 Schematic of the Labram instrument[21].

The excitation wavelength is supplied by an internal He-Ne 20 mW, polarised 500:1 and wavelength 632.817 nm, laser mounted at the back of the instrument. An entrance for another external laser beam is also placed on the back side (laser wavelength available includes virtually any laser within 440-800 nm). The spectrograph is the box on the right side of the instrument and forms a spectrum on the Peltier CCD detector that is placed under the microscope. The external laser available is an Ar^+ 514.532 nm. Figure 3.8 shows a layout of the connections for a Raman spectrometer.

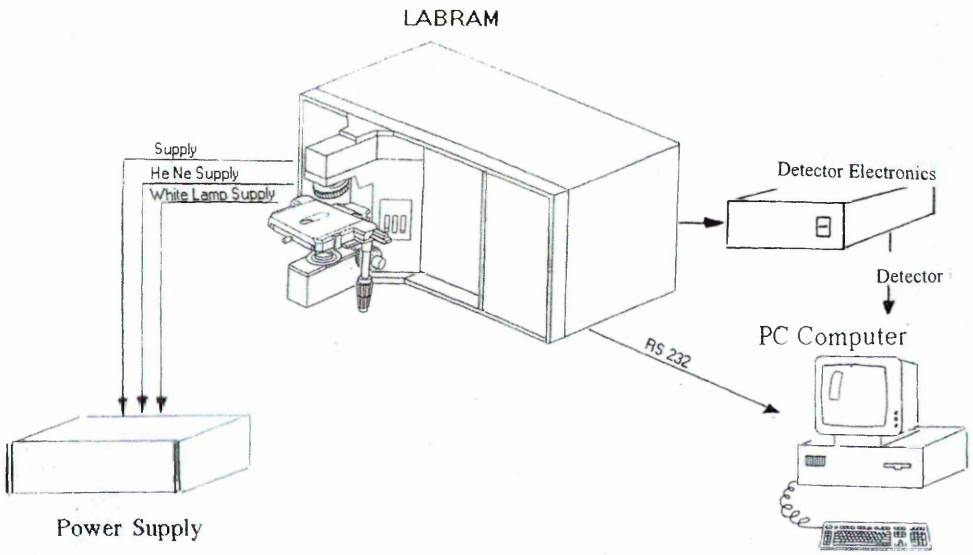

Figure 3.8 Layout of the connections for a Raman spectrometer[21]

References

[1] P. K. Sharma, M. H. Jilavi, H. Schmidt, V. K. Varadan, *Int. J. Inorg. Mater.*, **2**, 407 (2000).

[2] L.E. Shea, J. McKittrick, O. A. Lopez, E. Sluzky, *J. Am. Ceram. Soc.*, **79**, 3257 (1996).

[3] H. Eilers B.M. Tissue, *Chem. Phys Letters*, **251**, 74 (1996).

[4] P. Maestro, D. Huguenin, *J. Alloys Comp.*, **225**, 520 (1995).

[5] L.E. Shea, J. McKittrick, C. F. Bacalski, E. J. Bosze, *Displays*, **19**, 169 (1999).

[6] M. Akinc and D. Sordelet, *J. Colloid Interface Sci.*, **122**, 47, (1988).

[7] E. Matijevic and W. P. Hsu, *J. Colloid Interface Sci.*, **118**, 506, (1987).

[8] M. J. Kim and E. Matijevic, *J. Mater. Res.*, **6**, 840, (1991).

[9] E. T. Goldburt, B. Kulkarni, R. N. Bhargava, J. Taylor M. Libera, *J. Lumin.*, **72-74**, 190 (1997).

[10] T. Ye, Z. Guiwen, Z. Weiping, X. Shangda, *Mat. Res. Bull.*, **32**, 501, (1997).

[11] Y. Nishisu and M. Kobayashi, *US Patent Data Base 5413736: Particulate fluorescent Material of* $(Y_{1-x}, Eu_x)_2O_3$ *and process of preparing the same*, (1995).

[12] Y. D. Jiang, Z. L. Wang, F. Zhang, H. G. Paics, and C. J. Summers, *J. Mater. Res.*, **13**, 2950, (1998)

[13] S. Ekambaram, K. C. Patil, *J. Alloys Comp.*, **217**, 104 (1995)

[14] A. Newport, J. Silver, A. Vecht, , *J. Electrochem. Soc.*, **147**, 3944, (2000)

[15] A. Huignard, T. Gacoin, J. P. Biolot, *Chem. Mat.*, **12**, 1090, (2000)

[16] N.N. Greenwood, A. Earnshaw, *Chemistry of the Elements* (2nd Edition), Elsevier, chapter 22, (1998)

[17] T. S. West, *Complexometry with EDTA and related reagents*, BDH Chemicals Ltd, (1969)

[18] J. I. Goldstein, D. E. Newbury, P. Echlin, D. C. Joy, C. Fiori, E. Lifshin, *Scanning Electron Microscopy and X-Ray Microanalysis*, Plenum Press, chapter 7, (1981)

[19] J. M. Hollas, *Modern Spectroscopy*, J. Wiley & Sons, chapter 5, (1987)

[20] J. Silver, R. Withnall, *Chemical Reviews*, **104**, 2833, (2004)

[21] Labram Raman Instrument Manual, ISA Dilor-Jobin Yvon-Spec

Chapter 4 Wet Chemical Preparation and Characterisation of Rare-Earth Doped Yttria

Introduction

Rare earth doped yttrium oxide is commonly used in phosphors for optical displays and lighting applications. The earliest report of Y_2O_3 and its properties as a phosphor host was probably in 1961, when Wickersheim and Lefever reported on the optical properties of Eu and Tb doped yttrium oxides[1] and in 1962, a flame fusion process for the synthesis of Y_2O_3:Eu for use as an efficient phosphor in fluorescent lamps was reported by Lefever and Clark[2] .

The photoelectronic processes of rare earth doped yttria have long been of interest. In 1963 Chang[3] reported that the most prominent emission of $Y_2O_3:Eu^{3+}$ is a $^5D_0 \rightarrow {}^7F_2$ band centered at 611 nm and the intensity of this emission is influenced by rare-earth co-dopants. Furthermore Peterson and Bridenbaugh demonstrated that emission from Tb^{3+} ions can be quenched by non-radiative transfer to other rare-earth ions[4]. Subsequently Axe and Weller presented evidence for non-radiative resonant energy transfer between Eu^{3+} and other rare-earth ions in Y_2O_3 [5].

In 1964, further work on the luminescence of rare earth ions, especially Eu^{3+} in different hosts, appeared. Specifically Wickersheim and Lefever presented the excitation and emission spectra of $Y_2O_3:Eu^{3+}$, and noted its high efficiency and unusual performance at elevated temperatures[6]. Bril and Wanmaker, also in 1964, studied the fluorescent properties of different Eu-activated phosphors[7]. Ropp and co-workers published in the same year work on solid state reactions that produced phosphors involving oxides of trivalent rare earth cations[8], and this was extended to a study of the spectral properties of rare-earth oxide phosphors, revealing that fluorescence occurs only in matrices where the cation possesses no unpaired electrons[9].

Dieke, in 1968, presented a comprehensive study of the electronic spectra of lanthanide ions in different oxide lattices[10], which provided a theoretical basis for understanding the nature of excitation and emission processes in the whole rare earths series. In 1982, optical spectra, energy levels and crystal field of tri-positive rare-earth ions in Y_2O_3, were studied by Leavitt, Gruber, Chang and Morrison[11].

In 1965, the crystal structure of Y_2O_3 was reported by Wyckoff[12], who found that Y_2O_3 is body-centred, with two Y^{3+} crystallographic sites. Both sites are six coordinate, that is, each Y^{3+} is surrounded by six atoms of oxygen located at the corners of a cube. Two of the corners are vacant and situated in a body or face diagonal of the cube. Therefore, the Y^{3+} ion can have two symmetries. The body diagonal is referred to as S_6 and the face diagonal, C_2. Two kinds of layers form the unit cell. One is composed of C_2 sites only, and in the other one both sites are present in a ratio C_2 to S_6 of 3:1.

The nature of the crystallographic site of substitutional ions in the yttria host have also been of interest. Studies by Mandel[13] on $Y_2O_3:Yb^{3+}$ and Toma and Palumbo[14] on $Y_2O_3:Bi^{3+}$, revealed that Y_2O_3 activated phosphors contain substitutional ions at both non-centrosymmetric C_2 and centrosymmetric S_6 sites.

Chang and Gruber studied the luminescence of the $Y_2O_3:Eu^{3+}$ in 1964[15]. They postulated that all the emissions of Eu^{3+} were due to C_2 sites. No emissions were found due to S_6 sites. Nevertheless, studying emission spectra, showed five lines in the region of the $^7F_0 \rightarrow {}^5D_1$ transitions. Only three of these five lines could be assigned to C_2 symmetry, therefore they speculated the other two lines could be due to Eu^{3+} ions located at S_6 sites.

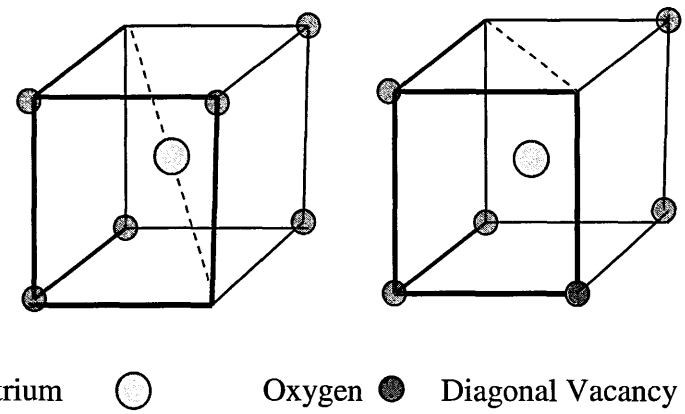

Figure 4.1 The two crystallographic sites in Y_2O_3.

There has long been intense interest in the application of "wet chemical" routes to ceramic materials, including mixed metal oxides, implicit in which is the molecular level mixing of precursors which has been shown to facilitate control of microstructural and textural properties. These processing routes have been given further impetus in recent years which a drive towards the production of nanoparticulate materials[16]. Furthermore the development in the 1990's of high resolution screen technology such as flat panel (FPD's) and field emissive displays (FED's) has created the need of a generation of phosphors with new or enhanced properties [17]. In addition, it is essential that the phosphor layer that forms the viewing screen is thin (1 to 5 μm) and composed of closely packed particles. There is thus an identifiable need to produce submicron particles with spherical morphology for these displays, and during the past decade intensive research has been undertaken to control the factors that lead to the preparation of phosphor nanoparticles of defined morphology.

Many techniques have been employed to prepare these powder phosphors, such as wet chemical synthesis[18], combustion[19] or pulsed laser deposition[20]. Early studies were carried out by Sordelet and Aknic, who developed the method of the hydrolysis of urea[21] initiated by Matijevic[22], and the even earlier work of Willard and Tang[23]. Monosized yttria precursor particles powders of high homogeneity and uniformity result due to the

generation of solid phase simultaneously and evenly throughout the solution, by homogeneous precipitation in aqueous solutions. Using the method of hydrolysis of urea has allowed the production of more efficient phosphor materials at lower temperatures (< 1100°C) than previously used in industry via solid-state reactions (1700°C).

Due to the fine size distribution and the density of the particles obtained, the urea homogeneous precipitation method[24-31]was chosen as suitable for this study. Y_2O_3:RE^{3+} phosphor particles prepared using the urea homogeneous precipitation method were studied using different techniques. The crystallinity and structure of the phosphor powders were established using powder XRD and Raman spectroscopy. Their dimensions and morphology were studied using SEM. ESR studies were carried out with the aim of determining the local environment of the Er^{3+} ions in the lattice. The luminescent properties were determined using laser induced emission spectroscopy.

Energy transfer processes have been reported to take place between RE luminescent centres. Sometimes these processes can enhance the intensity of the emission, whereas in different circumstances the addition of a co-dopant to a system using a low phonon energy host lattice can help to dissipate the population of certain energy levels. These phenomena are of great interest in the control of the luminescent properties and will be further studied for Er^{3+}-Yb^{3+} and Er^{3+}-Eu^{3+} co-dopant systems.

4. 2 Results and discussion

4.2.1 Structural characterization of Y_2O_3

Powder XRD patterns were routinely measured to ascertain sample homogeneity (i.e. solid solution formation) of particular importance at substitution levels up to 20 mol%

used here, and later in Chapter 5 where the cubic-monoclinic transition in $Gd_{2-x}Y_xO_3$ is monitored. A typical powder X-ray diffraction pattern of a hydroxycarbonate precursor is shown in Figure 4.2. The broad peaks present, strongly suggest an amorphous structure. Crystalline yttria was formed on firing in air at 980°C (confirmed by fitting the data to the Joint Committee Powder Diffraction Spectroscopy, data file number 25-1200, p538, 1986) (Figure 4.3) . The values obtained from a refinement study of the structure are summarized in Table 4.1. Structure refinement studies were carried out using *UnitCell.* It is a non-linear least squares cell refinement program with regression diagnostics developed by T. J. B. Holland, University of Cambridge.

It was important to assess if the Y_2O_3:RE powder phosphors formed a single phase solid. Solid solutions are very common in crystalline materials, and can be described as a crystalline phase with variable composition. There are minimum requirements to be met in the formation of such solids, such as the fact that the ions replacing each other must have the same charge (to avoid the creation of vacancies or interstitials) and that the substituting ions must be similar in size to the substituted one (a difference up to 15% in ionic radii). These two requirements are met for the ions in this study. For the different rare earth phosphors prepared and the different doping levels used no remarkable changes in the X-ray diffraction pattern were detected, and all were consistent with formation of the cubic polymorph. These results strengthen the assumption that the rare earth atoms substitute at yttrium sites in the Y_2O_3 lattice when the doped phosphor powder is produced, forming substitutional solid solutions.

Table 4.1 Refined structure of Y_2O_3.

***a*/ Å**	10.5716±0.0022
cell volume (Å^3):	1181.47

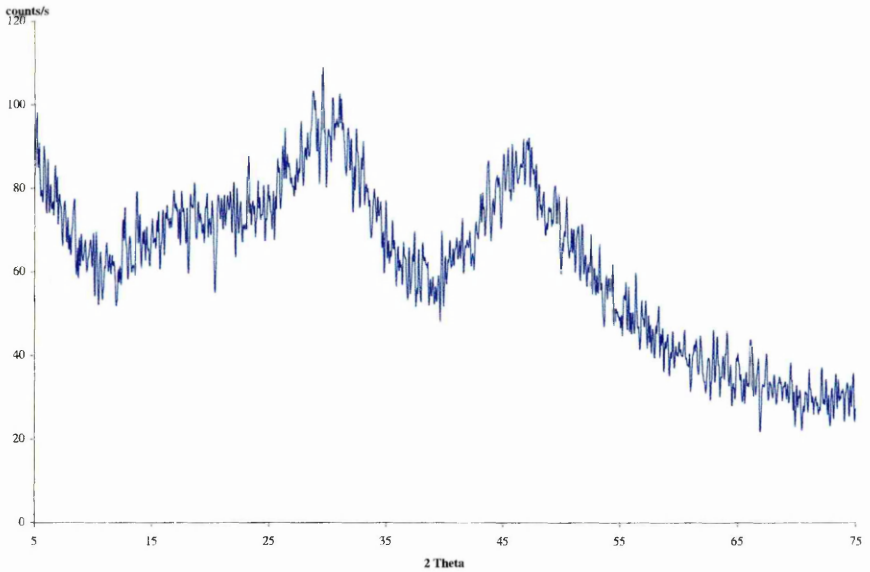

Figure 4.2 XRD pattern of the spherical phosphor precursor particles.

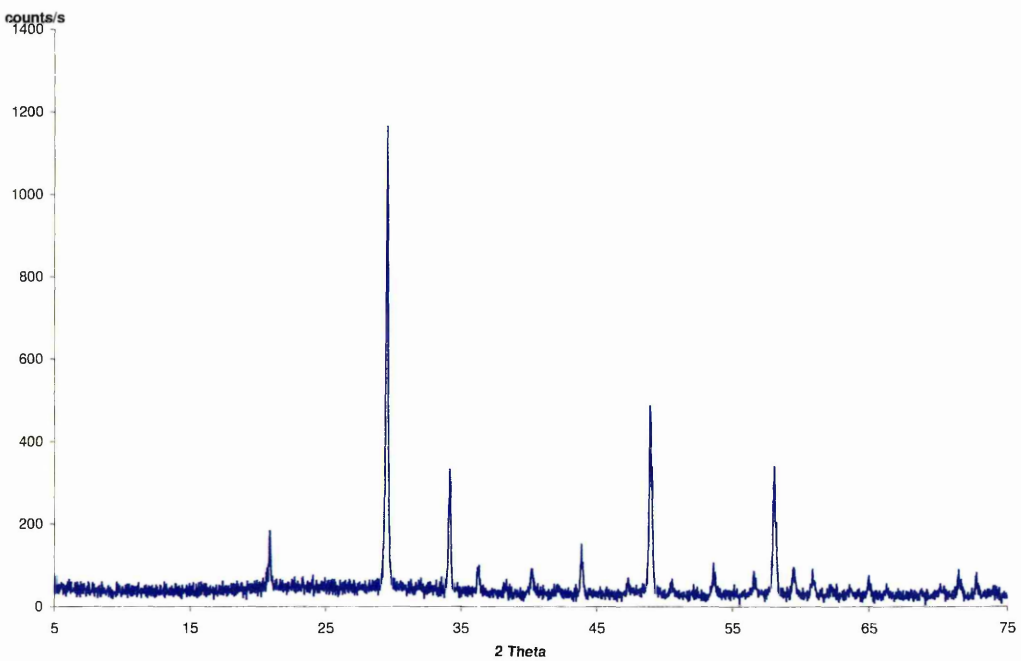

Figure 4.3 XRD pattern of the Y_2O_3 sample fired at 980°C for 6 hours.

As the lattice parameters of solid solutions often show a small but detectable variation with composition, samples containing nominal concentrations of Yb^{3+} from 1 mol% to 20 mol% in the Y_2O_3 host lattice were prepared to study the changes in the cell

parameters when a foreign ion was introduced. It is believed that the size of the ions that randomly substitute ions of the lattice forming the solid solutions, governs the changes in the lattice parameters. In accord with Vegard's law, a slight reduction in the a value when the Yb^{3+} concentration was increased was observed (Table 4.2). This is a consequence of the difference in the cationic ionic radii. $r(Yb^{3+})$= 0.858Å and $r(Y^{3+})$= 0.892Å. This was extended to a consideration of the effect of Eu^{3+} doping at 20 %, where a larger *a* value was calculated, compared to Y_2O_3 doped with Yb^{3+} at the same concentration, in line with expectation for an ion having a larger ionic radius than Yb^{3+} ($r(Eu^{3+})$= 0.95Å).

Table 4.2 Variation in the cell parameters of Y_2O_3:Yb^{3+} and Y_2O_3:Eu^{3+} as a function of the concentration of the doping ion.

	Dopant ion and level					
	1% Yb	**2% Yb**	**5% Yb**	**8% Yb**	**20% Yb**	**20% Eu**
a value (Å)	10.5391 ±0.0070	10.5283 ±0.0078	10.5198 ±0.0657	10.5190 ±0.0058	10.5069 ±0.0110	10.6062 ±0.0032
cell volume(Å^3)	1170.619	1167.007	1164.196	1163.912	1159.908	1193.097

In addition to the XRD results, structural information was obtained using Raman spectroscopy. Spectra of the pure polycrystalline Y_2O_3 host lattice were recorded (Figure 4.4) to be used as a control for luminescence measurements of doped samples. Cubic Y_2O_3 is predicted to have twenty-two Raman lines[32-37], and those detected are listed in Table 4.3. These spectra verify that the phosphor powders crystallize in the cubic phase and furthermore, facilitate normalization of the emission bands by reference to the Raman band at 378 cm^{-1}. A shift in this Raman band was found when using different dopants (Table 4.4). This is consistent with the increase of the mass of the dopant ion on moving across

the lanthanide series. This provides further evidence for substitutional solid solution formation. This shift has been previously reported but has not been detected for lattices containing erbium.

Table 4.3 Assignment of Raman spectrum of cubic Y_2O_3 (cm^{-1}).

Schaak *et al* [33]	White *et al* [35]	Gouteron *et al* [34]	Repelin *et al* [37]	Experimental results
597 F_g	603	592 F_g	591 F_g+A_g	591
	576	567 E_g	564 F_g+A_g	
			526 F_g	
473 F_g	480	468 F_g	469 F_g+A_g	468
434 F_g	440	430 F_g	429 F_g+A_g	431
		402 F_g	399 F_g	402
381 F_g+A_g	389	383 E_g		
		379 F_g	376 F_g+A_g	378
333 E_g	337	330 F_g	329 F_g+A_g	330
320 F_g+E_g	325	318 F_g	318 F_g	317
		194 E_g	193 F_g+E_g	194
		182 F_g	179 F_g	180
164 F_g+A_g	162	161 F_g+A_g	161 F_g+A_g	161
133 F_g		130 F_g	129 F_g	131
			116 F_g	

Table 4.4 Detected Raman band shift for Y_2O_3 doped lattices (cm^{-1}).

Y_2O_3	Y_2O_3:Eu (10mol%)	Y_2O_3:Er (10mol%)	Y_2O_3:Yb (10mol%)
378	375	378	379

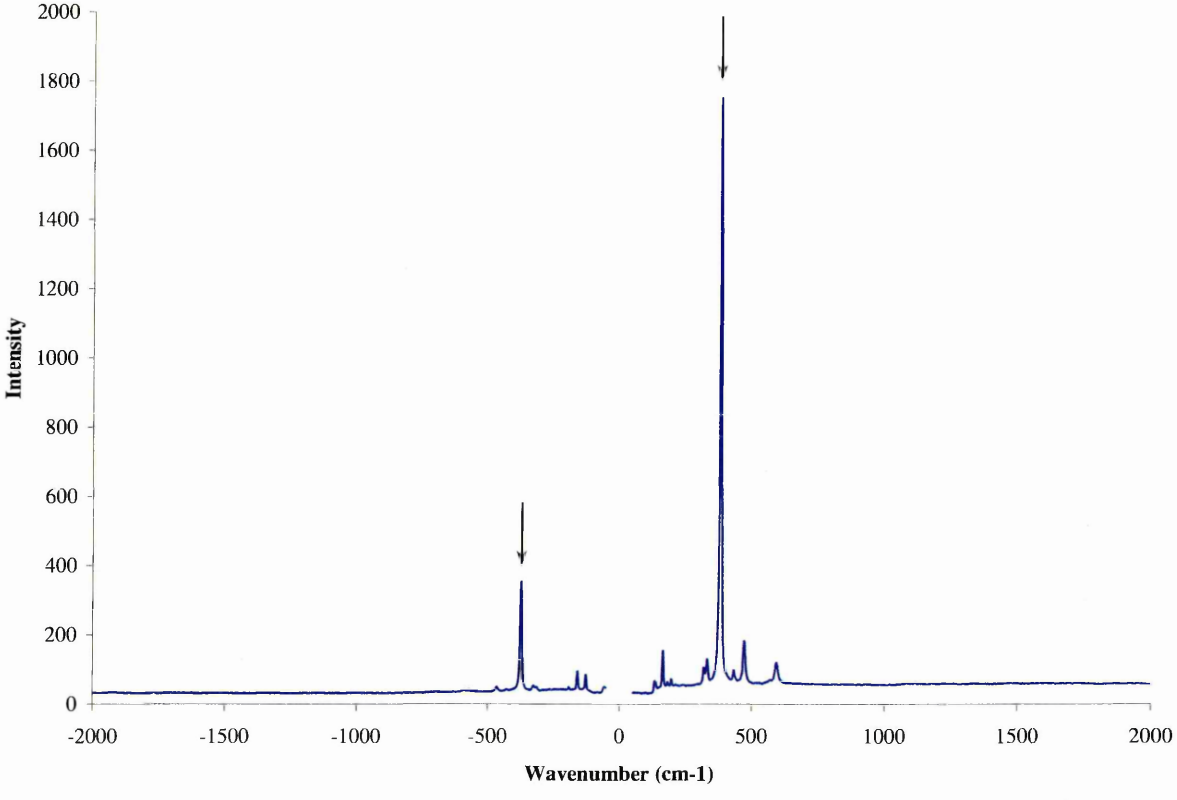

Figure 4.4 Anti-Stokes and Stokes Raman spectrum of Y_2O_3. The Raman band at 378 cm^{-1} is marked with arrows in both the Stokes and anti-Stokes regions.

4.2.2 The influence of the reaction conditions on the morphology of the Y_2O_3 phosphor powders

The particles were synthesised from aqueous solutions of Y^{3+} of 6.27×10^{-3}M and 1.25×10^{-2}M nominal concentrations, respectively. Following addition of 15 g of urea and boiling for 45 minutes, the particle size of the precipitate was estimated by SEM. SEM

images of precipitates from these solutions are illustrated in Figure 4.5. The uniformity of the particles is clearly demonstrated. The diameter of 25 particles per micrograph was measured. The average diameter was 386±25nm for the sample developed from the former solution and 702±52nm for the sample obtained from the latter. This suggests that the number of initially created nuclei does not vary with the initial yttrium concentration. Rather that, an increase in the cation concentration produces longer grains due to a more rapid deposition.

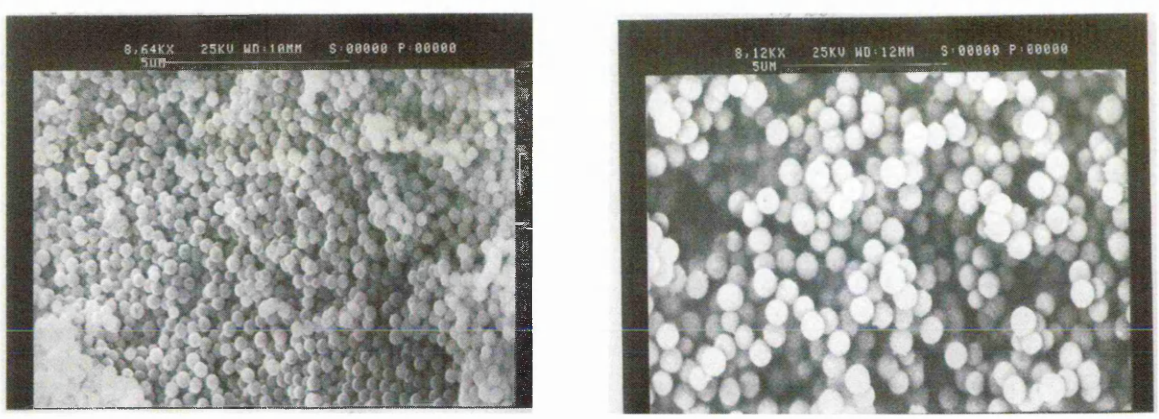

(a) (b)

Figure 4.5 SEM micrographs of the precipitate obtained from the Y^{3+} solutions (a) 6.27×10^{-3} M, and (b) 1.25×10^{-2} M.

Solutions where the initial concentration of $Y^{3+}$was 6.27×10^{-3}M were boiled for 45 minutes, 60 minutes and 90 minutes to determine the effect of the ageing time on the size of the spherical Y_2O_3 precursor particles. The particle size of the precipitate obtained was estimated by SEM, again measuring 25 particles per micrograph. The average particle sizes obtained were 386±25 nm when the ageing time was 45 minutes, 487±17 nm for the 60 minutes ageing time sample and 517±31 nm for the sample boiled for 90 minutes (Figure 4.6). Again, this supports the supposition that the number of nuclei remains constant during the precipitation process[38].

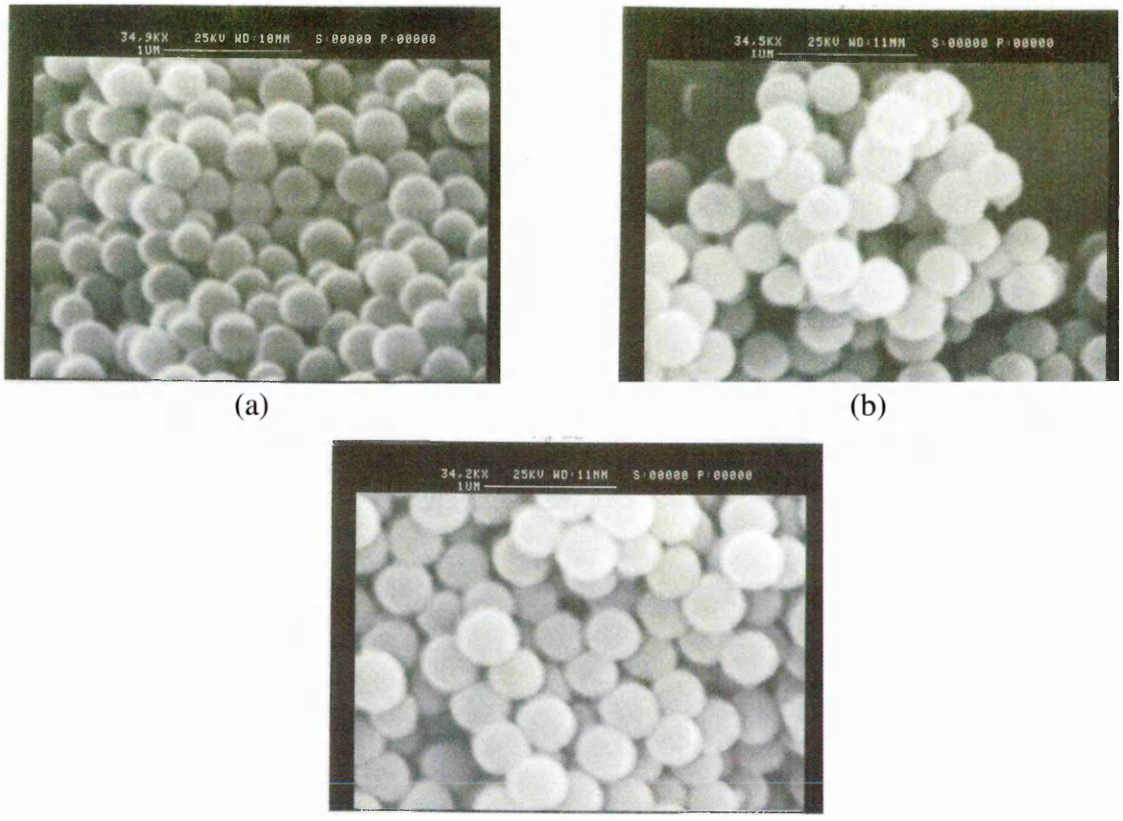

Figure 4.6 Influence of the ageing time on the size of the precipitate. (a) 45 minutes (b) 60 minutes and (c) 90 minutes.

Clearly, the particles formed following precipitation had spherical morphology. As such it is important to ascertain whether or not a spherical shape is maintained on firing to induce crystallization. Figure 4.7 shows the microstructure of the powders on firing up to 1200°C for 6 hours. A reduction in the particle size was observed on transformation of the hydroxycarbonate to the oxide, followed by agglomeration and distortion of the spherical shape when the firing temperature was increased. This could be a consequence of partial melting of the sample during the firing process. This effect was most significant at 1200°C. Samples fired at 980°C were found to be crystalline by powder XRD maintained an approximately spherical morphology.

The final average particle sizes as a function of ageing time and firing temperature are summarised in Table 4.5.

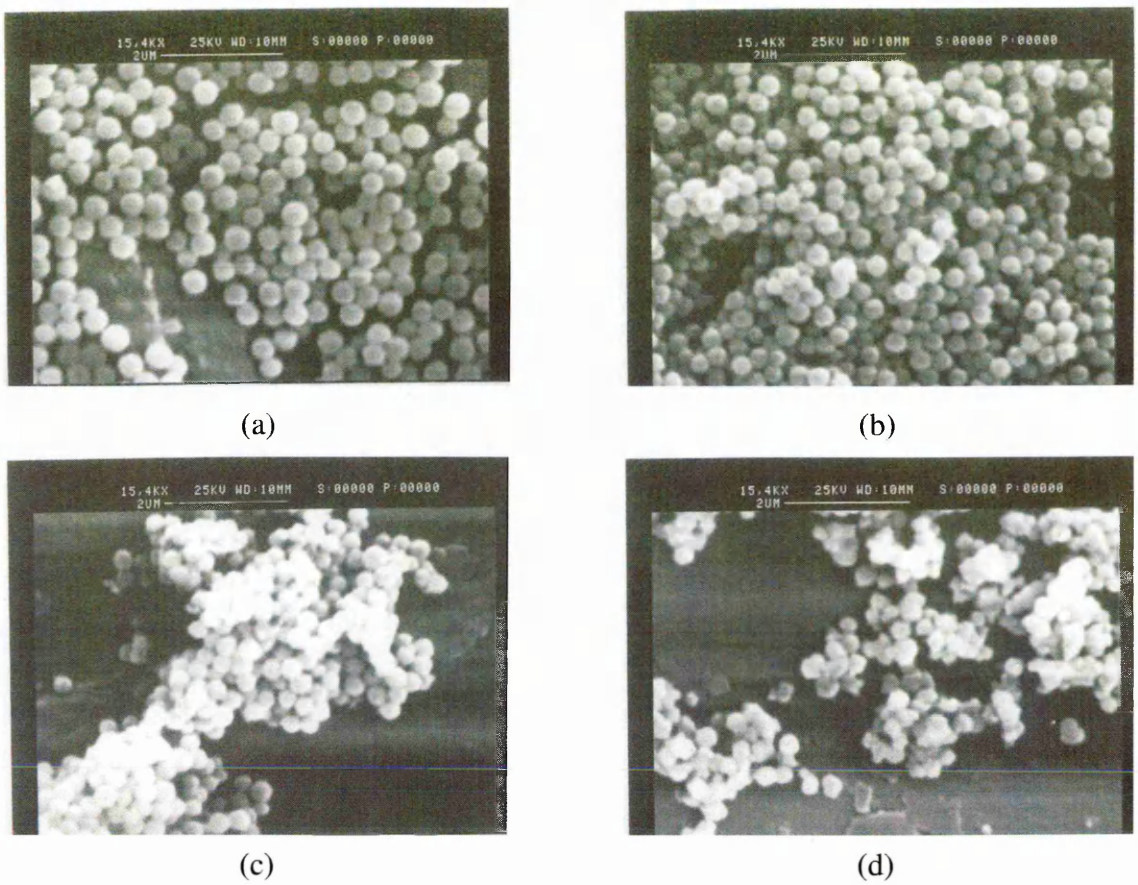

Figure 4.7 Effect of the firing temperature on the Y_2O_3 precursor particles. (a) unfired sample (b) fired at 800°C (c) fired at 980°C (d) fired at 1200°C. The scale bars shown = 2 μm.

Table 4.5 Evolution of particle size with firing temperature.

		Firing temperature			
Y^{3+} Concentration	**Ageing time**	**Unfired**	**800°C**	**980°C**	**1200°C**
1.25×10^{-2}M	45'	702±52nm	603±48nm	598±37nm	588±41nm
6.27×10^{-3}M	45'	386±25nm	308±26nm	292±23nm	271±31nm
	60'	487±17nm	381±18nm	359±35nm	341±27nm
	90'	517±31nm	412±30nm	380±18nm	350±21nm

A linear relationship was found between particle size and firing temperature, and final precipitate sizes can be approximately predicted. This is shown in Figure 4.8. The equations calculated for these straight lines omitting unfired data are:

Concentration	Ageing time	Equation
1.25×10^{-2}M	45'a	y = 611.33 – 7.5 x
6.27×10^{-3}M	45'b	y = 442.67 – 31 x
	60'	y = 400.33 – 20 x
	90'	y = 327.33 – 18.5 x

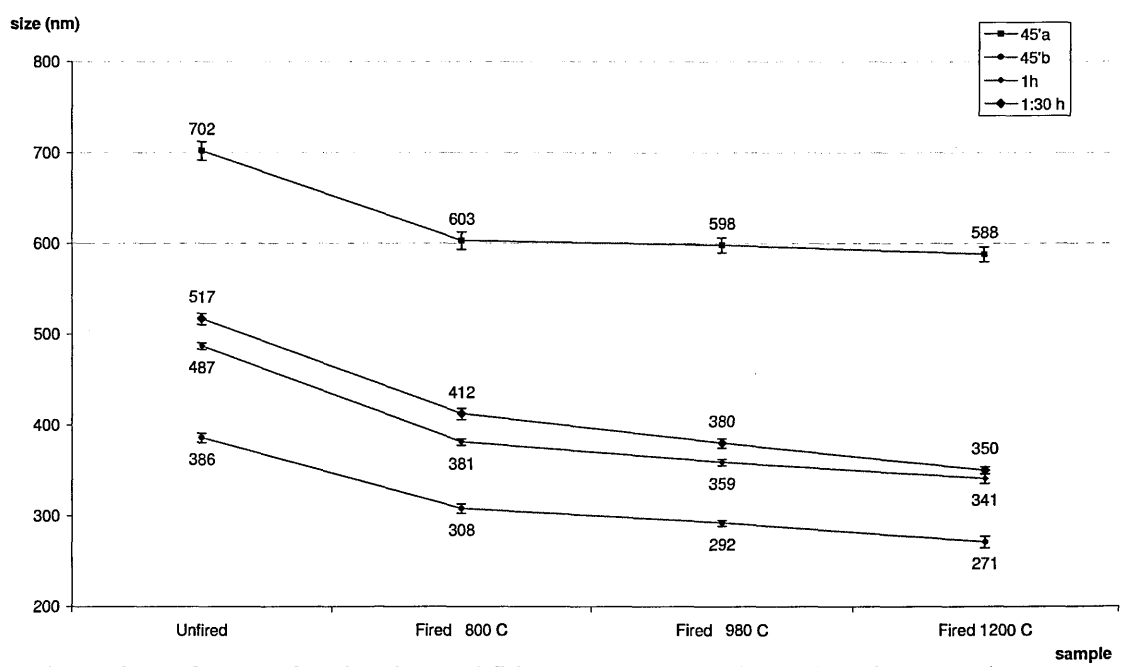

Figure 4.8 Influence of ageing time and firing temperature on the particle size. Error bars show SE, N=25.

In summary, the urea precipitation method has been shown to be suitable for the preparation of uniform spherical powder Y_2O_3:RE phosphors, facilitating control over particle size and morphology by judicious manipulation of processing parameters. Other

factors such as the initial urea concentration[38] have been reported to affect the morphology of the phosphor precursor whereas the addition of reagents such as disodium EDTA can help to achieve very small particle sizes[39] (in the order of a few nanometres). Being able to control the spherical nature of the precipitates and fired materials is of great importance in order to produce close packed aggregates and improve the resolution of device applications where they might be used.

4.2.3 ESR measurements on $Y_2O_3:Er^{3+}$

ESR measurements on the samples have been carried out with a view to studying the Er^{3+} local environment in the host lattice.

A broad signal attributed to Er^{3+} ions was found in fired samples only. This signal was not detected from un-doped Y_2O_3. We suggest that additional signals are due to impurity Fe^{3+} which is incorporated into yttria lattice on firing. Spectra of the unfired and fired Y_2O_3:Er (1mol%) samples are shown in Figure 4.9 (a and b). However, little information of the local environment can be obtained.

The spectra recorded were reminiscent of Er^{3+} in $ErBa_2Cu_3O_7$. It should be noted that even though spectra of Er^{3+} have provided useful structural information in single crystal hosts, successful measurements on powder phosphors had necessitated the use of high microwave frequencies.

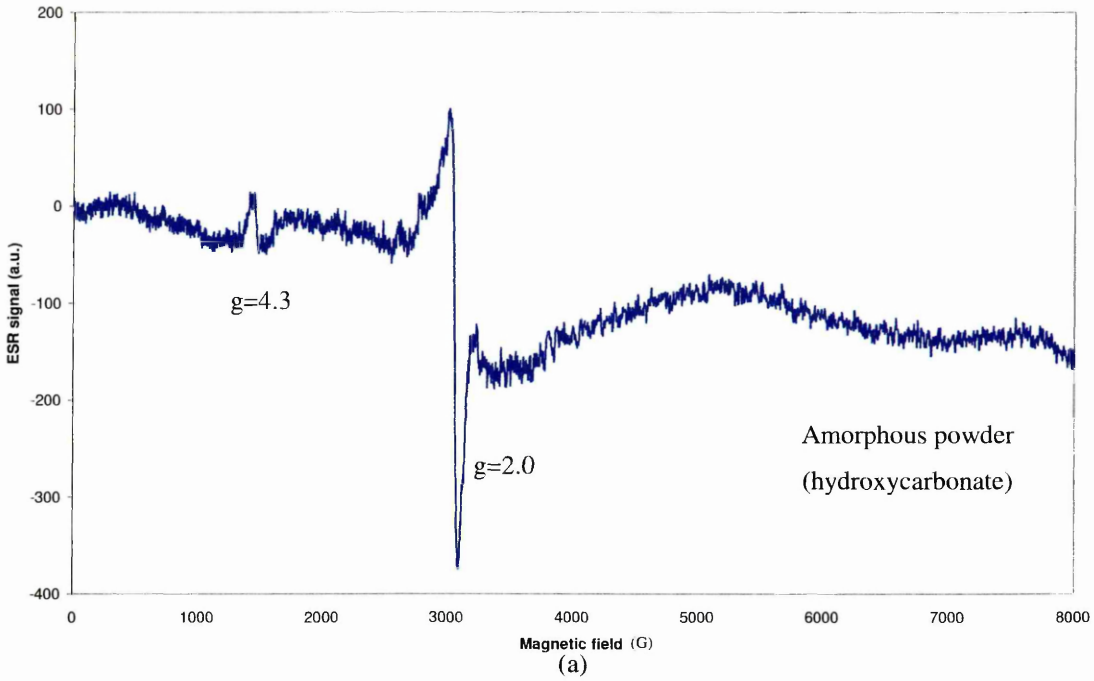

(a)

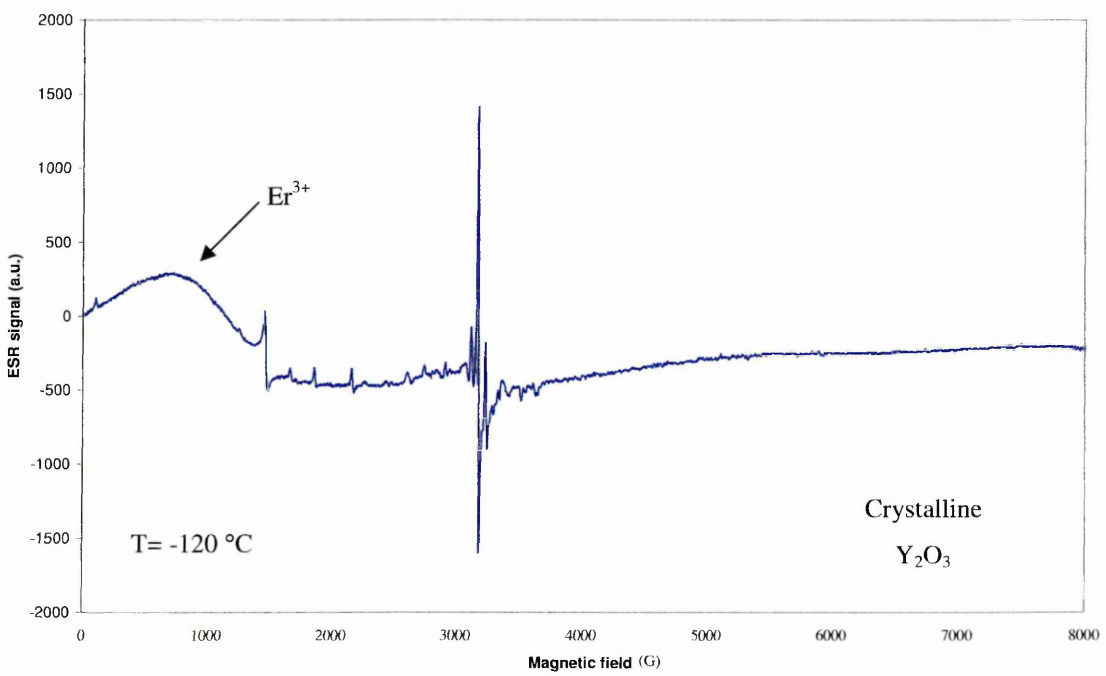

(b)

Figure 4.9 ESR signal of Y_2O_3:Er1% samples (a) unfired (b) fired 980°C.

4.2.4 Luminescence properties of Y_2O_3:RE phosphors

Raman calibration

Pure and erbium doped Y_2O_3 samples were analysed using Raman and laser-induced luminescence spectroscopy to study the emission characteristics of the luminescent centre. The effect of the addition of Yb^{3+} and Eu^{3+} as co-dopants was also assessed. It should be noted that when the energy of the incoming laser is adjusted such that it coincides with one electronic transition in the crystal resonant effects may increase the Raman scattering intensity. This effect has not been addressed in this study, and it is assumed that when normalising with the Raman intensity of the undoped Y_2O_3 lattice a comparable error is introduced in all measurements.

Because the wavelengths of neon emission lines are stable and well established, they can be used to calibrate the spectrometer . In the spectrograph wavelength calibration , the CCD array detector was illuminated with neon light, spectra were taken and the position of the peaks compared with reference data. All the recorded data were very similar and therefore only one of the series is shown as an example. The experimental results and the reference values are compared in Table 4.6 and a typical neon calibration spectrum is shown in Figure 4.10.

Table 4.6 Calibration of laser Raman spectrometer for helium-neon excitation.

	Reference			Results		
	Wavelength (nm)	**Frequency (cm^{-1}_{vac})**	**Apparent Raman shift (cm^{-1}_{vac})**	**Wavelength (nm)**	**Frequency (cm^{-1}_{vac})**	**Apparent Raman shift (cm^{-1}_{vac})**
1	638.29	15662	136	638.36	15665	133
2	640.22	15615	183	640.29	15618	180
3	642.17	15567	231	642.31	15569	229
4	650.65	15364	434	650.73	15367	431
5	653.28	15302	496	653.35	15306	492
6	659.89	15149	649	659.97	15152	646
7	667.82	14969	829	667.91	14972	826
8	671.70	14883	915	671.77	14886	912
9	692.94	14427	1371	693.02	14430	1368
10	702.40	14232	1566	702.48	14235	1563
11	703.24	14215	1583	703.30	14219	1579
12	717.39	13935	1863	717.45	13938	1860
13	724.51	13798	2000	724.63	13800	1998
14	743.88	13439	2359	743.94	13442	2356
15	748.88	13349	2449	748.93	13352	2446
16	753.57	13266	2532	753.69	13268	2530
17	808.24	12369	3429	808.38	12370	3428
18	812.89	12298	3500	812.98	12300	3498
19	813.64	12287	3511	813.74	12289	3509
20	826.71	12092	3706	826.77	12095	3703

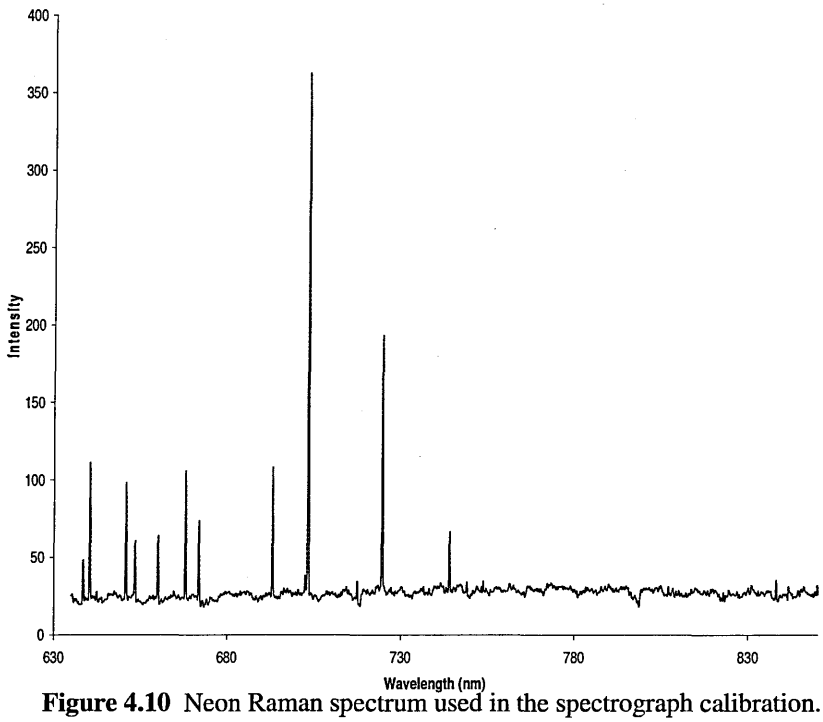

Figure 4.10 Neon Raman spectrum used in the spectrograph calibration.

Raman setting assessment

Stokes and anti-Stokes emission were studied for the Er^{3+} luminescent centre. When excited with 632.8nm radiation, Stokes emissions in Er^{3+} are produced by the absorption of one photon, whereas anti-Stokes emissions are produced by the absorption of two photons[40]. The intensity of the emission in one photon processes shows a linear relationship with the incident energy, while two photon processes exhibit a quadratic relationship[41]. In general, as the energy density of a laser-beam is not constant as we move outward from the centre of the beam[42] (it gradually decreases in the shape of a Gaussian curve[43]), the ratio between the intensity (I) of Stokes and anti-Stokes emissions will change depending on the confocal pinhole selected to carry out the measurements. In general:

$$\frac{\textbf{Small size}\ \text{I up-conversion}}{\text{I down-conversion}} > \frac{\textbf{Large size}\ \text{I up-conversion}}{\text{I down-conversion}}$$

An experiment was designed to determine the optimum confocal pinhole to be used in order to generate spectra of sufficient intensity to enable the study of the weaker emission bands, and to obtain a good intensity ratio for the anti-Stokes and Stokes emission bands.

Spectra of the sample $Y_2O_3:Er^{3+}$ (2 mol%) were measured using different confocal pinhole diameters, which were varied from 100μm to 900μm in 100μm increments. The spectra obtained were normalised with the Y_2O_3 Raman band at 378 cm^{-1} and the emission bands integrated. Three spectra are shown in Figure 4.11 (a, b and c), where the increase in intensity and also the variation in ratio between anti-Stokes and Stokes bands can be observed. Figure 4.12 is a plot of the confocal pinhole size versus intensity ratio of the emissions.

The confocal pinhole finally selected for the luminescent measurements was 400 μm due to the intensity of spectra and low saturation.

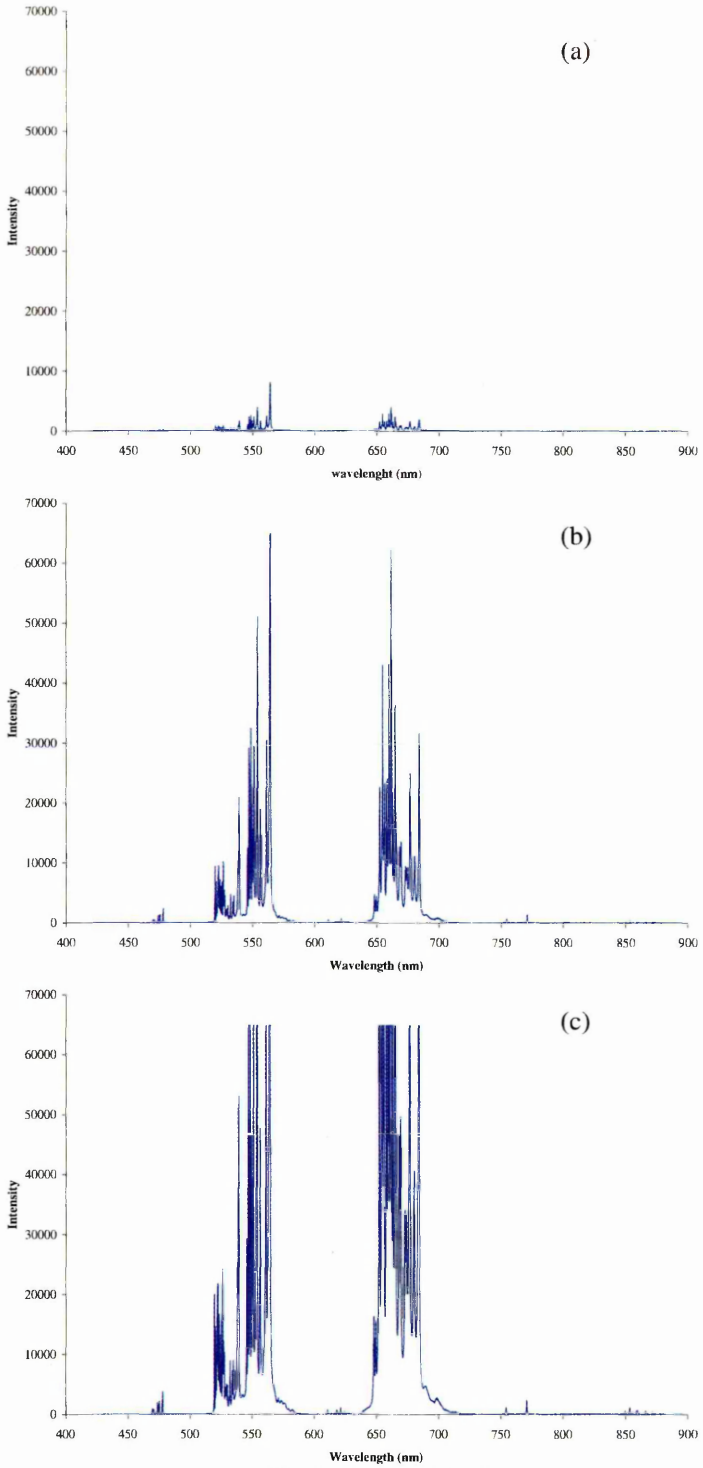

Figure 4.11 Luminescent spectrum of Y_2O_3:Er 2 mol% obtained using (a) 100 (b) 400, and (c) 900 μm confocal pinholes.

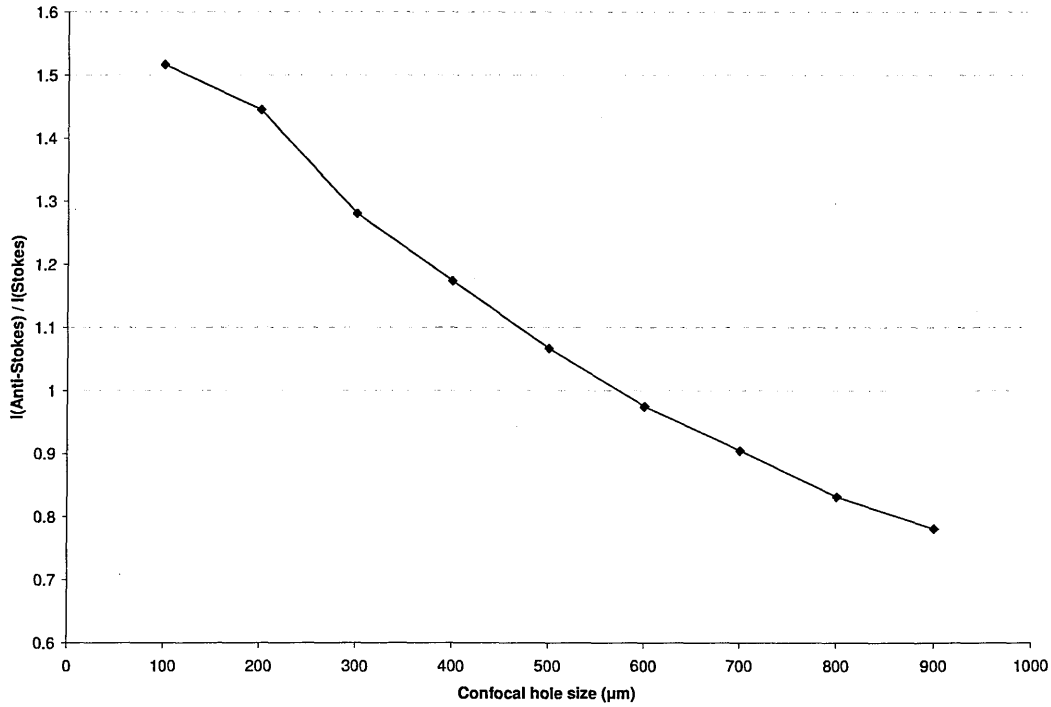

Figure 4.12 Influence of the confocal pinhole size on the anti-Stokes and Stokes emission bands ratio for $Y_2O_3:Er^{3+}$ 2 mol%

Y_2O_3:Er phosphors

Laser-induced spectroscopy under 632.8 nm wavelength excitation using a helium-neon laser source has been used to study the up-converting and down-converting properties of these $Y_2O_3:Er^{3+}$ phosphors.

A single Raman band typical of the Y_2O_3 cubic lattice is seen in both spectra at a wavenumber shift of 378cm^{-1} and has been used to normalize the signal.

The anti-Stokes emission spectrum of $Y_2O_3:Er^{3+}$ in the range 420-630 nm at room temperature is shown in Figure 4.13, and the Stokes emission spectrum in the range from 634 to 895 nm is shown in Figure 4.14. Over the entire wavelength range, six emission manifolds were detected. These correspond to electronic transitions in the Er^{3+} ion from different excited states, two additional manifolds (a and b) were also detected, thought to arise from Stark splittings due to the crystal field around the Er^{3+} activator ions[39]. Previous studies on these powder phosphors helped to assign the main emission bands to the

following excited state-ground state transitions. The emission arising from the level $^4I_{11/2}$ was too weak to allow further studies. Table 4.7 summarises the emission bands detected in the spectra.

Table 4.7 Assignments of Stokes and anti-Stokes emission bands of $Y_2O_3:Er^{3+}$.

	emission band range	
emission assignment	**nm**	**cm^{-1}**
$^4F_{7/2} \rightarrow {}^4I_{15/2}$	468-479	21367-20876
$^2H_{11/2} \rightarrow {}^4I_{15/2}$	518-540	19307-18518
$^4S_{3/2} \rightarrow {}^4I_{15/2}$	546-566	18315-17667
(a)	610-632	16393-15823
$^4F_{9/2} \rightarrow {}^4I_{15/2}$	648-685	15432-14598
(b)	754-772	13623-12593
$^4I_{9/2} \rightarrow {}^4I_{15/2}$	785-830	12738-12048
$^4I_{11/2} \rightarrow {}^4I_{15/2}$	845-882	11834-11337

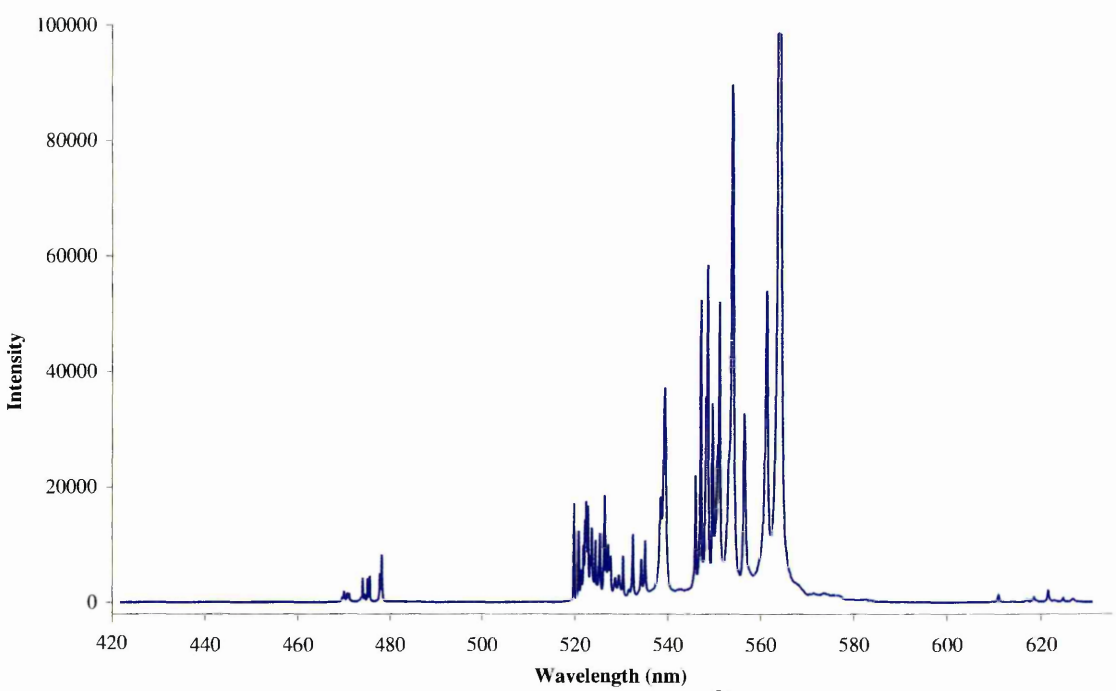

Figure 4.13 Anti-Stokes emission spectrum of $Y_2O_3:Er^{3+}$ (1mol%) at room temperature in the 420-630 nm region. Relative intensities are in arbitrary units.

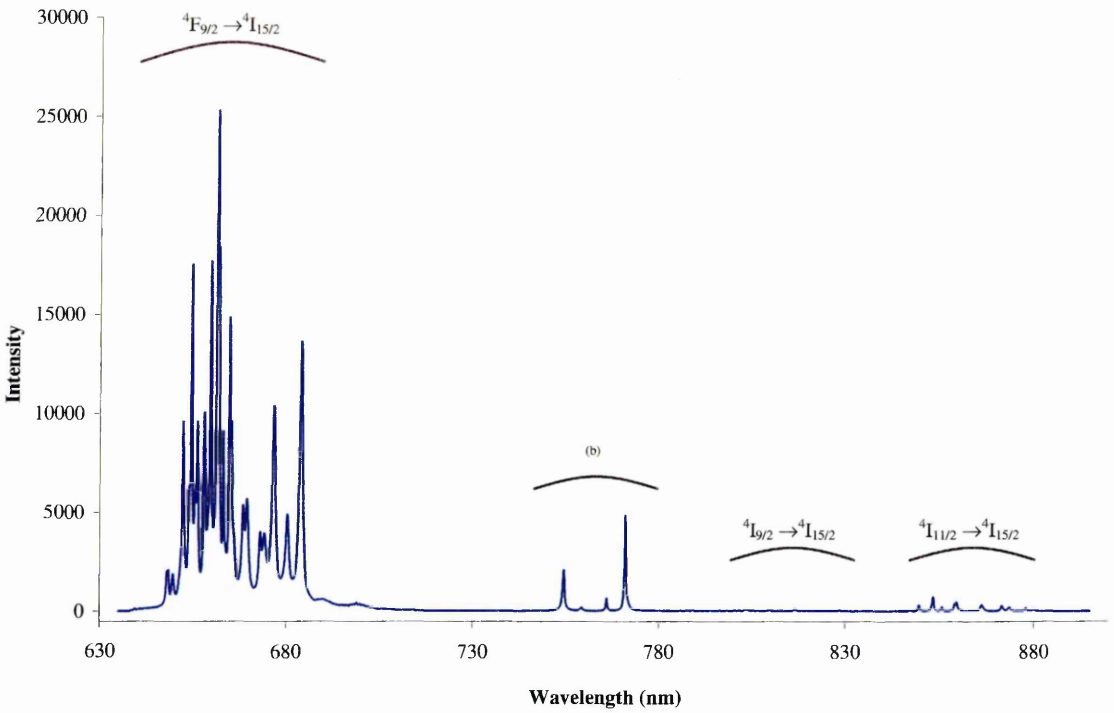

Figure 4.14 Stokes emission spectrum of $Y_2O_3:Er^{3+}$ (1mol%) at room temperature in the 630-900 nm region. Relative intensities are in arbitrary units.

The emission bands of the activator are formed by a series of multiple peaks, each arising from the relaxation processes from the Stark components of an excited electronic state. These Stark components are affected by the crystal field from O^{2-} ions, and therefore the appearance of the emission spectrum of a given luminescent centre may vary when the surrounding crystal field changes[44]. Recent studies on Eu^{3+} doped in various oxide and oxosalt lattices[45] indicate that the position and shape of the emission lines is very sensitive to small differences in the crystal field, even when its effect is small for the low-lying levels of rare earth ions. This factor can be of particular importance in the control of the luminescence properties of the activator in phosphors (see chapters 5 and 6).

Studies reported earlier in this chapter showed that firing at either 800 °C or 980 °C transforms the hydroxycarbonate precursor particles of the desired diameter to the oxide phosphor powder without losing the spherical shape. However, the efficiency of the phosphor is a factor of predominant importance. In order to determine the effect of firing

temperature on the phosphor efficiency, Y_2O_3 samples containing 1mol% Er^{3+} have been fired at 800°C and 980°C.

The Raman spectra obtained from both samples show the seven emission manifolds, as can be seen in Figures 4.15 and 4.16. It is clear that materials fired at 980 °C produce the more intense emissions for all the detected transitions, despite the reported reduction in sphericity. For this reason, in order to improve the phosphor efficiency, the higher temperature was chosen to fire the powder phosphor samples.

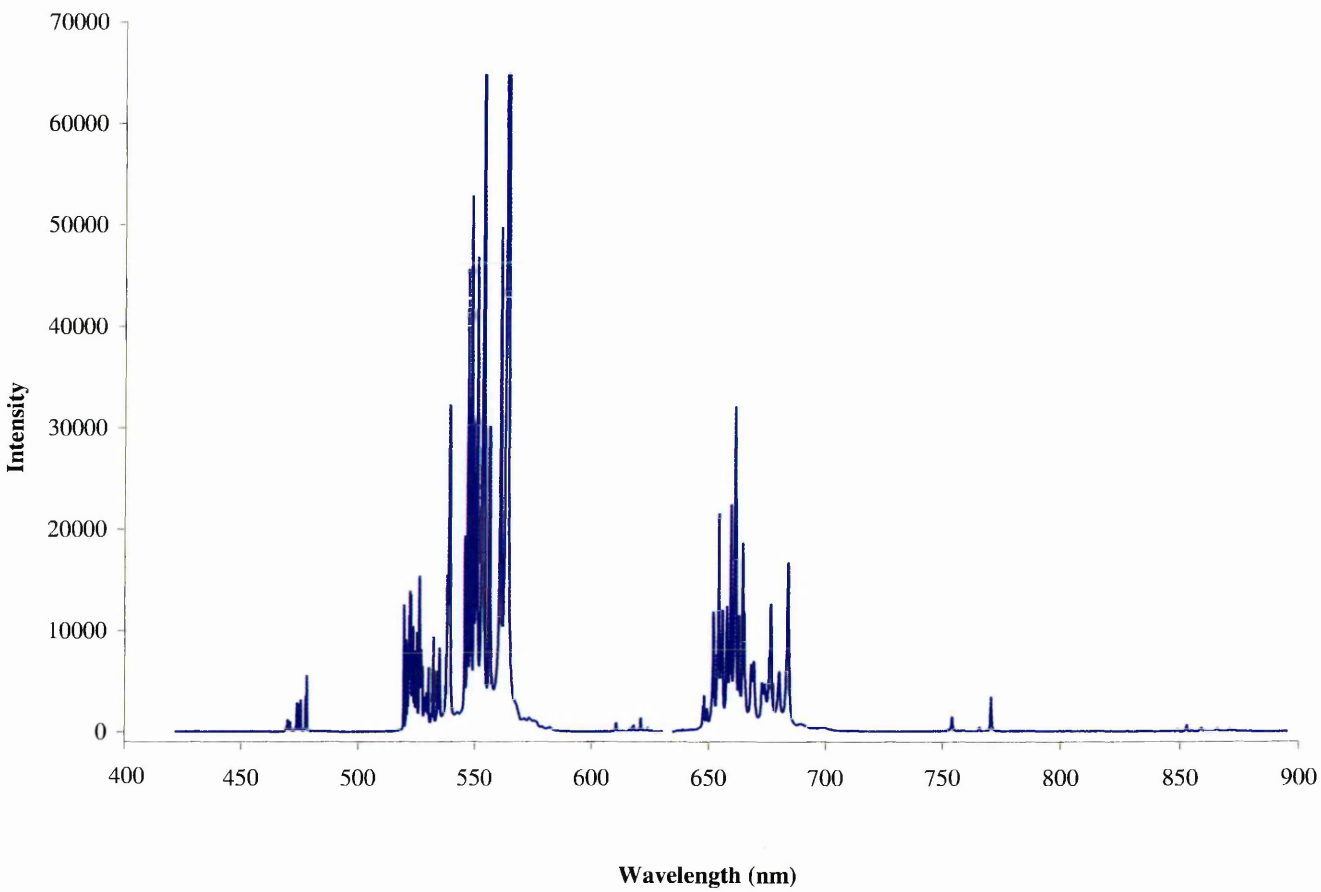

Figure 4.15 Raman spectrum of Y_2O_3:Er (1 mol%) phosphors fired in air at 800 °C.

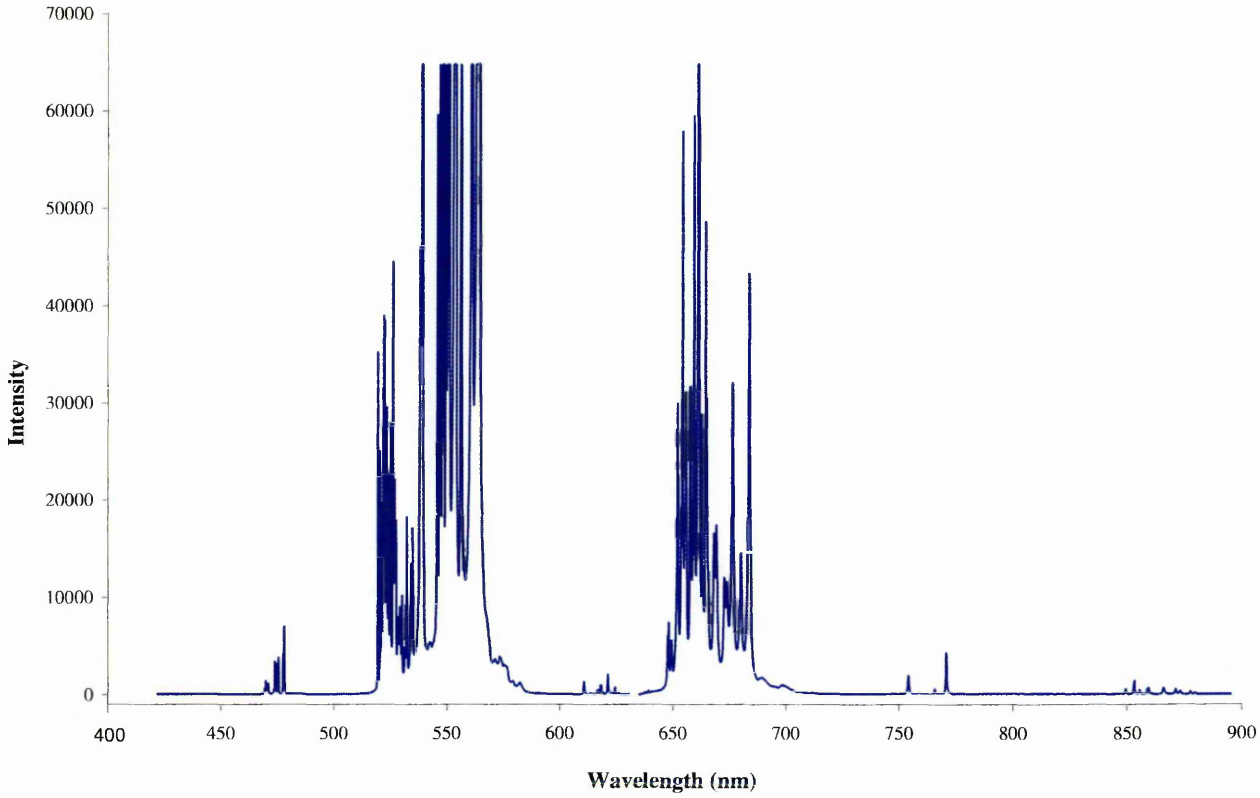

Figure 4.16 Raman spectrum of Y_2O_3:Er (1 mol%) phosphors fired in air at 980 °C.

Y_2O_3 powder phosphor samples doped with nominal concentrations of 1, 2, 3, 4, 5 and 8 mol% Er^{3+} were prepared to study the effect of the concentration of the dopant ion on the luminescent properties. The luminescence spectra were normalized and the signals integrated.

The intensity of emission bands in the spectra reached a maximum when the activator concentration was 3 mol%, a steady decrease in both up-conversion and down-conversion emission intensities was detected at higher concentrations. Concentration quenching effects were detected from the sample containing 5 mol% Er^{3+}, where the emission bands due to the $^4F_{7/2} \rightarrow {}^4I_{15/2}$ transition, and the bands denoted a and b in Table 4.7 cannot be detected. In this sample the main Stokes manifold ($^4F_{9/2} \rightarrow {}^4I_{15/2}$) tended to saturate even for short collection times (0.25 s). In addition, the spectrum of the Y_2O_3:Er (8

mol%) sample also shows a very strong saturation for the transition $^4F_{9/2} \rightarrow {}^4I_{15/2}$ whereas the band due to the $^4I_{11/2} \rightarrow {}^4I_{15/2}$ transition was not detected.

The ratio between the intensity of the anti-Stokes and Stokes emission bands was calculated for each sample, and plotted against the activator concentration (Figure 4.17). It was found that the signal intensity ratio also maximizes for the 3 mol% Er^{3+} sample. The reduction in the number of emission manifolds detected in the spectra, and the reduction in the up-conversion efficiency of the phosphors for activator concentrations above 4 mol% suggest that the up-conversion processes are much more strongly affected by the distance between luminescent centres than the down-conversion ones, and therefore concentration quenching effect for the two photon phenomenon takes place at much lower dopant levels. This result also suggests that for high activator concentration the absorption of a second photon is less favoured, which may suggest the relaxation process starts before the second photon can be absorbed.

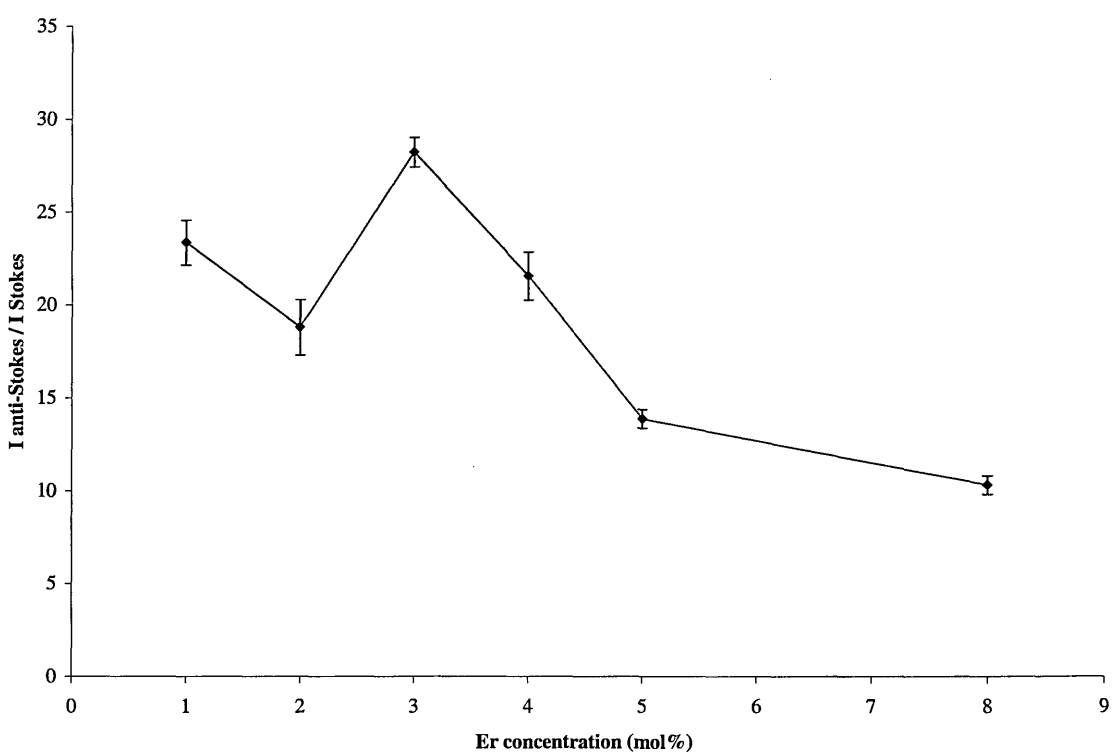

Figure 4.17 Evolution of the anti-Stokes and Stokes emissions intensity ratio as a function of Er^{3+} concentration. Error bars show SD, N=5

Y_2O_3:Er,Yb phosphors

In order to determine the influence of adding a second substitutional lanthanide ion to the system, studies on samples containing Er^{3+}-Yb^{3+} have been carried out.

It is well established that Yb^{3+} ions can be used to sensitize Er^{3+} ions and enhance its up-conversion properties[46], and the materials containing these two cations have been widely studied under 980 nm excitation sources. The energy transfer mechanism involving the levels $^2F_{5/2}$ from Yb^{3+} and $^4I_{11/2}$ from Er^{3+} has been commonly accepted as the most suitable for the process, but this process has not been studied where the excitation source energy does not correspond to the energy increment between $^2F_{7/2} \rightarrow ^2F_{5/2}$ (Yb^{3+}).

Work carried out in the early 70's[47] and based on models published by Miyakawa and Dexter[48] discussed energy transfer processes between Er and Yb ions associated with the emission or absorption of phonons.

In the present study luminescence spectroscopy (λ_{exc}=632.8 nm) was used to investigate the effect of the Yb^{3+} concentration on both the up-converting and down-converting properties of cubic-Y_2O_3:Er,Yb materials: $Y_{1.96}Er_{0.02}Yb_{0.02}O_3$, $Y_{1.94}Er_{0.02}Yb_{0.04}O_3$, $Y_{1.88}Er_{0.02}Yb_{0.10}O_3$, $Y_{1.82}Er_{0.02}Yb_{0.16}O_3$, $Y_{1.78}Er_{0.02}Yb_{0.20}O_3$ and $Y_{1.58}Er_{0.02}Yb_{0.40}O_3$. A new proposal for the energy transfer processes taking place under these conditions is discussed below. The Y_2O_3:Er (1 mol%) material was used as a reference.

The emission spectra of all materials were integrated and the intensity of each transition evaluated. The ratio of the integrated intensities of the $^4S_{3/2} \rightarrow ^4I_{15/2}$ / $^4F_{9/2} \rightarrow ^4I_{15/2}$ and $^2H_{11/2} \rightarrow ^4I_{15/2}$ /$^4F_{9/2} \rightarrow ^4I_{15/2}$ transitions was studied as a function of the Yb^{3+} concentration and is presented in Figure 4.18. The intensity ratio of the signals decreases as the Yb^{3+} concentration increases indicating that the presence of Yb^{3+} in the sample plays

an active role in the de-excitation process, and that a new relaxation pathway has been opened up by introducing this ion to the system.

Figure 4.19 summarises the relative emission intensities for different $Y_2O_3:Er^{3+},Yb^{3+}$ samples as a function of the intensities observed for the $Y_2O_3:Er^{3+}$(1mol%) control sample. A variation in the intensity of the emissions arising from different excited states compared to those from the control sample is observed as the concentration of Yb^{3+} is changed. The most notable was an approximately 2-fold increase in the red signal due to the $^4F_{9/2} \rightarrow ^4I_{15/2}$ transition when Yb^{3+} concentration was 2 mol% compared to the $Y_2O_3:Er^{3+}$(1mol%) control.

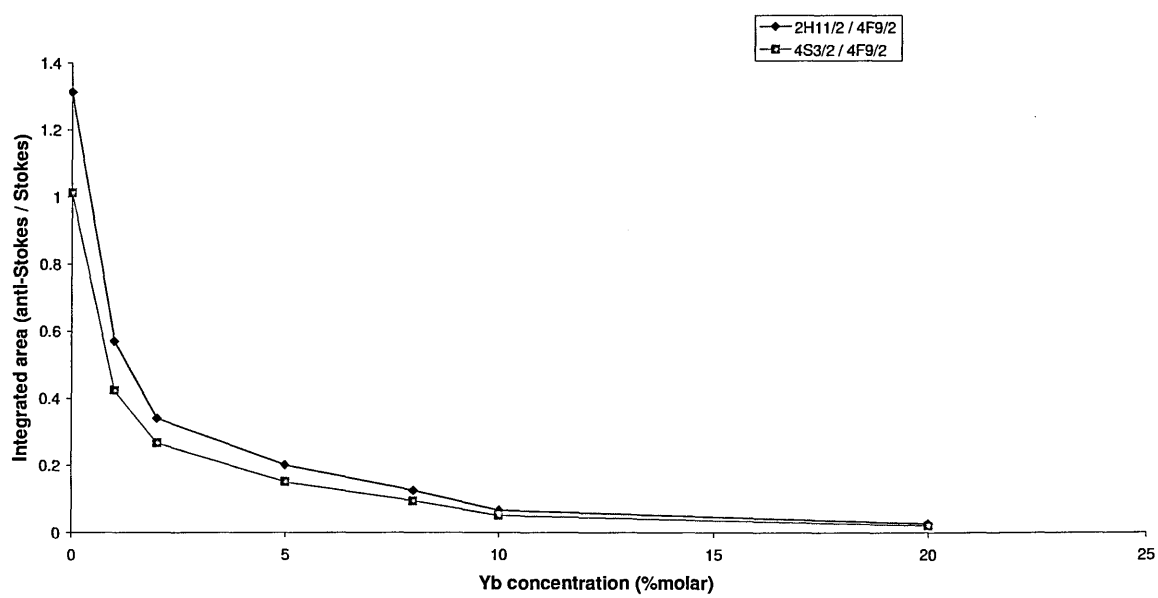

Figure 4.18 Evolution of the anti-Stokes and Stokes emissions intensity ratio as a function of Yb^{3+} concentration.

It should be noted that even though Yb^{3+} deactivates the up-conversion, this is more apparent at concentrations above 5 mol%. Interestingly at low Yb^{3+} concentrations enhancement of the up-conversion intensity has been found. This may be due to the Er^{3+} - Er^{3+} resonant energy transfer in the absence of Yb^{3+}, and thus dissipating some of the radiation. When Yb^{3+} is present at levels of 1 mol% the Er^{3+} - Er^{3+} quenching ceases as there is now Er^{3+} - Yb^{3+} interaction where the energy loss by energy transfer is smaller.

Then only as the Yb^{3+} concentration increases do we see further loss of the anti-Stokes bands and concomitant growth of the Stokes bands.

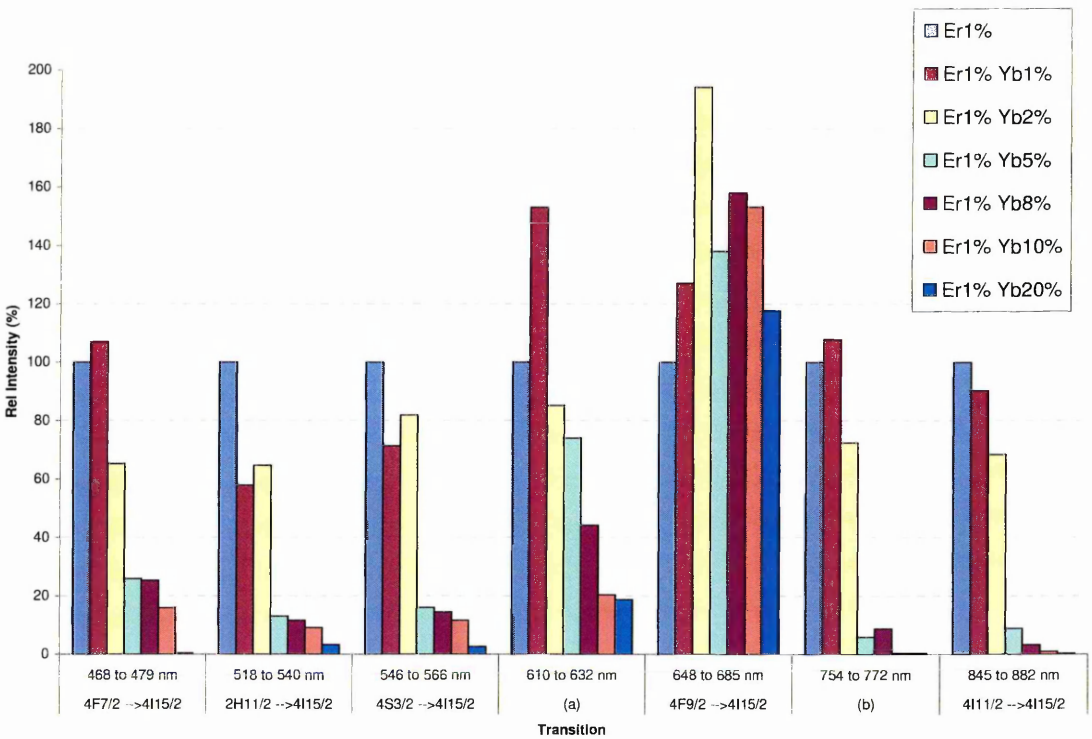

Figure 4.19 Relative intensity of the emission bands in co-doped Y_2O_3:Er;Yb phosphors compared with single doped Y_2O_3:Er.

Very significant variations were found in the spectrum from the sample containing 1 mol% of Yb^{3+}. This spectrum is shown in Figure 4.20. The intensity of the red emission due to the $^4F_{9/2} \rightarrow ^4I_{15/2}$ transition and the blue-green emission due to the $^4F_{7/2} \rightarrow ^4I_{15/2}$ transition are enhanced by *ca.* 10 % and 20% respectively, compared to those of the Y_2O_3:Er (1 mol%) control sample. Conversely, the intensity of the observed yellow-green emissions due to the $^2H_{11/2} \rightarrow ^4I_{15/2}$ and $^4S_{3/2} \rightarrow ^4I_{15/2}$ transitions decrease from that observed in the control sample. This response can be explained by considering energy transfer processes from Er^{3+} to Yb^{3+}. Since the energy difference between the Er^{3+} and Yb^{3+} levels involved in the process are not equivalent, the energy transfer may be associated with phonon emission.

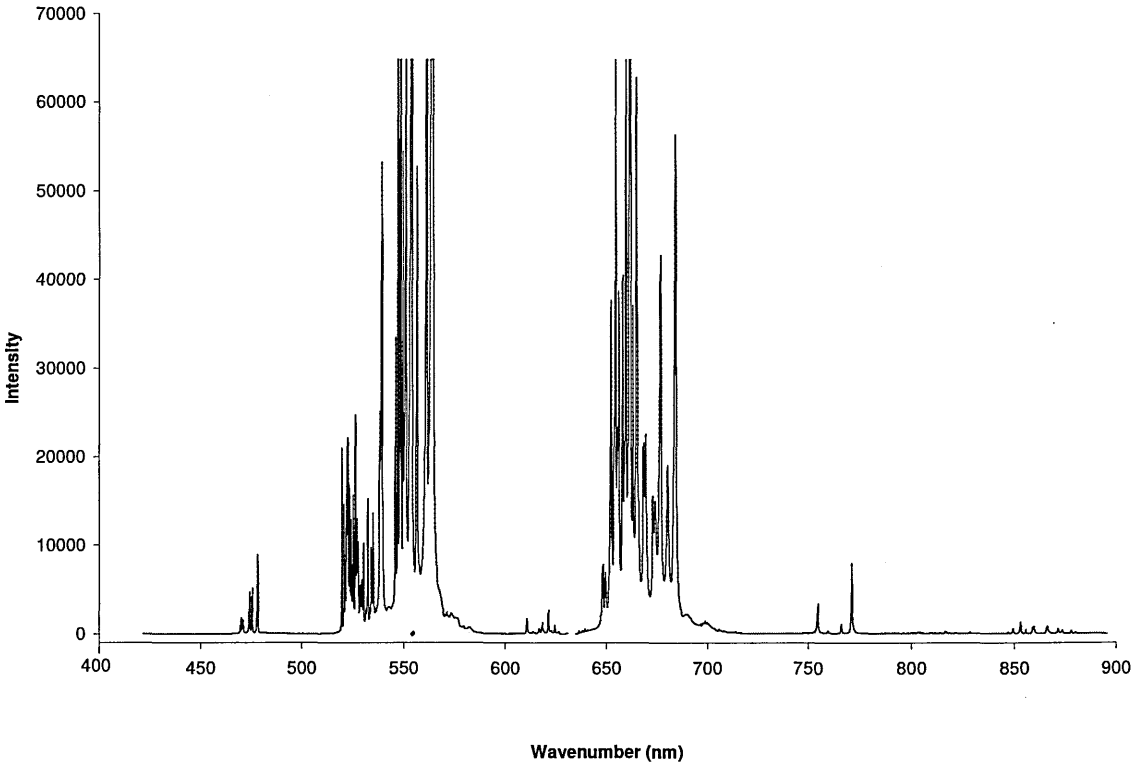

Figure 4.20 Raman spectrum of Y_2O_3:Er(1mol%);Yb(1mol%) phosphors fired in air at 980°C.

For ions embedded in a crystal lattice, internal electric and magnetic field can break certain symmetries, and dipole forbidden transitions may become possible by mixing states with different parity. While typical upper-state lifetimes are of the order of a few nanoseconds for allowed transitions, forbidden transitions of isolated ions can have upper – state lifetimes ranging from a few microseconds to milliseconds. These are called metastable states. Their population[39], allows the absorption of a second photon and $^2P_{3/2}$ energy level can be reached using 632.8 nm excitation sources. Once the Er^{3+} ion has been excited to this level, non-radiative decay can occur to levels such as $^4H_{11/2}$. The energy difference between this level and the $^4F_{9/2}$ in Er^{3+} approximates to the energy difference between the ground level in Yb^{3+} ($^2F_{7/2}$) and the next available energy level ($^2F_{5/2}$). Excited Er^{3+} can thus transfer that energy to a nearby Yb^{3+}, via the cross relaxation mechanism $^4H_{11/2} \rightarrow {}^4F_{9/2}$ (Er^{3+}) : $^2F_{7/2} \rightarrow {}^2F_{5/2}$ (Yb^{3+}) (Figure 4.21). Once this energy transfer has taken place, Er^{3+} ions can fall back to the ground state releasing a red photon in the 648 to 685 nm range. The intensity of the emission due to this relaxation path is added to the signal

obtained from Er^{3+} ions following the normal relaxation pathway explained in previous papers[39, 40]. Moreover, this proposed mechanism can also explain the blue-green $^4F_{7/2} \rightarrow {}^4I_{15/2}$ transition enhancement by means of a back transfer of the energy previously absorbed by the Yb^{3+} ions (Figure 4.22). Yb^{3+} ions excited to the $^2F_{5/2}$ can transfer this energy to nearby Er^{3+} ions in the ground state. Er^{+3} ions are excited to the $^4I_{11/2}$ level and, before they have time to release that energy, absorb another photon from surrounding Yb^{3+}, reaching the $^4F_{7/2}$ level. This absorbed energy can be released by a transition to the ground state. The emission taking place is a blue-green photon of wavelength between 468 and 479 nm. These energy transfers from Er^{3+} to Yb^{3+} ions also explain the decrease of the emission intensity due to the $^2H_{11/2} \rightarrow {}^4I_{15/2}$ and $^4S_{3/2} \rightarrow {}^4I_{15/2}$ transitions. The level by level cascade relaxation route is not followed by all the Er^{3+} ions in the lattice. Some of the Er^{3+} ions bypass the levels where these processes originate and therefore lower their intensity.

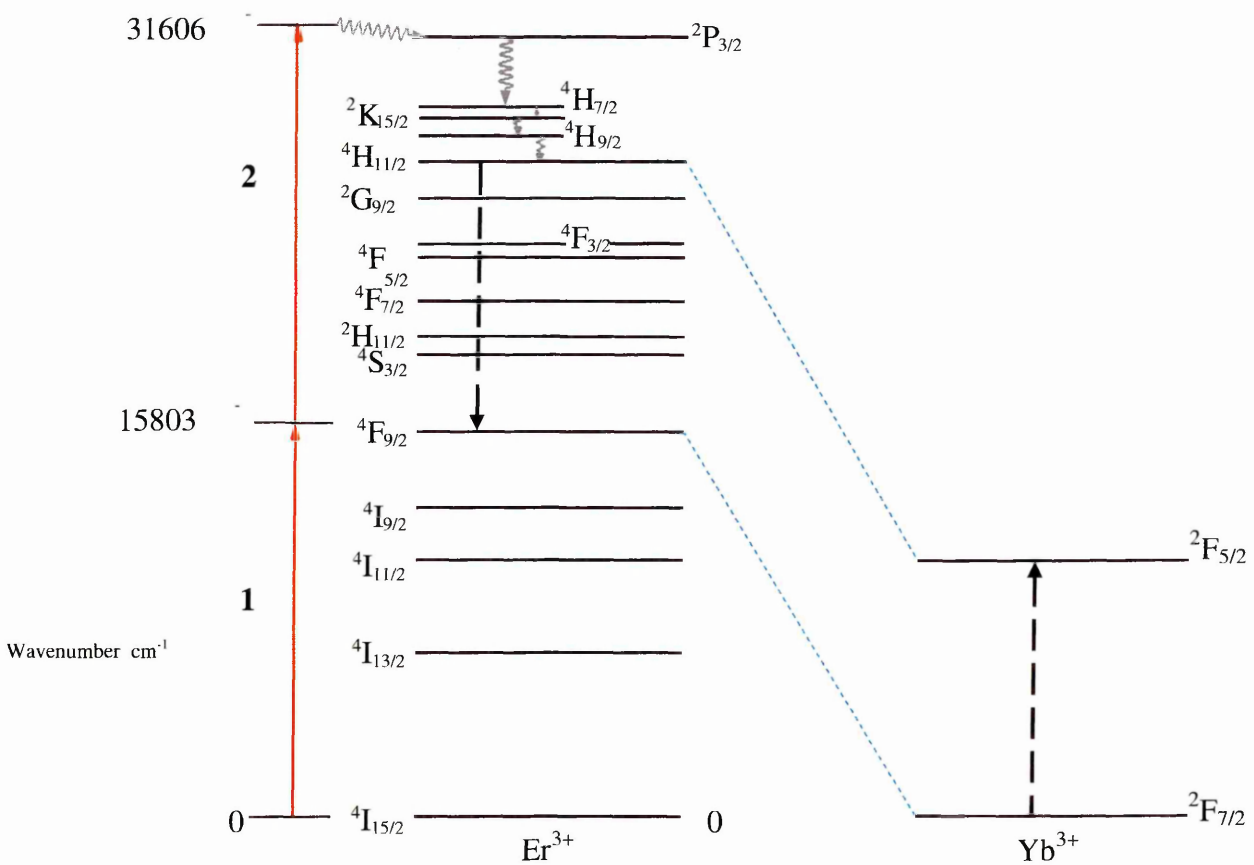

Figure 4.21 Proposed energy transfer mechanism in Y_2O_3:Er,Yb co-doped phosphors.

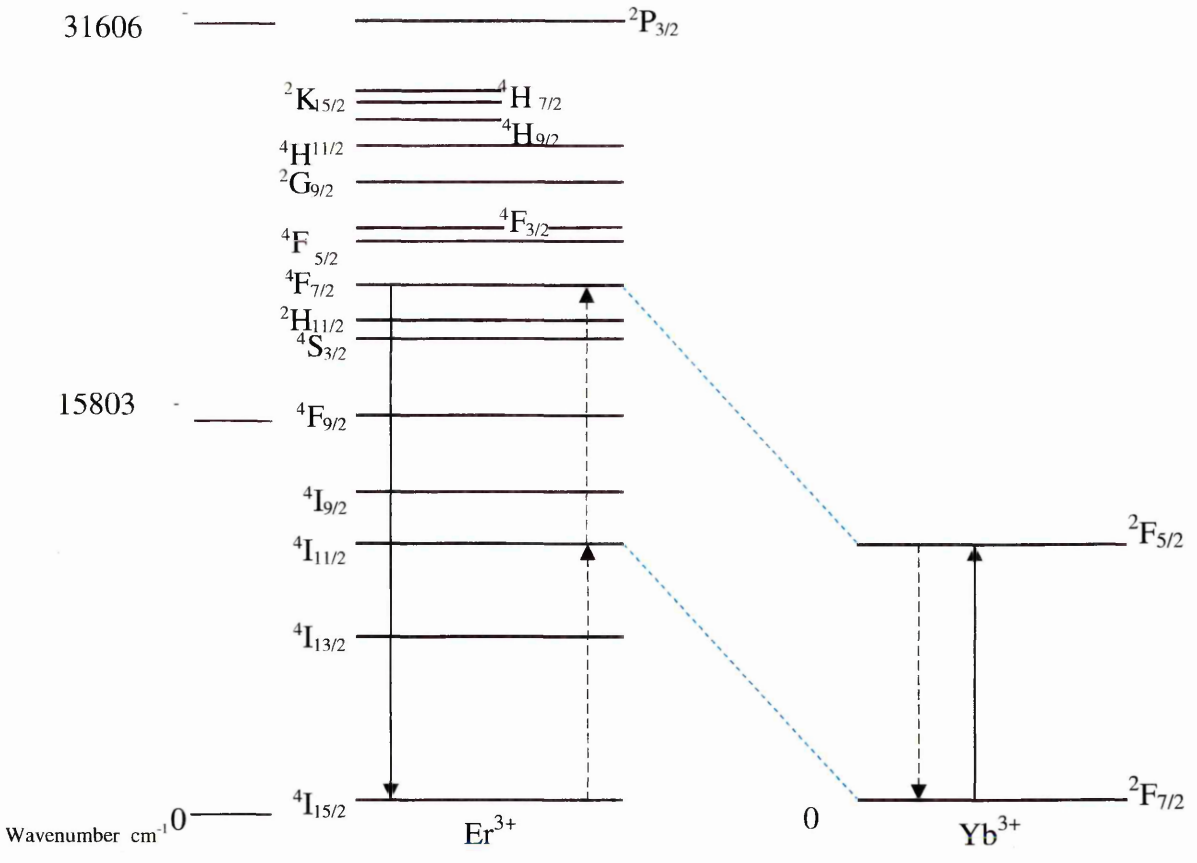

Figure 4.22 Proposed energy back-transfer mechanism in Y_2O_3:Er,Yb co-doped phosphors.

In this study, the Er^{3+} to Yb^{3+} interaction has been assessed. This interaction has been detected, and the energy loss found to be weaker than energy loss due to Er^{3+} to Er^{3+} interaction. Although not every Er^{3+} to Yb^{3+} ratio has been proven to be successful in enhancing Er^{3+} emission it has been shown that a small amount of Yb^{3+} (about 1mol%) helps to intensify some of the up-conversion properties of Er^{3+} luminescent centres. A novel energy transfer mechanism has been proposed explaining the changes observed in the Er^{3+} spectra.

From Figure 4.19, it was observed that the intensity of the emission bands arising from the $^4F_{5/2}$ levels and the unassigned levels a and b were affected in the same way by increasing Yb^{3+}, which suggests that all three emissions could arise from the same energy level.

Y_2O_3:Eu phosphors

$Y_2O_3:Eu^{3+}$ samples were prepared to be used as controls in the study of the $Y_2O_3:Er^{3+},Eu^{3+}$ phosphor systems as Eu^{3+} ions also get excited by the 632.8nm radiation.

A single Raman band typical of the Y_2O_3 cubic lattice is observed in both spectra at a wavenumber shift of 378cm^{-1} and has been used to normalize the signal.

The anti-Stokes emission spectrum of $Y_2O_3:Eu^{3+}$(5 mol%) in the range 420-630 nm at room temperature is shown in Figure 4.23, and the Stokes emission spectrum in the range from 634 to 895 nm is shown in Figure 4.24. Over the entire wavelength range, ten emission manifolds were detected arising from excited state levels $^5D_0$, $^5D_1$, $^5D_2$ and $^5D_3$. Previous studies on these powder phosphors helped to assign the main emission bands to the transitions summarized in Table 4.8[41].

Table 4.8 Assignments of Stokes and anti-Stokes emission bands of $Y_2O_3:Eu^{3+}$.

	vibrational band emission range	
emission assignment	**nm**	**cm^{-1}**
$^5D_2 \rightarrow {}^7F_J$	465-520	21510-19218
$^5D_3 \rightarrow {}^7F_J$		
$^5D_1 \rightarrow {}^7F_0$	525-527	19029-18951
$^5D_1 \rightarrow {}^7F_1$	532-538	18772-18584
$^5D_1 \rightarrow {}^7F_2$	546-554	18313-18039
$^5D_0 \rightarrow {}^7F_0$	580	17233
$^5D_0 \rightarrow {}^7F_1$	582-593	17179-17864
$^5D_0 \rightarrow {}^7F_2$	611-631	16365-15845
$^5D_0 \rightarrow {}^7F_3$	650-663	15375-15070
$^5D_0 \rightarrow {}^7F_4$	683-712	14634-14035

Most of these summarized manifolds arise in the same wavelength bands as much more intense emissions previously reported for Er^{3+}. Therefore the influence of the former ion in the emission intensity from Eu^{3+} cannot be assessed due to overlap. Thus it was decided to probe the changes in the Er^{3+} spectrum when this second dopant was included in the system.

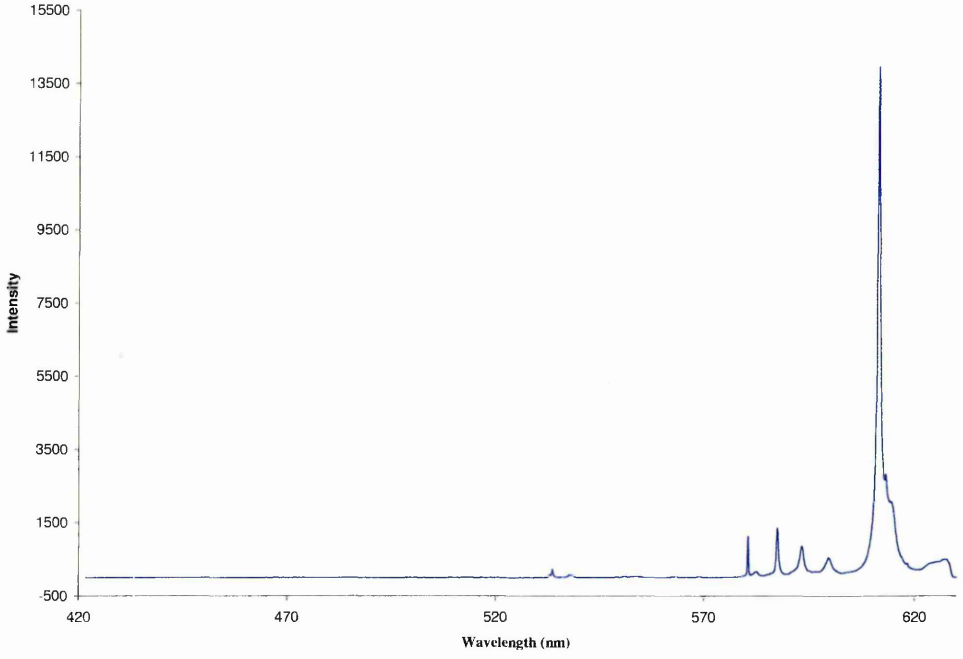

Figure 4.23 Anti-Stokes emission spectrum of $Y_2O_3:Eu^{3+}$ (5 mol%) at room temperature in the region of 420-630 nm. Relative intensities in arbitrary units.

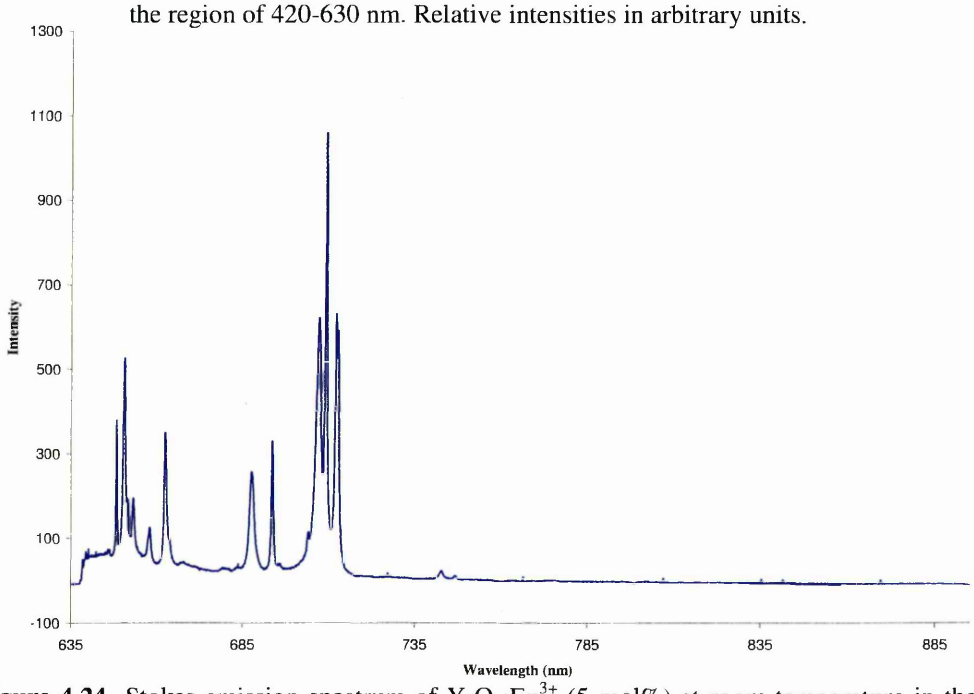

Figure 4.24 Stokes emission spectrum of $Y_2O_3:Eu^{3+}$ (5 mol%) at room temperature in the region of 634-895 nm. Relative intensities in arbitrary units.

Y_2O_3:Er,Eu phosphors

To study of the effect of Eu co-doping Y_2O_3:Er phosphors, samples containing different nominal concentrations of both ions have been prepared. Keeping the Er^{3+} concentration constant at 2 mol%, different samples containing 1, 2, 5, 10 and 20 mol% Eu^{3+} were prepared. In addition, samples containing 1, 2, 5, 10 and 20 mol% Er^{3+} were prepared keeping the Eu^{3+}concentration constant at 2 mol%. A sample doped with 1mol% of both $Er^{3+}$and Eu^{3+}, and a sample doped with 20mol% Er^{3+} and 1mol% Eu^{3+} were also prepared.

Raman spectra of all compositions were obtained after firing the samples at 980°C.

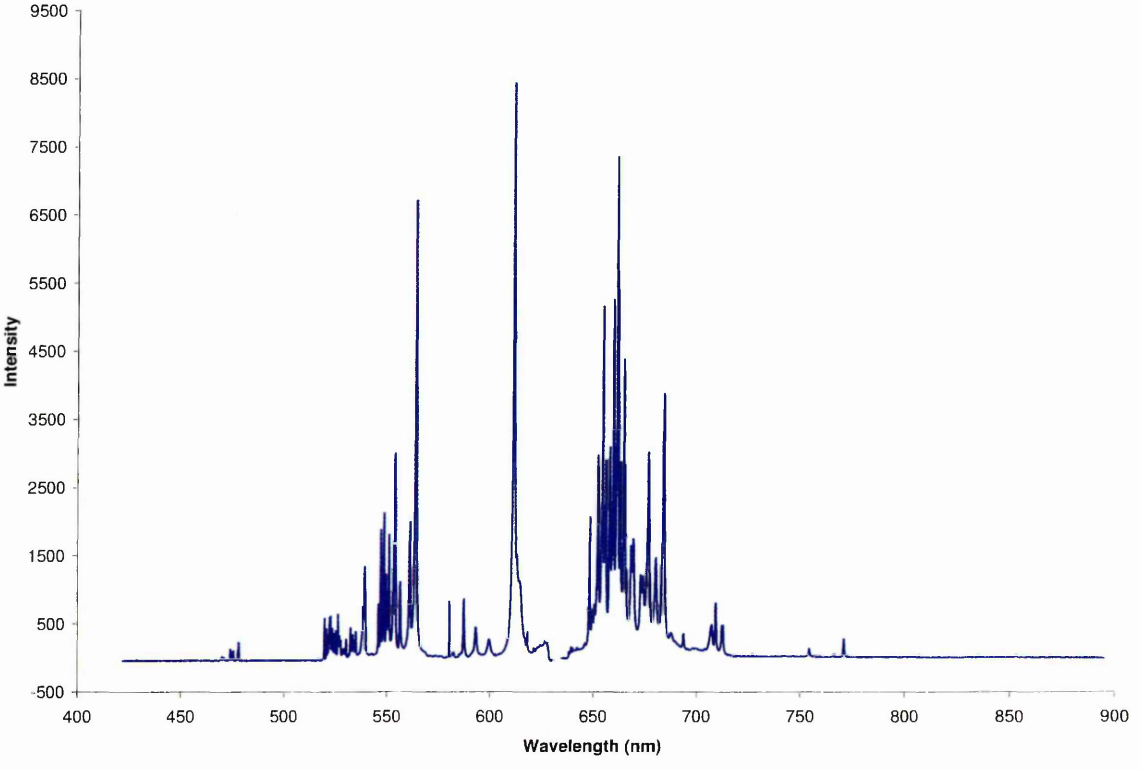

Figure 4.25 Emission spectrum of Y_2O_3:Er(2 mol%),Eu(5 mol%) powder phosphor at room temperature. Relative intensities in arbitrary units.

Although a typical Eu^{3+} signal and the emission bands where Er^{3+} signals are expected can be observed in the Raman spectrum of the Y_2O_3:Er(2 mol%),Eu(5 mol%) sample shown in Figure 4.25, the relative intensities of the Stokes and anti-Stokes emission bands in the Er^{3+} signal change in comparison with the Y_2O_3:Er (2 mol%) control spectrum shown in Figure 4.26. This effect can be explained as result of Er^{3+} - Eu^{3+} interaction, although noticeable quenching effects were also observed. Other changes in the Er^{3+} signal, attributable to Er^{3+} to Eu^{3+} interaction, were also observed. These result from enhancement of the emission bands due to the $^4F_{7/2} \rightarrow {}^4I_{15/2}$ transition and the emission band designated previously as b (a was not studied due to overlapping with stronger Eu^{3+} emissions) (Figure 4.27), and deactivation of the $^4I_{11/2} \rightarrow {}^4I_{15/2}$ emission with increasing Eu^{3+} concentration (Figure 4.28). Although all the main emission manifolds were affected by the presence of this second rare earth ion, the emission bands due to the $^4I_{9/2} \rightarrow {}^4I_{15/2}$ transition show no change in intensity with Eu^{3+} concentration.

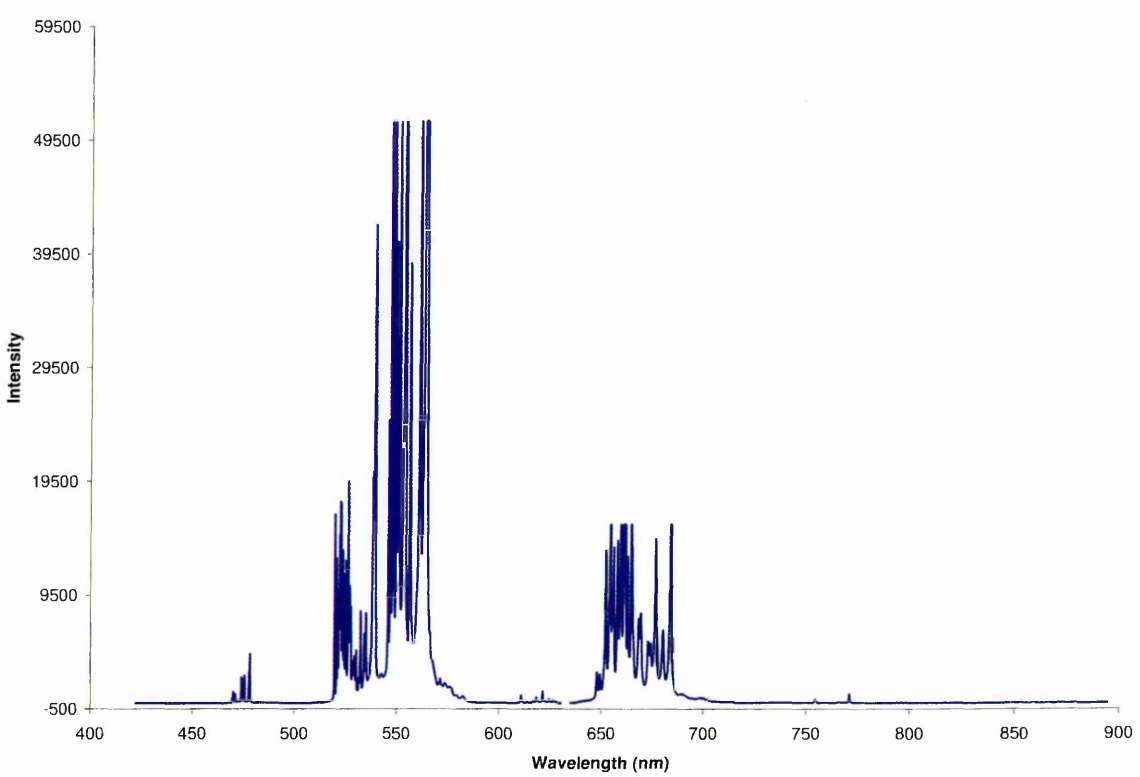

Figure 4.26 Emission spectrum of Y_2O_3:Er(2 mol%) powder phosphor at room temperature. Relative intensities in arbitrary units.

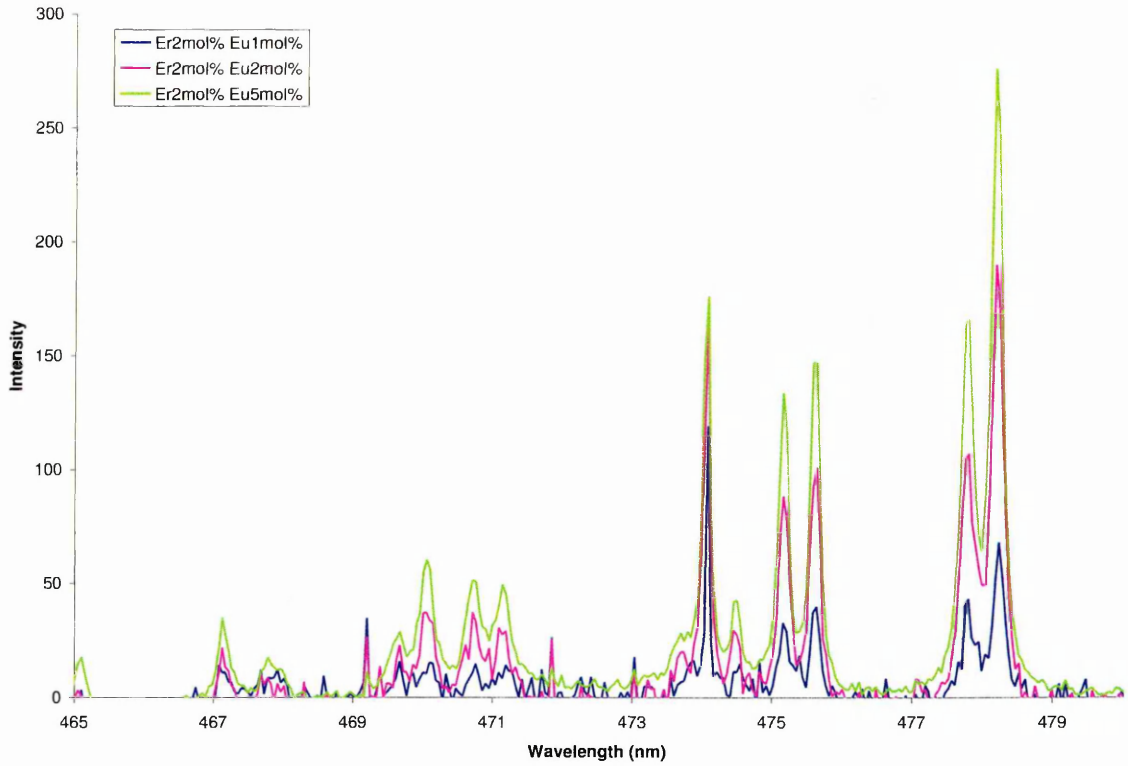

Figure 4.27 Enhancement of emission bands in $^4F_{7/2} \rightarrow {}^4I_{15/2}$ transition.

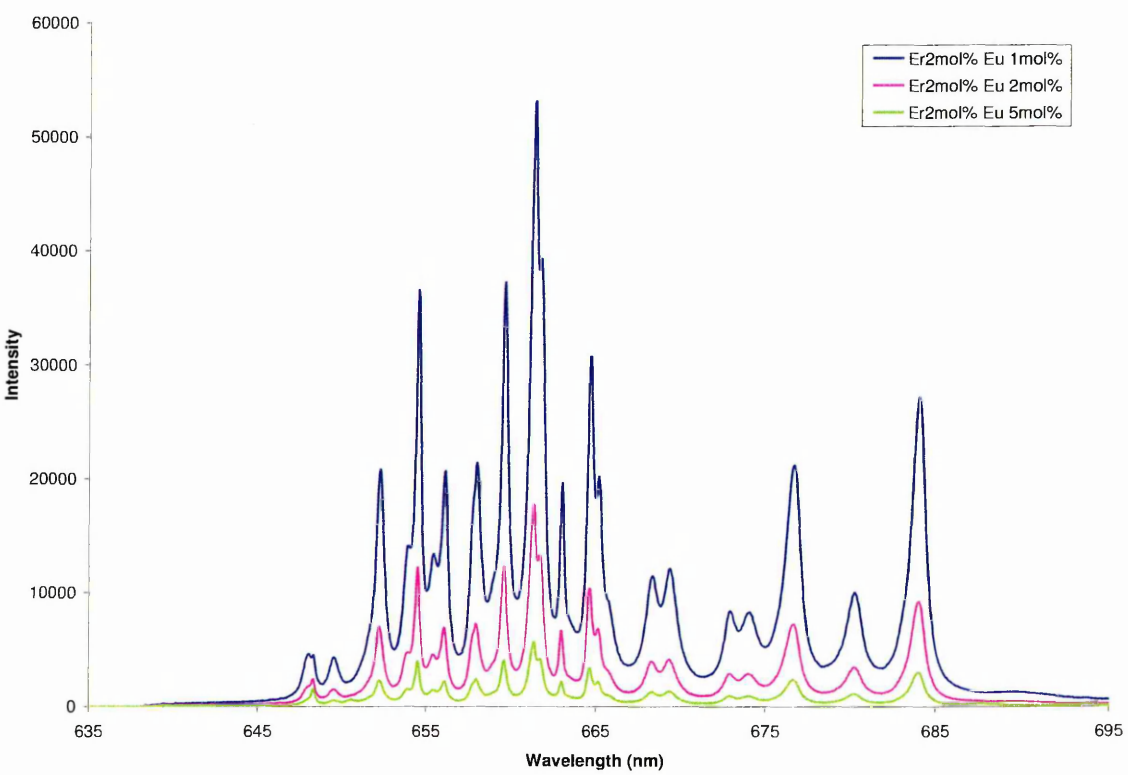

Figure 4.28 Deactivation of the $^4I_{11/2} \rightarrow {}^4I_{15/2}$ emission with increasing Eu^{3+} concentration.

To account for these phenomena, the existence of Er^{3+} to Eu^{3+} interactions at different energy levels is suggested. The de-excitation of the anti-Stokes emission from Er^{3+} ions can be explained by means of resonant energy transfer with the $^5D_1$ level in Eu^{3+}. Er^{3+} ions are excited to the $^2P_{3/2}$ level after absorbing two photons in the red, with a wavelength of 632.8nm. Following a non-radiative decay, the electron reaches the $^2H_{11/2}$ level. The energy difference between this level and the ground state in Er^{3+} approximates to the energy difference between the ground level state in the Eu^{3+} ion ($^7F_0$) and the excited $^5D_1$ energy level. By means of a cross relaxation mechanism, the excited Er^{3+} ion can transfer this energy to a neighbour Eu^{3+}. Thus, the Eu^{3+} can be promoted to the $^5D_0$ level from the ground state level. These energy levels in Er^{3+} and Eu^{3+} are very close in energy and it is suggested a resonant energy transfer process takes place, weakening the Er^{3+} anti-Stokes emission in the presence of Eu^{3+}. The Er^{3+} ions excited to the $^4F_{9/2}$ level (by one photon absorption or by non-radiatively decay from excited states) continue their normal relaxation process to the ground state without weakening the intensity of this emission. The loss in the green emission intensity in comparison with the red signal is thus accounted for.

Previous studies of Y_2O_3:Er phosphors demonstrated that in the $^2H_{11/2} \rightarrow {}^4I_{15/2}$ transition, erbium ions in both C_2 and S_6 sites made contributions to the emission bands[40]. When studying the $^2H_{11/2} \rightarrow {}^4I_{15/2}$ transition as a function of the concentration of Eu^{3+} different behaviour from the bands arising from C_2 and S_6 sites was observed. Figure 4.29 shows how the emission bands due to Er^{3+} in C_2 sites were deactivated while emission bands arising from Er^{3+} in S_6 sites were enhanced with increased concentration of Eu^{3+}. These results suggest that the energy transfer process is favoured in the higher symmetry site S_6.

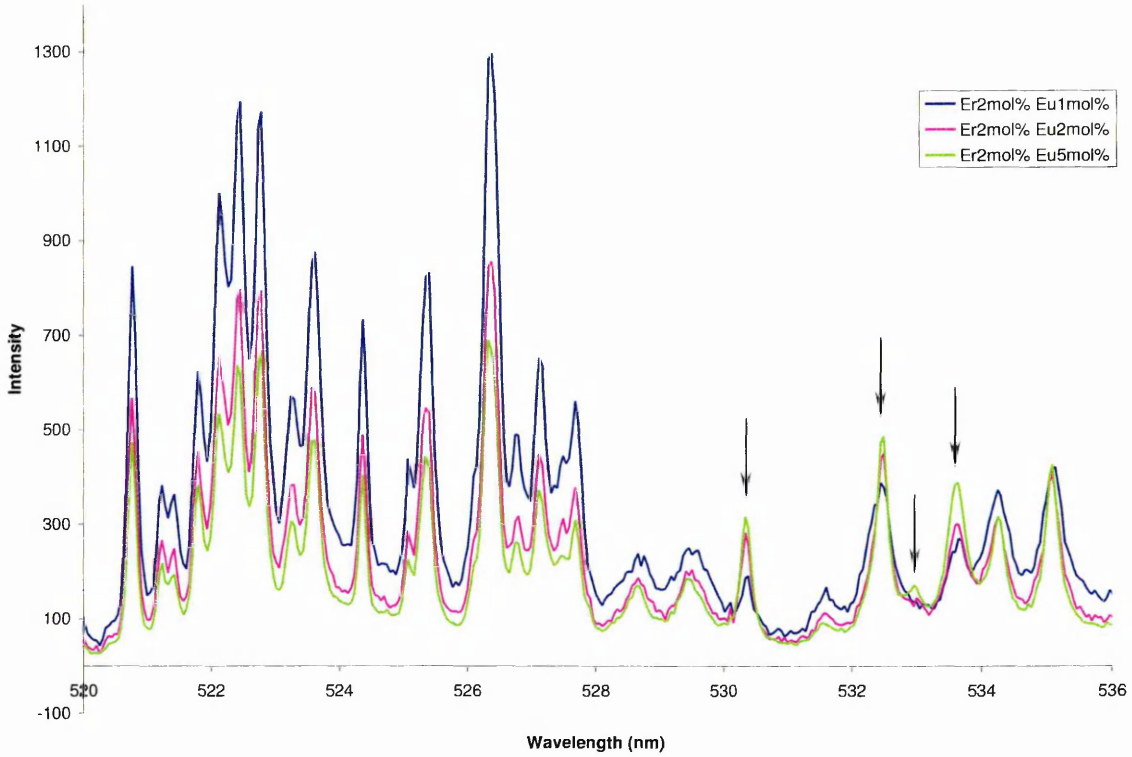

Figure 4.29 Deactivation of emission bands due to Er^{3+} in C_2 sites and enhancement of emission bands arising from Er^{3+} in S_6 sites (indicated by arrows).

When an energy level is highly populated, excited state absorption and cooperative up-conversion processes lead to the excitation to higher levels. As $^4F_{7/2}$ level lies close to $^2H_{11/2}$ in Er^{3+}, this effect can be observed in the co-doped samples. The population of the $^2H_{11/2}$ level in Er^{3+} in S_6 sites is higher with increasing Eu^{3+} co-doping causing the population of the $^4F_{7/2}$ and the intensity of emission bands arising from that level is enhanced.

The deactivation of the $^4I_{11/2}$ has been reported using a 488nm excitation source[49], a result in accordance with observations made in this study.

These phenomena described on samples containing fixed 2 mol% Eu^{3+} and variable concentration of Er^{3+}. Although a stronger concentration quenching effect was observed with increasing Eu^{3+} concentration in the sample.

In the samples containing 2% Eu^{3+} and variable Er^{3+} concentrations, the same behaviour is observed but with even stronger concentration quenching effect. However red emissions of Er^{3+} in both samples are not as affected by the concentration quenching as green emissions.

The addition of Eu^{3+} to Y_2O_3:Er phosphors does not contribute to an enhancement of their luminescent properties. For all the samples the intensity of the emission bands was significantly weaker. A possible mechanism for the interaction of these two rare earth atoms has been proposed although it does not contribute to an enhancement of the luminescent properties of Er^{3+} or Eu^{3+} ions in Y_2O_3. The behaviour of the band arising from the $^4F_{5/2}$ level and the band denoted as b is again the same with increasing Eu^{3+} concentration. It is believed that the intensification of the $^4F_{5/2}$ emission band arises from overpopulation of the low lying level $^2H_{11/2}$. This behaviour of the band b reinforces the previous suggestion of a and b bands arising from the $^4F_{5/2}$ level after a non radiative decay to an intermediate state.

References

[1] K.A. Wickersheim and R.A. Lefever. *J. Opt. Soc. Am.*, **51**, 1147 (1961).

[2] R.A. Lefever and G.W. Clark. *Rev. Sci. Instruments*, **33**, 769 (1962).

[3] N. C. Chang, *J. Appl. Phys.*, **34**, 3500, (1964).

[4] G. E. Peterson and P. M. Bridenbaugh, *J. Opt. Soc. Am.*, **53**, 494, (1963).

[5] J. D. Axe and P.F. Weller, *J. Chem. Phys.* **40,** 10, (1964).

[6] K. A. Wickersheim and R. A. Lefever, *J. Electrochem. Soc.,* **111,** 307, (1964).

[7] A. Bril and W. L. Wanmaker, *J. Electrochem. Soc.,* **111**, 1363, (1964).

[8] R.C. Ropp. *J. Electrochem.Soc.*, **111**, 538 (1964).

[9] R.C. Ropp, *J. Electrochem. Soc.,* **111**, 311 (1964).

[10] G. H. Dieke, H. M. Crosswhite, H. Crosswhite, *Spectra and energy levels of rare earth ions in crystals*, New York, Interscience Publishers (1968).

[11] R. P. Leavitt, J. B. Gruber, N. C. Chang and C. A. Morrison., *J. Chem. Phys.,* **76,** 4775 (1982).

[12] W.G. Wyckoff., *Crystal Structures,* Interscience Publishers. Inc., New York (1965).

[13] M. Mandel. *Appl. Phys. Letters*, **2,** 197 (1963).

[14] S. Z. Toma and D. T. Palumbo, *J. Electrochem. Soc.,* **115,** 64C (1968).

[15] C. Chang and J.B. Gruber, *J. Chem. Phys.*, **41**, 3227 (1964).

[16] D. Segal, *J. Mater. Chem*, **7**, 1297 (1997).

[17] P. Maestro, D. Huguenin, *J. Alloys. Comp.*, **225**, 520 (1995).

[18] P. K. Sharma, M. H. Jilavi, H. Schmidt, V. K. Varadan, *Int. J. Inorg. Mater.*, **2**, 407 (2000).

[19] L.E. Shea, J. McKittrick, O. A. Lopez, E. Sluzky, *J. Am. Ceram. Soc.*, **79**, 3257 (1996).

[20] H. Eilers B.M. Tissue, *Chem. Phys. Letters*, **251**, 74 (1996).

[21] C. A. Spindt, C. E. Holland, A. Rosenberg and I. Brodie., *IEEE Trans. Electron Devices,* **38,** 2355 (1991).

[22] E. Matijevic. *Acc. Chem. Res.*, **14,** 22 (1981).

[23] C. A. Spindt. *Surface Sci.*, **266,** 145 (1991).

[24] Akinc, M.; Sordelet, D. *J. Colloid Interface Sci*, **122**, 47 (1998).

[25] Milosevic, O.; Jordovic, B.; Uskokovic, D. *Mater. Lett.*, **19**,165 (1994).

[26] Kim, M. J.; Matijevic, E. *J. Mater. Res.*, **6**, 840 (1991).

[27] Giesche, H.; Matijevic, E. *J. Mater. Res.*, **9**, 436 (1994).

[28] Nishisu, Y.; Kobayashi, M. U.S. Patent 5,413,736, (1995).

[29] Pei, Y.; Liu, X. *Chin. J. Lumin.*,**17**, 5 (1996).

[30] Jiang, Y. D.; Wang, Z. L.; Zhang, F.; Paris, H. G.; Summers, C. J.*J. Mater. Res.*, **13**, 2950 (1998).

[31] Vecht, A.; Gibbons, C.; Davies, D.; Jing, X.; Marsh, P.; Ireland,T. G.; Silver, J.; Newport, A. *J. Vac. Sci. Technol. B*, **17**, 750 (1999).

[32] R. B. Hunt, R.G. Pappalardo, *J. Lumin.*, **34**, 133 (1985).

[33] G. Schaack, J. A. Köningstein, *J. Opt. Soc. Am*, **60**, 1110 (1970).

[34] J. Gouteron, J. Zarembowitch, A. Lejus, *Acad. Sci. Ser. C*, **283**, 243 (1979).

[35] W.B. White, V. G. Keramidas, *Spectrochimica Acta A*, **28**, 501 (1972).

[36] D. Bloor, J. R. Dean, *J. Phys. C: Solid State Phys*, **5**, 1237 (1972).

[37] Y. Repelin, C. Proust, E. Husson, J. M. Beny, *J. Solid State Chem.*, **118**, 163 (1995).

[38] D. Sordelet, M. Akinc, *J. Colloid Interf. Sci*, **122**, 47 (1988).

[39] J. Silver , M.I. Martinez-Rubio, T.G. Ireland, G.R. Fern, R. Withnall, *J. Phys. Chem. B*, **105**, 948 (2001).

[40] J. Silver , M.I. Martinez-Rubio, T.G. Ireland, G.R. Fern, R. Withnall, *J. Phys. Chem. B*, **105**, 7200 (2001).

[41] J. Silver , M.I. Martinez-Rubio, T.G. Ireland, G.R. Fern, R. Withnall, *J. Phys. Chem. B*, **105**, 9107 (2001).

[42] W. Demtröder, *Laser Spectroscopy*, pp 268, Springer-Verlag (1982).

[43] W. Demtröder, *Laser Spectroscopy*, pp 244, Springer-Verlag (1982).

[44] G. Blasse, B.C. Grabmaier, *Luminescent materials*, pp 16, Springer-Verlag (1994).

[45] O. A. Serra , S. A. Cicillini, R. R. Ishiki, *J. Alloys Comp.*, **303-304**, 316 (2000).

[46] S. Shionoya, W.M. Yen, *Phosphors Handbook*, pp 644, CRC Press (1998).

[47] E. Okamoto, H. Masui, K. Muto, K. Awazo, *J. Appl. Phys.*, **43**, 2122 (1972).

[48] T. Miyakawa, D.L. Dexter, *Phys. Rev. B*, **1**, 2961, (1970).

[49] C. Strohhofer, P. G. Kik, A. Polman, *J. Appl. Phys.*, **88**, 4486 (2000).

Chapter 5 Wet Chemical Preparation and Characterisation of Erbium Doped Gd_2O_3 and $Gd_{2-x}Y_xO_3$ Phosphors

Introduction

Rare earth oxides have been widely used and studied as phosphor host lattices. For a material to be considered a good phosphor host it must have narrow size distribution, non agglomeration properties and spherical morphology. It is also necessary to minimise energy loss by phonon decay; therefore good phosphor host lattices have low phonon energies[1]. Gd^{3+} has been considered a suitable candidate to be used in host materials due to the lowest excited 4f level $^6P_{7/2}$ having an associated energy of approximately 32000 cm^{-1}, which does not correspond with the energy of any other 4f excited states of other rare earths. For this reason, there is little likelihood of quenching due to charge transfer effects from the $^6P_{7/2}$ excited level in gadolinium to any other excited states in other rare earth ions caused by the cation when used as host crystal[2].

The first report of Gd_2O_3 as host material was by Rice and Shazer in 1970[3]. This study considered the non radiative relaxation processes in this oxide, subsequently numerous studies have been carried out on Gd_2O_3:Eu, such as the luminescence studies reported by Despert-Ghys in 1980[4], where the emission of Eu^{3+} was assigned to the three distinct C_s crystallographic sites in the monoclinic phase. Comparative studies of Eu^{3+} energy transfer processes in cubic Gd_2O_3 and Y_2O_3 were carried out in 1987 by Blasse[5]. During the 1990's numerous studies on the luminescence of Eu^{3+} in Gd_2O_3 crystalline lattices were carried out. Okuyama[6], used spray pyrolysis to prepare spherical particles and studied emission intensity as a function of the doping level. The luminescent properties of other rare earths such as terbium[7] and samarium[8] doped into Gd_2O_3 have appeared in the literature and the first research work on Gd_2O_3:Er has been published[9, 10]. The activator luminescent properties were studied under UV and green excitation sources. Er and Yb up-conversion properties in co-doped Gd_2O_3 have also been reported[11].

Crystallographic studies on co-doped Gd_2O_3 lattices were reported by Wyckoff in 1965[12]. Rare earth oxides of general formula R_2O_3 (where R is a rare earth ion), are materials with high melting point (above 2350 °C)[13] They exist in three different crystallographic phases often designated A, B and C. The structure adopted depends on the ionic radii and electronegativities of the cations. La_2O_3 is a typical example of the A-type. It has a hexagonal structure belonging to the *C3m* space group, and is characterised by a large metal to oxygen separation and it is the phase formed by rare earths with ionic radii ratio to oxygen ($^{r\,(R)}/_{r\,(O)}$) greater than 0.87 (La, Ce, Pr, Nd). The B-type is monoclinic, with space group *C2/m*. It is formed by intermediate sized rare earths (Sm, Eu, Gd). All the atoms lie in two layers at a distance ½ b_o. The parameters of the six formula units per unit cell for Gd_2O_3 are:

$$a= 14.061\text{Å} \quad b= 3.566\text{Å} \quad c= 8.760\text{Å} \quad \beta= 100^\circ\,6'$$

The structure has three crystallographically non-equivalent cations, with sevenfold coordination[4, 14]. The C-type is cubic, and belongs to the *Ia*3 space group. It is the phase formed by rare earths with $^{r\,(R)}/_{r\,(O)}$ between 0.6 and 0.87 (Tb, Dy, Ho, Er, Tm, Yb, Lu). The cations occupy two crystallographically inequivalent 6-coordinate sites, C_2 and S_6. The ratio of C_2:S_6 is 3:1.

However transformations from one phase to another as a function of temperature and pressure have been reported[15]. When there is temperature dependent polymorphism, the A-type structure is obtained at high temperatures, whereas B-type and C-type structures are typically those of the medium and low temperature forms respectively[13].

Mixed rare earth yttrium sesquioxides $RE_xY_{2-x}O_3$ are host lattices of great interest to phosphor science and have been recently synthesized[16]. They were developed and studied in an attempt to enhance the emission properties of activator centres in phosphors.

It has been found that, for Gd^{3+} substitution, at concentrations lower than 20 mol% the guest occupies exclusively the lower symmetry sites C_2[16, 17] and S_6 occupation increases steadily at higher concentrations. Y^{3+} and Gd^{3+} with similar ionic radii and the same crystal structure type allow the synthesis of the mixed oxide sesquioxides lattices over a wide concentration range[18]. $(Gd,Y)_2O_3$:Eu materials have been found to be very efficient X-ray phosphors[19]. So far, no studies have been published on the effect of these lattices on the luminescent properties of Er^{3+} activator centres, and the aim of the work reported in this chapter is to assess the changes in the crystallographic properties of the lattices and their effect on the emission properties of the activator.

5. 1 Results and discussion I .- Gd_2O_3

5.1.1 Structural characterization of Gd_2O_3

Powder XRD patterns were routinely measured to characterise the prepared crystal lattices and establish sample homogeneity (i.e. solid solution formation) when incorporating the luminescent centres. Samples were fired at different temperatures to establish the crystal phase formed. Cubic gadolinium oxide resulted on firing in air at 980 °C (confirmed by fitting the data to the Joint Committee Powder Diffraction Standards, data file number 12-0797, p186, 1987) The XRD pattern of a Gd_2O_3 undoped sample is shown in Figure 5.1. Patterns of the samples fired in air at 1500°C were also obtained. Although the patterns fitted with the XRD pattern of monoclinic gadolinium oxide, (data from the Joint of Committee Powder Diffraction Standards, data file number 12-0474, p186, 1987), low signal to noise ratio was always obtained, probably due to very small crystal size, therefore further investigation with alternative methods was needed in order to confirm the phase formed. The pattern obtained from a monoclinic Gd_2O_3 undoped sample

is shown in Figure 5.2. The values obtained from a refinement study of both structures using the UnitCell program are summarized in Table 5.1 and Table 5.2.

It was important to assess if the Gd_2O_3:Er powder phosphors formed a single phase solid. For the different doped samples prepared no remarkable changes in the X-ray diffraction pattern were detected, and all were consistent with formation of the cubic polymorph for the lower temperature fired samples, whereas the monoclinic phase was obtained for the doped samples fired at 1500°C. These results support the assumption that the rare earth ions substitute at gadolinium sites in the Gd_2O_3 lattice when the doped phosphor powder is produced, forming substitutional solid solutions.

Table 5.1 Refined structure of cubic Gd_2O_3.

***a*/ Å**	10.7781±0.0033
cell volume /Å^3	1252.0791

Table 5.2 Refined structure of monoclinic Gd_2O_3.

***a*/ Å**	13.3682±0.6651
***b*/ Å**	3.5278±0.1381
***c*/ Å**	8.6034±0.3249
β °	84.1295±6.1995
cell volume /Å^3	403.6160

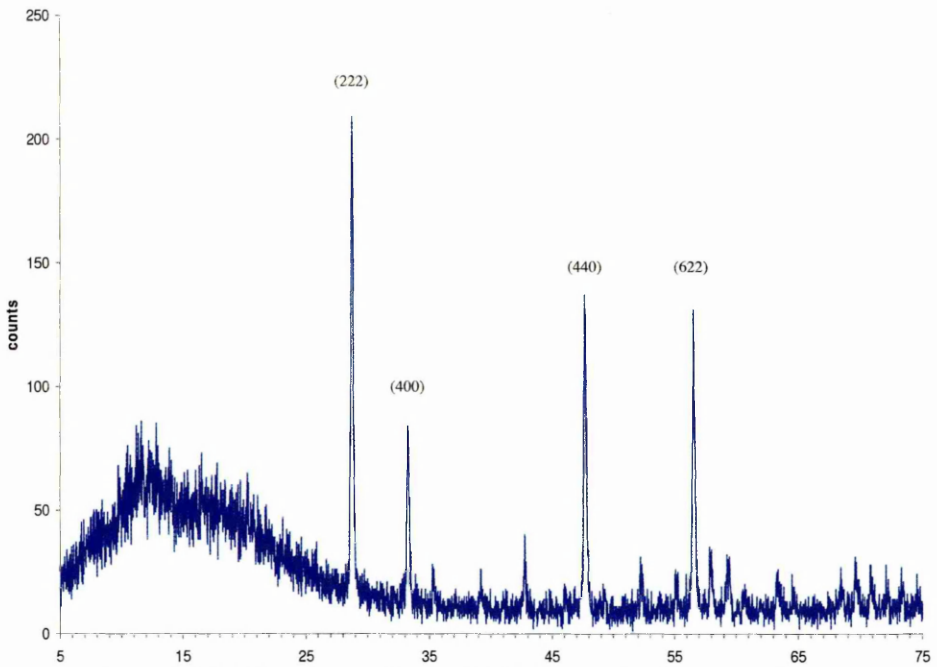

Figure 5.1 XRD pattern of the cubic Gd_2O_3 sample, fired at 980°C for 6 hours.

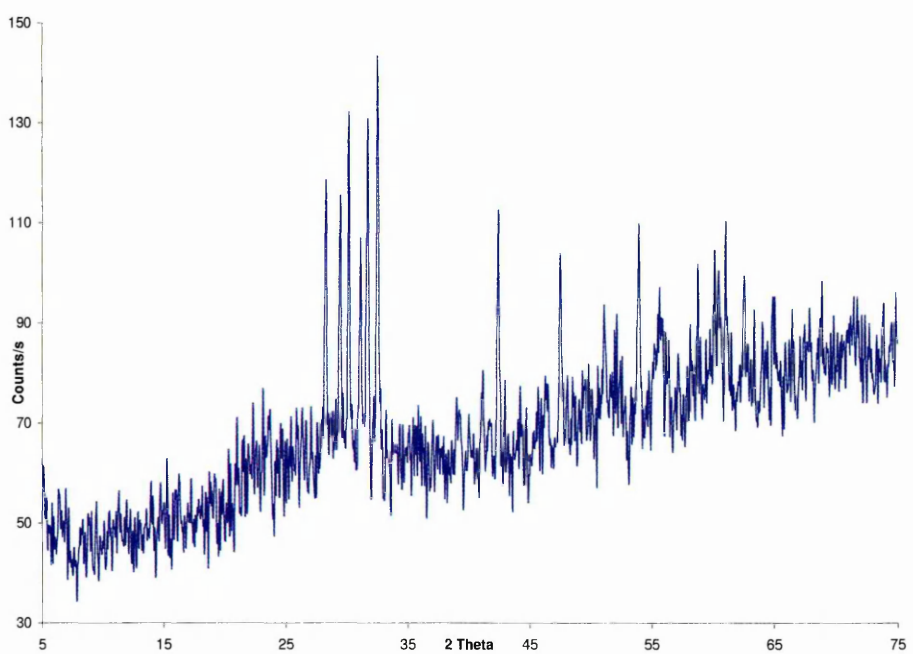

Figure 5.2 XRD pattern of the monoclinic Gd_2O_3 sample fired at 1500°C for 6 hours.

In order to circumvent the problem of low signal-to-noise ratio in the XRD pattern of powder fired at 1500 °C, structural information was also obtained using Raman spectroscopy. Spectra of the pure polycrystalline Gd_2O_3 host lattice were recorded (Figure 5.3) to be used as a control for luminescence measurements. The Raman spectrum of the

Gd_2O_3 powder phosphors fired at 980 °C was identical to Raman spectra of commercial cubic Gd_2O_3[20, 21]. The Raman frequencies detected are listed in Table 5.3. The spectra verify that the phosphor powders crystallize in the cubic phase. Raman spectra of Gd_2O_3 phosphor powders fired at 1500 °C were also obtained (Figure 5.4). The spectra were compared with those of monoclinic Gd_2O_3[22]. Monoclinic Gd_2O_3 is predicted to have twenty one active Raman frequencies, and those detected are listed in Table 5.4. Combining the results obtained by XRD diffraction and Raman spectroscopy it can be concluded that the crystallographic phase formed when firing at high temperature is monoclinic Gd_2O_3.

Raman spectra of the undoped samples were used as a tool to normalise the emission bands of the doped materials by reference to the Raman band at 361 cm^{-1} in the cubic phase samples, and the band at 268 cm^{-1} in the monoclinic phase samples due to the easy detection in both Stokes and anti-Stokes regions of the spectrum. The Raman bands in the doped samples show a shift consistent with the increase of the atomic mass of the dopant ion on moving across the lanthanide series. This effect provides further evidence for substitutional solid solution formation.

Table 5.3 Assignment of Raman spectrum of cubic Gd_2O_3 (cm^{-1}).

A. Garcia Murillo *et al* [20]	**Experimental results**
565	568
441.4 A_g	444
359.5 B_g	361
313.5 A_g	316
117 B_g	
93	

Table 5.4 Assignment of Raman spectrum of monoclinic Gd_2O_3 (cm^{-1}).

Gouteron *et al* [22]	Experimental results	Gouteron *et al* [22] (cont.)	Experimental results (cont.)
590 A_g	590	218 A_g	218
580 A_g		176 A_g	176
483 A_g	483	150 A_g	
442 A_g	442	115 B_g	
427 B_g	430	109 A_g	108.8
416 B_g	416	98 B_g	95.5
385 B_g	386	84 A_g	
299 B_g	298	71 B_g	72.1
269 A_g	268		

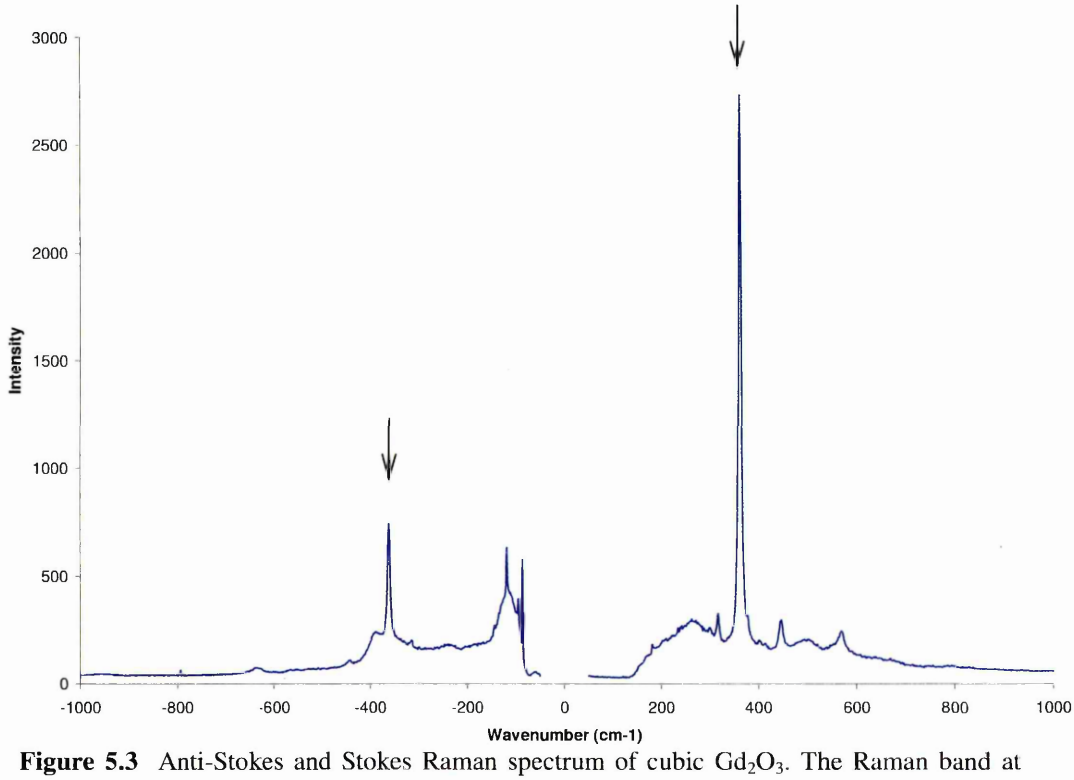

Figure 5.3 Anti-Stokes and Stokes Raman spectrum of cubic Gd_2O_3. The Raman band at 361 cm^{-1} is marked with arrows in both the Stokes and anti-Stokes regions.

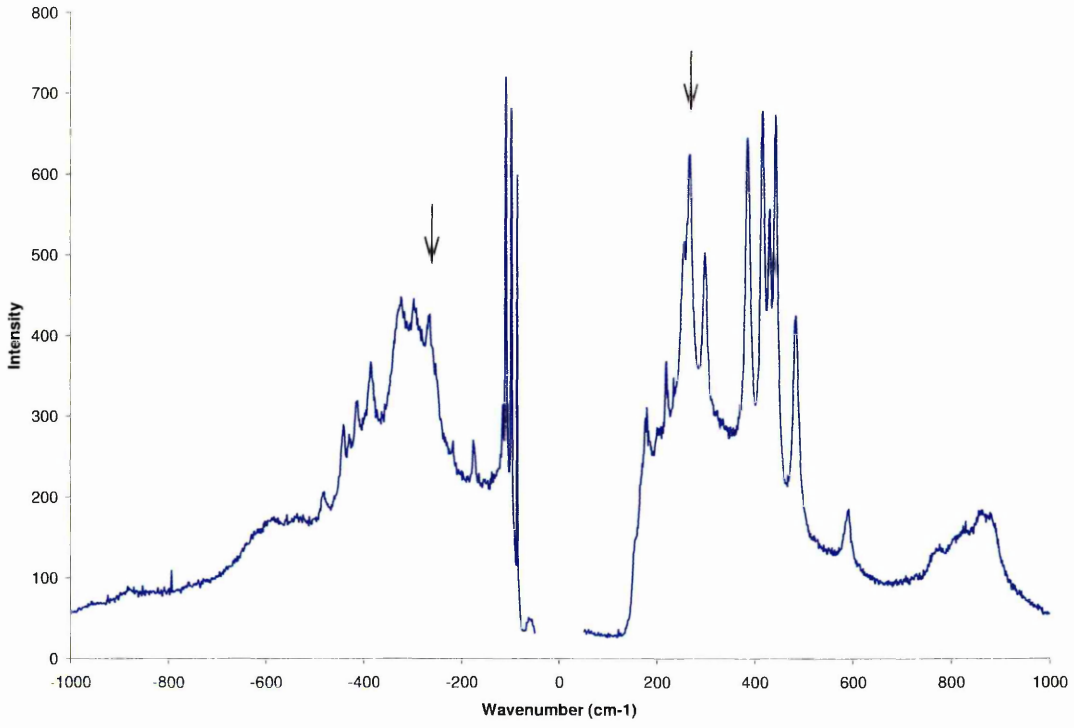

Figure 5.4 Anti-Stokes and Stokes Raman spectrum of monoclinic Gd_2O_3 at room temperature. The Raman band at 268 cm^{-1} is marked with arrows in both the Stokes and anti-Stokes regions. Intensities are in arbitrary units.

5.1.2 Morphologic characterization of the Gd_2O_3 phosphor powders.

Materials were synthesised from aqueous solutions of Gd^{3+} having concentrations of 6.27×10^{-3} M. Following addition of 15 g of urea and boiling for 1 hour, the average particle size of the hydroxycarbonate precursor particles was estimated by SEM. Typical precipitates obtained from these solutions are illustrated in Figure 5.5. The uniformity of the particles and the difference in size between the samples is illustrated. In accord with the work reported in Chapter 3, the diameter of 25 particles per micrograph was measured. The calculated average diameter was 430 ± 21nm. The circular shape of all the particles shown

suggests spherical particles, taking into account random orientation in three dimensions. The regularity in size suggests that the particles grow over the initially formed precipitation nuclei, and that not many new nuclei are formed after precipitation started.

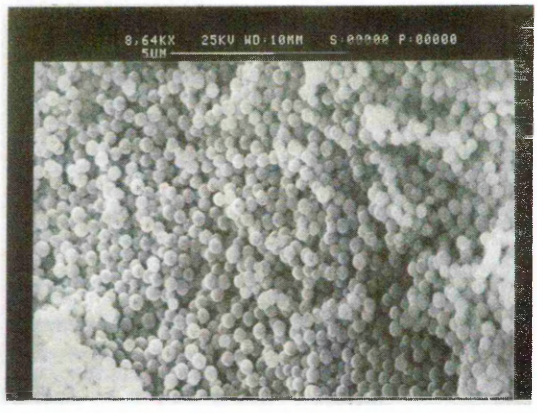

Figure 5.5 SEM micrographs of the precipitate obtained from the Gd^{3+} 6.27×10^{-3} M solution.

It was important to ascertain whether or not a spherical shape is maintained after firing to induce crystallization, as this is a required characteristic of the materials used in the manufacturing of close packed, high resolution devices. Figure 5.6 shows the microstructure of the powders on firing at 980°C and 1500°C for 6 hours. Samples fired at 980°C maintained the spherical morphology and no signs of strong agglomeration or sintering were detected, whereas samples fired at higher temperature in order to obtain the monoclinic phase were found to be completely sintered and agglomerated, losing the initial spherical shape of the precursor particles, although the initial structure can still be detected. This could be a consequence of partial melting of the sample during the firing process. Annealing the samples at lower temperatures (1200°C-1400°C), even doing so for longer times where the sintering and agglomeration phenomena were not as strongly detected, proved to be unsuccessful in producing the desired monoclinic phase.

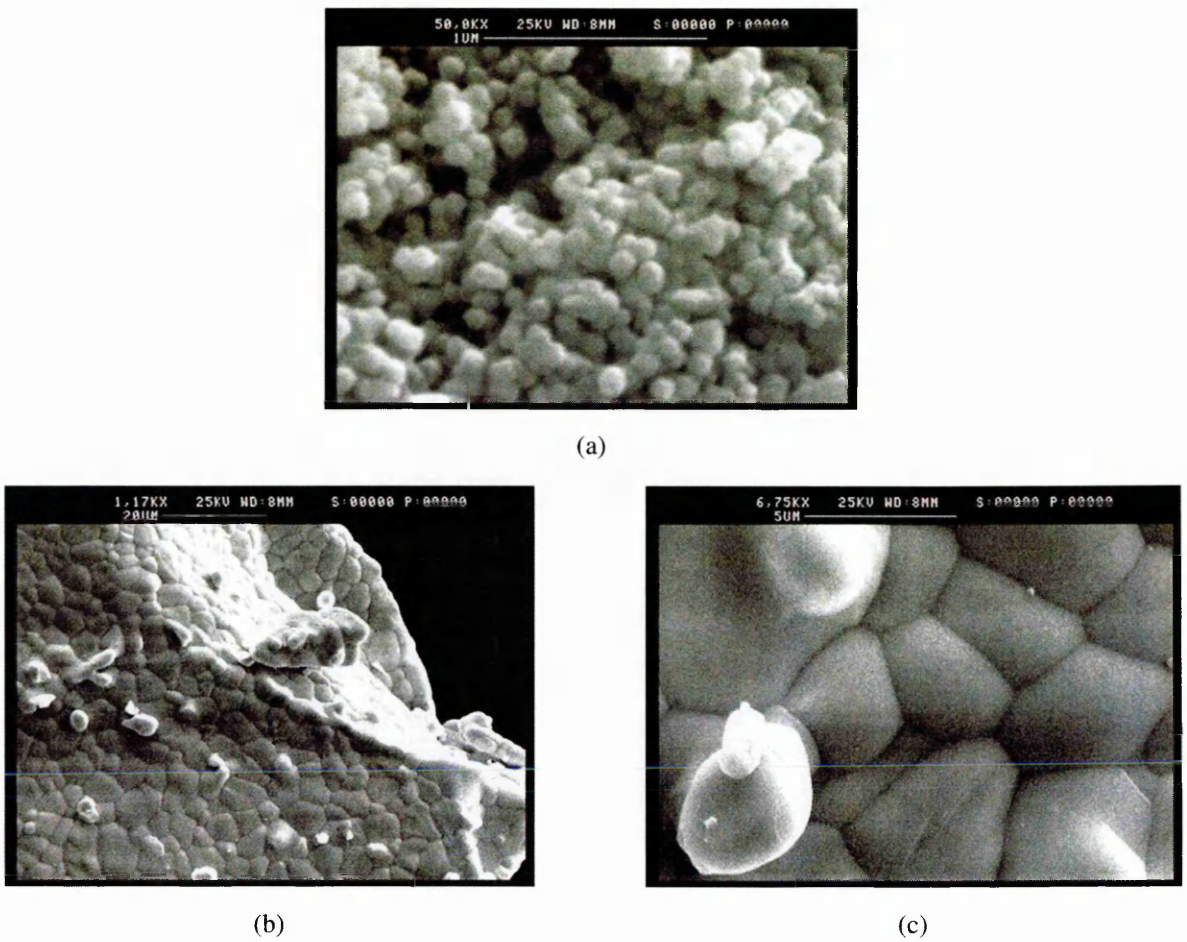

Figure 5.6 Effect of the firing temperature on the Gd_2O_3 precursor particles (a) fired at 980°C for 6 hours, (b) and (c) fired at 1500°C for 6 hours.

In summary, the urea precipitation method has been shown to be suitable for the preparation of uniform and spherical $Gd_2O_3:Er^{3+}$ powder phosphors, facilitating the control over particle size and morphology in a similar way of that of the preparation of Y_2O_3:RE described in the previous chapter.

Unfortunately, the preparation of monoclinic $Gd_2O_3:Er^{3+}$ powder phosphors involved annealing at such high temperatures that the morphology of the precursor particles was not retained. It is necessary to investigate alternative methods such us spray

pyrolysis in order to synthesize this monoclinic phase in a morphologically controlled manner allowing close packed aggregation.

5.1.3 Luminescent properties of Gd_2O_3:Er phosphors

The emission characteristics of pure and erbium doped Gd_2O_3 samples were studied using Raman and laser-induced luminescence spectroscopy. Because the wavelengths of neon emission lines are stable and well established, it was used as standard for calibration of the detector. The experimental results and the reference values are compared in Table 4.6 and a typical neon calibration spectrum is shown in Figure 4.10 in the previous chapter.

Stokes and anti-Stokes emission were studied for the Er^{3+} luminescent centre using the same instrumental parameters used to study Y_2O_3:RE phosphor powders described in Chapter 4, in order to allow comparison between the results. Therefore the confocal pinhole selected to carry out luminescent measurements was 400 nm.

Laser-induced spectroscopy under 632.8 nm wavelength excitation using a helium-neon laser source has been used to study the up-converting and down-converting properties of both cubic and monoclinic Gd_2O_3:Er^{3+} powder phosphors.

A single Raman band typical of the Gd_2O_3 cubic lattice is seen in both spectra at a wavenumber shift of 361 cm^{-1} and has been used to normalize the signal. The Raman frequency chosen to normalize the emission from Er^{3+} in monoclinic Gd_2O_3 lattices is 268 cm^{-1}.

The anti-Stokes emission spectrum of cubic Gd_2O_3:Er^{3+} in the range 420-630 nm at room temperature is shown in Figure 5.7, and the Stokes emission spectrum in the range from 634 to 895 nm is shown in Figure 5.8. The signal obtained from Er^{3+} in this cubic lattice is very similar to that obtained from Er^{3+} in Y_2O_3 and very similar splitting on the

bands can be detected. Over the entire wavelength range, six emission manifolds were detected (Table 5.5). These correspond to electronic transitions from the Er^{3+} ion from different excited states. Two additional manifolds (a and b) analogous to those detected in the Y_2O_3 based powder phosphors were also detected. The main differences found between the emission of Er^{3+} in these two lattices were a slight narrowing of the bands and displacement to shorter wavelengths, as well as a significant weakening of the $^4F_{7/2} \rightarrow {}^4I_{15/2}$ emission band. This is caused by less effective energy absorption of the second photon necessary for the up-conversion process due to the higher phonon energy of this Gd_2O_3 lattice (~600 cm^{-1}) than the previously studied Y_2O_3. In addition, the bands denoted a and b diminished in intensity, being detected only by a single emission line in the case of the band a and two very weak lines for the band b. The repeat of the behaviour of these two bands in accordance with the changes observed in the band $^4F_{7/2} \rightarrow {}^4I_{15/2}$ reinforce the suggestion that bands a and b arise from the same excited state as the former.

Table 5.5 Comparison between the emission bands found in $Y_2O_3:Er^{3+}$ and $Gd_2O_3:Er^{3+}$ powder phosphors.

	emission range (nm)	
emission assignment	**$Y_2O_3:Er^{3+}$**	**$Gd_2O_3:Er^{3+}$**
$^4F_{7/2} \rightarrow {}^4I_{15/2}$	468-479	464-477
$^2H_{11/2} \rightarrow {}^4I_{15/2}$	518-540	517-539
$^4S_{3/2} \rightarrow {}^4I_{15/2}$	546-566	545-563
(a)	610-632	611
$^4F_{9/2} \rightarrow {}^4I_{15/2}$	648-685	647-683
(b)	754-772	755 and 770
$^4I_{9/2} \rightarrow {}^4I_{15/2}$	785-830	784-822
$^4I_{11/2} \rightarrow {}^4I_{15/2}$	845-882	844-878

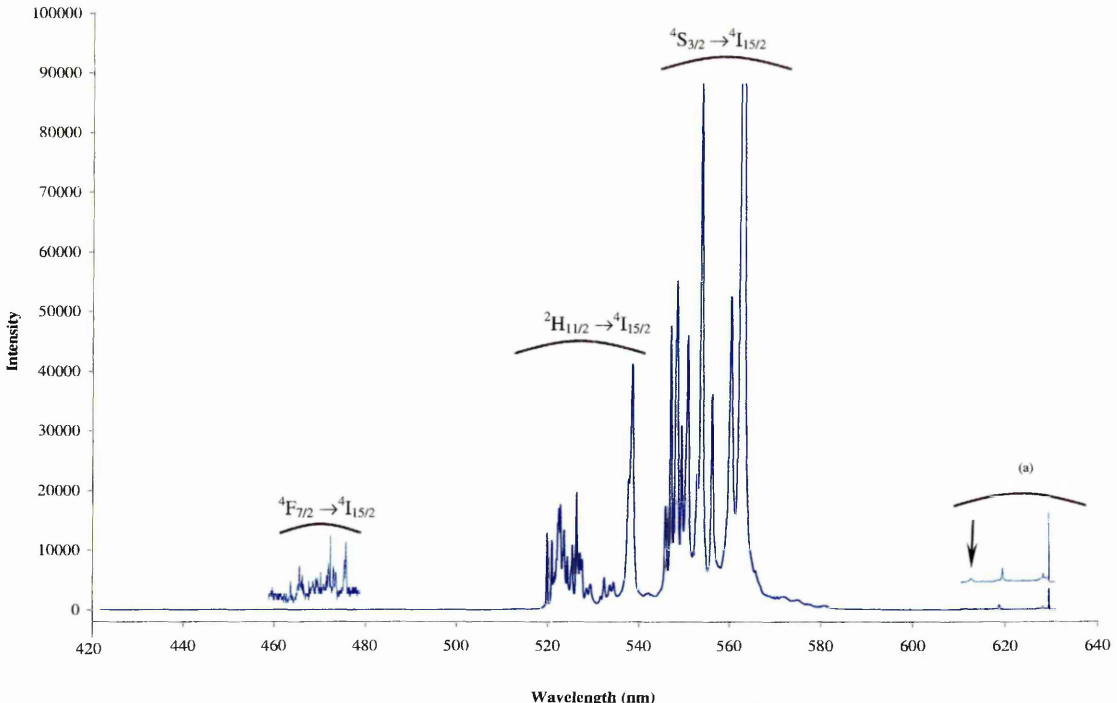

Figure 5.7 Anti-Stokes emission spectrum of cubic $Gd_2O_3:Er^{3+}$ (1 mol%) at room temperature in the region of 420-630 nm. The line detected in emission a is marked with an arrow. Intensities in arbitrary units.

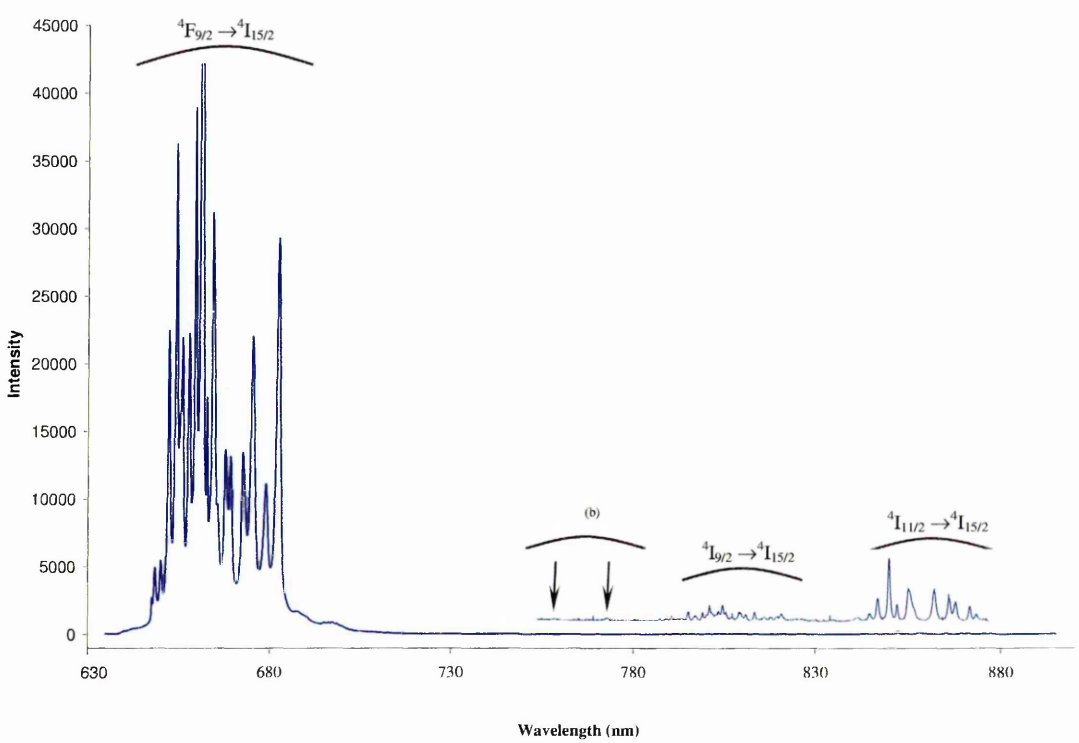

Figure 5.8 Stokes emission spectrum of cubic $Gd_2O_3:Er^{3+}$ (1 mol%) at room temperature in the region of 630-900 nm. Emission b marked with arrows. Intensities are in arbitrary units.

Closer analysis of the spectra of monoclinic $Gd_2O_3:Er^{3+}$ revealed further differences in comparison with the cubic Gd_2O_3 host. Most notably, only five emission manifolds were observed in the monoclinic phase as compared with 8 detected in the cubic lattice(Table 5.6). Figures 5.9 and 5.10 show typical spectra of Er^{3+} in Gd_2O_3. The splitting in the emission bands from Er^{3+} luminescent centres is very different from that of the activator in cubic lattices and it is summarised in Figure 5.11. The emission bands are formed by a series of multiple peaks, each one arising from the relaxation processes of the Stark components of an excited electronic state. These Stark components are affected by the crystal field as different host lattices situate atoms at different distances from the luminescent centre and cause variation in the electrostatic interactions. Therefore, the multiplicity of bands of the emission spectra of a given luminescent centre may vary when the surrounding crystal field changes[23]. The position of the bands does not change greatly, allowing the emission bands to be assigned to particular relaxation processes by comparison with the spectra obtained from cubic phases, but the line position varies indicating different splitting in the degenerate energy levels.

Table 5.6 Comparison between the emission bands found in monoclinic and cubic $Gd_2O_3:Er^{3+}$ powder phosphors.

	band emission range (nm)	
emission assignment	**Cubic $Gd_2O_3:Er^{3+}$**	**Monoclinic $Gd_2O_3:Er^{3+}$**
$^4F_{7/2} \rightarrow {}^4I_{15/2}$	464-477	-
$^2H_{11/2} \rightarrow {}^4I_{15/2}$	517-539	519-536
$^4S_{3/2} \rightarrow {}^4I_{15/2}$	545-563	543-559
(a)	611	-
$^4F_{9/2} \rightarrow {}^4I_{15/2}$	647-683	644-691
(b)	755 and 770	-
$^4I_{9/2} \rightarrow {}^4I_{15/2}$	784-822	795-836
$^4I_{11/2} \rightarrow {}^4I_{15/2}$	844-878	845-870

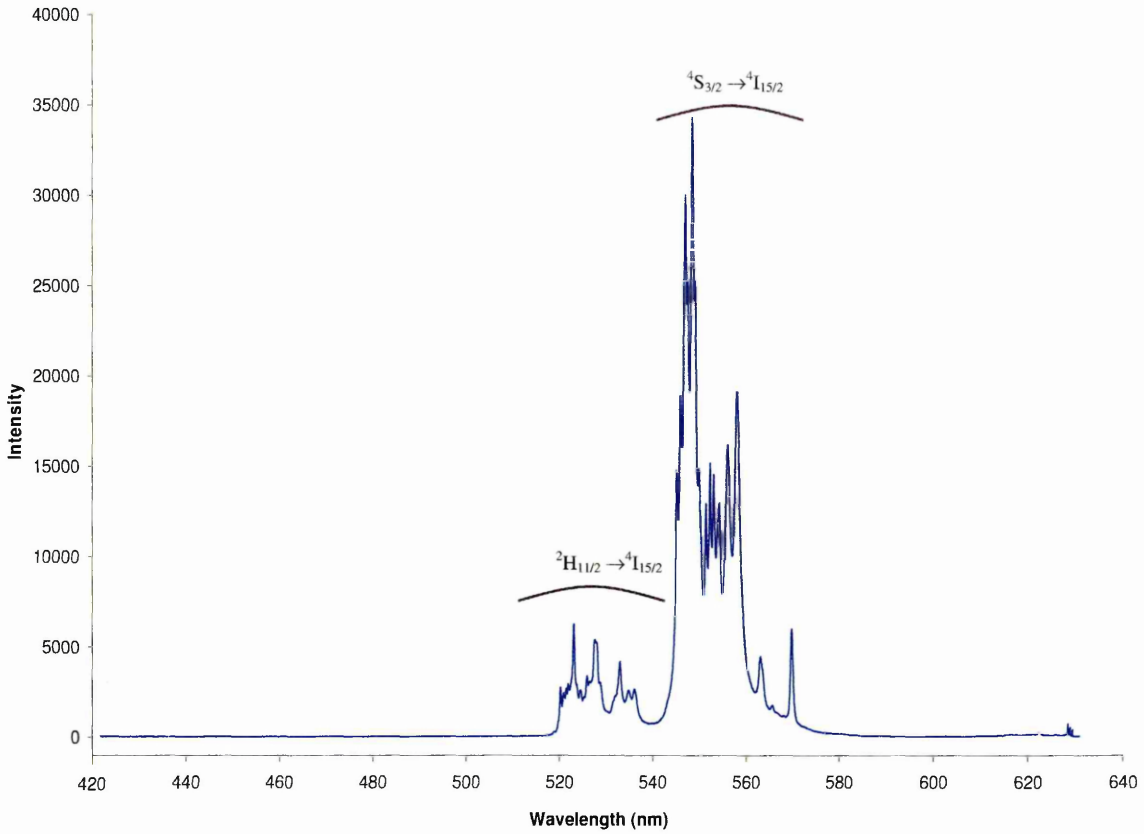

Figure 5.9 Anti-Stokes emission spectrum of monoclinic $Gd_2O_3:Er^{3+}$ (1 mol%) at room temperature in the region of 420-630 nm. Intensities are in arbitrary units.

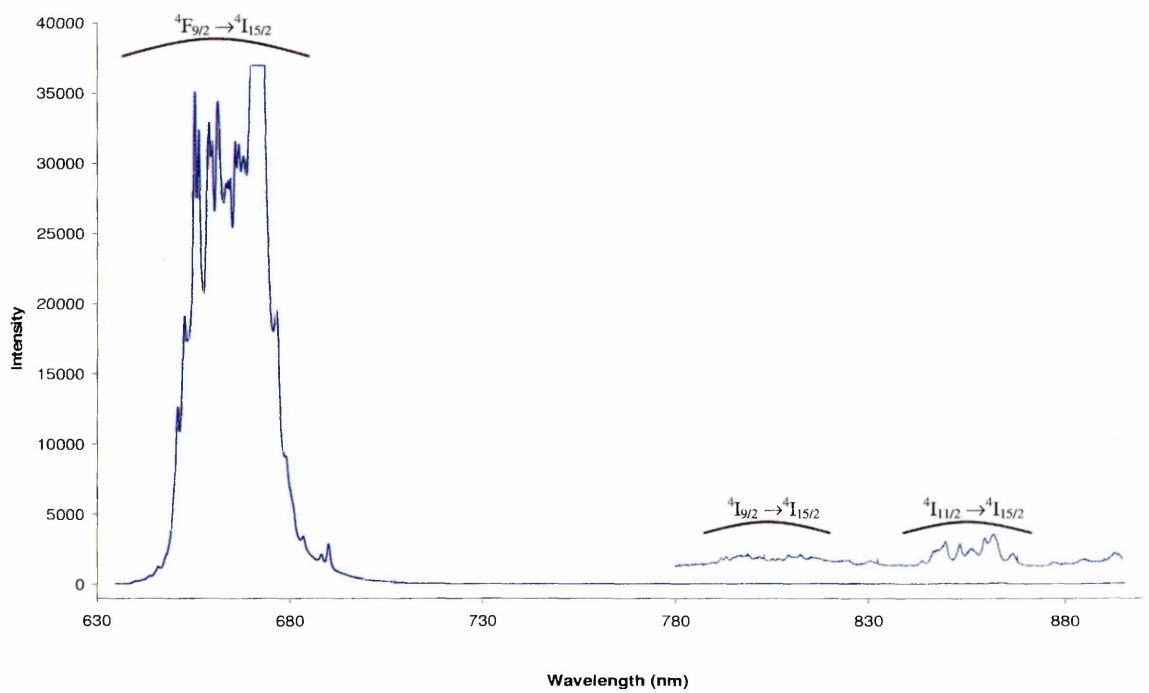

Figure 5.10 Stokes emission spectrum of monoclinic $Gd_2O_3:Er^{3+}$ (1 mol%) at room temperature in the region of 630-900 nm. Emission b marked with arrows. Intensities are in arbitrary units.

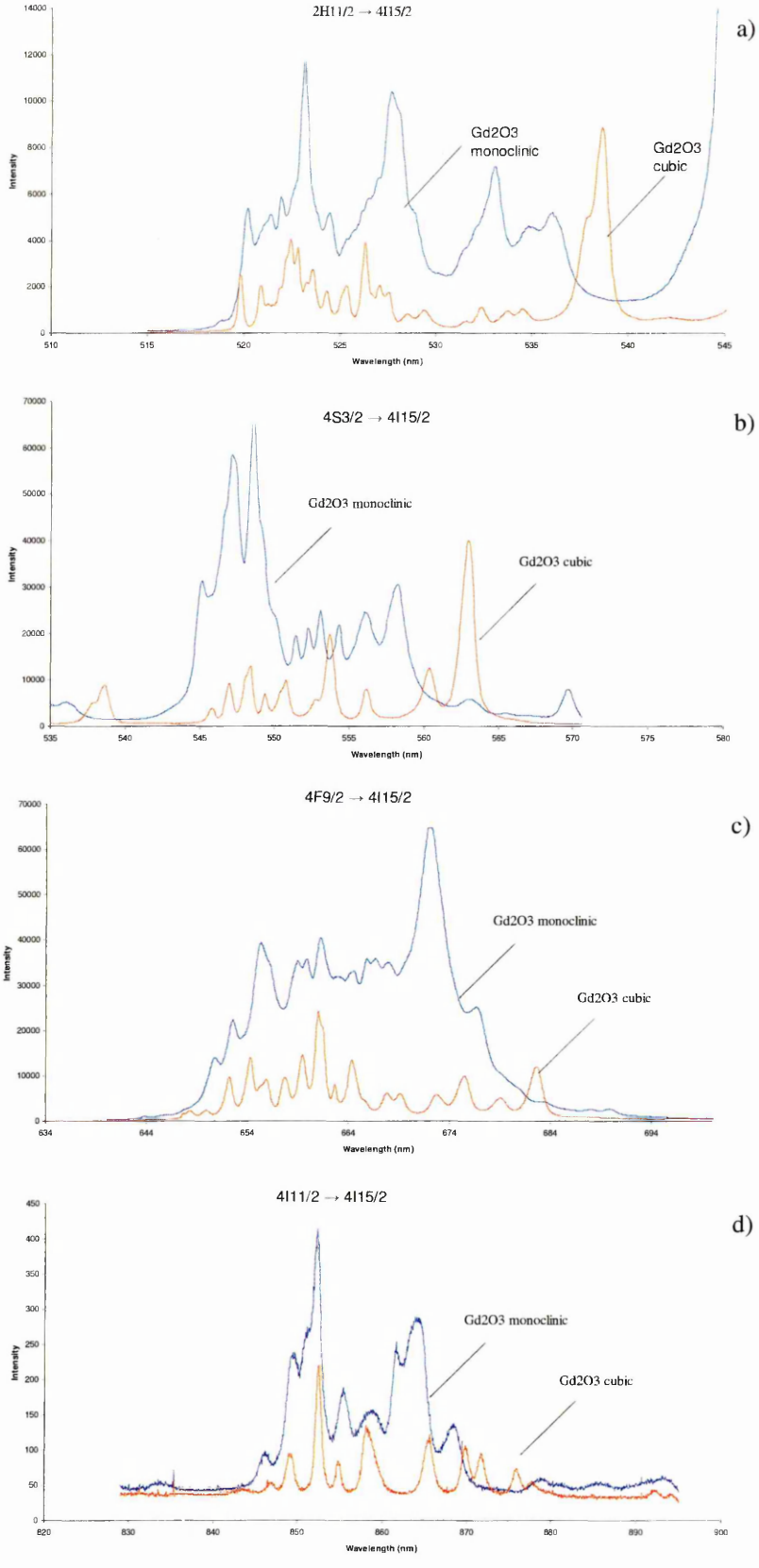

Figure 5.11 Emission bands of Er^{3+} luminescent centres in cubic and monoclinic Gd_2O_3.

a) $^2H_{11/2} \rightarrow {}^4I_{15/2}$ b) $^4S_{3/2} \rightarrow {}^4I_{15/2}$ c) $^4F_{9/2} \rightarrow {}^4I_{15/2}$ and d) $^4I_{11/2} \rightarrow {}^4I_{15/2}$.

In summary, emission bands from Er^{3+} were detected in both cubic and monoclinic Gd_2O_3 and assigned to relaxation processes from excited states. The position of the emission bands was compared with those of Er^{3+} in Y_2O_3. The emission spectra obtained from the cubic Gd_2O_3 is similar in many ways to that obtained from Y_2O_3 containing the same number of bands, having approximately the same emission wavelength and with very similar splitting patterns. The main difference observed on closer inspection of the spectra, was the reduction in intensity of the $^4F_{7/2} \rightarrow {}^4I_{15/2}$ emission band and the associated a and b bands which may be a consequence of the higher phonon energy of the Gd_2O_3 crystal lattice.

The crystallographic studies by X-ray diffraction of the samples fired at high temperature, were not conclusive. Differences found in the Raman spectra with cubic Gd_2O_3 and comparison with published data [20-22] allowed determination of the crystalline phase formed. The differences between the spectra obtained from the low temperature fired sample and the high temperature fired one confirmed the suggestion of two different crystal phases in the sample. Although the Stark splitting of the energy levels in this crystallographic phase and in the cubic phase of Gd_2O_3 is different, similarities in the spectra such as the number, position and extension of the emission bands, allowed its assignment to energy levels and therefore to relaxation transitions of Er^{3+} in monoclinic Gd_2O_3. Thus, the differences observed in these two crystal lattices may be attributed to different local crystal field experienced by Er^{3+}.

5. 2 Results and discussion II .- $Gd_{2-x}Y_xO_3$

In order to further probe the differences in emission characteristics in RE_2O_3 hosts, a range of samples of general composition $Gd_{2-x}Y_xO_3$:Er was prepared. As such, it was important to elucidate any structural modifications caused by the addition of Y^{3+} to Gd_2O_3. To this end undoped samples containing different nominal concentrations of gadolinium and yttrrium oxides were also prepared. Samples containing various nominal concentrations of gadolinium and yttrium oxides were synthesised by the urea homogeneous precipitation method, followed by firing at 980 °C and 1500 °C for six hours.

5.2.1. Structural characterization of $Gd_{2-x}Y_xO_3$

Powder XRD patterns were routinely measured to characterise synthesised crystal lattices and establish sample homogeneity (i.e. solid solution formation) when incorporating the luminescent centres. Cubic phases were obtained for all of the samples on firing in air at 980 °C. All samples showed were single phase as gauged by XRD. The patterns were all very similar to those of pure Gd_2O_3 and Y_2O_3. When these patterns were refined using the program *UnitCell* it was observed that the cell parameters for the complex oxide lattice were in between those of the pure oxides in accord with Vegard's law and characteristic of substitutional solid solution formation. The pattern of the undoped sample $GdYO_3$ is shown in Figure 5.12.

XRD patterns of the samples fired in air at 1500 °C were also obtained. For all the samples studied a single phase pattern was obtained. Patterns obtained from the samples containing nominal concentrations of Gd_2O_3 in the mixture between 100% and

80% matched with the monoclinic pattern obtained for pure Gd_2O_3. However, the substitution of Gd^{3+} for Y^{3+} above these levels yielded the cubic phase.

The signal to noise ratio in the patterns obtained from these samples was as the previously obtained for the pure oxide in the monoclinic phase and further study with Raman spectroscopy is necessary in order to provide more conclusive structural assignment. This is illustrated in Figure 5.13 where the pattern of the samples $Gd_{1.8}Y_{0.2}O_3$ and $Gd_{1.4}Y_{0.6}O_3$ fired at 1500 °C is shown. Again, inclusion of Er^{3+} in the samples formed a single phase solid. For the dopant levels no remarkable changes in the X-ray diffraction patterns were detected, and all were consistent with formation of the cubic polymorph for the samples fired at 980 °C. However a monoclinic phase was obtained for the doped samples fired at 1500 °C where the nominal Y^{3+} concentration was below 20 mol%. For higher concentrations cubic phases were found.

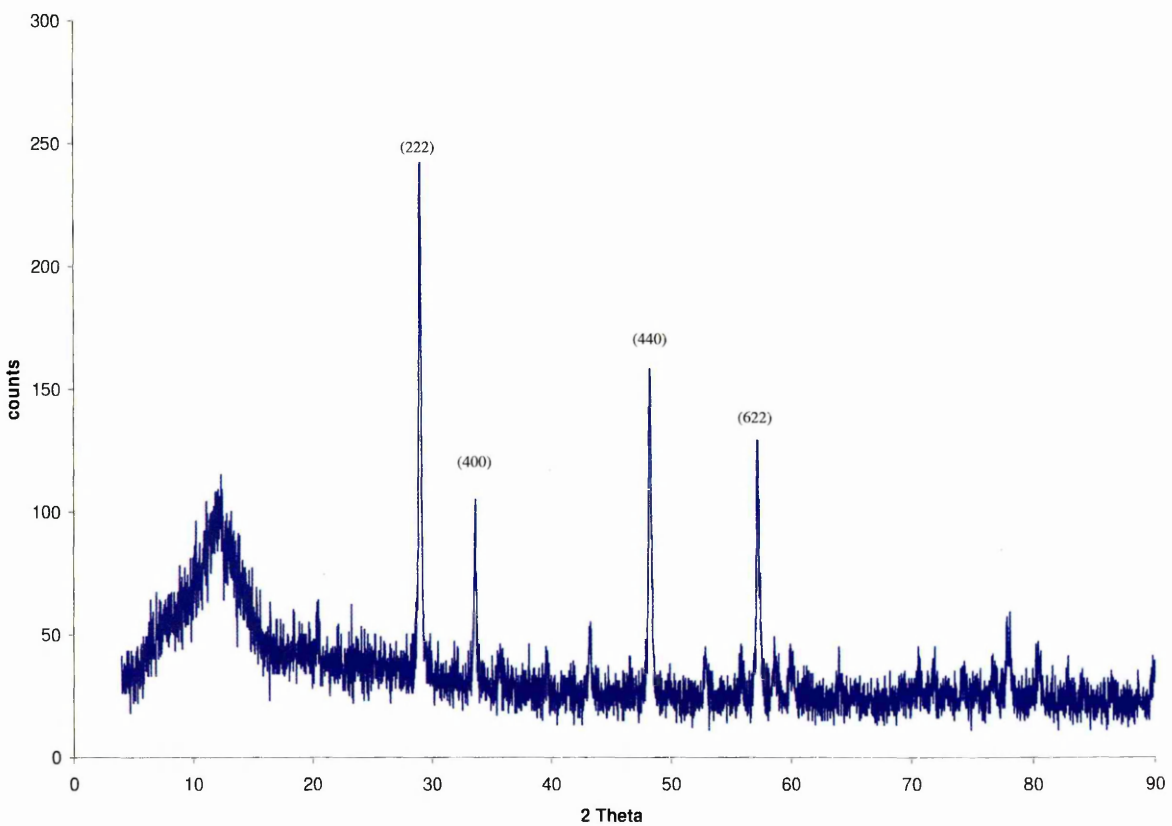

Figure 5.12 XRD pattern of the cubic $GdYO_3$ sample, fired at 980 °C for 6 hours.

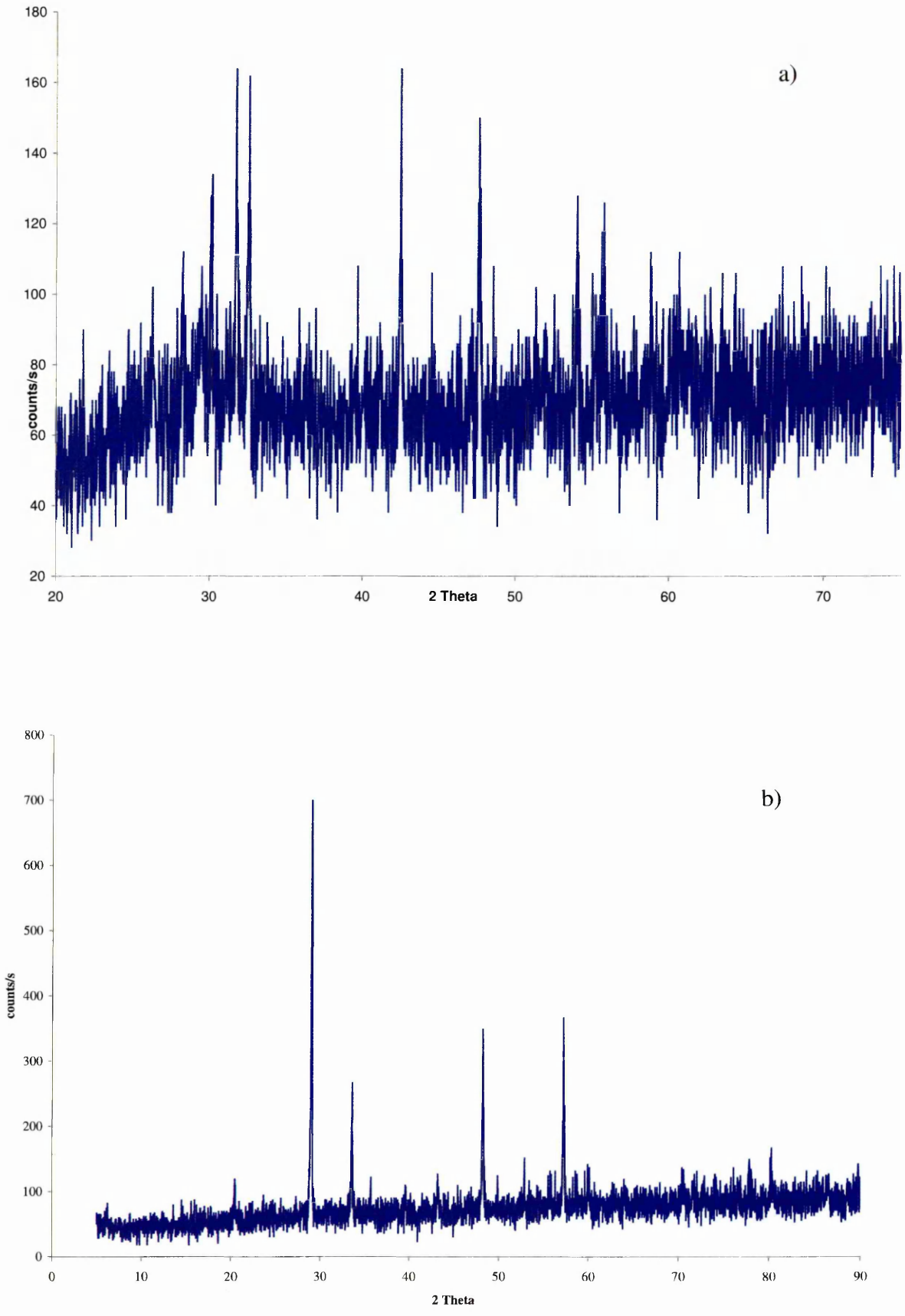

Figure 5.13 XRD pattern of the a) $Gd_{1.8}Y_{0.2}O_3$,and b) $Gd_{1.4}Y_{0.6}O_3$ samples in air fired at 1500 °C for 6 hours.

As with single oxide lattices, structural information was also obtained using Raman spectroscopy. Spectra of the pure polycrystalline $Gd_{2-x}Y_xO_3$ host lattices were recorded and normalized with the intensity of pure Gd_2O_3. The Raman spectrum of the powders fired at 980°C showed a single phase formed similar to that obtained for cubic Gd_2O_3. A shift in the Raman band at 261 cm^{-1} with increasing Y_2O_3 concentration, consistent with a decrease in the atomic mass of the rare earth ion was detected. The Raman frequencies detected are listed in Table 5.7, which verify that the phosphor powders crystallize in the cubic phase.

Table 5.7 Band shift detected for the mixed oxide lattices (cm^{-1}).

Sample	Raman band
Y_2O_3	375.47
$G_{0.2}Y_{1.8}O_3$	374.33
$G_{0.4}Y_{1.6}O_3$	373.95
$G_{0.6}Y_{1.4}O_3$	372.79
GYO_3	371.61
$G_{1.4}Y_{0.6}O_3$	366.88
$G_{1.6}Y_{0.4}O_3$	366.88
$G_{1.8}Y_{0.2}O_3$	364.51
$G_{1.9}Y_{0.1}O_3$	362.16
Gd_2O_3	360.98

Raman spectra of powders fired at 1500 °C were also measured. The spectra were compared with those of monoclinic Gd_2O_3[22]. Samples containing less than 20 mol% nominal concentration Y_2O_3 in the complex oxide were found to crystallise in the monoclinic phase, whereas for samples containing over 20 mol% nominal concentration of

Y_2O_3 only cubic phase can be detected, and no residual monoclinic material was detected. This result confirms what was suggested from XRD, and it can be concluded that the substitution of Y^{3+} in the Gd^{3+} oxide lattice results in a change from monoclinic to cubic. Raman spectra of the undoped $G_{1.8}Y_{0.2}O_3$ and $G_{1.4}Y_{0.6}O_3$ samples fired at 980 °C and 1500 °C are shown in Figures 5.14 and 5.15, where the change from cubic to monoclinic phases is illustrated for the former sample whereas the latter remained unchanged.

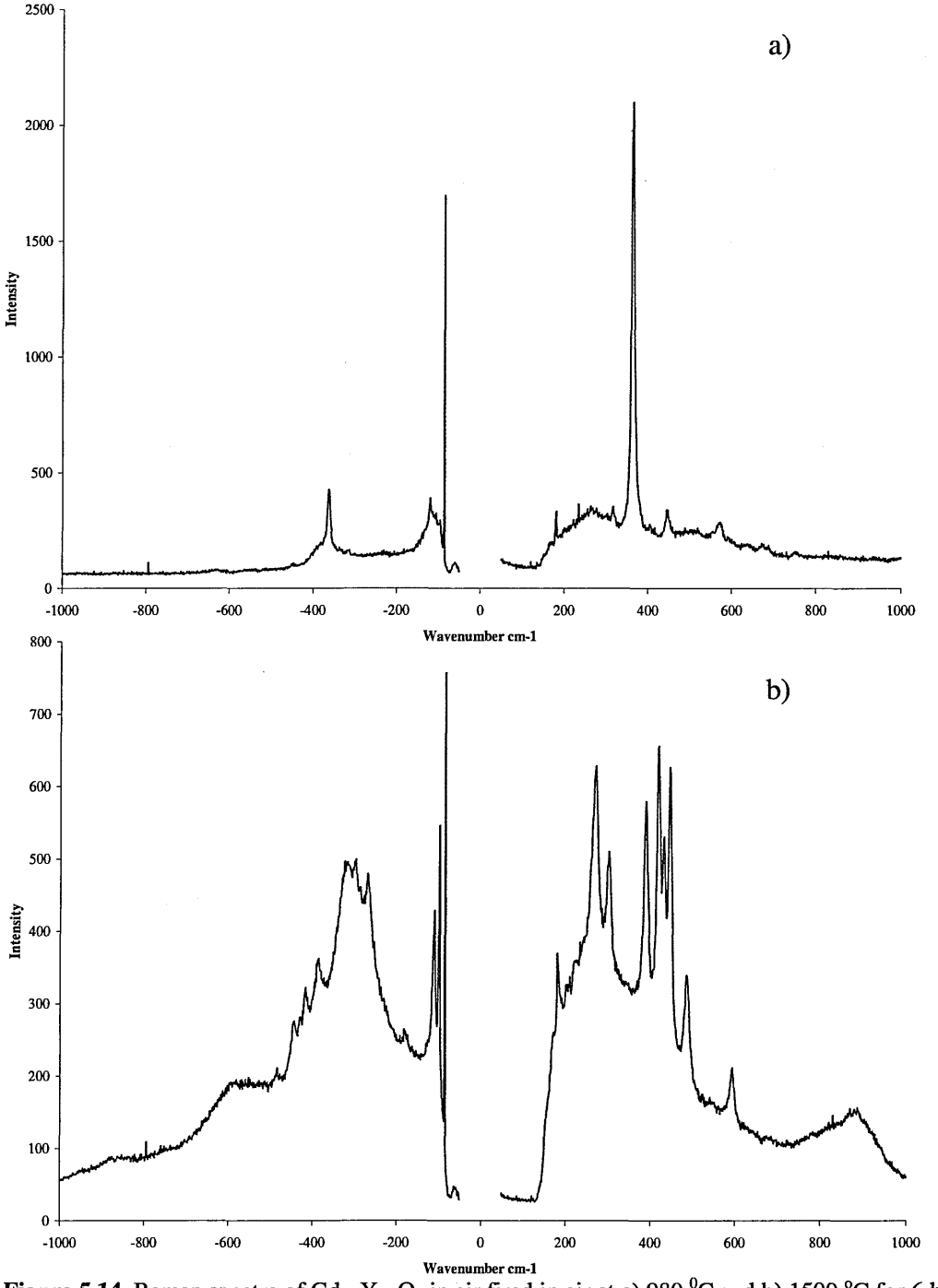

Figure 5.14 Raman spectra of $Gd_{1.8}Y_{0.2}O_3$ in air fired in air at a) 980 °C and b) 1500 °C for 6 hours.

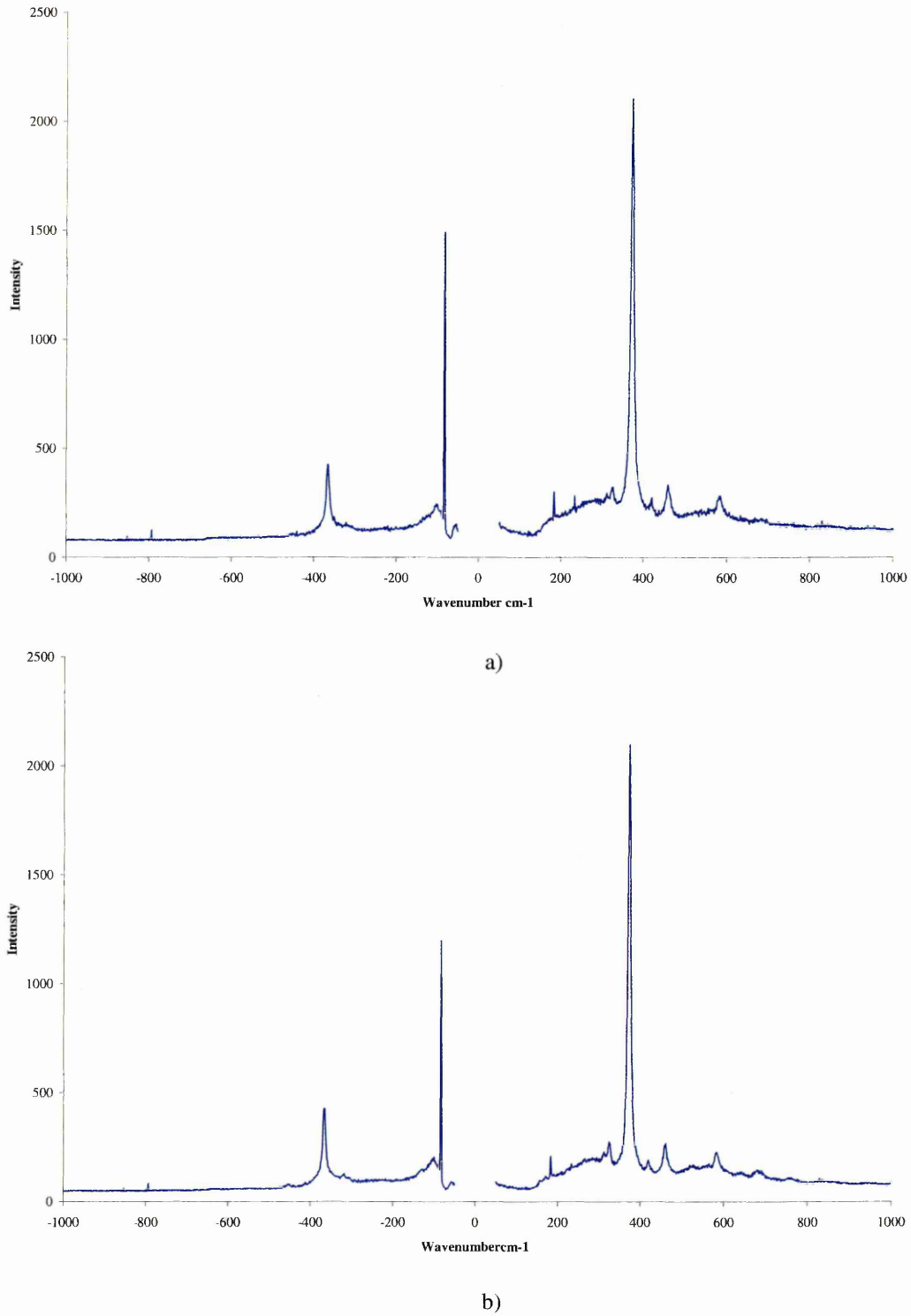

Figure 5.15 Raman spectra of $Gd_{1.4}Y_{0.6}O_3$ in air fired in air at a) 980 ^{0}C and b) 1500 ^{o}C for 6 hours.

The spectra of the undoped samples were also used as a tool to normalise the emission bands of the doped samples by reference to the Raman band at 361 cm^{-1} in the

cubic phase samples, and the band at 268 cm^{-1} in the monoclinic phase. This Raman line is readily detected in both Stokes and anti-Stokes regions.

5.2.2 Luminescent properties of $Gd_{2-x}Y_xO_3$:Er phosphors

The emission characteristics of pure and erbium doped $Gd_{2-x}Y_xO_3$ samples were studied using Raman and laser-induced luminescence spectroscopy. The procedures used were the same as those for Gd_2O_3:Er phosphors (see Section 5.1.3).

A single Raman band, typical of the Gd_2O_3 cubic lattice, is seen in the spectra of all of the samples fired at 980^0C at a wavenumber shift of 361-375 cm^{-1} depending on the degree of Y^{3+} substitution in the lattice, and has been used to normalize the signal. The Raman frequency chosen to normalize the emission from Er^{3+} in monoclinic Gd_2O_3 lattices is 268 cm^{-1}

The anti-Stokes emission spectrum of cubic $GdYO_3$:Er^{3+} in the range 420-630 nm and 634-895 nm is shown in Figure 5.16. Spectra recorded from Er^{3+} in these mixed oxide cubic lattices are very similar to those obtained from Er^{3+} in the pure oxide lattices. Over the entire wavelength range, Er^{3+} centres in the mixed lattices show the six emission manifolds detected for the luminescent centre in pure Y_2O_3 and Gd_2O_3 summarised in Table 5.5, and the two additional bands a and b. The same splitting on the emission bands can be detected, as expected. A slight narrowing of the bands and displacement to shorter wavelengths was also detected for increasing Y^{3+} substitution.

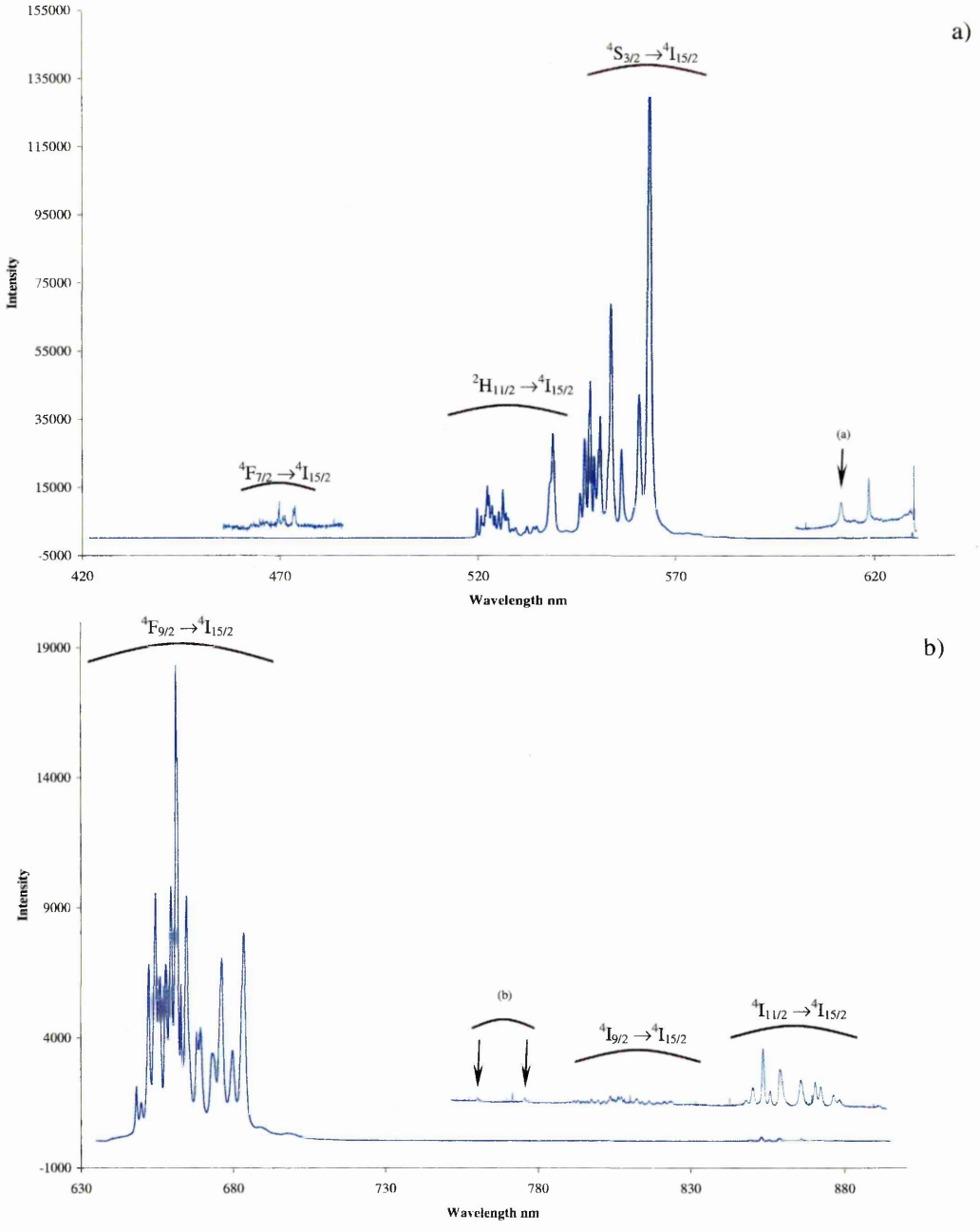

Figure 5.16 a) Anti-Stokes emission spectrum of cubic $GdYO_3:Er^{3+}$ (1 mol%) at room temperature in the region of 420-630 nm. The line detected in emission a is marked with an arrow, b) Stokes emission spectrum of cubic $GdYO_3:Er^{3+}$ (1 mol%) at room temperature in the region of 630-900 nm. Emission b marked with arrows. Intensities are in arbitrary units.

The *f-f* transitions of the Er^{3+} luminescent centre are sensitive to the crystal environment[24,25], and the relative intensity of the emission bands changes with variation in

crystal composition. This effect is thought to be due to the crystal field changes induced by the lattice distortion. Different crystal compositions produce different Stark splittings in the Er^{3+} excited energy levels. This phenomenon may be of use to tailor lattices tuned to a particular excitation source, thus favouring one or two photon absorption processes.

It was observed that anti-Stokes emission arising from $^2H_{11/2}$ and $^4S_{3/2}$ levels were strengthened at low Gd^{3+} levels. Indeed the strongest signal detected for the luminescent centre was from the composite $Gd_{0.4}Y_{1.6}O_3:Er^{3+}$ (1mol%). On the other hand stronger Stokes emission from the $^4F_{9/2} \rightarrow {}^4I_{15/2}$ transition was observed for composites with high Gd_2O_3 content, being the strongest for the pure Gd_2O_3 lattice. Spectra of samples illustrating this effect are shown in Figure 5.17.

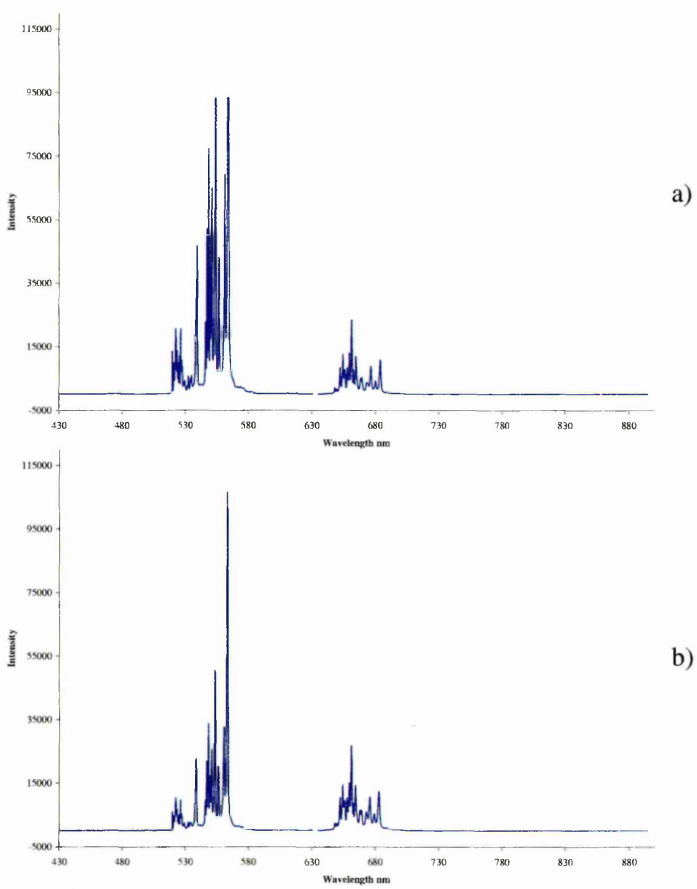

Figure 5.17 a) Emission spectrum of cubic $Gd_{0.4}Y_{1.6}O_3:Er^{3+}$ (1 mol%), and b) Emission spectrum of cubic $Gd_{1.6}Y_{0.4}O_3:Er^{3+}$ (1 mol%) at room temperature in the region of 430-900 nm. Intensities are in arbitrary units.

In the spectra, signals arising from a single phase (cubic or monoclinic) were detected. Closer analysis of the spectra of Gd_2O_3-Y_2O_3 composites fired at higher temperature (1500^0C) helped to determine the crystal lattices obtained. Analysis of the emission spectra uphold the assumptions made earlier in the chapter, and it can be concluded that composites containing less than 20 mol% Y^{3+}crystallize in the monoclinic phase whereas a Y^{3+} for Gd^{3+} substitution over that level produces cubic lattices. Moreover, in spectra recorded from all of the samples contribution from a single crystal lattice have been detected. The Raman spectrum of the sample $Gd_{1.8}Y_{0.2}O_3$ is shown in Figure 5.18.

The number of bands and the splitting from Er^{3+} luminescent centres in the mixed lattices are very similar to those defined earlier for the pure oxides, with a shift to shorter wavelengths with increasing Gd^{3+}. Therefore the crystal field experienced by the luminescent centres in mixed composites is comparable to that in pure oxides, allowing the emission bands to be assigned to particular relaxation processes by comparison with the spectra obtained from cubic phases. Line position variation indicates slightly different splitting in the degenerate energy levels, as expected. When studying the intensity of the emission, a decrease in intensity with higher Gd^{3+} was observed. For the same lattice composition enhancement in luminescence intensity was found for the phosphor powder fired at higher temperature. However, this firing temperature should be avoided so as not to agglomerate the sample during the firing process and to allow close packing of phosphor particles.

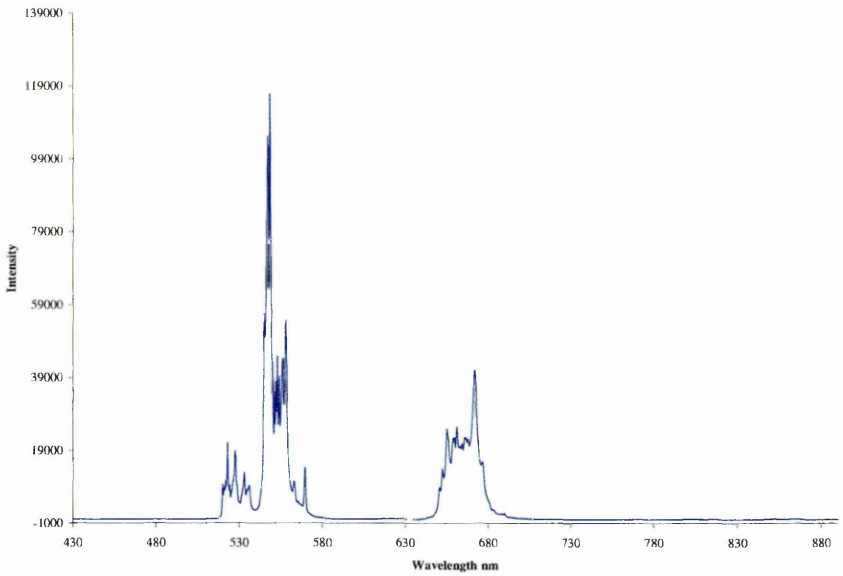

Figure 5.18 Emission spectrum of monoclinic $Gd_{1.8}Y_{0.2}O_3:Er^{3+}$ (1 mol%) at room temperature in the region of 430-900 nm. Intensity is in arbitrary units.

In summary, emission bands from Er^{3+} were detected in both cubic and monoclinic $Gd_{2-x}Y_xO_3$ composites and assigned to relaxation processes from excited states. The position of the emission bands were compared with those of Er^{3+} in Y_2O_3 and Gd_2O_3. The emission spectra obtained from the complex lattices was found to be similar in many ways to that obtained from the pure oxides containing the same number of bands, having approximately the same emission wavelength and with very similar splitting patterns. The main difference observed on closer inspection of the spectra, was the variation in the intensity ratio of the Stokes and anti-Stokes bands depending of the composition of the lattice which may be a consequence of the changes in the crystal field experienced by the luminescent centre.

The crystallographic studies by X-ray diffraction facilitated the determination of the phases obtained. Patterns from the samples fired at high temperature crystallised in monoclinic phase, were not conclusive and further investigation with Raman spectroscopy was needed. Differences found in the Raman spectra with cubic Gd_2O_3 and Y_2O_3, and

comparison with published data [20-22] allowed determination of the crystalline phase formed, although a shift in the Raman lines was detected. In addition, comparison of the emission of Er^{3+} in composites obtained at 980 °C and 1500 °C confirmed the suggestion of two different crystal phases. Although the Stark splitting of the energy levels caused by these crystallographic phases are not exactly as the produced by the pure oxides, similarities in the spectra such as the number position and extension of the emission bands, allowed their assignment to corresponding energy levels and therefore to relaxation transitions of Er^{3+}. Thus, the differences observed in these crystal lattices may be attributed to different local crystal fields experienced by Er^{3+}.

References

[1] J. Silver , M. I. Martinez-Rubio, T. G. Ireland, G. R. Fern, R. Withnall, *J. Phys. Chem. B*, **105**, 948 (2001).

[2] S. Shionoya, W. M. Yen, *Phosphors Handbook*, pp 193, CRC Press (1998).

[3] D. K. Rice, L. G. de Shazer, *J. Chem. Phys.*, **52**, 172, (1970).

[4] J. Dexpert-Ghys, M. Fraucher, P. Caro, *Phys. Rev. B,* **23**, 607, (1981).

[5] M. Buijs, A. Meyerkink, G. Blasse, *J. Lumin.* **37,** 9, (1987).

[6] Y. C. Kank, S.B. Park, I. W. Lenggaro, K. Okuyama, *J. Phys. Chem. Sol.,* **60,** 379, (1999).

[7] Y. L Soo, S. W. Huang, Y. H Kao, *Mod. Phys. Lett. B,* **15**, 205, (2001).

[8] Y. Zhou, J. Lin, S. Wang, *J. Solid State Chem.*, **171**, 391 (2003).

[9] M. L. Pang, J. Lin, J. Fu, R. B. Xin, C. X. Luo, Y. C. Han, *Opt. Mat.*, **23**, 547 (2003).

[10] H. Guo, Y. Li, D. Wang, W. Zhang, M. Yin, L. Lou, S. Xia, *J. Alloy Compd.*, **376**, 23 (2004).

[11] T. Hirai, T. Orikoshi, *J. Colloid. Interf. Sci.,* **269,** 103 (2004).

[12] W. G. Wyckoff., *Crystal Structures,* Interscience Publishers. Inc., New York (1965).

[13] A. F. Wells, *Structural Inorganic Chemistry*, 5th ed., Clarendon Press, Oxford (1984).

[14] H. T. Hintzen, H. M. van Nooer, *J. Phys. Chem. Solids*, **49,** 873 (1988).

[15] E. Husson, C. Proust, P. Gillet, J. P. Itie, *Mat. Res. Bull.*, **34**, 2085 (1999).

[16] M. Mitric, P. Onnerud, D. Rodic, R. Tellgren, A. Szytula, M. L. Napijalo, *J. Phys. Chem. Solids*, **54,** 967 (1993).

[17] P. A. Tanner, K. L. Wong, *J. Phys. Chem. B*, **108**, 136 (2004).

[18] D. Rodic, B. Antic, M. Mitric, *J. Magn. Magn. Mater.*, **140**, 1181 (1995).

[19] W. Rossner, H. Boddinger, J. Leppert, B. C. Grabmaier, *IEEE Trans. Nucl. Sci.*, **NS40**, 376 (1993).

[20] A. Garcia-Murillo, C. Le Luyer, C. Dujardin, C. Pedrini, J. Mugnier, *Opt. Mat.*, **16,** 39 (2001).

[21] H. Guo, W. Zhang, M. Yin, L. Lou, S. Xia, *J. Rare Earth*, **22,** 365 (2004).

[22] J. Zarembowitch, J. Gouteron, A. M. Lejus, *J. Raman Spectrosc.*, **9,** 263 (1980).

[23] G. Blasse, B. C. Grabmaier, *Luminescent materials*, pp 16, Springer-Verlag (1994).

[24] G. Wakefield, E. Holland, P.J. Dobson, J. L. Hutchison, *Adv. Mater.*, **13,** 1557 (2001).

[25] Y.C. Kang, H.S. Roh, B.S. Park, *Adv. Mater.*, **12**,451 (2000).

Chapter 6 Chemical Preparation and Characterisation of Rare-Earth Doped Yttrium Orthovanadate

Introduction

Yttrium vanadates have been known to be good hosts for phosphors since the 1960s[1] and have been also used for the luminescence study of rare earth ions[2].

This compound has been investigated by a large number of researchers[3] and different synthetic routes have been developed including sol-gel[4,5], combustion[6], and solution methods[7,8] starting from different precursors and with different experimental conditions, to obtain small (< 5μm) highly efficient phosphors. To solve problems arising from the amphoteric character of V_2O_5 resulting in the formation of mixtures of polyvanadates studies on phase composition[9], Y_2O_3 - V_2O_5 solid solutions[10] and effects of variables such as pH[11] have been carried out, as well as numerous luminescence and crystal characterisation studies. YVO_4:Eu has been widely studied as red emitter since first reports from Levine and Palilla[12], and more recently studies on wider range of rare-earth dopants have been published[13] as well as studies of Er-Yb co-doped materials[14,15,16,17].

Crystallographic studies on yttrium vanadate lattices were reported by Wyckoff in 1965[18]. YVO_4, known as Wakefieldite(Y) is the mineral representative of the rare earth vanadates. YVO_4 crystallizes in the D_{4h}^{19} structure of zircon, consisting of linked VO_4 and YO_4 tetrahedra. The symmetry is tetragonal and there are four formula units per unit cell, which has edge lengths:

$$a = 7.123\text{Å} \qquad c = 6.291\ \text{Å}$$

A perspective drawing of the unit cell is shown in Figure 6.1.

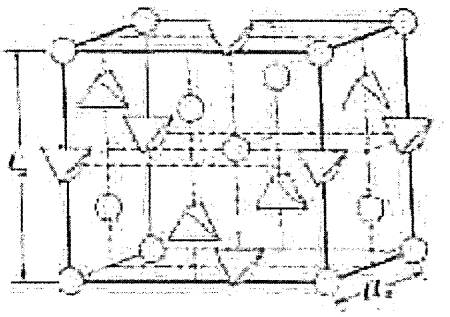

Figure 6.1 Perspective drawing of the tetragonal arrangement. Circles represent Y atoms. V atoms are at the centres of the small tetrahedra whose corners mark the position of the oxygen atoms.

YVO_4:Eu is used as a red phosphor for cathode ray tube applications[19], and as a colour corrector for high-pressure mercury vapour lamps[10]. It is also the oldest laser host lattice for Nd^{3+} lasers[1], and there is growing interest in its use as an Er^{3+} host[20] since a three level laser has been shown to work at room temperature.

In this work, two synthetic routes were used to obtain tetragonal YVO_4. A solution synthesis, based in the homogeneous urea precipitation method used to obtain the materials previously described in Chapters 4 and 5. The second synthetic method is a modification of combustion route described by Ekambaram and Patil[6] using an aqueous solution containing yttrium nitrate, and ammonium nitrate (oxidisers), ammonium metavanadate, and 3-methylpyrazole-5-one (3M5O) as fuel. The aim of this study is to assess the performance of these materials as phosphors and to test the theories suggested in Chapter 3 regarding energy transfer between co-dopants in the host lattice.

6.1 Results and discussion

6.1.1 Structural characterization of YVO_4

A typical powder XRD pattern of a precursor obtained from the precipitation method is shown in Figure 6.2. Three reflections can be distinguished, and despite being broad and weak, they can be assigned to the strongest diffraction peaks of yttrium orthovanadate (confirmed by fitting the data to the Joint of Committee Powder Diffraction Spectroscopy, data file number 17-0431). Their occurrence suggests incipient crystallization, with very small crystallite size.

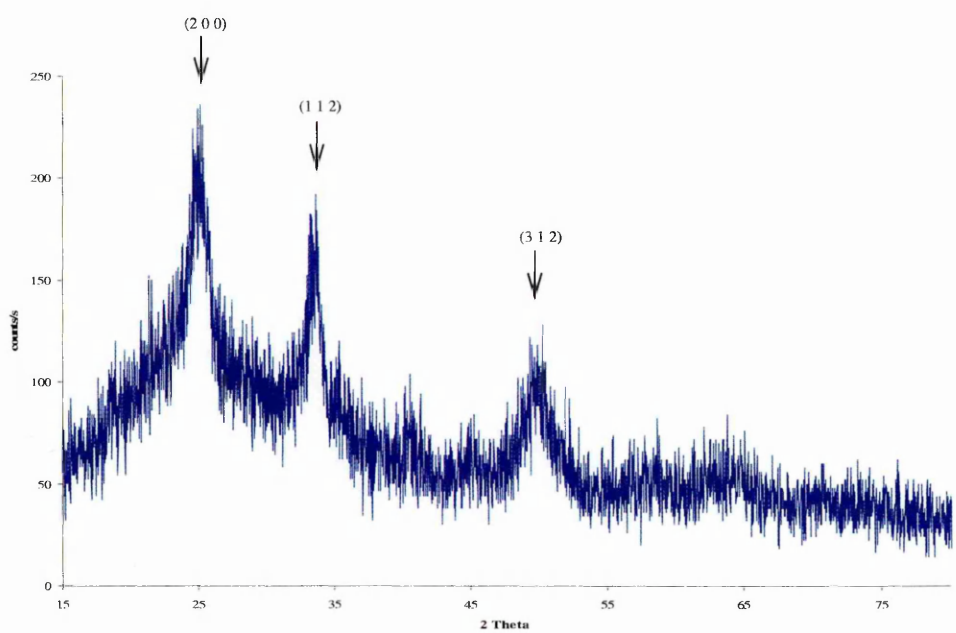

Figure 6.2 XRD pattern of the spherical phosphor precursor particles synthesised by the solution method.

Firing the precursor powders at 980°C produced a dark brown powder consistent with the formation of YVO_4 as gauged by XRD.

Following combustion synthesis, a white powder whose XRD pattern was also consistent with YVO_4 was obtained. However, two extra peaks at $2\theta = 20^0$, and 26^0 were detected in both cases, (Figures 6.3 and 6.4) consistent with the strongest reflections in the XRD pattern of V_2O_5 (confirmed by fitting the data to the Joint of Committee Powder Diffraction Spectroscopy, data file number 41-1426), and the formation of this oxide on the surface of the phosphors under these firing conditions is suggested.

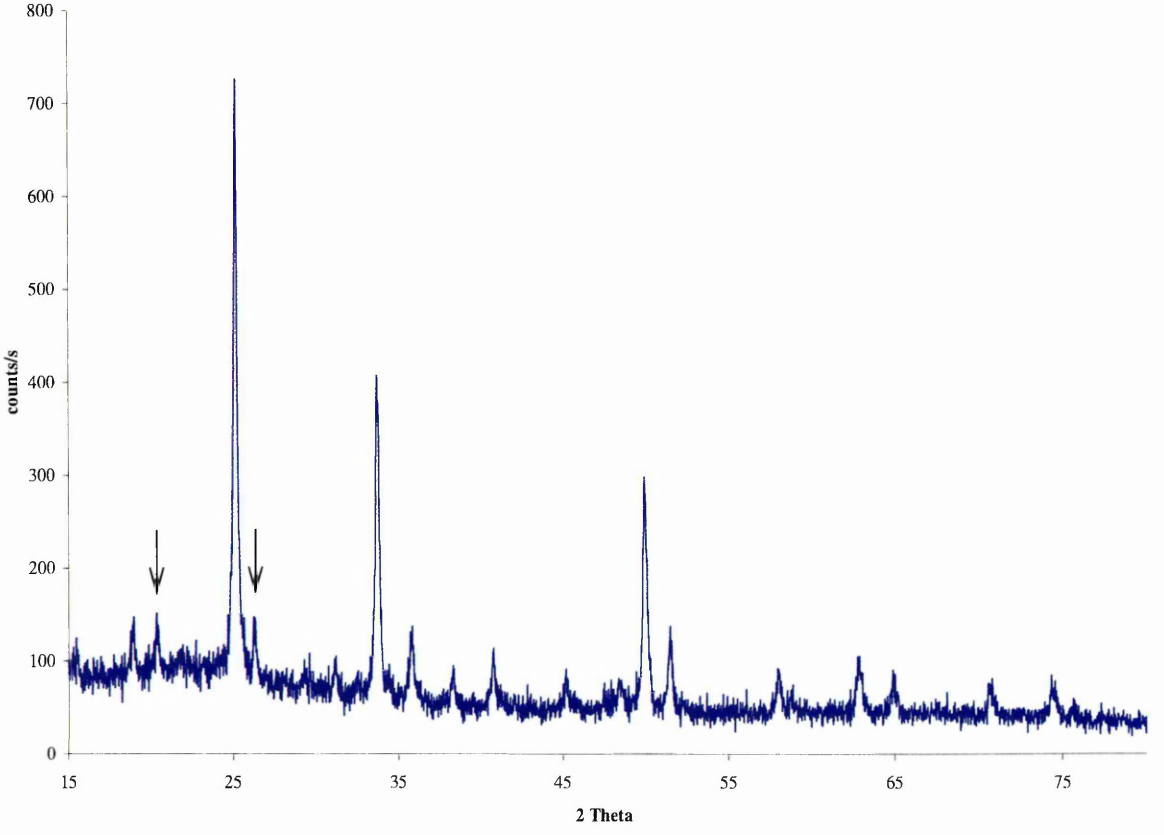

Figure 6.3 XRD pattern of the phosphor powder synthesised by the solution method and fired in air at 980 ^{0}C. Extra peaks found are marked with arrows.

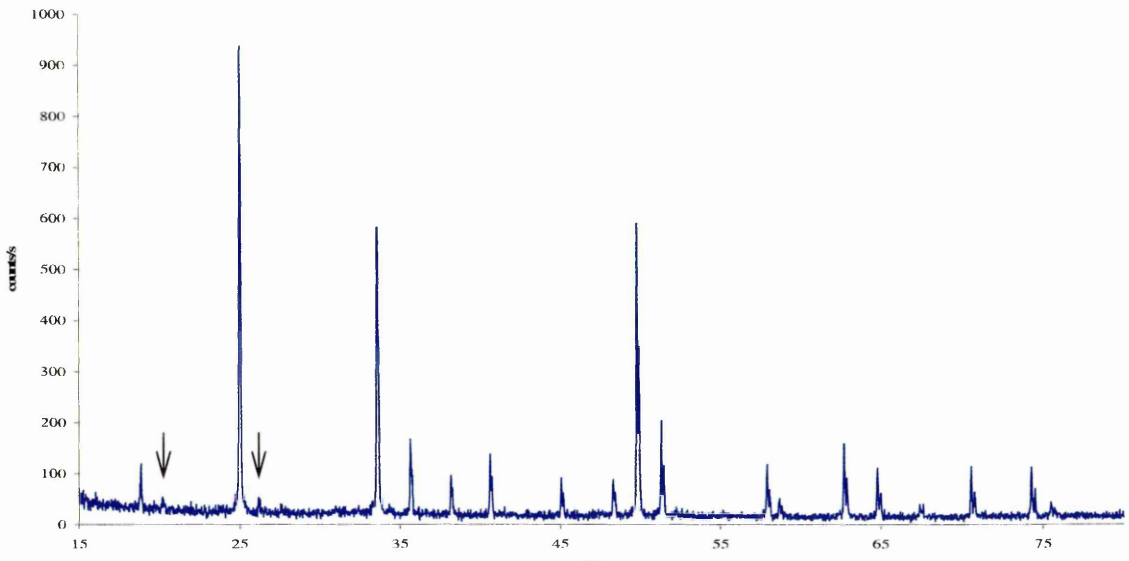

Figure 6.4 XRD pattern of the phosphor powder synthesised by the combustion method and fired in air at 980 ^{0}C. Extra peaks found are marked with arrows.

Clearly removal of the secondary oxide was imperative as V_2O_5 formation caused a brown colouration, an undesired characteristic that results in light absorption, and weakening of the signal of the phosphors. It was found that this oxide could be removed by washing in a 30 % NaOH solution, where V_2O_5 was dissolved as VO_4^{3-} ion.[9] XRD patterns obtained after washing confirm the removal of the undesired impurity (Figure 6.5).

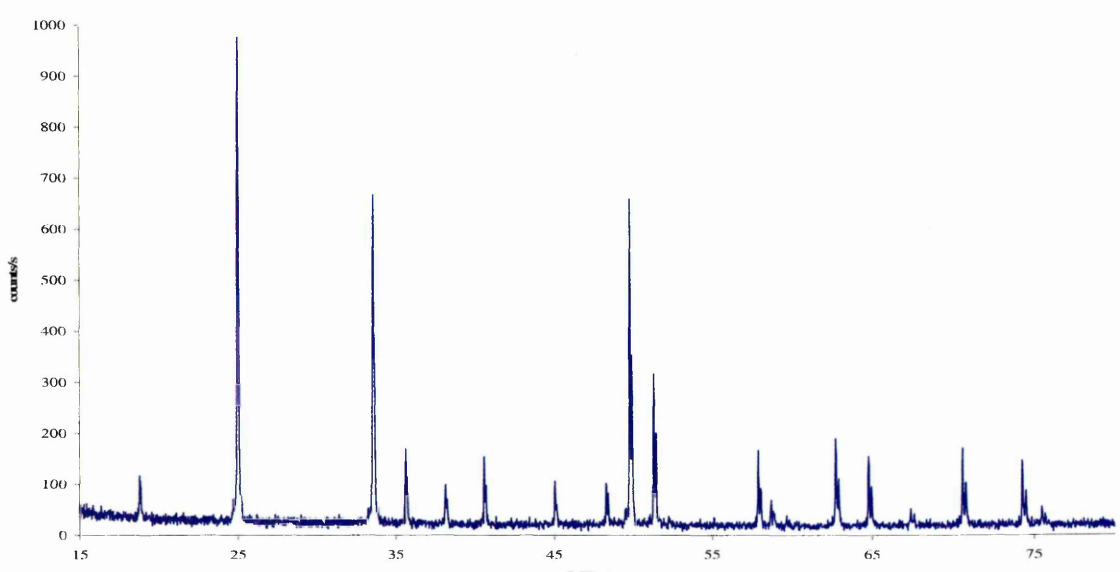

Figure 6.5 XRD pattern of the washed phosphor powder.

The precursor powders obtained from precipitation were fired at different temperatures to monitor the transformation into the crystalline phosphor. Firing at 200 and 400^{0}C did not change the structure of the precursor (Figure 6.6), but crystalline yttrium orthovanadate was formed on firing in air at temperatures of 600^{0}C or higher as can be seen in Figure 6.7. The values obtained from a refinement study of this structure using the *UnitCell* program are summarized in Table 6.1.

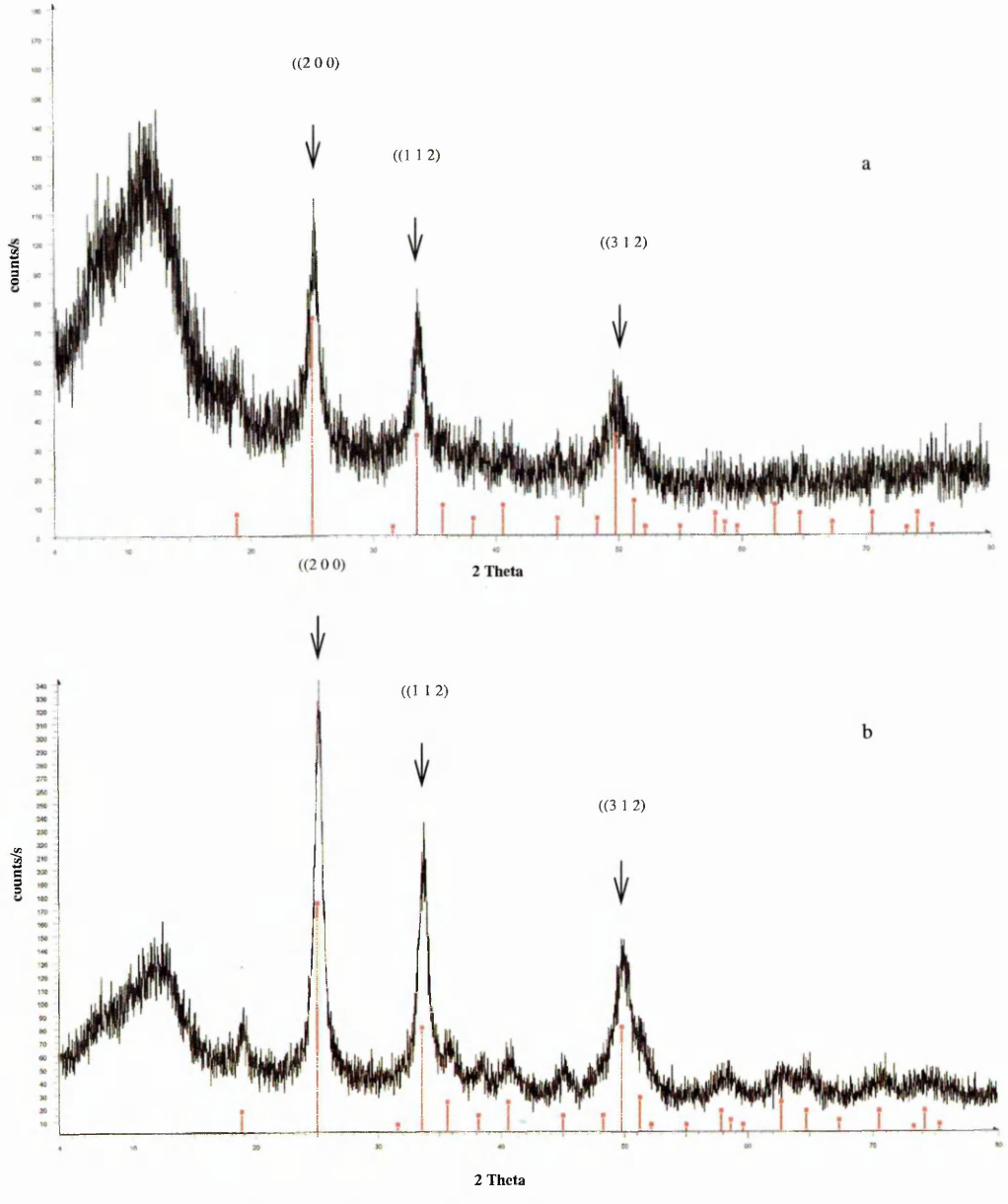

Figure 6.6 XRD pattern of the phosphor precursor particles synthesised by the solution method and fired in air at a) 200, and b) 400 ^{0}C

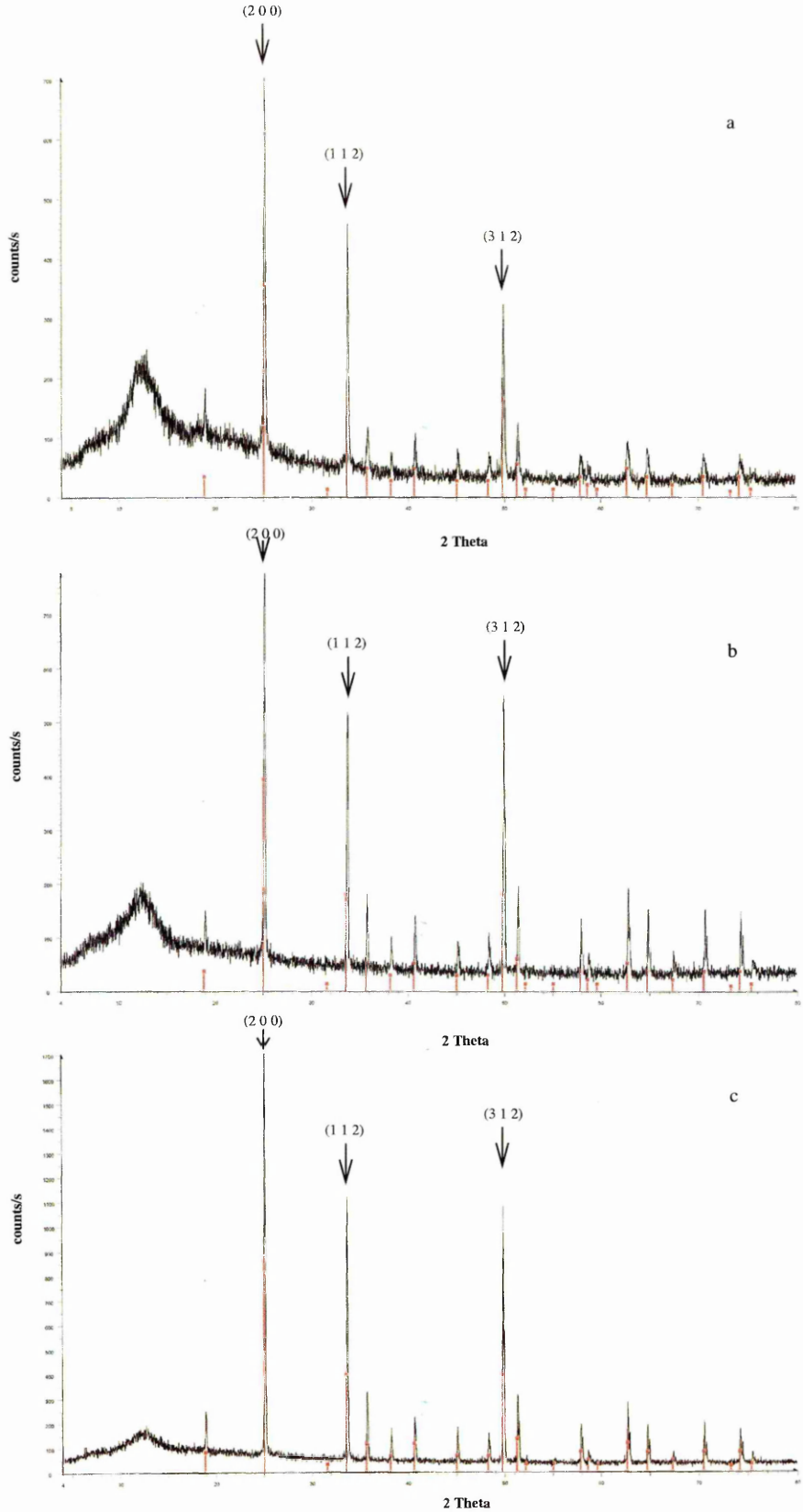

Figure 6.7 XRD pattern of the YVO_4 phosphor particles synthesised by the solution method fired in air at a) 600, b)800, and c) 980 ^{0}C.

Sample homogeneity (i.e. solid solution formation), of particular importance at substitutional levels up to 20 mol% used here, was also assessed in YVO_4:RE (where RE is a rare earth ion) powder phosphors synthesised by the solution route. For all compositions examined, no major structural changes in the X-ray diffraction pattern were detected. Patterns recorded were all consistent with the formation of the tetragonal polymorph. This strengthens the assumption that the rare earth atoms substitute at yttrium sites in the lattice when the doped phosphor powder is produced, forming substitutional solid solutions.

Table 6.1 Refined structure of YVO_4

***a*/ Å**	7.1020±0.0045
***c*/ Å**	6.2704±0.0060
cell volume/ Å^3	316.27

As lattice parameters of solid solutions often show small but detectable variations with composition, samples containing nominal concentrations of Yb^{3+} from 1 to 10 mol% in the YVO_4 host lattice were prepared in order to study the changes in the cell parameters when a foreign ion was introduced. It is believed that the size of the ions that randomly substitute ions of the lattice forming the solid solutions, governs the changes in the lattice parameters. In accordance with Vegard's law, a slight reduction in the a value when the Yb^{3+} concentration was increased was observed (Table 6.2). This is a consequence of the difference of the cationic radii. $r(Yb^{3+})$= 0.858Å and $r(Y^{3+})$= 0.892Å in six fold coordination.

Table 6.2 Variation on the cell parameters of $YVO_4:Yb^{3+}$ as a function of the concentration of the dopant ion.

	Doping level				
	1% Yb	**2% Yb**	**5% Yb**	**8% Yb**	**10% Yb**
***a*/ Å**	7.1141 ±0.0025	7.0995 ±0.0029	7.0994 ±0.0032	7.0971 ±0.0036	7.0848 ±0.0043
***c*/ Å**	6.2831 ±0.0033	6.2723 ±0.0037	6.2722 ±0.0042	6.2723 ±0.0047	6.2670 ±0.0065
cell volume/ Å^3	1170.619	1167.007	1164.196	1163.912	1159.908

In addition, structural information was obtained using Raman spectroscopy. Spectra of the pure polycrystalline YVO_4 host lattice were recorded (Figure 6.8) to be used as a standard for luminescence measurements. Cubic YVO_4 is predicted to have thirteen active Raman modes[1,21], being internal vibrations of the VO_4^{3-} tetrahedra, and external vibrations due to rotations and translations of the tetrahedra with respect to Y^{3+}. Miller *et al.*[1] reported eight and those detected are listed in Table 6.3. These spectra verify that the phosphor powders synthesised are yttrium orthovanadate, and moreover, facilitate normalization of the emission bands by reference to the Raman band at 891 cm^{-1}. A shift in this Raman band was found when using different dopants (Table 6.4). This is consistent with the increase in the mass of the dopant ion on moving across the lanthanide series and provides further evidence for substitutional solid solution formation.

Table 6.3 Assignment of Raman spectrum of tetragonal YVO_4 (cm^{-1}).

	Miller *et al*[1]	Experimental results
External modes		
	156 B_g	157
	162 E_g	164
	259 E_g	
Internal modes		
	260 B_g	261
	377 A_g	378
	487 B_g	489
	816 B_g	816
	838 E_g	838
	891 A_g	890

Table 6.4 Raman band shift (cm^{-1}).

YVO_4	YVO_4:Eu (20 mol%)	YVO_4:Er (20 mol%)	YVO_4:Yb (20 mol%)
891	879	888	890

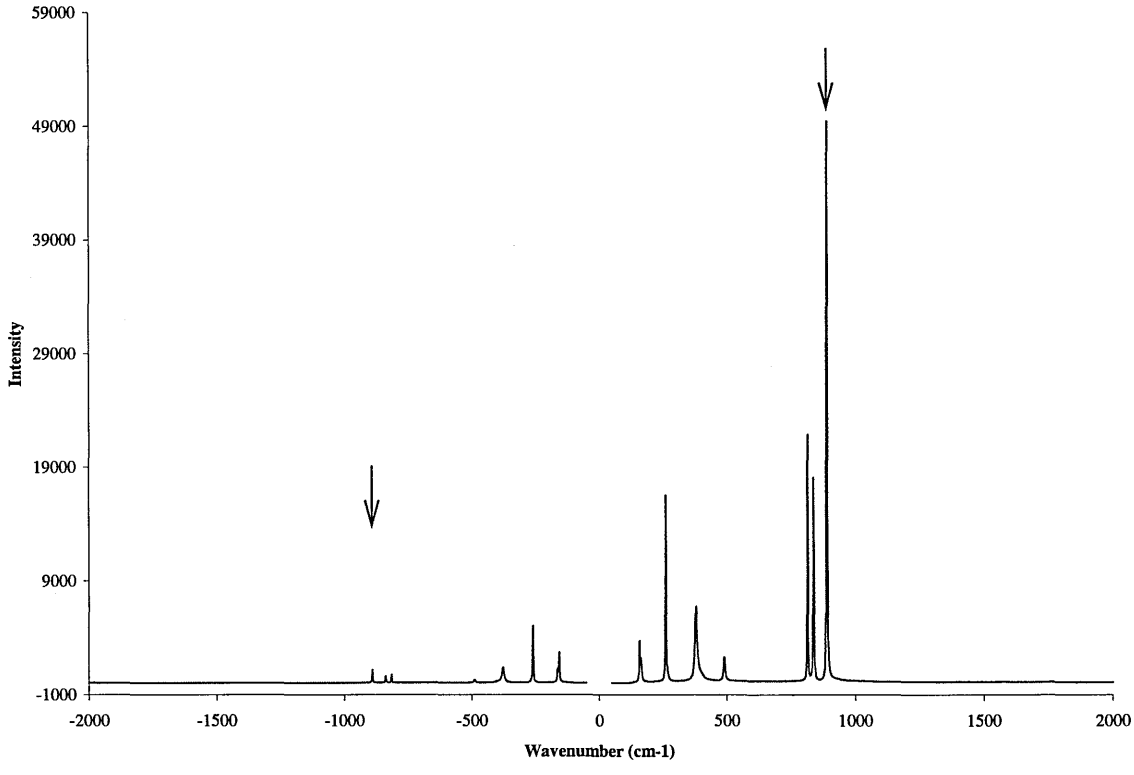

Figure 6.8 Anti-Stokes and Stokes Raman spectrum of YVO_4. The Raman band at 891 cm^{-1} is marked with arrows in both the Stokes and anti-Stokes regions.

6.1.2 The influence of the reaction conditions on the morphology of the YVO_4 phosphor powders

Studies carried out on the Y_2O_3 lattice[22] indicated a variation in precipitate morphology depending on the initial Y^{3+}: urea ratio. Variations in the initial reaction conditions were examined to assess their influence on the final morphology of the precipitate, as it is important to obtain precipitates regular in size, and as close as possible to spherical morphology to allow close packing in device applications.

Here, particles were synthesised from aqueous solutions of Y_2O_3, NH_4VO_3 and urea. Different $V^{5+}_{(aq)}$ to $Y^{3+}_{(aq)}$ ratios were examined as well as various urea

concentrations. It was found that the order in which the reagents were added was also important. For example, NH_4VO_3 was found to be only partially soluble when added to a colourless acidic solution containing Y_2O_3 and ammonium EDTA. Moreover, different vanadate species exist in solution[11] depending on the concentration and pH. A complicated series of hydrolysis-polymerisation reactions occur and the determination of the equilibria, stoichiometries and structures is still in dispute since equilibrium is only reached slowly (in months in some cases). It is anticipated that the stoichiometry of solid products is related to the nature of the precursor species in solution. In solution the following protonation and condensation equilibria occurs:

In aqueous alkaline solution

$$[VO_4]^{3-} + H^+ \rightleftharpoons [HVO_4]^{2-}$$

$$2\,[HVO_4]^{2-} \rightleftharpoons [VO_7]^{4-} + H_2O$$

$$[HVO_4]^{2-} + H^+ \rightleftharpoons [H_2VO_4]^-$$

$$3\,[H_2VO_4]^- \rightleftharpoons [V_3O_9]^{3-} + 3\,H_2O$$

$$4\,[H_2VO_4]^- \rightleftharpoons [V_4O_{12}]^{4-} + 4\,H_2O$$

In aqueous acid solution

$$10\,[V_3O_9]^{3-} + 15\,H^+ \rightleftharpoons 3\,[HV_{10}O_{28}]^{5-} + 6\,H_2O$$

$$[H_2VO_4]^- + H^+ \rightleftharpoons H_3VO_4^-$$

$$[HV_{10}O_{28}]^{5-} + H^+ \rightleftharpoons [H_2V_{10}O_{28}]^{4-}$$

$$H_3VO_4 + H^+ \rightleftharpoons VO_2^+ + 2\,H_2O$$

$$[H_2V_{10}O_{28}]^{4-} + 14H^+ \rightleftharpoons 10\,VO_2^+ + 8\,H_2O$$

Changes in the solution colour were observed in this work prior to the formation of the precipitate, probably due to the hydration of brown V_2O_5 precipitates that redissolve at low pHs to produce pale yellow solutions.

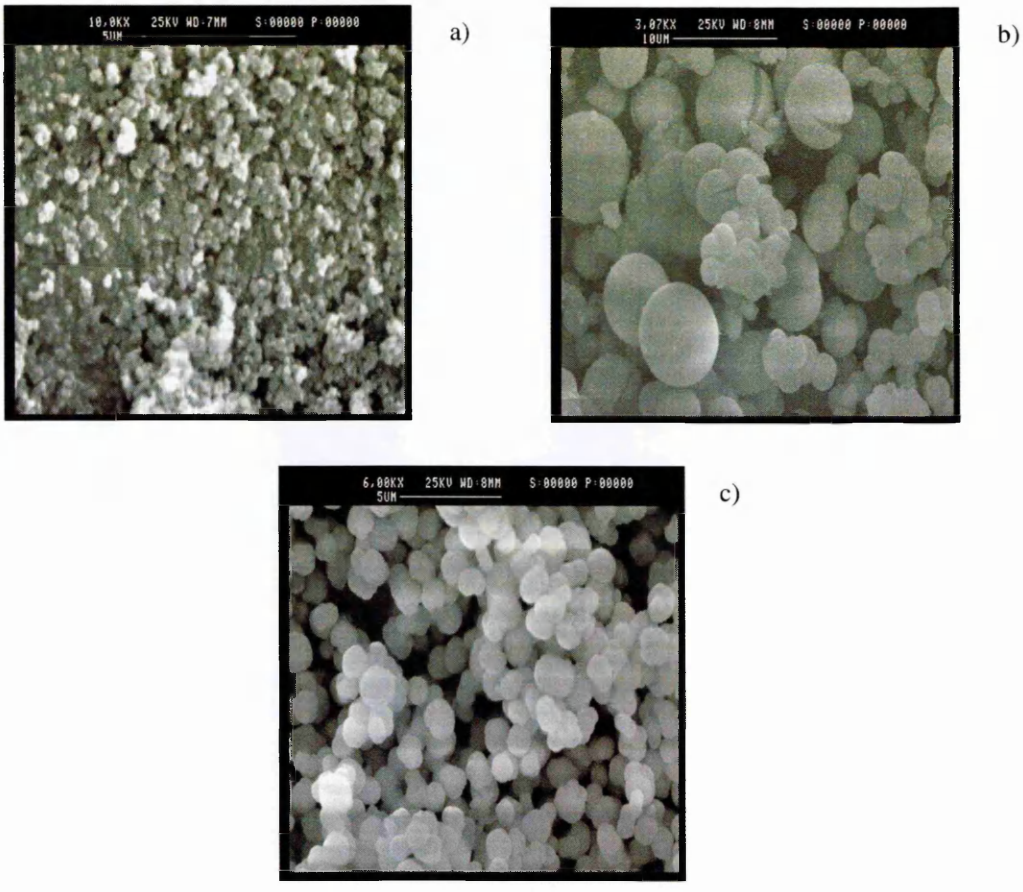

Figure 6.9 SEM micrographs of the precipitate obtained from the solutions of concentrations a) $[Y^{3+}]$ 1.68×10^{-2}M, $[V^{5+}]$ 2.19×10^{-2}M, [urea] 1.6M b) $[Y^{3+}]$ 1.68×10^{-2}M, $[V^{5+}]$ 2.19×10^{-2}M, [urea] 0.9M c) $[Y^{3+}]$ 2.5×10^{-3}M, $[V^{5+}]$ 3.38×10^{-3}M, [urea] 0.5M.

The microstructure of the precipitates was gauged using SEM, and Figure 6.9 illustrates different morphologies of the precursor particles obtained from a range of initial reagent concentrations and ratios. It was noted that spherical particles were obtained for samples containing excess $Y^{3+}_{(aq)}$ and urea concentration 1M, but the particle size was irregular. The variation in particle size of materials obtained from the same batch suggests

that not all the precipitation nuclei are formed at the beginning of the reaction, increasing the number of nucleation seeds during the precipitation process. Further tests to improve regularity as well as reducing particle size of the precursors were carried out changing $[V^{5+}]_{(aq)}$ to $[Y^{3+}]_{(aq)}$ ratios (1:1.35, 1:1.50, 1:1.52, 1:1.53 and 1:1.60) and concentration of urea in the initial solution (0.5, 0.6, 0.9, and 1.5 M). It was found that the optimum size and morphology was obtained from diluted initial solutions containing a $[V^{5+}]_{(aq)}$ to $[Y^{3+}]_{(aq)}$ ratio of 1:1.35 and initial urea concentration 0.5 M as can be observed in Figure 6.9 c).

The spherical shape was not retained even for samples fired at temperatures as low as 600°C, and sintering of the particles during firing was observed. The particle size of materials obtained from dilute $[Y^{3+}]_{(aq)}$ solutions was found to be over 25 μm in size after firing at 980°C, when the desired particle size was $\leq 5\mu$m.

Hence, from this initial empirical study, it was apparent that the optimum initial reagent concentration was $[Y^{3+}]$ 1.68×10^{-2} M, $[V^{5+}]$ 2.19×10^{-2} M, [urea] 1.6 M based upon the small particle size and morphology of the fired phosphor powder obtained. The microstructure of different phosphor powders on firing at 980°C in air for 1 hour is shown in Figure 6.10.

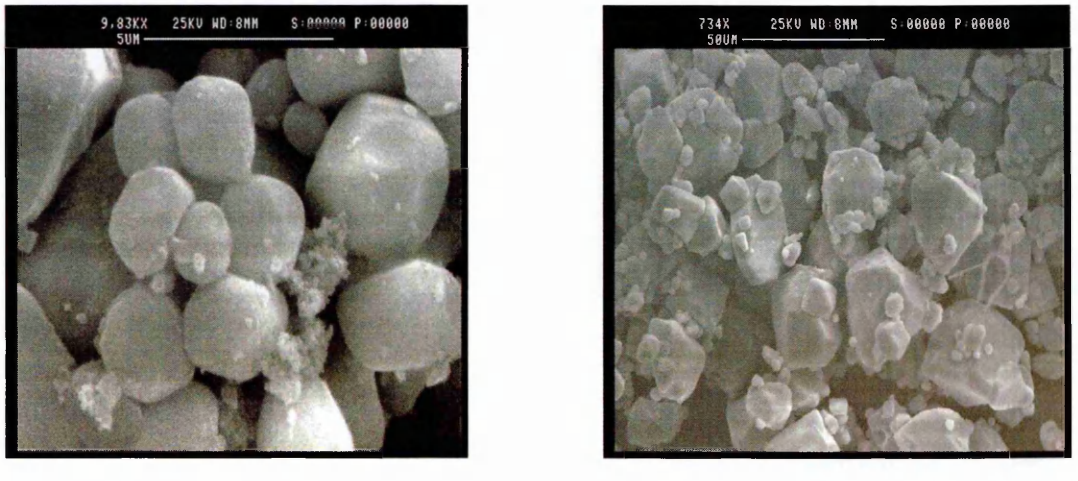

a) b)

Figure 6.10 SEM micrographs of the fired phosphor powders obtained from the solutions of concentrations a) $[Y^{3+}]=1.68\times10^{-2}$ M, $[V^{5+}]=2.19\times10^{-2}$ M, [urea]=1.6 M and b) $[Y^{3+}]=2.5\times10^{-3}$ M, $[V^{5+}]=3.38\times10^{-3}$ M, [urea]=0.5 M.

The white powder obtained from the combustion synthetic route was also examined by SEM. Figure 6.11 shows typical micrographs of the materials obtained. This method produced powders of 5-8 μm in size, but materials were porous and the particle morphology could not be controlled. These are undesired characteristics as phosphor powders should be dense solids to maximize emission intensity and adopt a close packed array. Further investigation is needed on characteristics of the materials obtained by this method, to determine if they show intense luminescence under the excitation conditions.

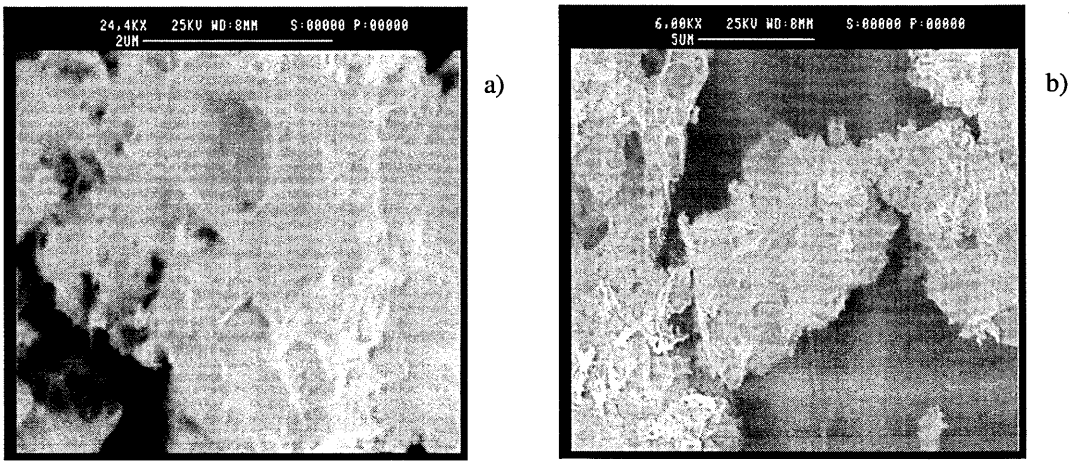

Figure 6.11 SEM micrographs of the fired phosphor powders obtained from the combustion method: a) 2 μm and b) 5 μm scale.

In summary, the urea precipitation method and combustion route have been shown to be suitable for the preparation of powder YVO_4:RE phosphors. Control over particle size and morphology by judicious manipulation of processing parameters was achieved using the homogeneous precipitation method, but morphological control was not possible when the combustion route was followed. Other factors such as urea initial concentration and $V^{5+}_{(aq)}$:$Y^{3+}_{(aq)}$ ratio were found to affect the morphology of the phosphor precursor whereas the addition of complexing agents such as ammonium EDTA can help to achieve small particle size. Being able to control the sphericity of the precipitates and fired materials is of great importance in order to produce close packed aggregates and improve the resolution of device applications where they might be used.

6.1.3. Luminescence properties of YVO_4:RE phosphors

Pure and erbium doped YVO_4 samples were analysed using Raman and laser-induced luminescence spectroscopy. The effect of the addition of Yb^{3+} and Eu^{3+} as co-dopants was also assessed to complement the studies reported in Chapters 4 and 5.
Because the wavelengths of neon emission lines are stable and well established, these were used as standard for calibration of the detector. The experimental results and the reference values are compared in Table 4.7 and a typical neon calibration spectrum is shown in Figure 4.10 in Chapter 4.

YVO_4:Er phosphors

Stokes and anti-Stokes emission were studied for the Er^{3+} luminescent centre using the same instrumental parameters used to study Y_2O_3:RE and Gd_2O_3:RE phosphor powders described in Chapter 4 and Chapter 5, in order to allow comparison between the results. Therefore the confocal pinhole selected to carry out luminescent measurements was 400nm.
Laser-induced spectroscopy under 632.8 nm wavelength excitation using a helium-neon laser source has been used to study the up-converting and down-converting properties of YVO_4:Er^{3+} powder phosphors. A single Raman band typical of the YVO_4 lattice is seen in both spectra at a wavenumber shift of 891 cm^{-1} and has been used to normalize the signal.

The anti-Stokes emission spectrum of YVO_4:Er^{3+} (2 mol%) synthesised by the homogeneous precipitation method, in the range 420-630 nm at room temperature is shown in Figure 6.12, and the Stokes emission spectrum of the same sample in the range from 634 to 895 nm is shown in Figure 6.13. Over the entire wavelength range, five emission manifolds corresponding to electronic transitions in the Er^{3+} ion from different excited

states were detected (summarised in Table 6.5), compared with the eight detected for Y_2O_3. No emission from the level $^4F_{7/2} \rightarrow {}^4I_{15/2}$ or the bands thought to be associated to this level (a and b) was detected and the emission arising from the levels $^4I_{9/2}$, $^4I_{11/2} \rightarrow {}^4I_{15/2}$ was stronger with respect to the intensity of the same bands in the cubic lattice.

Table 6.5 Assignments of Stokes and anti-Stokes emission bands of $YVO_4:Er^{3+}$ compared with those observed from $Y_2O_3:Er^{3+}$.

	emission range			
	YVO_4		**Y_2O_3**	
emission assignment	**nm**	**cm^{-1}**	**nm**	**cm^{-1}**
$^4F_{7/2} \rightarrow {}^4I_{15/2}$	-	-	468-479	21367-20876
$^2H_{11/2} \rightarrow {}^4I_{15/2}$	520-533	19230-18761	518-540	19307-18518
$^4S_{3/2} \rightarrow {}^4I_{15/2}$	544-559	18382-17667	546-566	18315-17667
(a)	-	-	610-632	16393-15823
$^4F_{9/2} \rightarrow {}^4I_{15/2}$	647-684	15455-14619	648-685	15432-14598
(b)	-	-	754-772	13623-12593
$^4I_{9/2} \rightarrow {}^4I_{15/2}$	785-830	12738-12048	785-830	12738-12048
$^4I_{11/2} \rightarrow {}^4I_{15/2}$	846-858	11820-11655	845-882	11834-11337

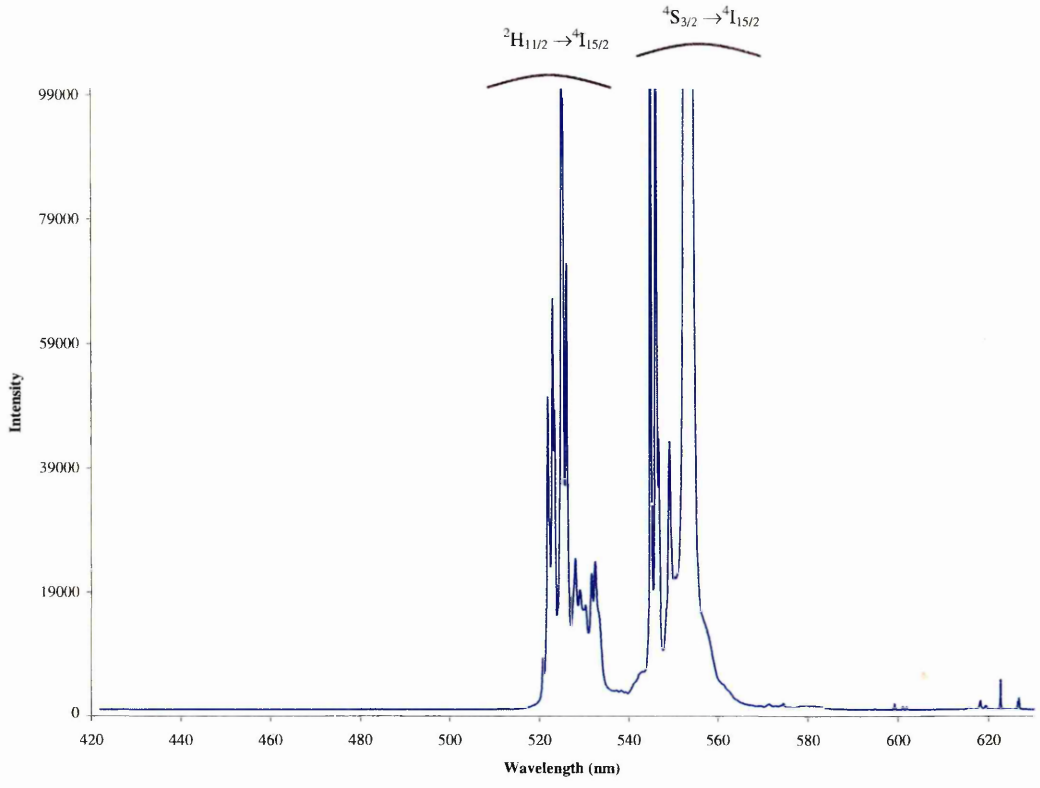

Figure 6.12 Anti-Stokes emission spectrum of $YVO_4:Er^{3+}$ (2 mol%) at room temperature in the region of 420-630 nm. Relative intensities are in arbitrary units.

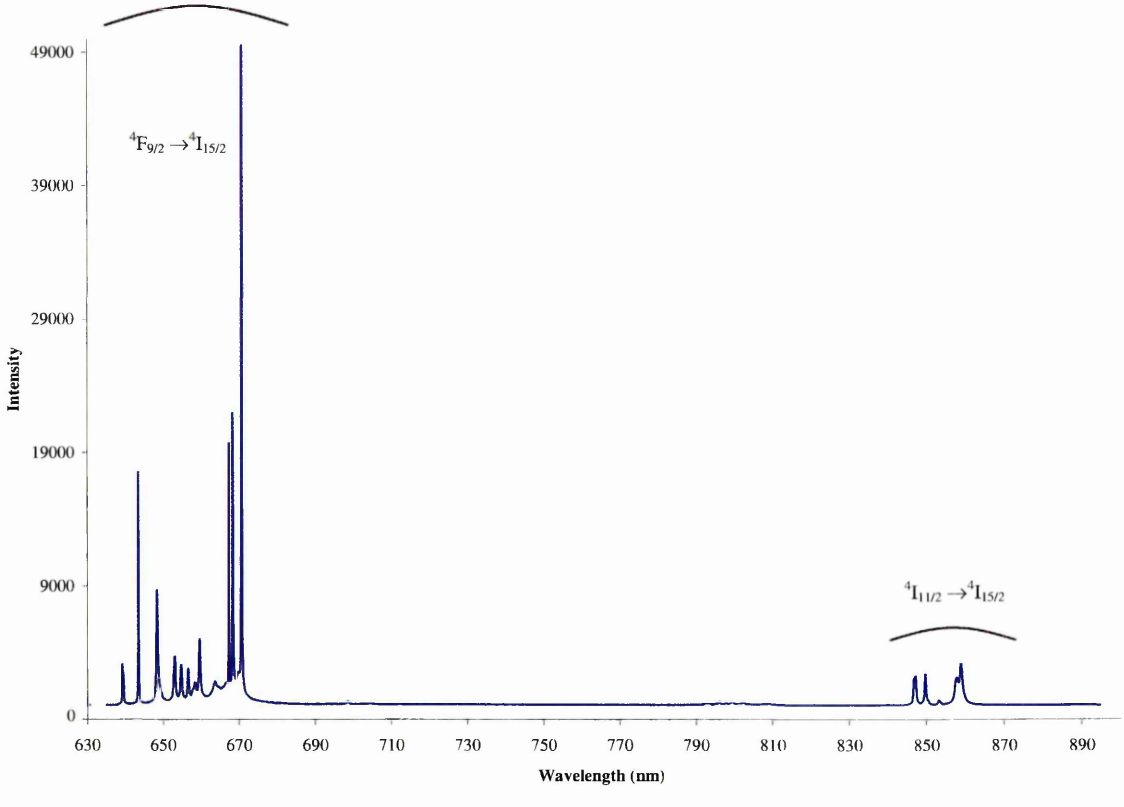

Figure 6.13 Stokes emission spectrum of $YVO_4:Er^{3+}$ (2 mol%) at room temperature in the region of 630-900 nm. Relative intensities are in arbitrary units.

As can be observed in Figure 6.12 and Figure 6.13, the emission bands of the activator are formed by series of multiple peaks, each one arising from the relaxation processes from the Stark components of an excited electronic state. The nature of these Stark components is dependent on the local crystal field[23]. Recent studies on Eu^{3+} doped in various oxide and oxosalt lattices[24] indicate that the position and shape of the emission lines is very sensitive to small differences in the crystal field, even when its effect is inherently small for the low-lying levels of rare earth ions. Moreover, studying the emission spectra of Er^{3+} in the tetragonal lattice, a remarkable change in the Stokes : anti-Stokes emission ratio was found. While anti-Stokes emission was strong and well defined, Stokes signals were in comparison very weak. This phenomenon indicates that the two photon process is favored in this lattice. This factor is of particular importance in the control of the luminescence properties of the activator, and illustrated how tuning of the emission of the phosphor may be facilitated by choosing the appropriate lattice.

YVO_4 powder phosphor samples doped with nominal concentrations of 1, 2 and 5 mol% Er^{3+} were prepared to study the effect of the concentration of the dopant ion on the luminescent properties. The luminescence spectra were normalized and the signals integrated.

The intensity of emission bands in the spectra showed a steady increase in intensity for all of the bands in the Stokes and anti-Stokes regions (Figure 6.14), as opposed to the behaviour of Er^{3+} doped in Y_2O_3 lattices, where signals reached a maximum when the activator concentration was 3 mol%, followed by intensity decrease in both up-conversion and down-conversion for higher activator concentrations. This effect shows that phonon assisted deactivation processes together with resonant energy transfer between activator ions are less effective in YVO_4 lattices. The relaxation mechanisms are not as affected by the closeness of activator ions in the lattice than previously studied yttrium oxide

phosphors, and therefore concentration quenching effects take place at greater concentration of Er^{3+}.

Spectra of the samples synthesised by the combustion method were also studied, the intensity of the bands were integrated and compared with those obtained from phosphors synthesised by the urea precipitation method. The same emission bands were found in both spectra but with different intensities. Emissions from phosphors obtained by the combustion route were found to be weaker, which can be attributed to the porous structure of the phosphor particles. Therefore further studies using co-dopants were only carried out on phosphors synthesised by the urea precipitation method described in Chapter 3.

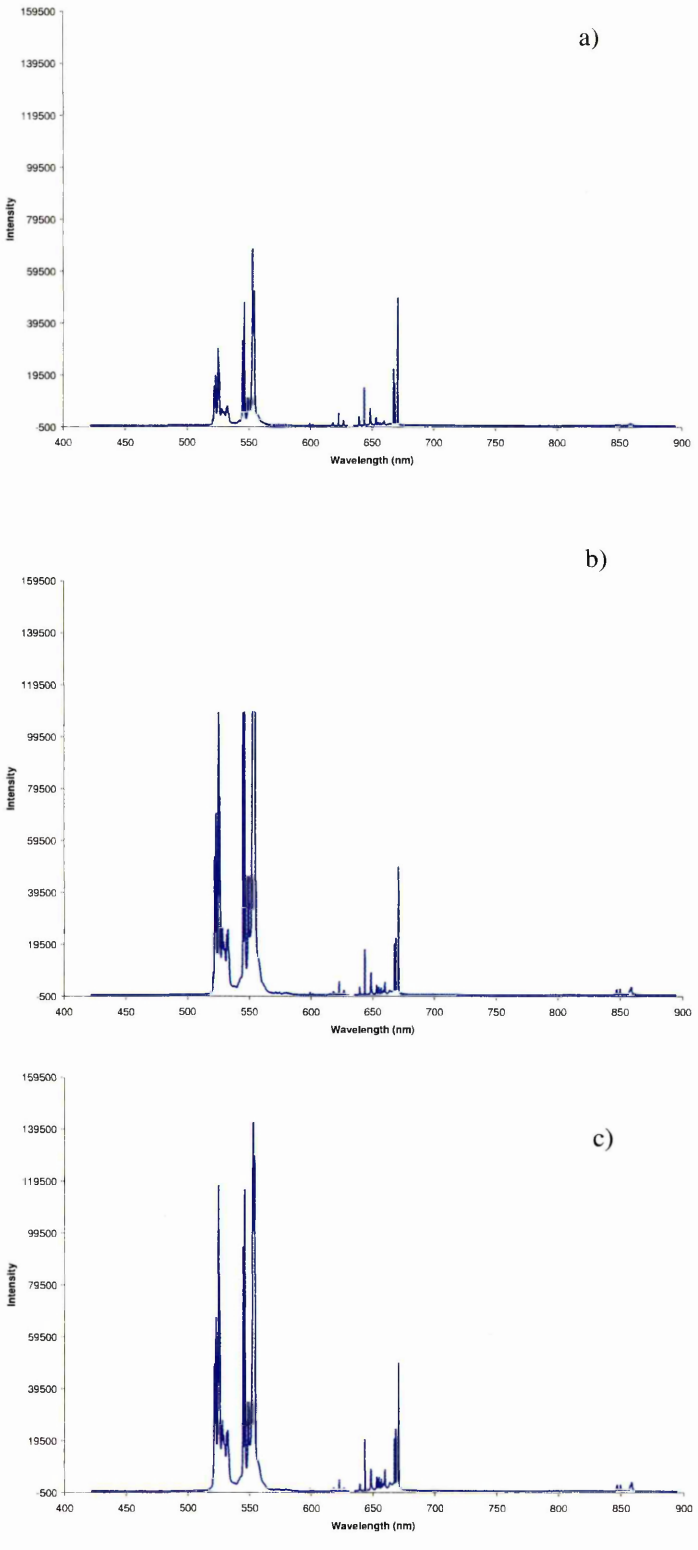

Figure 6.14 Evolution of the anti-Stokes and Stokes emissions intensity ratio at room temperature as a function of Er^{3+} concentration in the region 400–900 nm a) YVO_4:Er (1 mol%), b) YVO_4:Er (2 mol%), and c) YVO_4:Er 5 mol%. Relative intensities are in arbitrary units

YVO_4:Er,Yb phosphors

In order to determine the influence of adding a second substitutional lanthanide ion to the system, studies with co-doped samples containing Er^{3+}-Yb^{3+} have been carried out. Work carried out in the early 70's[24] and based on models published by Miyakawa and Dexter[23] discussed energy transfer processes between Er and Yb ions associated with the emission or absorption of phonons.

It is well established that Yb^{3+} ions can be used to sensitize Er^{3+} and enhance its up-conversion properties[23], and the materials containing these two cations have been studied under various wavelength excitation sources with evidence of energy transfer between the two ions[14-17]. However, it appears that no evidence of the emissions arising from $^2H_{11/2} \rightarrow {}^4I_{15/2}$ or $^4S_{3/2} \rightarrow {}^4I_{15/2}$ transitions were reported. The energy transfer mechanism involving the levels $^2F_{5/2}$ from Yb^{3+} and $^4I_{11/2}$ from Er^{3+} has been commonly accepted as the most suitable for the process, but this process has not been studied where the excitation source energy does not correspond to the energy increment between $^2F_{7/2} \rightarrow {}^2F_{5/2}$ (Yb^{3+}).

In the present study luminescence spectroscopy (λ_{exc}=632.8 nm) was used to investigate the effect of the Yb^{3+} concentration on both the up-converting and down-converting properties of Er and Yb co-doped yttrium vanadate materials: $Y_{1.96}Er_{0.02}Yb_{0.02}VO_4$, $Y_{1.94}Er_{0.02}Yb_{0.04}VO_4$, $Y_{1.88}Er_{0.02}Yb_{0.10}VO_4$, $Y_{1.78}Er_{0.02}Yb_{0.20}VO_4$ and $Y_{1.58}Er_{0.02}Yb_{0.40}VO_4$. YVO_4:Er (1 mol%) material was used as a reference.

The emission spectra of all materials were integrated and the intensity of each transition evaluated. Figure 6.15 summarises the relative emission intensities for YVO_4:Er^{3+},Yb^{3+} phosphor samples containing a fixed 1 mol% Er and a variable nominal concentration of Yb^{3+} in the lattice compared with the emission intensities observed for the YVO_4:Er^{3+} 1 mol% control sample. A variation in the intensity of the emissions arising

from different excited states compared to those from the control sample is observed as the concentration of Yb^{3+} changed. The most notable was an approximately 3-fold increase in the blue-green signal due to the $^2H_{11/2} \rightarrow {}^4I_{15/2}$ transition when Yb^{3+} concentration was 5 mol%.

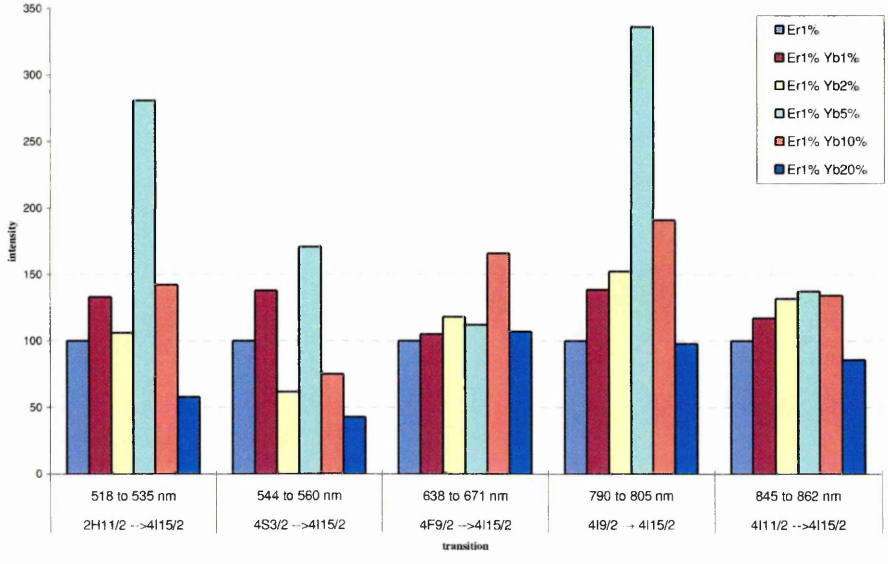

Figure 6.15 Evolution of the anti-Stokes and Stokes emissions intensity ratio as a function of Yb^{3+} concentration.

It should be noted that Yb^{3+} activates the emission of YVO_4:Er phosphors, this is most apparent at concentrations of 5 mol% (Figure 6.16) where all transitions are enhanced due to more efficient energy absorption. Interestingly the increase of Yb concentration in the lattice produced a steady increase of emission intensity for almost all the electronic transitions detected. Deactivation was only detected for really high concentrations of the activator (20 mol%). In the absence of Yb, energy is lost by Er - Er resonant energy transfer dissipating some of the radiation. When Yb^{3+} is present in the lattice, Er^{3+} - Er^{3+} quenching ceases as there is now an Er^{3+} - Yb^{3+} interaction where the energy loss by energy transfer is smaller. Then, only as the Yb^{3+} concentration increases over 10 mol%

loss of emission intensity is detected. Moreover, when the intensity of the emission bands arising from transitions from level $^2H_{11/2}$ to the ground state are studied, it was found that these bands are stronger in YVO_4 than in Y_2O_3 or Gd_2O_3crystal lattices. It is suggested that this intensity enhancement is produced by a non radiative decay from the $^4F_{7/2}$ level, from which emissions due to the $^4F_{7/2} \rightarrow {}^4I_{15/2}$ are not detected in YVO_4:Er phosphors.

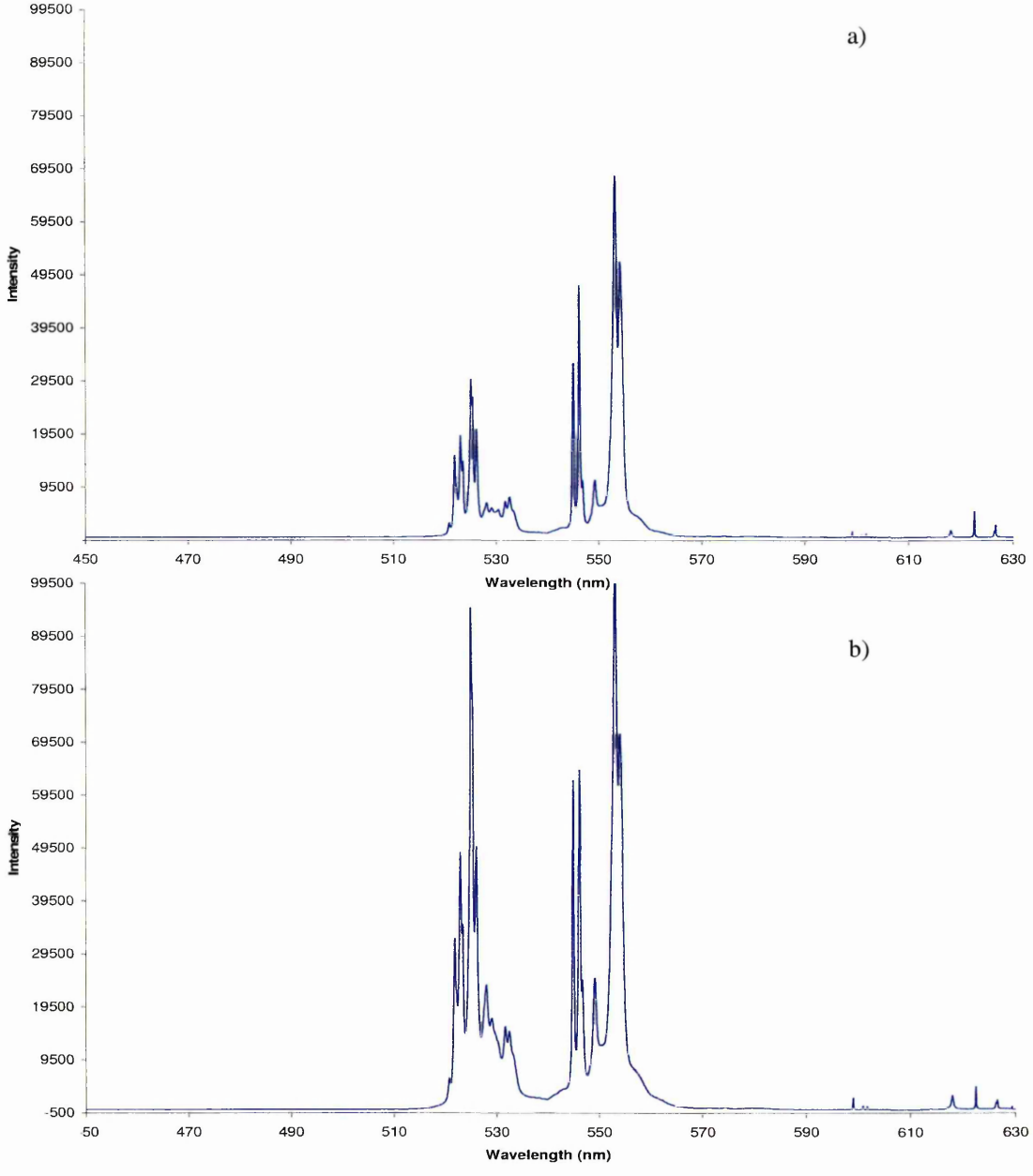

Figure 6.16 Anti-Stokes emission spectrum of a) YVO_4:Er (1 mol%) and b) YVO_4:Er, Yb (1, 5 mol%) at room temperature in the region of 450-630 nm. Relative intensities are in arbitrary units.

These variations in emission intensity with Yb concentration can be explained by reference to the energy transfer mechanism postulated in Chapter 4 for Y_2O_3:Er, Yb phosphors (Figure 4.22). The only difference will be the non radiative decay from the excited level $^4F_{7/2}$ after receiving the energy back transfer from lower levels, and hence enhancing emissions originated in $^2H_{11/2}$ and $^4S_{3/2}$ levels. Since the energy differences between the Er^{3+} and Yb^{3+} levels involved in the process are not equivalent, the energy transfer may be associated with phonon emission.

In this study, the Er^{3+} to Yb^{3+} interaction has been assessed. This interaction has been detected and the energy loss is weaker than energy loss due to Er^{3+} to Er^{3+} interactions. Enhancement of luminescent emissions has been reported for almost every transition when sensitizer concentration was lower than 10 mol%, although the most pronounced results were obtained for phosphors synthesised at a nominal 5 mol% concentration. A novel energy transfer mechanism has been proposed explaining the changes observed in the Er^{3+} spectra.

Bands arising from the $^4F_{5/2}$ levels and the unassigned levels a and b for Y_2O_3:Er phosphors were not detected in any of the emission spectra, reinforcing the idea that the three bands arise from associated energy levels.

YVO4:Eu phosphors

YVO_4:Eu samples were prepared to be used as controls in the study of the YVO_4:Er^{3+}, Eu^{3+} phosphor samples.

A single Raman band typical of the YVO_4 lattice is seen in Stokes and anti-Stokes spectral regions at a wavenumber shift of 891cm^{-1} and was used to normalize the signal.

YVO_4:Eu samples were prepared containing different nominal concentration of Eu (1, 2 and 5 mol%). The emission spectra of all materials were integrated and the intensity of each transition evaluated.

The anti-Stokes emission spectrum of Y_2O_3:Eu(5 mol%) in the range 420-630 nm at room temperature is shown in Figure 6.17, and Figure 6.18 shows the same range for the YVO_4:Eu phosphor. Over the entire wavelength range, ten emission manifolds were detected arising from excited state levels $^5D_0$, $^5D_1$, $^5D_2$ and $^5D_3$ on Y_2O_3:Eu, whereas only six were detected from YVO_4:Eu. Previous studies[2,25] on these powder phosphors helped to assign the main emission bands to the transitions summarized in Table 6.6. The emission band due to the $^5D_0 \rightarrow {}^7F_0$ transition was only detected for samples containing 2 mol% nominal activator concentration, and bands due to transitions $^5D_2 \rightarrow {}^7F_J$, $^5D_3 \rightarrow {}^7F_J$ and $^5D_0 \rightarrow {}^7F_3$ could only be detected (although too weak to allow further study) when the activator concentration was 5 mol%. Moreover, when the spectra were studied as a function of activator concentration it was found that emissions from transitions assigned to $^5D_1 \rightarrow {}^7F_0$ and $^5D_1 \rightarrow {}^7F_2$ showed an intensity maximum for 2 mol% activator concentration, weakening for further activator concentration increases. Whereas the intensity on emission bands corresponding to $^5D_1 \rightarrow {}^7F_1$, $^5D_1 \rightarrow {}^7F_1$, $^5D_0 \rightarrow {}^7F_2$ and $^5D_0 \rightarrow {}^7F_4$ transitions steadily increased with activator concentration increase.

Table 6.6 Assignments of Stokes and anti-Stokes emission bands of $YVO_4:Eu^{3+}$.

	emission range			
	YVO_4		Y_2O_3	
emission assignment	**nm**	**cm^{-1}**	**nm**	**cm^{-1}**
$^5D_2 \rightarrow {}^7F_J$ $^5D_3 \rightarrow {}^7F_J$	465-520	-	465-520	21510-19218
$^5D_1 \rightarrow {}^7F_0$	520-528	19230-18939	525-527	19029-18951
$^5D_1 \rightarrow {}^7F_1$	535-540	18692-18519	532-538	18772-18584
$^5D_1 \rightarrow {}^7F_2$	544-566	18382-17668	546-554	18313-18039
$^5D_0 \rightarrow {}^7F_0$	580	-	580	17233
$^5D_0 \rightarrow {}^7F_1$	584-596	17123-16779	582-593	17179-17864
$^5D_0 \rightarrow {}^7F_2$	608-622	16447-16077	611-631	16365-15845
$^5D_0 \rightarrow {}^7F_3$	650-657	-	650-663	15375-15070
$^5D_0 \rightarrow {}^7F_4$	696-706	14368-14164	683-712	14634-14035

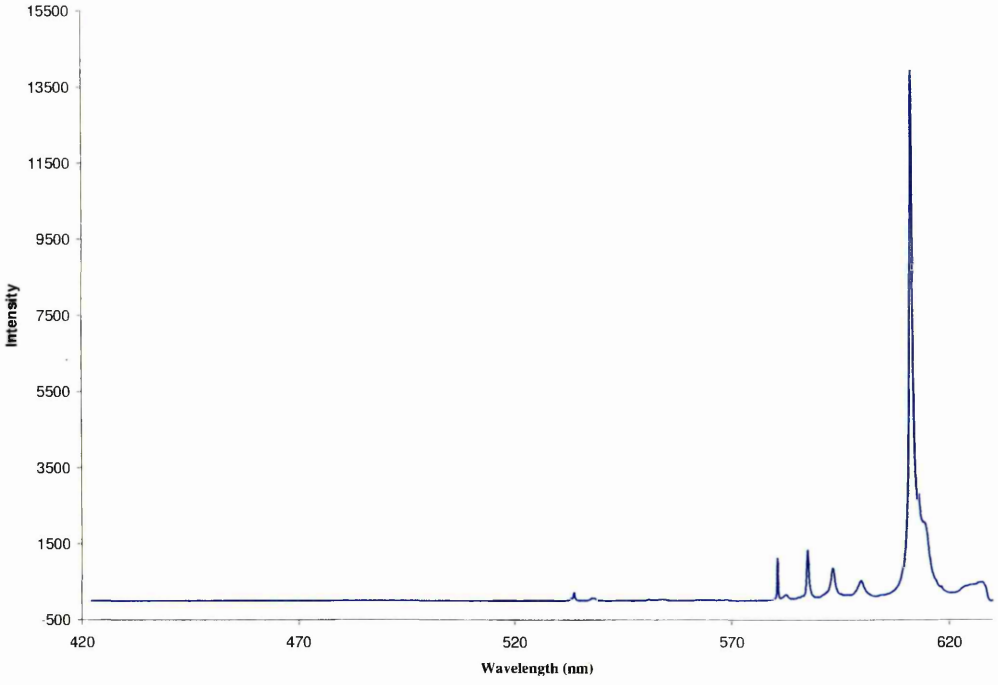

Figure 6.17 Anti-Stokes emission spectrum of Y_2O_3:Eu^{3+} (5 mol%) at room temperature in the region of 420-630 nm. Relative intensities are in arbitrary units.

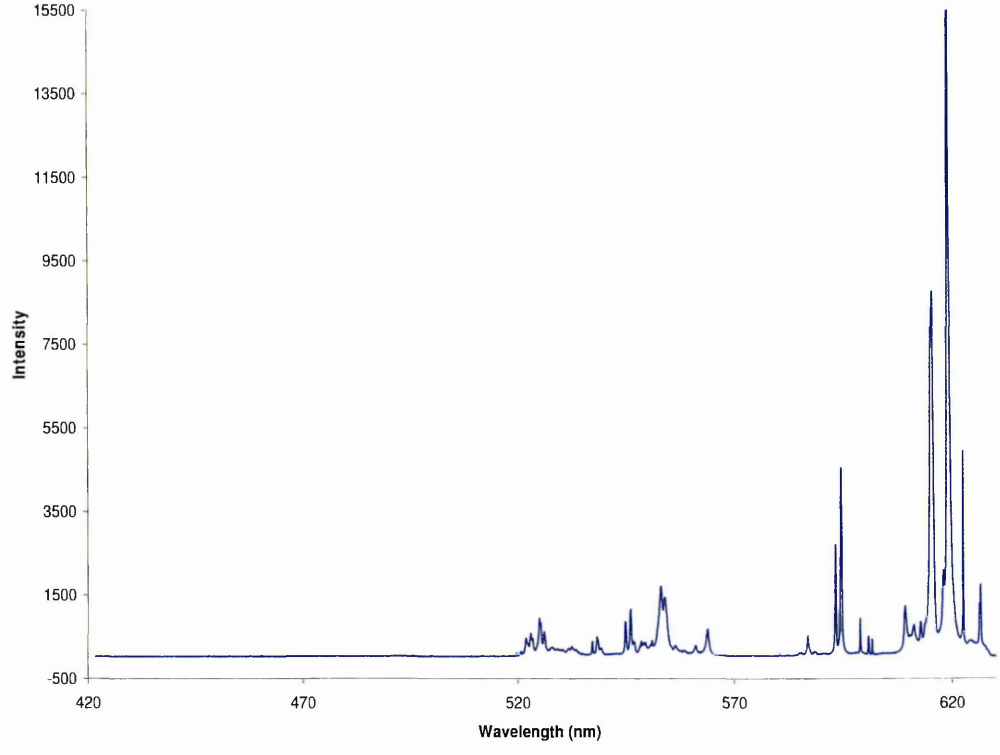

Figure 6.18 Anti-Stokes emission spectrum of YVO_4:Eu^{3+} (5 mol%) at room temperature in the region of 420-630 nm. Relative intensities are in arbitrary units.

A different splitting and bandwidth is found for the YVO_4:Eu phosphors compared with Y_2O_3:Eu. This variation may be attributed to different crystal fields experienced by the activator ions. Moreover, the intensity of the emissions is higher for these phosphors even for those samples containing lower activator concentrations.

Most of the manifolds summarised cannot be detected in co-doped Er-Eu phosphors, as they arise in the same wavelength band. Er bands are much stronger and prevent the Eu signal being detected. Therefore the influence of the former ion in emissions bands arising from Eu^{3+} ions cannot be assessed due to the overlapping. It has been decided to analyse the changes in the Er^{3+} spectrum when this second dopant ion was included in the system.

YVO_4:Er,Eu phosphors

To study the effect of Eu co-doping on YVO_4:Er phosphors, samples containing different nominal concentrations of both ions have been prepared. Keeping the Er^{3+} concentration constant at 2 mol%, samples containing 1, 2, 5, 10 and 20 mol% Eu^{3+} were prepared. In addition, samples containing 1, 2, 5, 10 and 20 mol% Er^{3+} were prepared keeping the Eu^{3+}concentration constant at 2 mol%. A sample doped with 1 mol% of both $Er^{3+}$and Eu^{3+}, and a sample doped with 20 mol% Er^{3+} and 1 mol% Eu^{3+} were also prepared.

Raman spectra of all synthesised samples were obtained after firing at 980°C. The emission spectra of all materials were integrated and the intensity of each transition evaluated.

Although the characteristic Eu^{3+} signal and emission bands from Er^{3+} were found together in the spectra, (Figure 6.19), the relative intensities of the Stokes and anti-Stokes emission bands in the Er^{3+} emission had changed in comparison with those observed for YVO_4:Er 2 mol% spectrum shown in Figure 6.14. Moreover, the relative intensity of the

anti-Stokes bands from the $^2H_{11/2}$ and $^4S_{3/2}$ levels in Er also changed, with emission arising from the former level now being more intense. These effects can be explained as a result of Er^{3+}- Eu^{3+} interactions, although noticeable quenching effects were also observed. Another phenomenon observed was that for co-doping Eu levels above 10 mol%, only the emissions from europium was detected. Enhancement in the intensity of Eu transitions was also found, evidenced by amplification in emissions from transitions $^5D_1 \rightarrow {}^7F_1$ and $^5D_0 \rightarrow {}^7F_2$ (other bands may also have been amplified but they arise exactly where stronger bands from erbium appear and the effect can not be quantified).

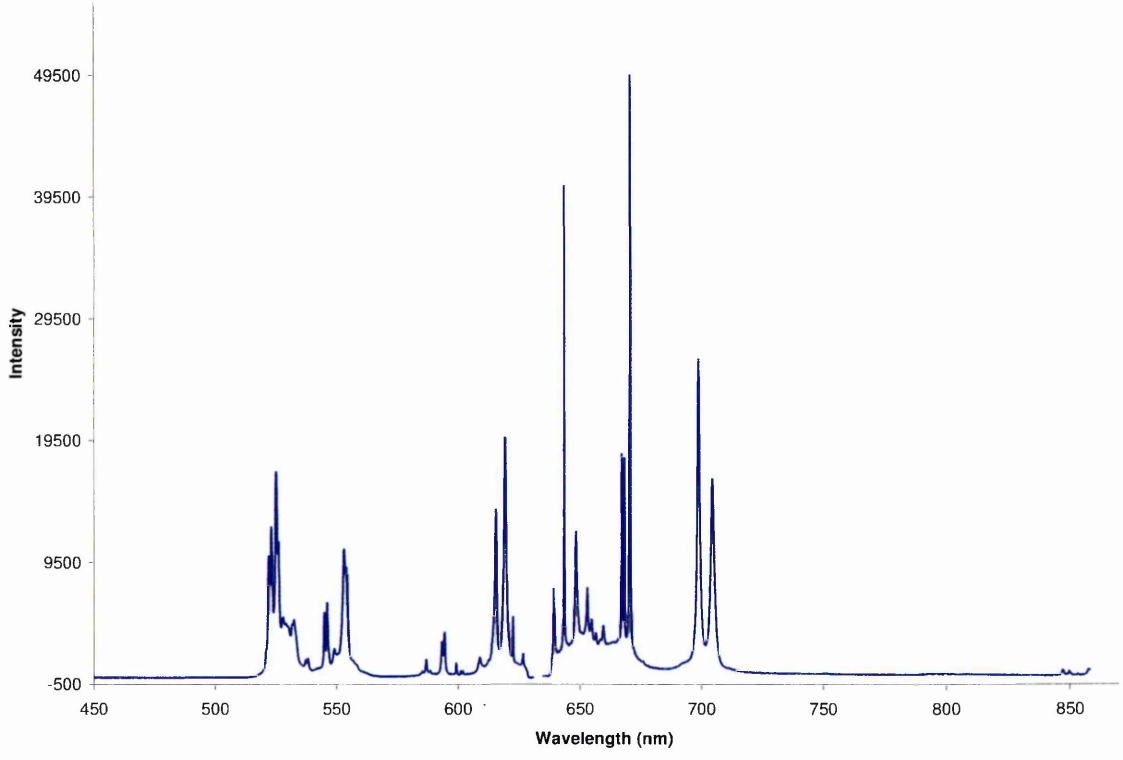

Figure 6.19 Emission spectrum of Y_2O_3:Er(2 mol%),Eu(5 mol%) powder phosphor at room temperature in the region 450-900 nm. Relative intensities are in arbitrary units.

It appears that invoking Er^{3+} to Eu^{3+} interactions as an explanation for the Er emission amplification as proposed in Chapter 4 for Y_2O_3:Er,Eu phosphors can be used here for YVO_4:Er,Eu phosphors. The de-excitation of the anti-Stokes emission from Er^{3+}

ions can be explained by means of resonant energy transfer between the $^5D_1$ level in Eu^{3+} and $^2H_{11/2}$ in Er^{3+}. Er^{3+} ions are excited to the $^2P_{3/2}$ level after absorbing two photons in the red, with a wavelength of 632.8 nm. Following non-radiative decay, the electron reaches the $^2H_{11/2}$ level. The energy difference between this level and the ground state in Er^{3+} approximates to the energy difference between the ground state level in the Eu^{3+} ion ($^7F_0$) and the excited $^5D_1$ energy level. By means of a cross relaxation mechanism, the excited Er^{3+} ion can transfer this energy to a neighbouring Eu^{3+}. Thus, Eu^{3+} can be promoted to the $^5D_0$ level from the ground state level. These energy levels in Er^{3+} and Eu^{3+} are very close in energy and a resonant energy transfer process takes place, weakening the Er^{3+} anti-Stokes emission in the presence of Eu^{3+}. The Er^{3+} ions excited to the $^4F_{9/2}$ level (by one photon absorption or non radiative decay from excited states) continue their normal relaxation process to the ground state without weakening the intensity of this emission. The loss in green emission intensity in comparison with the red signal is thus explained. On the other hand, $^2H_{11/2}$ is a hot band arising from thermal population from the low lying level $^4S_{3/2}$ [26]. The latter is now transferring energy to two resonant levels, one in erbium and one in europium, resulting in a greater deactivation from emissions arising from this energy level.

Thermal studies of Y_2O_3:Er[26,27] and Y_2O_3:Eu[25] phosphors showed the emission resulting from the $^2H_{11/2} \rightarrow {}^4I_{15/2}$ transition in Eu to be still active at -190°C, whereas emission from the $^5D_0$ in Eu was not detected below -100°C, but the band was still active at that temperature for YVO_4 co-doped phosphors. The energy of a 632.8 photon is not sufficient to populate $^5D_0$ from the ground level $^7F_0$ in Eu. The transition is however possible at room temperature due to the thermal population of levels $^7F_1$, $^7F_2$ and $^7F_3$, when the sum of the thermal and photon energy equals the energy gap. The intensities of these bands are proportional to the population of the level from which the emission arise obeying a Boltzmann-type distribution given by:

$$I = Ae^{\left(-\frac{\Delta E}{kT}\right)}$$

where I is the integrated intensity of the emission, A combines such parameters as radiative probabilities, degeneracies and photon energies of the transition. ΔE is the thermal energy and k is Boltzmann constant. The intensities of the Raman band at 260 cm^{-1}, the 524 nm emission line of Er and the 619 nm emission line from Eu were integrated and its natural logarithm represented versus 1/T (Figure 6.20). From the slope of the plots ΔE was derived:

Band	Raman band 260 cm^{-1}	Er band 524 nm	Eu band 619nm
ΔE / cm^{-1}	259±0.01	481±11.42	606±8.08

As in Chapter 4, these results militate towards resonant energy transfer, to account for population of the $^5D_0$ level in Eu, as at low temperatures the 632.8 nm excitation source is insufficient to overcome the energy gap. It should be noted that the temperature dependence of the emission bands would not be observed if the photon energy of the exciting light matched or exceeded that of the $^5D_0 \rightarrow {}^7F_0$ transition. Therefore it can be concluded that the observed emissions at low temperature are caused by population of Eu originated by resonant energy transfer.

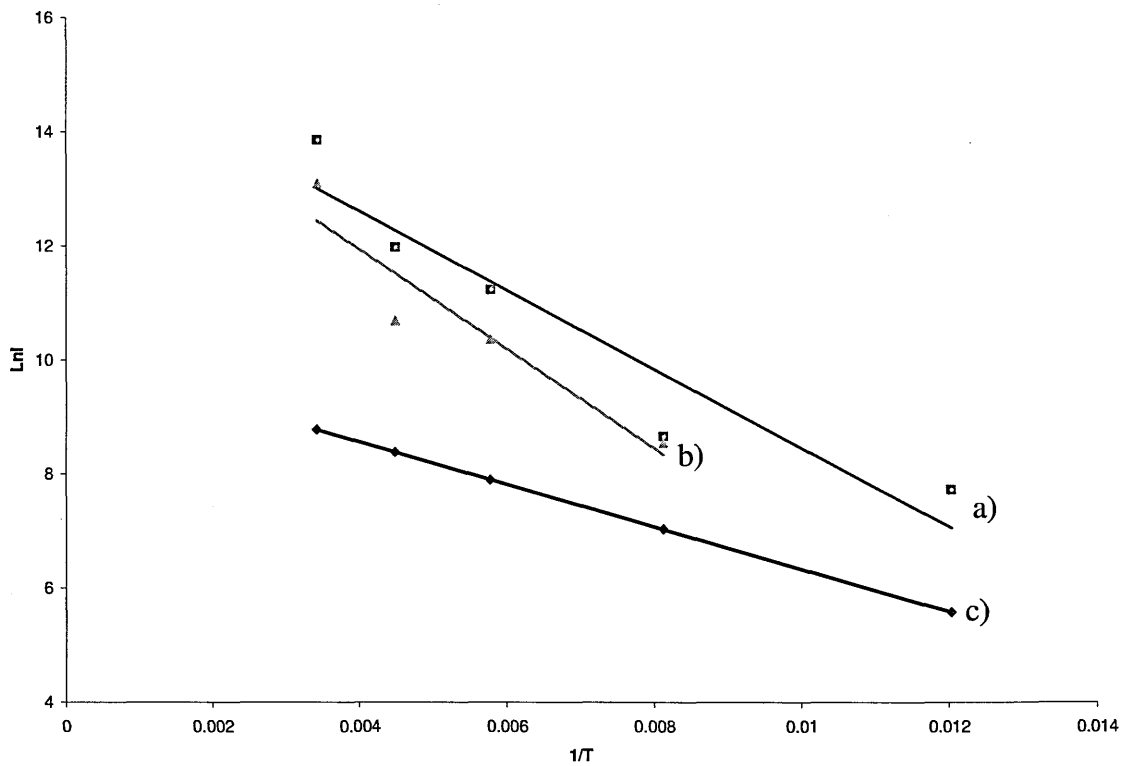

Figure 6.20 Plot of the natural logarithm of the band intensity versus the reciprocal of the absolute temperature for a) 524 nm emission band from Er b) 619 nm emission band from Eu, and c) anti-Stokes Raman band of YVO_4 at -260 cm^{-1}.

In summary, the addition of Eu^{3+} to YVO_4:Er phosphors does not enhance their luminescent properties. Indeed, for all the samples studied, the intensity of the emission bands was significantly weaker. A mechanism for the interaction of these two rare earth atoms has been proposed. The hypothesis has been supported by the results obtained from studies of the emission as a function of temperature.

References

[1] S. A. Miller, H. H. Caspers and H. E. Rast. *Phys. Rev.*, **168**, 964 (1968).

[2] G. H. Dieke, H. M. Crosswhite, H. Crosswhite, *Spectra and energy levels of rare earth ions in crystals*, New York, Interscience Publishers (1968).

[3] U. Kolitsch, D. Holtstam, *Eur. J. Mineral*, **16**, 117, (2004).

[4] A. Huignard, V. Buissette, G. Laurent, T. Gacoin, J. P. Boilot, *Chem. Mat.*, **14**, 2264, (2002).

[5] Y. T. Kim, Gopukumar, K. B. Kim, B. W. Cho, *J. Power Sources*, **112**, 504, (2002).

[6] S. Ekambaram, K. C. Patil, *J. Alloys Comp.*, **217**, 104 (1995).

[7] A. Newport, J. Silver, A. Vecht, , *J. Electrochem. Soc.*, **147**, 3944, (2000).

[8] A. Huignard, T. Gacaoin, J. P. Boilot, *Chem. Mat.*, **12**, 1090, (2000).

[9] S. Erdei, F. W. Ainger, *J. Crystal Growth*, **174**, 293, (1997).

[10] S. Erdei, N. M. Rodriguez, F. W. Ainger, W. B. White, D. Ravichandran, L. E. Cross, *J. Mat. Chem.*, **8**, 99, (1998).

[11] N. N. Greenwood and A. Earnshaw, *Chemistry of the elements*, Elsevier 2nd Edition (1997).

[12] A. K. Levine and F. C. Palilla, *Trans N. Y. Acad Sci. Ser.* **27**, 517, (1965).

[13] S. Golab, P. Solarz, G. Dominiak-Dzik, T. Lukasiewicz, W. Ryba-Romanowski, *J. Alloys Comp.*, **341**, 165, (2002).

[14] T. Tsuboi, *Physica B*, **294**, 84, (2000).

[15] T. Tsuboi, *Phys. Rev. B*, **62**, 4200, (2000).

[16] R. E. Di Paolo, E. Cantelar, X. M. Xang, T. Tsuboi, F. Cusso, *J.Phys.:Condens. Matter*, **13**, 7999, (2001).

[17] V. Buissette, A. Huignard, T. Gacoin, J. P. Boilot, P. Aschehoug, *Surf. Sci.*, **532-535**, 444, (2003).

[18] R. G. B. Wyckoff, *Crystal Structures Vol 3*, Intersciences Publishers, Inc. New York (1965).

[19] S. Erdei, *J. Mat. Sci.*, **30**, 4950, (1995).

[20] J. A. Capobianco, P. Kabro, F. S. Ermeneux, R. Moncorge, M. Betinelli, E. Cavalli, *Chem. Phys.*, **214**, 329, (1997).

[21] A. Jayaraman, G. A. Kourouklis, G. P. Espinosa, A. S. Cooper and L. G. Van Uitert. *J. Phys. Chem. Solids*, **48**, 755 (1987).

[22] M. Akinc, D. Sordelet, *J. Colloid Interface Sci*, **122**, 47 (1998).

[23] T. Miyakawa, D. L. Dexter, *Phys. Rev. B*, **1**, 2961, (1970).

[24] E. Okamoto, H. Masui, K. Muto, K. Awazo, *J. Appl. Phys.*, **43**, 2122 (1972).

[25] J. Silver , M.I. Martinez-Rubio, T.G. Ireland, G.R. Fern, R. Withnall, *J. Phys. Chem. B*, **105**, 9107 (2001).

[26] J. Silver , M.I. Martinez-Rubio, T.G. Ireland, G.R. Fern, R. Withnall, *J. Phys. Chem. B*, **105**, 948 (2001).

[27] J. Silver , M.I. Martinez-Rubio, T.G. Ireland, G.R. Fern, R. Withnall, *J. Phys. Chem. B*, **105**, 7200 (2001).

Chapter 7 Conclusions and further work

Conclusions

Cubic yttrium oxide (Y_2O_3:RE), cubic and monoclinic gadolinium oxide (Gd_2O_3:RE), cubic and monoclinic gadolinium yttrium oxide ($Gd_{2-x}Y_xO_3$:RE) and tetragonal yttrium vanadate (YVO_4:RE) rare earth doped phosphors were synthesised and characterised using powder X-ray diffraction (XRD), scanning electron microscopy (SEM), Raman spectroscopy and laser induced emission spectroscopy. The urea precipitation method has been shown to be suitable for the preparation of uniform spherical powder phosphors, facilitating the control over particle size and morphology by judicious manipulation of processing parameters such as reactant concentration, aging time and firing temperature. Combustion synthesis was also used to produce pure and doped YVO_4. X-ray diffraction patterns showed sample homogeneity for activator doping levels up to 20 mol%, and the inclusion of yttrium oxide in gadolinium oxide lattices showed the formation of only cubic phase when the concentration of the former was above 20 mol%. Structural information was also obtained using Raman spectroscopy. Spectra of the powders fired at 980 °C showed a single phase formed in the synthesis of all the samples. Raman spectroscopy was used as a tool for phase identification when it could not be verified by XRD. A shift in the Raman bands with activator concentration, compatible with a decrease in the atomic mass of the rare earth ion was detected.

Laser-induced emission spectroscopy under 632.8 nm wavelength excitation using a helium-neon laser source has been used to study the up-converting and down-converting properties of these phosphors. Phosphors singly doped with erbium at different concentrations were prepared and concentration quenching assessed. Y_2O_3:Er phosphors showed decrease in emission intensity for activator concentration over 3%, whereas YVO_4 based phosphors showed a steady increase in intensity for all of the bands in the Stokes and Anti-Stokes regions over the entire concentration range. Comparison of the emission of Er

in all the lattices was also carried out. Emission bands arising from the transitions $^4I_{9/2}$, $^4I_{11/2} \rightarrow {}^4I_{15/2}$ were stronger for YVO_4:Er with respect to the intensity of the same bands in the cubic Y_2O_3 lattice, whereas no emission from the level $^4F_{7/2} \rightarrow {}^4I_{15/2}$ or the bands thought to be associated with this level (a and b) was detected. The signal obtained from Er^{3+} in cubic Gd_2O_3 lattices was very similar to that obtained from in Y_2O_3, and similar splitting at the bands was detected. The main differences found were a slight narrowing of the bands and displacement to shorter wavelengths, as well as a significant weakening of the $^4F_{7/2} \rightarrow {}^4I_{15/2}$ emission band caused by less effective energy absorption of the second photon necessary for the up-conversion process, due to the higher phonon energy of this Gd_2O_3 lattice. Analysis of monoclinic Gd_2O_3:Er revealed differences in comparison with the cubic host. Most notably, only five emission manifolds were observed, and the splitting in the emission bands is very different from that of the activator in cubic lattices. The position of the bands did not change greatly, allowing the emission to be assigned to particular relaxation processes by comparison with the spectra obtained from cubic phases, but the line position varies indicating different splitting within the degenerate energy levels.

Er and Yb co-doped phosphors were prepared for theY_2O_3 and YVO_4 host lattices. The ratio of the integrated intensities of the $^4S_{3/2} \rightarrow {}^4I_{15/2}$ / $^4F_{9/2} \rightarrow {}^4I_{15/2}$ and $^2H_{11/2} \rightarrow {}^4I_{15/2}$ /$^4F_{9/2} \rightarrow {}^4I_{15/2}$ transitions decreases as the Yb^{3+} concentration increases in the cubic lattice, indicating that the presence of Yb^{3+} in the sample plays an active role in the de-excitation process, and that a new relaxation pathway has been opened up by introducing this ion to the system. A variation in the intensity of the emissions arising from different excited states compared to those from the control sample is observed as the concentration of Yb^{3+} changed. The most notable was an approximately 2-fold increase in the red signal due to the $^4F_{9/2} \rightarrow {}^4I_{15/2}$ transition when Yb^{3+} concentration was 2 mol%. The presence of

Yb together with Er deactivates the up-conversion, which is more apparent at concentrations above 5mol% Yb, but at low Yb^{3+} concentrations there is some evidence for enhancement of the up-conversion. This may be attributed to Er^{3+} - Er^{3+} resonant energy transfer in the absence of Yb^{3+}, and thus dissipating some of the radiation. When Yb^{3+} is present at levels of 1mol% the Er^{3+} - Er^{3+} quenching ceases as there is now Er^{3+} - Yb^{3+} interaction where the energy loss by energy transfer is smaller. Then only as the Yb^{3+} concentration increases further loss of the anti-Stokes bands and concomitant growth of the Stokes bands is detected.

Conversely, it has been found that Yb^{3+} activates the emission of YVO_4:Er phosphors, this is more apparent at concentrations of 5 mol%. Interestingly the increase of Yb concentration in the lattice produced a steady increase of emission intensity for almost all the electronic transitions detected. Deactivation was only detected for relatively high concentrations of the activator (20 mol%). Only as the Yb^{3+} concentration in increased above 10 mol% was a reduction in emission intensity detected. This effect can be explained by considering energy transfer processes from Er^{3+} to Yb^{3+} in both lattices. Since the energy difference between the Er^{3+} and Yb^{3+} levels involved in the process are not equivalent, the energy transfer is associated with phonon emission explaining the host lattice dependence of this effect.

The $^2P_{3/2}$ energy level in Er can be reached using a 632.8 nm excitation source. Once the Er^{3+} ion has been excited to this level, it decays non-radiatively to levels such as $^4G_{11/2}$. The energy difference between this level and the $^4F_{9/2}$ in Er^{3+} approximates to the energy difference between the ground level in Yb^{3+} ($^2F_{7/2}$) and the next available energy level ($^2F_{5/2}$). Therefore it is feasible that excited Er^{3+} can transfer that energy to a nearby Yb^{3+}, via the cross relaxation mechanism $^4G_{11/2} \rightarrow {}^4F_{9/2}$ (Er^{3+}) : $^2F_{7/2} \rightarrow {}^2F_{5/2}$ (Yb^{3+}). Once this energy transfer has taken place, Er^{3+} ions can fall back to the ground state releasing a red photon in the range 648 and 685 nm. The intensity of the emission due to this

relaxation path is added to the signal obtained from Er^{3+} ions following the relaxation pathway in absence of Yb^{3+}. Moreover the proposed mechanism to enhance the blue-green $^4F_{7/2} \rightarrow ^4I_{15/2}$ transition involves a back transfer of the energy previously absorbed by the Yb^{3+} ions. Yb^{3+} ions excited to the $^2F_{5/2}$ can transfer this energy to nearby Er^{3+} ions in the ground state. Er^{3+} ions are excited to the $^4I_{11/2}$ level and, before they have time to release that energy, absorb another photon from surrounding Yb^{3+}, reaching the $^4F_{7/2}$ level. This absorbed energy can be released by a downward transition to the ground state. The emission taking place is a blue-green photon of wavelength between 468 and 479 nm. These energy transfers from Er^{3+} to Yb^{3+} ions also explain the decrease of the emission intensity due to the $^2H_{11/2} \rightarrow ^4I_{15/2}$ and $^4S_{3/2} \rightarrow ^4I_{15/2}$ transitions. The level by level cascade relaxation route is not followed by all the Er^{3+} ions in the lattice. Some of the Er^{3+} ions bypass the levels where these processes originate and therefore lower their intensity. The relaxation process is slightly different in YVO_4. There is non radiative decay from the excited level $^4F_{7/2}$, and after receiving the energy back transfer from lower levels the energy decays non-radiatively to lower levels, hence enhancing emissions originated in $^2H_{11/2}$ and $^4S_{3/2}$ levels.

Y_2O_3:Eu and YVO_4 samples were prepared to be used as controls in the study of the Er-Eu co-doped phosphor systems. Most of its emission manifolds arise in the same wavelength bands as much more intense emissions previously reported for Er. Therefore it was decided to assess the changes in the Er^{3+} spectrum when this second dopant was included in the system. In general a deactivation of luminescence was found due to resonant energy transfer between the $^2H_{11/2}$ level in Er and $^5D_1$ level in Eu. But also change in the anti-Stokes / Stokes ratio for Er was detected, further demonstrating the existence of this interaction. The de-excitation of the anti-Stokes emission from Er^{3+} ions can be explained by means of resonant energy transfer between the $^5D_1$ level in Eu^{3+} and $^2H_{11/2}$ in Er^{3+}. Er^{3+} ions are excited to the $^2P_{3/2}$ level after absorbing two photons in the red

(632.8nm). Following a non-radiative decay, the electron reaches the $^2H_{11/2}$ level. The energy difference between this level and the ground state in Er^{3+} approximates to the energy difference between the ground level state in the Eu^{3+} ion ($^7F_0$) and the excited $^5D_1$ energy level. By means of a cross relaxation mechanism, the excited Er^{3+} ion can transfer this energy to a neighbour Eu^{3+}. Thus, the Eu^{3+} can be promoted to the $^5D_0$ level from the ground state level. These energy levels in Er^{3+} and Eu^{3+} are very close in energy and an energy transfer resonant process takes place, weakening the Er^{3+} anti-Stokes emission in the presence of Eu^{3+}. The Er^{3+} ions excited to the $^4F_{9/2}$ level (by one photon absorption or no radiatively decay from excited states) continue their normal relaxation process to the ground state without weakening the intensity of this emission. The loss in the green emission intensity in comparison with the red signal is thus explained.

For the $^2H_{11/2} \rightarrow {}^4I_{15/2}$ transition in Y_2O_3 phosphors, Er ions in both C_2 and S_6 sites made contributions to the emission bands. When studying the $^2H_{11/2} \rightarrow {}^4I_{15/2}$ transition as a function of the concentration of Eu^{3+} it was found that the bands arising from C_2 sites were deactivated while emission bands arising from Er^{3+} in S_6 sites were enhanced with increased concentration of Eu^{3+}. These results suggest that the energy transfer process is favoured in the higher symmetry site S_6. For the YVO_4:Er,Eu phosphors, the relative intensity of the Anti-Stokes bands from the $^2H_{11/2}$ and $^4S_{3/2}$ levels in Er also modified, with emission arising from the former level being now stronger. Enhancement in the intensity of Eu transitions has also been found, detecting amplification in emissions from transitions $^5D_1 \rightarrow {}^7F_1$ and $^5D_0 \rightarrow {}^7F_2$ (other bands may also have been amplified but they arise exactly where stronger bands from erbium appear and the effect can not be quantified). $^2H_{11/2}$ is a hot band arising from thermal population from the low lying level $^4S_{3/2}$ which is now transferring energy to two resonant levels, one in erbium and one in europium, resulting in a greater deactivation from emissions arising from this energy level.

Thermal studies in Y_2O_3:Er and Y_2O_3:Eu phosphors showed the emissions from $^2H_{11/2} \rightarrow {}^4I_{15/2}$ transition in Eu still active at -190 °C, whereas emission from the $^5D_0$ in Eu exhibited a temperature dependence, not being detected for temperatures below -100 °C, but the band was still active at that temperature for YVO_4 co-doped phosphors. The energy of a 632.8 photon is not sufficient to populate $^5D_0$ from the ground level $^7F_0$ in Eu. The transition is however possible at room temperature due to the thermal population of levels $^7F_1$, $^7F_2$ and $^7F_3$, when the sum of the thermal and photon energy equals the energy gap. $^5D_0$ level in Eu can not be achieved at low temperatures as the excitation source is insufficient to cover the energy gap, and it can be concluded that the presence of the band in the spectra confirms the hypothesis of resonant energy transfer.

7. 2 Further work

This project could be further developed by studying the effect of co-dopants (Yb and Eu) on the luminescent properties of erbium based phosphors incorporated into cubic and monoclinic gadolinium oxide and cubic and monoclinic gadolinium yttrium oxide.

In addition, further work in relation to this project could involve the study of the luminescent properties of other rare-earth elements such as praseodymium, samarium, terbium, dysprosium, holmium and thulium in the host lattices used herein.. The 3+ ions of these elements have excited energy levels close in energy to those in erbium ions, and the study of co-doped samples in the different host lattices investigated in this research work would be of interest to further understand energy transfer mechanisms in rare earth doped crystals, and their influence on luminescence. This could lead to new uses for the materials concerned. It would also be interest to study different combinations of rare earth dopants in order to tailor the lanthanide – host lattice combinations that better suit the

needs of a particular application, as well as maximising the emission intensity and wavelength range for a particular ion or combination of ions.

As has been stated previously in this thesis, the use of excitation sources resonant with excited energy levels in the luminescent centre may produce enhanced intensity of Raman bands, leading to error when using these bands for emission normalisation. A good way to ascertain the intensity of the Raman scattering separated from the luminescent emissions is to vary the duration of the excitation. A series of experiments where phosphors are excited with short pulses of light (a few nanoseconds) will provide a better measurement of the Raman band intensity. This intensity would later be used to normalise the luminescent spectra of the activator ions in an attempt to reduce experimental error.

YVO_4 lattices absorb UV radiation and charge-transfer processes have been reported. It would be interesting to asses the luminescent properties of the erbium activator and co-dopant systems under this type of radiation in this lattice.